NONLINEAR EDGE WAVES IN MECHANICAL TOPOLOGICAL INSULATORS

D D J M SNEE

PhD

2021

NONLINEAR EDGE WAVES IN MECHANICAL TOPOLOGICAL INSULATORS

DAVID DOUGLAS JOHN MARTIN SNEE

A thesis submitted in partial fulfilment of the requirements of the University of Northumbria at Newcastle for the degree of Doctor of Philosophy

Research undertaken in the Faculty of Engineering and Environment

January 2021

Acknowledgements

It is with immense gratitude that I acknowledge the support, both professionally and personally, of my principal supervisor Dr Yiping Ma. A brilliant mentor whose knowledge, wisdom, and passion for all things science has been an unparalleled inspiration throughout my time as a PhD student. I would also like to thank the staff in the Department of Mathematics, Physics, and Electrical Engineering at Northumbria University for their support and guidance, not only throughout my postgraduate experience but also during my undergraduate years.

On a personal level, I would like to express my overwhelming gratitude to my family who have supported me and nourished my immense passion for science throughout my life. The only reason I am in the position to produce such a piece of work is due to the love and support of those closest to me, including those who are no longer with us.

Finally, I would like to thank my girlfriend who has supported me throughout my time as a PhD student. My emotional rock who has brought me back to reality during tough times and who has reminded me, many times over, that there is a light at the end of any tunnel.

Abstract

We show theoretically that the classical 1D nonlinear Schrödinger (NLS) and coupled nonlinear Schrödinger (CNLS) equations govern the envelope(s) of localised and unidirectional nonlinear travelling edge waves in a 2D mechanical topological insulator (MTI). The MTI consists of a collection of pendula with weak Duffing nonlinearity connected by linear springs that forms a mechanical analogue of the quantum spin Hall effect (QSHE). It is found, through asymptotic analysis and dimension reduction, that the NLS and CNLS respectively describe the unimodal and bimodal properties of the nonlinear system.

The governing bimodal CNLS is found to be non-integrable by nature and as such we discover new solutions by exploring the spatial dynamics of the reduced travelling wave ODE with general parameters. Such solutions include travelling fronts and, by numerically continuing these fronts, one can find vector soliton (VS) in non-integrable CNLS equations. The equilibria can also undergo both pitchfork and Turing bifurcation in the reversible spatial dynamical system and we discuss relevant conditions for the existence and consequences of such critical values.

We briefly discuss the necessity of the developed front condition in forming such structures and present an analytical framework for front-grey soliton collisions by utilising conserved quantities of the non-integrable CNLS. The existence/stability of front and VS solutions can be inferred by spatial hyperbolicity and linear stability of the background fields, with the criteria presented here. VS solutions are considered in the form of bright-bright, bright-dark, and dark-dark solitons and their collision dynamics are explored qualitatively in the non-integrable regime. The Turing analysis presents the existence of periodic and localised patterned states in the CNLS, and we compare these solutions to those found in the analysis of the Swift-Hohenberg equation.

Theoretical predictions from the 1D (C)NLS are confirmed by numerical simulations of the original 2D MTI for various types of travelling waves and rogue waves. As a result of topological protection the edge solitons persist over long time intervals and through irregular boundaries. Due to the robustness of topologically protected edge solitons (TPES) it is suggested that their existence may have significant implications on the design of acoustic devices. Space-time simulations show a clear possibility of utilising MTIs in acoustical cloaking with TPES a vital player in such processes.

Declaration

I declare that the work contained in this thesis has not been submitted for any other award and that it is all my own work. I also confirm that this work fully acknowledges opinions, ideas and contributions from the work of others.

Any ethical clearance for the research presented in this thesis has been approved. Approval has been sought and granted by the Faculty Ethics Committee on 26/10/2017.

I declare that the Word Count of this Thesis is 59,850 words

Name: **David Douglas John Martin Snee**

Signed:

Date: 31/01/2021

List of Publications, Presentations, and Grants

Publications

- Snee, D.D. and Ma, Y.-P., 2019. Edge solitons in a nonlinear mechanical topological insulator. *Extreme Mechanics Letters*, 100487.

To be Submitted

- Snee, D.D. and Ma, Y.-P., Fronts and solitons in the two-component coupled nonlinear Schrödinger equation.
- Snee, D.D. and Ma, Y.-P., Energy Transfer Amongst Vector Edge Solitons in a nonlinear mechanical topological insulator.

Contributed Talks

- Snee, D.D., 2020. *Coupled Nonlinear Schrodinger Equations and their Applications to Nonlinear Mechanical Topological Insulators*, Virtual British Early Career Mathematicians' Colloquium 14-15 July, University of Birmingham.
- Snee, D.D., 2019. *Coupled Nonlinear Schrodinger Equations and their Applications to Nonlinear Mechanical Topological Insulators*, MPEE Research Seminar 23 October, Northumbria University.
- Snee, D.D., 2019. *Generalised Coupled Nonlinear Schrodinger Equation and its Applications to Nonlinear Mechanical Topological Insulators*, 3rd IMA Conference on Nonlinearity and Coherent Structures 10-12 July, Northumbria University.
- Snee, D.D., 2019. *Generalised Coupled Nonlinear Schrodinger Equation and its Applications to Nonlinear Mechanical Topological Insulators*, British Applied Mathematics Colloquium 24-26 April, University of Bath.
- Snee, D.D., 2018. *Edge Solitons in a Nonlinear Mechanical Topological Insulator*, Mathematics and Mathematical Physics Series 6 June, Northumbria University.

- Snee, D.D., 2018. *Edge Solitons in a Nonlinear Mechanical Topological Insulator*, LMS Northern Regional Meeting and Workshop on Advances in the Theory of Nonlinear Waves 23-25 May, Northumbria University.

Accepted Talks

- Snee, D.D., 2020. *Coupled Nonlinear Schrodinger Equations and their Applications to Nonlinear Mechanical Topological Insulators*,SIAM Conference on Nonlinear Waves and Coherent Structures, University of Bremen. (Cancelled)
- Snee, D.D., 2020. *Coupled Nonlinear Schrodinger Equations and their Applications to Nonlinear Mechanical Topological Insulators*, Joint BMC-BAMC Meeting, Glasgow University. (Postponed)

Poster Presentations

- Snee, D.D., 2018. *Edge Solitons in a Nonlinear Mechanical Topological Insulator*, UK-Japan Workshop on Analysis of Nonlinear Partial Differential Equations 16-18 May, Swansea University.

Awarded Grants

- British Applied Mathematics Colloquium 2019 travel award.

Remember to look up at the stars and not down at your feet. Try to make sense of what you see, and wonder about what makes the universe exist. Be curious.

- **Professor Stephen Hawking**

Contents

List of Figures

List of Tables

Abbreviations

AUTO	Auto-07p software
CNLS	Coupled Nonlinear Schrödinger Equation
cSH23	Conservative quadratic-cubic Swift-Hohenberg Equation
dSH23	Dissipative quadratic-cubic Swift-Hohenberg Equation
EGV	Equal group velocity
FCGLE	Forced-complex Ginzburg-Landau Equation
FM	Focusing Makanakov system
FPUT	Fermi-Pasta-Ulam-Tsingou (lattice)
GVD	Group velocity dispersion
IDFT	Inverse discrete Fourier transform
MTI	Mechanical topological insulator
NLS	Nonlinear Schrödinger Equation
ODE	Ordinary Differential Equation
PDE	Partial Differential Equation
PTI	Photonic topological insulator
QHE	Quantum Hall effect
QSHE	Quantum spin Hall effect
RHO	Reversible homoclinic orbit
SHATS	Spatially hyperbolic and temporally stable
SPM	Self-phase modulation
TI	Topological insulator
TPES	Topologically protected edge solitons
TPVES	Topologically protected vector edge solitons
XPM	Cross-phase modulation

Chapter 1

Background material: a review of current literature

The ability to robustly control light and sound is of fundamental interest and has broad applications in various subdisciplines of physics, including but not limited to photonics and acoustics (phononics) [100, 127, 72]. Traditional materials found in nature are limited in their functionalities to manipulate wave propagation, which has led to the emergence over the past few decades of metamaterial designs that borrow certain ideas from condensed matter physics [47, 113, 201, 140]. As a preface to the work contained in this thesis, the following introductory chapter presents a review of the current literature on the subject of robust, nonlinear wave propagation, as well as wave propagation in theoretically and experimentally developed metamaterials. In particular, appropriate to the work presented here, we will explore and analyse the current literature on coherent, travelling structures of nonlinear wave equations, with a particular interest in the scalar and vector nonlinear Schrödinger (NLS) equations. A brief insight into the type of structures one expects in certain regimes of the NLS equations is given, as well as the stability and collision properties of the structures. In this chapter we will also introduce the concept of a topological insulator (TI) and describe the physical behaviours that differentiate them from standard insulating materials. We discuss and review recent advancements of metamaterials utilising these physical behaviours, with a specific focus on those systems formed using mechanical components. Appropriate to our work, we discuss the linear and nonlinear (if any) analysis of these experimentally realised or theoretically proposed systems.

Nonlinear wave equations have gathered much attention over the past century, particularly due to the great difficulty in forming a general analysis for such equations. The theory of nonlinear waves in continuous systems has already formed a cornerstone of nonlinear science [5], whilst the theory of nonlinear

waves in discrete systems has flourished more recently, especially in the context of nonlinear optics and Bose-Einstein condensates [107]. In mechanical lattices, the study of nonlinear waves dates back to the classical 1D Fermi-Pasta-Ulam-Tsingou (FPUT) lattice [68], whose 1D and 2D extensions are still of great interest in recent literature [109, 36, 46]. In particular, the FPUT system may be reduced in the continuum limit to the Korteweg-de Vries (KdV) equation [5], which is a nonlinear wave equation usually portrayed with a highest-spatial derivative order of 3 and a simple nonlinear term that is a product of the field variable and its spatial derivative.

Arguably, the two nonlinear wave equations which boast the greatest interest from academics are the KdV equation [123] and the NLS equation [4], as well as their variants/extensions. The key reasoning behind this is the 'universality' of the two equations. The two equations arise naturally in many systems, across multiple disciplines, when one has a nonlinear, dispersive system that is maximally balanced. When the system is weakly dispersive and weakly nonlinear, with quadratic nonlinearity, then the underlying envelope dynamics of the system are described by the KdV equation [5]. Similarly, if the system is weakly nonlinear, with a cubic/Kerr nonlinearity, but now a finite dispersion at the scale of the carrier wave, then the envelope dynamics are governed by the NLS equation [176]. For this reason, KdV-type equations appear to govern the propagation of (quasi)-monochromatic wave-packets in many areas such as plasmas [206, 163] and shallow water waves [123], with NLS-type equations appearing in areas such as nonlinear optics [50] and magnetic-spin waves [215]. The problems presented in our work are shown to exhibit a cubic nonlinearity, so we now streamline our focus to the literature studying the NLS equation.

1.1 Nonlinear Schrödinger equations

As mentioned previously, the NLS is a maximally balanced equation universally obtained by considering slowly-varying envelopes of a weakly-nonlinear, dispersive system; any dissipation must be negligible. In general, the scalar NLS equation may be written as,

$$iu_t + d_1 u_{xx} + g_1 u|u|^2 = 0 \tag{1.1}$$

where $u = u(x,t)$ is a complex envelope dependent on both space and time variables. The parameters d_1 and g_1 are the dispersion and nonlinear coefficients respectively. Variations of this equation in 1D include the derivative NLS [150] and the cubic-quintic NLS [143], as well as discretisations [3, 57]. Note

that Eq. (1.1) may be rescaled, so that the coefficients are removed from the equation, by the following transformation of variables,

$$t = \frac{-\tilde{t}}{d_1}, \quad u = \sqrt{2\left|\frac{d_1}{g_1}\right|}\tilde{u}. \tag{1.2}$$

By substituting the transformation (1.2) into Eq. (1.1), and dropping the $\sim$ notation, one recovers the NLS in its 'standard' form,

$$iu_t - u_{xx} - 2su|u|^2 = 0, \tag{1.3}$$

where the sign of $s = \text{sgn}(d_1 g_1)$ provides very different dynamics, permitting contrasting solutions. In short, the case of $s = 1$ corresponds to anomalous-dispersion or self-focusing (shortened to focusing), where as $s = -1$ corresponds to normal-dispersion (denoted as defocusing). For this reason, the two regimes are usually presented as two different systems, namely the focusing/defocusing NLS system. To distinguish the key differences between the two regimes we present a brief description of the two.

The focusing system is the regime in which the NLS equation was first formally derived [111, 50] and is embedded in the history of nonlinear optics. A stationary, single frequency light beam propagating in a medium with a nonlinear refractive index is described by the NLS, where u represents the electric field in this context [166]. In this setting, the type of dispersion relies on how the refraction index changes as a function of the wavelength of the light beam. One has normal (anomalous) dispersion if the refraction index decreases (increases) when the wavelength of the light is increased [32]. It has already been mentioned that the NLS also governs the complex amplitude of a quasi-monochromatic pulse in dispersive, weakly-nonlinear media, such as optical fibres. In this context, the dispersion that we talk about is the group velocity dispersion (GVD) imposed by a frequency dependence of the refractive index [4]. The consequence of GVD is that the different frequency components making up the pulse will travel with different group velocities, effectively broadening the pulse shape. The GVD may be formulated by considering the wavenumber as a function of the frequency and producing the second derivative of this function. Fundamentally, if the GVD is positive (negative) then the longer wavelengths travel faster (slower) than shorter wavelengths. In relation to the NLS equation, the positive GVD corresponds to the defocusing regime and the negative GVD the focusing regime [4]. In the defocusing case the front of the envelope travels faster than the back, whilst in the focusing case the pulse becomes shortened/-compressed over time.

One important aspect of pulses travelling through optical-Kerr media is the induction of self-phase modulation (SPM) [14]. Through this self-modulation, the front of the envelope is shifted to larger wavelengths, whilst the back is shifted to shorter wavelengths. As one can see, this SPM caused by the nonlinearity can effectively balance the GVD of the dispersive term in the self-focusing regime $(s = 1)$, whereas the defocusing regime $(s = -1)$ will exhibit the normal dispersion. Simultaneously, the modulational instability tells a similar story as this phenomenon is only present in the case of anomalous dispersion. Modulational instability (pseudonym Benjamin-Feir instability [24]) is a phenomenon in dispersive systems where deviations from a periodic waveform (Stoke's wave) are reinforced by the nonlinearity, causing the breakup of the wave into trains of pulses. This instability can be analysed by considering the gain spectrum of the NLS [14] via linear stability analysis, where it is found that the instability may only be present in the focusing regime. Formally, there is the possibility of exponential growth of a perturbed solution only in the focusing regime, and is only possible for an interval of perturbation wavenumbers within this regime; the growth rate is given by the gain function of the analysis. In the context of Bose gases, where the NLS describes oscillations of the gas at zero temperature [154], the focusing regime corresponds to an attraction of particles and the defocusing regime a repulsion of particles [209].

Beyond the scalar NLS, the underlying envelope dynamics of dispersive, weakly nonlinear media with two nonlinearly-interacting components are often governed by coupled/vector NLS-type equations. Coupled NLS (CNLS) equations arise naturally when multiple wavefunctions interact nonlinearly, with similar group velocity, and plays a key role in the optics setting by describing nonlinear phenomena in birefringent optical fibers [138] and photorefractive materials [213]. A general N -component CNLS equation can also be constructed for Bose-Einstein condensates (BECs) with N components [112] and is often referred to in BEC literature as the Gross-Pitaevskii (GP) equations [152, 21]. The cubic CNLS system may be written with general coefficients as,

$$iu_t + d_1 u_{xx} + u(g_1|u|^2 + g_2|v|^2) = 0, \tag{1.4}$$

$$iv_t + d_2 v_{xx} + v(g_3|v|^2 + g_4|u|^2) = 0, \tag{1.5}$$

where we now have the two component fields $u = u(x,t)$ and $v = v(x,t)$. In general, the type of dispersion imposed by the coefficients of the CNLS is difficult to categorise without imposing specific choices. We note the inclusion now of cross-modulation terms (XPM). In the setting of nonlinear optics, this XPM corresponds to a nonlinear effect where one wavelength of light causes an ef-

fect on the phase of another wavelength of light. In a broader sense, there is an effect from one wavefunction onto another wavefunction, which subsequently feeds an effect back onto the original wavefunction described by the system (1.4-1.5). As one would expect, the equations decouple into two NLS equations without the presence of XPM or reduce to one NLS equation when one wavefunction is trivial, i.e. reduces to Eq. (1.1) when $v = 0$. Small differences in the nonlinear coefficients g_{1-4} can then cause large differences in the spatio-temporal behaviour of the fields u, v; small differences may cause stronger/weaker nonlinearites in which plane waves may gain or lose energy to the other component. Generally, the system (1.4–1.5) has been shown to be integrable in three different, key regimes. Rescaling such that $d_1 = d_2 = 1$, the three regimes are given as *(i)* focusing $(g_{1-4} = 2)$, *(ii)* defocusing $(g_{1-4} = -2)$, and *(iii)* mixed dispersion $(g_{1,4} = \mp 2, g_{2,3} = \pm 2)$. The focusing system is often referred to as the Manakov system [136] and, for denotation purposes, we will refer to the remaining two regimes as the defocusing and mixed Manakov systems. The Manakov systems have provided a stage for ongoing analysis of modulational instability [162, 60] and in the modelling of physical phenomena [158, 159]. The linear stability of background fields in the Manakov systems are well studied in [60], where spectral analysis of the CNLS is considered. We note that the CNLS may be extended to N components [112], however, the dynamics of the equation become more complicated and inherently more difficult to study analytically due to an increase in the parameter space. For the purpose of our work we briefly note the N-component CNLS, but focus on solutions of the scalar and 2-component vector equations.

1.1.1 Scalar solitons

One may expect significant difference of propagation dynamics for the focusing and defocusing NLS equations. The balance of the dispersive and nonlinear terms in the focusing regime, leading to modulational instability, permits the propagation of robust travelling pulses called *solitons*. Solitons are self-reinforced, localised wave packets which maintain a constant shape and group velocity in finite time and soliton solutions are supported in the NLS due to its well-known integrability property. When solitons interact with each other in the medium they behave elastically, i.e. they propagate through each other leaving no sign of an interaction other than through a phase and positional shift. Many physical disciplines typically refer to solitary waves as solitons, despite the fact that solitary waves may exhibit inelastic collision dynamics. We will adopt this more-general definition, grouping together stably-propagating soli-

tary waves and solitons, and denoting both as solitons. This grouping only becomes apparent in the multi-component case where inelastic collisions are a common possibility. For this reason, we describe a soliton here as a localised, self-reinforced wave packet that exhibits little to no dispersion over a long time-frame, but may exhibit significant loss of energy during collisions.

The key property of the NLS equation, as it is written in Eq. (1.3), is the integrable nature of the equation. More specifically, the equation is directly solvable and exact solutions may be derived through special techniques. One such technique is the Inverse-Scattering Transform (IST) which, in its purest form, is a nonlinear Fourier transform of the PDE. The IST was first formulated for the focusing NLS by Zakharov and Shabat [166], with an extension to the defocusing NLS by the same authors [209]. We also note a thorough comparison of how the initial value problem is solved in the linear case $(s = 0)$ and nonlinear case $(s = \pm 1)$ in [59]. Generally, the steps in which one applies the corresponding method may be written as the functional chains,

$$\text{Linear problem:} \quad u(x,0) \xrightarrow{\text{FT}} \hat{u}(k,0) \to \hat{u}(k,t) \xrightarrow{\text{IFT}} u(x,t) \tag{1.6}$$

$$\text{Nonlinear problem:} \quad u(x,0) \xrightarrow{\text{ST}} ST(0) \to ST(t) \xrightarrow{\text{IST}} u(x,t) \tag{1.7}$$

where FT and IFT denote the (Inverse) Fourier transform, and ST and IST denote the (Inverse) scattering transform [59]. The field variable $\hat{u}$ represents the solution in Fourier space with k the wavenumber. In general, the linear problem is solved by moving into Fourier space, evolving the problem in this space in time through initial data, and then transforming back into physical space. This does, however, require the Fourier mapping to be invertible. Both the linear and nonlinear analysis depend on the particular boundary conditions that one considers; here we consider those solutions $u(x,t)$ which decay to 0 as $|x| \longrightarrow \infty$.

The transformation from physical space, into spectral data, used by Zakharov and Shabat [166, 208] is formed by first writing the NLS equation as a Lax pair [59]. The NLS may be represented by two homogeneous, linear ODEs of the form,

$$\Phi_x = X\Phi, \quad \Phi_t = T\Phi, \tag{1.8}$$

where X, T are the 2×2 Lax operators and Φ is a non-trivial solution. Crucial for integrability, the solution and the operators must also depend on a complex spectral variable $\lambda \in \mathbb{C}$. The system (1.8) representation for the NLS equation is known as the Zakharov-Shabat system [166]. To ensure a non-trivial solution, the operators must also satisfy, for all λ, the compatibility condition

$X_t - T_x + XT - TX = \mathbf{0}$, where $\mathbf{0} =$ zero matrix [59]. The specific structure of the operators depends on the PDE one is considering; the NLS operators take the form of,

$$X = i\lambda\sigma_3 + Q(x,t), \quad T = 2i\lambda^2\sigma_3 + 2\lambda Q + i\sigma_3(Q^2 - Q_x), \tag{1.9}$$

where

$$\sigma_3 = \begin{bmatrix} 1 & 0 \\ 0 & -1 \end{bmatrix}, \quad Q(x,t) = \begin{bmatrix} 0 & u(x,t) \\ -su^*(x,t) & 0 \end{bmatrix},$$

and u^* is the complex conjugation of u. By substituting the operators into the compatibility condition, one recovers the original NLS system (1.3) and the NLS system governing the conjugate profile u^*. One then computes the transform into the scattering data by considering the first equation of (1.8) as an eigenvalue problem for the spectral parameter λ. Through some light matrix algebra, we then have the following problem,

$$\mathcal{L}\Phi = \lambda\Phi, \quad \mathcal{L} = i(\sigma_3 Q - \sigma_3\partial_x). \tag{1.10}$$

As discussed in [59], there are fundamental differences, in regards to the spectral parameter, between the linear problem and the nonlinear problem here. The Fourier transform provides real values of the spectral variable, which corresponds to the continuous (essential) spectrum of the operator $\mathcal{L}$. In the nonlinear problem, the spectral variable is defined on the continuous spectrum but also on the discrete spectrum, which is a discrete collection of complex values. The explicit solutions that correspond to these discrete values are precisely multi-soliton solutions, which are permitted through this modulational instability [59].

The inverse mapping of the nonlinear problem back to physical space is the most difficult step to compute, but we note that this is well-defined for integrable, nonlinear wave equations like the NLS [6]. For the purpose of our work we are more interested in the solutions obtained as a result of the IST, rather than the methodology itself, so we will use these results as they appear in the most general form. When the NLS is defocusing $(s = -1)$, we can see from the definition of the operator $\mathcal{L}$ that this is Hermitian. Due to this, we expect real eigenvalues only and there is no soliton solutions since there is no discrete spectrum. This is not surprising due to the previous description of the normal dispersion and modulational instability. In contrast, the focusing NLS $(s = 1)$ produces a non-Hermitian operator $\mathcal{L}$ which permits the discrete spectrum and soliton solutions. As previously discussed, the focusing solitons were first found using the IST in [166], but we use a similar formation of the solution presented

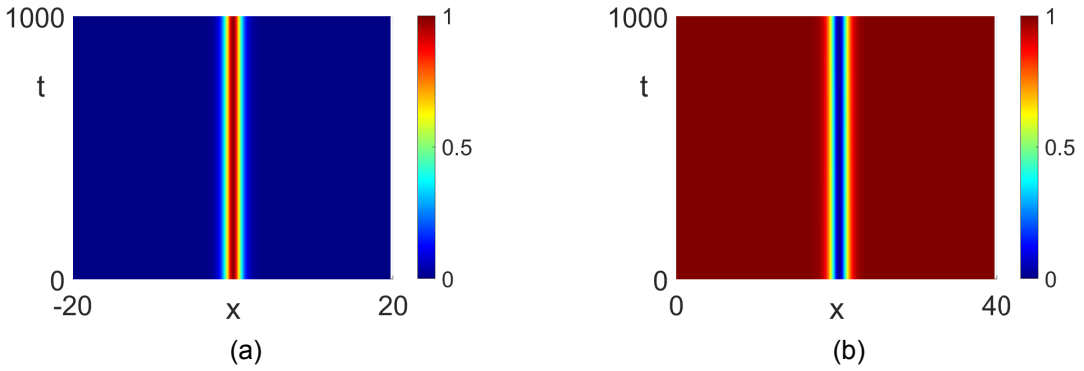

Figure 1.1: Example soliton solutions of the NLS equation (1.3). (a) Focusing-Bright soliton $(\xi = 0, \eta = 1)$. (b) Defocusing-Black soliton $\eta = 1$.

in [4, 5], i.e.

$$u(x,t) = \eta \,\text{sech}\left[\eta\left(x + 2\xi t - x_0\right)\right] \mathrm{e}^{i\theta(x,t)}, \tag{1.11}$$

where $\theta(x,t) = \xi x + (\xi^2 - \eta^2)t + \theta_0$, θ_0 is an arbitrary phase, and x_0 is an arbitrary envelope position. The quantities ζ, η are related to the eigenvalue of the IST analysis by $\lambda = \xi/2 + i\eta/2$. The solution decays to zero as $|x| \longrightarrow \infty$, which was imposed as the original boundary condition for the IST analysis. This soliton solution is known explicitly as the *bright soliton* and appears as a robust, self-enforced lump of energy propagating on a zero-background field. The bright solitons form a two-parameter family of solutions with ξ controlling the plane-wave wavenumber and the group velocity, and η controlling the amplitude and width of the soliton. An example solution is shown in Fig. 1.1(a) with $\xi = 0$ and $\eta = 1$.

If one instead assumes a boundary condition for the IST in which there is no longer a decay to a zero-background field, then the results are entirely different. For instance, if we impose a plane-wave at the boundary, i.e. $|u| \longrightarrow A$ as $|x| \longrightarrow \infty$ with A some real amplitude, then we have solutions for both the focusing and defocusing regimes. In the focusing regime these solutions are categorised as rogue wave solutions, which appear as a seemingly sporadic rise/depression of energy [151] from the background field. These solutions may also 'breathe' periodically in time [65] or space [15]. We will discuss rogue waves in greater detail in Sec. 3.2.4. In the defocusing regime, one may obtain a depression of energy known as a *dark soliton*. The key property of the continuous wave boundary conditions, compared to the zero boundary conditions, is that the continuous spectrum associated to the Lax pair (1.8), with the defocusing NLS Lax operators (1.9) substituted in, is defined as the real axis of the spectral variable $\lambda \in \mathbb{R}$ but off the forbidden, finite gap $-A < \lambda < A$ [59]. Within this gap real, discrete eigenvalues may exist and these real eigenvalues corre-

spond to a stable connection forming between two linearly stable plane-waves. The IST with data decaying to constant amplitude at the boundaries was first solved by Zakharov and Shabat [209], but we use the solution presented by Ablowitz [4, 5], i.e.

$$u(x,t) = \eta\left[\cos\phi + i\sin\phi\,\tanh\left[\eta\sin\phi\,(x - 2\eta\cos\phi - x_0)\right]\right]\mathrm{e}^{2i\eta^2 t + i\theta_0}, \quad (1.12)$$

parameterised by ϕ and the discrete eigenvalue quantity η. This solution is known as the *grey soliton*, and represents a $\pi-$shift of phase between the boundaries. Note that the boundary conditions, at an arbitrary point in time, are given by

$$u(x,t) = u(t)_{\pm} = \eta\,\mathrm{e}^{2i\eta^2 t + i\theta_0 \pm \phi},$$

as $|x| \longrightarrow \infty$. The solution travels with group velocity $2\eta\cos\phi$ and represents a depression in the background field, η, of intensity $\eta^2\sin^2\phi$. Note that the choice of $\phi = 0$ recovers the basic plane-wave solution with constant amplitude. With the particular choice of $\phi = \pi/2$ and $\theta_0 = -\pi/2$, the solution also represents a much simpler soliton form,

$$u(x,t) = \eta\,\tanh\left[\eta(x - x_0)\right]\mathrm{e}^{2i\eta^2 t}, \quad (1.13)$$

which is known as the *black soliton* [4]. Note that the black soliton represents a dip in the energy which drops to 0, hence the black naming convention, and initially satisfies the boundary conditions $u \longrightarrow \pm\eta$ as $|x| \longrightarrow \infty$. An example black soliton is shown to propagate in the NLS equation in Fig. 1.1(b) with $\eta = 1$. It is easy to check that these are exact solutions of the NLS by simple substitution of (1.11–1.13) into Eq. (1.3).

As mentioned previously, these solitons exhibit elastic collisions and conserve the soliton energy and velocity. This is very important when colliding solitons multiple times as the interaction of two solitons will have no impact on interactions further down the line, causing a cascade of collisions in which information is not lost to any radiation propagating away from the collision site. This is very useful when predicting the outcome of scalar interactions, but collisions where there is a distinct change to the soliton structure are often sought after for applications such as collision-based computing [159]. Theoretically, envelope solitons, which exhibit particle-like behaviour upon collision, may be utilised to perform logical operations, with some colliding solitons being viewed as data and others as operator solitons. Computations can then be envisioned as collisions inside a completely uniform medium and can offer advantages of high speed, high parallelism, and low power dissipation [98]. A particular exam-

ple of a plausible logical operation is that of a move operator, where a carrier soliton/particle is used to transfer/move information from one data soliton to another data soliton. One key issue with using the scalar solitons of the integrable scalar NLS equation (1.3) as a basis for collision-based computing is that useful computation is ruled out since the communication of information between the scalar solitons is not plausible. For this reason, vector solitons are used as the prototypical structures that theoretically enable the transfer of information in soliton collisions for collision-based computing [98]. This leads to the natural questioning of what vector soliton solutions one may expect from Eq. (1.4-1.5).

1.1.2 Vector solitons

We may first, briefly, focus our attention on the three regimes of the Manakov system which are shown to be integrable by the standard techniques [136, 155, 71, 210]. We note that we will not present the explicit formulations of the vector soliton solutions of the integrable systems here, but rather explore the literature which contains the different regimes, and consider how the behaviour changes as one moves into the nonintegrable CNLS. The Manakov system may be written as a corresponding Lax pair, just as we did for the NLS equation, by considering the operators (1.9) with different definitions of the matrices σ_3 (which we now denote Σ as to differentiate from the Pauli matrix) and Q. These matrices are now given as,

$$\Sigma = \begin{bmatrix} 1 & 0 & 0 \\ 0 & -1 & 0 \\ 0 & 0 & -1 \end{bmatrix}, \quad Q(x,t) = \begin{bmatrix} 0 & -s_1 u^*(x,t) & -s_2 v^*(x,t) \\ u(x,t) & 0 & 0 \\ v(x,t) & 0 & 0 \end{bmatrix}, \quad (1.14)$$

where we note that $s_1 = \pm 1$ and $s_2 = \pm 1$ [59, 155], corresponding to $g_{1,3} = \pm 2$ and $g_{2,4} = \pm 2$ respectively. As before, the compatibility condition $X_t - T_x + XT - TX = \mathbf{0}$ will reproduce the Manakov system for u, v and the Manakov system for the conjugate variables u^*, v^*, obtained by complex conjugation of Eq. (1.4–1.5). The scattering transform is then similar to the NLS for initial data with boundary conditions that decay to zero as $|x| \longrightarrow \infty$. We see, from the definition of Eq. (1.10), with the new matrices Σ and Q, that the operator $\mathcal{L}$ is Hermitian in the defocusing Manakov system $(s_{1,2} = -1)$. This signifies that we do not expect bright-bright solitons in the defocusing regime but in the focusing regime we do [110]. In a similar manner to the scalar NLS, if one instead imposes boundary conditions that decay to a plane-wave as $|x| \longrightarrow \infty$, then we may have the formation of dark-dark soliton solutions in the defocusing system [155] but not in the focusing system. The solutions of the mixed system

Table 1.1: Permitted soliton solutions in the integrable, Manakov systems. Bright (Dark) components are denoted B (D).

Regime	Soliton type	References
Focusing	BB	[110, 159]
Defocusing	BD	[155]
	DD	[155]
Mixed	BB	[106]
	BD	[188]
	DD	[135]

become more apparent when one first considers the linear stability/instability of the background field.

We note that stability is a key issue in the coupled system since modulational instability in one equation does not necessarily signify linear instability of the whole system. In fact, the nonlinear coupling of the system provides non-focusing instabilities, generated by the individual eigenmodes, permitted through the exchange of energy between linear perturbations of two comoving plane-waves [70]. For instance, when one considers the focusing Manakov system, self-phase instability is permitted with the disturbance primarily affecting one plane-wave component more than the other, and cross-phase instability is also permitted with an equal excitation of each plane-wave component and energy shared amongst them. In the coupled defocusing regime, only cross-phase instability is allowed [70] and this cross-phase instability is the key reasoning behind the generation of rogue wave solutions in the defocusing Manakov [22] and mixed Manakov [71] systems. It is clear to see that rogue wave dynamics are inherently richer in the CNLS equation, compared to the scalar NLS.

For an in-depth review of solutions to the different Manakov systems we refer to [189]. Due to the existence of nonfocusing instabilities, the mixed Manakov system permits both bright-bright [106] **AND** dark-dark [135] solitons. In the defocusing and mixed regimes a special set of vector solitons are also permitted, which are bright-dark soliton solutions [155, 188]. Whereas the bright component would usually not be permitted in the defocusing system, the dark soliton of the secondary component enables a potential well in which the bright soliton is allowed to propagate [112]. See Table. 1.1 for a summary of the permitted Manakov solitons. Note that we have assumed the mixed regime consists of a focusing-defocusing component setup. From here on, for denotation purposes, we will refer to bright (dark) soliton components as B (D).

When one has a non-integrable form of the CNLS, namely outside of the Manakov regimes, then the vector soliton solutions are no longer exact, stable

solutions. For non-integrable systems, one often searches for a particular solution and checks the stability through a numerical computation of the spectrum [165] as an afterthought. Providing that the vector soliton appears as a homoclinic/heteroclinic connection from a linearly-stable background field, then the opportunity for stability presents itself. There are a couple of key differences between soliton solutions of the integrable and non-integrable systems; inelastic collisions are much more frequent [187], there is inherent radiation upon collision [170, 52], and propagation dynamics become much less predictable [13, 202]. We also note that the difference between solitons, by the standard definition, and solitary waves is apparent here as these non-integrable solutions are technically solitary waves due to their shape-changing dynamics. For a review of soliton solutions in the defocusing integrable and non-integrable CNLS system, we refer to [112].

Collisions of solitons may exhibit behaviour unique to multiple-component integrable systems where one may have either elastic or inelastic interactions. Dynamically, there is a significant difference between elastic and inelastic collisions. Solitons involved in elastic collisions preserve the number of solitons and the energy of each soliton is conserved, i.e. energy redistribution between the components of a soliton but no energy transfer between the two colliding solitons. This elastic collision is precisely what occurs in the focusing Manakov system and is predictable via the state-transformation functions [97]. In particular, BB collisions which exhibit an energy transfer between the two components have grabbed significant attention, especially as a possible basis for collision-based computing [159, 97, 174] as well as soliton switching in optical fibres [158, 128]. We note that in the non-integrable regime, collisions can't be cascaded efficiently and useful collision-based computation must entail restoration of full-energy solitons [98]. In the mixed regime, one may find BB inelastic collisions which allow an energy transfer but also exhibit soliton suppression/amplification [189]. This may prove to be a vital observation since one can view one of the solitons as a tool in which to add (remove) energy to (from) the other soliton. It is also noted that the inelastic collisions of BB solutions have been extended to systems with $N > 2$ components [105, 99]. In direct contrast, DD solutions can not exhibit this energy transfer in the Manakov systems and are described by perfectly elastic collisions [145]. Finally, BD solutions also exhibit no energy transfer/inelastic collisions in the mixed and defocusing regimes, however, we note that CNLS systems with $N > 2$ components may exhibit energy transfer between the BD solitons providing that there are at least two bright components [189].

Moving away from the integrable regime, we expect collisions to be vastly

different and much more difficult to describe. Indeed, as one increases/decreases certain dispersion and nonlinear parameters the dynamics are much less predictable for arbitrary pulse/depression profiles. Take, for instance, the representation of the CNLS in the context of birefringent optical fibres. The system parameters in this case diverge from the integrable, focusing regime by a multiplicative factor of the XPM coefficients $(d_{1,2} = 1, g_{1,3} = 2, g_{2,4} = 4/3)$ [138]. Subsequent analysis on the collisions of BB solutions has shown that the collisions behave inelastically [187] and produce radiation from the collision point [170]. This is anticipated outside of the integrable regime, since one does not expect perfect collisions when there are no longer an infinite number of conservation laws to be obtained from a Lax pair. There is also unlikely to be an analytical description of the state-transformation function defining the collision, which means that outgoing soliton dynamics are less predictable. There has also been progress on soliton propagation [13] and inelastic collisions [52] in CNLS systems with further relaxation on the XPM terms. In Chapter 6 we will consider a qualitative, numerical analysis on near-elastic and inelastic collisions of BB and BD solitons in non-integrable regimes, where we propose varied choices of dispersion and nonlinear parameters.

We have presented a run-down of the nonlinear wave literature appropriate to the work carried out in this thesis. In particular, solutions of the scalar NLS are given by Eqs. (1.11–1.13) and are applicable, in these forms, to weakly-nonlinear, dispersive media with the NLS as an underlying equation governing the envelope dynamics. Vector soliton solutions in the integrable CNLS (Manakov systems) are categorised by the dispersion type, and bright/dark combinations in the current literature are reviewed. We briefly noted how these solutions are affected as one shifts away from the integrable regime, and gave an overview on the extra properties that one expects to see as a direct consequence of non-integrability.

1.2 Topological insulators

The theory of TIs was originally developed in condensed matter physics, with extensive literature on both one-dimensional and multi-dimensional systems [139, 88, 27, 17, 156]. The concept of a TI, in its simplest form, is that it is a unique material in which there is a clear dichotomy between the edge (surface in 3D) and the bulk components of the material. In short, electron conduction is only possible on the edges of the material and the bulk acts as an insulator. These conductive edge modes are a necessary consequence when an

insulator with a topologically non-trivial Hilbert space physically terminates and faces an insulator with a topologically trivial Hilbert space such as the vacuum state [17]. This mechanism will be explained in more detail in this section by considering the quantum mechanical description of the electronic properties of a material. One may then formulate key differences of TIs from more common states of matter such as a regular insulating/vacuum state or a conducting state. We note that we will focus our attention to 2D topological insulators, though there is also a significant amount of work produced on 3D [156] and in theoretically-imposed, higher-dimensional systems [88, 27].

Firstly, we introduce the single-particle Hamiltonian in 2D, $\hat{H}(\boldsymbol{r}, \boldsymbol{p})$, where $\boldsymbol{r}$ and $\boldsymbol{p}$ are position and momentum operators respectively. Through translational symmetry (spatial periodicity), one can exploit Bloch's theorem [117] on a single unit-cell of the material and classify the electronic properties using the following decomposition into Bloch states,

$$\psi_{n,\boldsymbol{k}}(\boldsymbol{r}) = e^{i\boldsymbol{k}\cdot\boldsymbol{r}} u_{n,\boldsymbol{k}}(\boldsymbol{r}), \tag{1.15}$$

where n is the band index, and $\boldsymbol{k}$ is defined over the first Brillouin zone. The eigenstates $u_{n,\boldsymbol{k}}$ are inherently periodic in $\boldsymbol{r}$ and are explicitly eigenstates of the particle Hamiltonian

$$\hat{H}_{\boldsymbol{k}} \equiv e^{-i\boldsymbol{k}\cdot\boldsymbol{r}} \hat{H}(\hat{\boldsymbol{r}}, \hat{\boldsymbol{p}}) e^{i\boldsymbol{k}\cdot\boldsymbol{r}}, \tag{1.16}$$

with the eigenvalues $E_n(\boldsymbol{k})$. The eigenvalues form energy bands (dispersion relation) and the physics of a band are governed by, not only the eigenvalues, but also how the geometric properties of $u_{n,\boldsymbol{k}}$ vary with respect to $\boldsymbol{k}$. For instance, a standard insulator will have a band gap of forbidden energy levels separating the occupied valence band from the empty conduction band; this is synonymous with the vacuum state where there is a conduction (valence) band described by electrons (positrons) [88]. The number of electrons is just the right amount to occupy the valence band and an occupied energy level will block the passage of other electrons via that energy level, forming low electron conductance in insulators. Notably, external energy must be provided to insulators to allow conduction and promote electrons across the band gap by increasing the temperature of the material. By direct comparison, in metals/semi-metals there is no band gap near the Fermi level and many electrons are free to move around unoccupied energy levels forming high conductivity in the material.

The key concept in the formation of topological insulators is that more unique states of matter may exist beyond the standard insulating state. An example of this is the (integer) quantum Hall state which was first observed in a 2D electron gas subject to a strong perpendicular magnetic field and low temperatures

[121]. The applied magnetic field leads to Landau quantisation of the cyclotron orbits and discrete Landau levels of energy. One can think of these Landau levels as a band structure like the insulating state, with N Landau levels filled, and an energy band gap between the filled valence levels and the empty conductance levels. In contrast to the ordinary insulator, the electric field causes cyclotron orbits to drift, forming a Hall current with discretised Hall conductivity

$$\sigma_{xy} = \frac{Ne^2}{h} \tag{1.17}$$

where e and h are the elementary charge and Planck's constant respectively [121, 88].

To understand precisely why the quantum Hall insulator is inherently different from the regular insulator, we borrow fundamental ideas from topology, i.e. we consider geometric properties of the band structure to determine what topological objects are invariant under smooth transformations of the Hamlitonian matrix $\hat{H}_{\boldsymbol{k}}$. The geometric properties of the Bloch states of each band n are encoded in the Berry curvature (flux),

$$\Omega_n(\boldsymbol{k}) = i(\langle \partial_{k_x} u_{n,\boldsymbol{k}} | \partial_{k_y} u_{n,\boldsymbol{k}} \rangle - \langle \partial_{k_y} u_{n,\boldsymbol{k}} | \partial_{k_x} u_{n,\boldsymbol{k}} \rangle), \tag{1.18}$$

which is a gauge-invariant local manifestation of the geometric properties in the $\boldsymbol{k}$ parameter space [17]. A topological invariant of the band is found by considering the total Berry curvature over the Brillouin zone (BZ), which is the closed-path integral

$$C_n = \frac{1}{2\pi} \int_{\mathsf{BZ}} \Omega_n(k_x, k_y) d^2\boldsymbol{k}. \tag{1.19}$$

It was shown in [181], with intermediary steps in [17], that the integral (Berry phase) can only take values that are integer multiples of 2π. The total Chern number, pseudonym Thouless-Kohmoto-Nightingale-den Nijs (TKNN) number, is then the summation of these values over all occupied bands $C = \sum_{n=1}^{N} C_n$ which is an integer quantity that will not vary as the Hamiltonian varies smoothly. Therefore, this value is a topological identifier that distinguishes between the insulator types. It is subsequently shown that the number of occupied bands and the total Chern number are equivalent $C = N$, which explains the quantisation of the Hall conductivity σ_{xy} as integer multiples of e^2/h [88]. Fermionic systems in which fermions completely fill Bloch bands with non-zero C_n are classified as *Chern insulators*.

There is a very apt comparison of this topological invariant to the topology of 3D shapes [88, 139]. One can think of the ordinary insulator as a shape with genus $g = 0$, and a quantum Hall insulator $g = 1$, where there is no way to

deform one insulator into the other through simple stretching and moulding of the shape (deforming the Hamiltonian). The fundamental idea behind a topological insulator is that, when the quantum Hall insulator and a regular insulator (such as the vacuum) are joined, there must be some process to account for the sudden difference in topological invariants of the two materials. Since the topological invariants are fixed per insulating material, the only way that this difference may be accounted for is if the energy gap vanishes at the interface. This signifies conducting states, connecting the bulk bands, that are shown to conduct only on the edge (surface) of the insulator [87], which is analogous to the process of cutting the genus 1 shape to transition into the genus 0 shape [139]. This is known as *bulk-edge correspondence* and is precisely the topological, physical phenomena that gives topological insulators their name. The critical properties of these conducting edge states are that they propagate unidirectionally (chiral) and they are immune to any disorder at corners/defects since there are no states available for this backscattering [88]. We note that the quantum Hall TI is a time-reversal symmetry breaking TI [17] and that the number of chiral edge states is equal to the difference of the total Chern number C across the interface of the topological insulator; this relationship may be written as

$$N_R - N_L = \Delta C \tag{1.20}$$

where N_R (N_L) is the number of right (left) travelling modes [88]. There is also the possibility of a fractional quantum Hall effect [124] that preserves time-reversal symmetry and establishes fractional Landau filling levels, however, we will not be considering TIs of this nature in this work.

The concept of the Chern number also added some further insight into the work of Hofstadter [90], where the author had previously considered non-interacting electrons on a squared crystal lattice under a perpendicular magnetic field. The lattice spacing, a, is fixed and the system is modelled by the Harper-Hofstadter model, which can be written as the tight-binding Bloch Hamiltonian

$$\hat{H} = -J \sum_{x,y} \left(\hat{a}^{\dagger}_{x+a,y} \hat{a}_{x,y} + e^{2\pi i \alpha x/a} \hat{a}^{\dagger}_{x,y+a} \hat{a}_{x,y} + \text{H.c.} \right), \tag{1.21}$$

where $\hat{a}^{\dagger}_{x,y}$ and $\hat{a}_{x,y}$ are respectively the creation and annihilation operators of a particle at site (x, y), J is the magnitude of the hopping amplitude, α is the magnetic flux, and H.c. denotes Hermitian conjugacy. One can see that a specific lattice site is connected to its four nearest neighbours in the square via the hopping magnitude. In the original paper [90] Hofstadter presents an analysis on a single Bloch band as one adapts the magnetic field flux α. A plot of the energy

spectrum against the flux reveals a self-similar fractal phase diagram known exclusively as the *Hofstader butterfly*. The fractal behaviour indicates infinite phases that are characterised by integer Hall conductance and, therefore, a corresponding Chern number. The Chern numbers, which take positive/negative/zero values, colour the butterfly in a very unique manner, highlighting the fractal nature of the diagram; see Fig. 5 in the article by Avron et al [19] where this image is shown. We will show in Sec. 1.2.2 that this model may also be used in order to form topological insulators in other settings, such as mechanical systems.

Arguably, the most commonly-portrayed quantum Hall insulator is that of the Haldane model, as it is used to model graphene subject to a periodical magnetic field [86]. The lattice and reciprocal lattice structure of graphene takes a honeycomb form which boasts a unique spectrum in $\boldsymbol{k}$ space. In particular, the spectrum exhibits Dirac cones in the band structure due to inversion and time-reversal symmetry [27, 88]. The key idea presented by Haldane was to break these symmetries, by including additional terms to the Bloch Hamiltonian, to lift the degeneracy at these Dirac cones and form an energy gap between the bands. The gapped state was shown to be a quantum Hall insulator with non-zero Hall conductance, governed by Eq. (1.17) with $N = 1$. Consequently, unidirectional edge states are found on the boundary between the honeycomb lattice and the vacuum, where the Chern number must undergo a transition from non-zero to zero. This model has formed a fundamental basis for the extension of quantum-Hall states to photonic/optical materials, which we will discuss briefly in Sec. 1.2.1.

One may question the consequences of keeping the time-reversal symmetry intact, and what effect this causes on the edge states of the system. In fact, it was shown by Kane and Mele [103, 104] that one can theoretically create a material that preserves time-reversal symmetry by considering two copies of the Haldane model and introducing the spin-orbit coupling concept into the system. Each copy of the Haldane model represents the spin up/down and the Hamiltonians are related via complex conjugation; this setup preserves the spin in each direction. This gave birth to the *quantum **spin**-Hall* state (QSH) of matter. The importance of the QSH state can be understood by first discussing the definition of the time-reversal symmetry ($\mathcal{T}$-symmetry) of electrons (spin 1/2 particles). For spin-half particles, the $\mathcal{T}$-symmetry is represented by the anti-unitary operator $\mathcal{T} = i\sigma_2\mathcal{K}$, where σ_2 is the second Pauli matrix acting on the two spin components and $\mathcal{K}$ is the complex conjugation operator [88, 17, 177]. The structure of $\mathcal{T}$ is very important here as one can make the simple observation that $\mathcal{T}^2 = -1$. This is significant in regards to the modes of the Bloch

Hamiltonian $\hat{H}_{\boldsymbol{k}}$, as one can note that Kramer's theorem applies here. Formally, when the full Hamiltonian preserves $\mathcal{T}$-symmetry, i.e. $[\hat{H}, \mathcal{T}] = 0$ [17], then the Bloch Hamiltonian satisfies

$$\hat{H}_{\boldsymbol{k}}(-\boldsymbol{k}) = \mathcal{T}\hat{H}_{\boldsymbol{k}}(\boldsymbol{k})\mathcal{T}^{-1}, \tag{1.22}$$

where this identity tells us that there exists Kramer's pairs of orthogonal states with equivalent energy at $\pm\boldsymbol{k}$ [88, 17]. There are special points of the band structure where the Kramer's pairs are degenerate and coincide at $\boldsymbol{k} = -\boldsymbol{k}$. For instance, if one considers the electrical properties of the 1D Brillouin zone, corresponding to the edge of a 2D insulator, then there exists two distinct points at $\mathcal{T}$-invariant momenta $k = 0, \pi$, where the Kramer's pairs are two-fold degenerate [88]. Moving away from these points, the spin up/down orientations distinguish between the pair and splits the degeneracy. The energy is a smooth function of k, therefore the degenerate momenta must be connected by some smooth curve. As stated in [88], there are two distinct ways in which this may happen. The first way is pairwise connections such that loops form between two degenerate momenta and there are $2n$ intersections of modes, for any energy level in the gap, in each of the half-momentum domain $\pm k$. This case is classified as a regular insulator since the edge states can be eliminated by deforming the Hamiltonian. The second way to connect the momenta is via a smooth curve in which each mode in the gap is intersected an odd number of times. In this case the band structure is no longer a regular insulator; see Fig. 3 in [88] for depictions of the two distinctions. The case where the material is no longer a regular insulator exhibits two oppositely polarised (opposite spin) edge modes that are time-reversed partners. An intuitive understanding of this is described in [1]. Assuming, for instance, that the perpendicular spin is conserved, then the orthogonality of the Kramer's pair states that there must be no backscattering between the two states unless $\mathcal{T}$-symmetry is broken. As one state approaches a topological defect, it can only be reflected if the spin is also flipped, and this process is forbidden so the state must certainly be transmitted. This, in short, details the topological protection of these edge states without the need of breaking $\mathcal{T}$-symmetry like in the QHE state. We also note that in the case of $\mathcal{T}^2 = +1$ Kramer's theorem does not apply. Though counterpropagating edge modes may exist, they are not topologically protected [1] so this situation is of no interest in our work.

A cleaner way to present the key differences between the regular insulator and QSH states is, once again, through the formation of topological invariants and Hall conductance. In the work presented here, we will be considering QSH

materials where the spin is conserved. In this case, the spin states have independent Chern numbers $C_\pm$ and, since $\mathcal{T}$-symmetry is conserved, they are of opposing signs $C_+ = -C_-$ and consequently opposite Hall conductance [29]. The total Chern number is then $C = 0$ and the total Hall conductance of the system, from (1.17), is then also $\sigma_{xy} = 0$. There is, however, another topological invariant that distinguishes between the regular insulator state and QSH state when $\mathcal{T}$ is preserved. Whereas the summation of the two Chern numbers cancels the two out, the difference of the two provides a total spin Chern number that governs the spin Hall conductance [167]. This spin Chern number, $C^{(S)}$, and related spin Hall conductance, $\sigma_{xy}^{(S)}$, are given by

$$C^{(S)} = \sum_\alpha \alpha C_\alpha, \qquad \sigma_{xy}^{(S)} = \frac{C^{(S)} e}{4\pi}, \tag{1.23}$$

where $\alpha = \pm$ [167, 29]. A topological invariant is then formed in relation to this spin Chern number by,

$$\nu = \frac{C^{(S)}}{2} \text{ mod } 2, \tag{1.24}$$

where the invariant may take two values $(\nu = 0, 1)$ which correspond to the regular (even number of mode intersections in the band gap) and QSH (odd number of mode intersections in the band gap) states [88]. In a similar manner to the number of edge states of the QH insulator being described by the bulk-edge correspondence of Eq. (1.20), the number of edge modes is governed by the difference of the spin Chern number between two materials, i.e. $N_k = \Delta C^{(S)}$, which will be even for systems with independent Chern numbers in each spin.

The QSH insulator was also the first to be realised experimentally, formed in HgTe quantum wells without the need of external magnetic fields [28, 122]. In such a material, the thickness of the potential well has a drastic effect on the topological properties, inducing a quantum state transition from a regular insulator phase to a quantum spin-Hall phase that exhibits the helical edge states. The existence of the QSH insulator has provided a fundamental basis for the formation of topological insulators in classical mechanical systems; we will discuss this further in Section 2.2.2.

1.2.1 Photonic topological insulators (PTIs)

We will now briefly discuss the extension of topological insulators into the field of photonic/optical materials, which have been shown to exhibit the previously defined integer quantum Hall state. We expect to see the QH state, as opposed to

QSH, due to the bosonic nature of photons. This has significant consequences on Kramer's theorem and, as such, only QH analogues may be typically formed [146]. There are exceptions to this, however, where specific properties of the system are introduced such as the use of coupled resonators to induce a half pseudo-spin degree of freedom [84, 146]. This system, on a squared lattice, forms a Hoftstadter model (1.21) for photons and permits whispering gallery modes propagating in opposite directions (spin) since $\mathcal{T}$-symmetry is left intact. A paper by Haldane and Ragu [85] was the first theoretical proposition of the QH state in photonic crystals. In this paper, they describe how it is plausible to create unidirectional waveguides, that form direct analogues of quantum chiral edge states, at the interface of two magneto-optical crystals. The non-reciprocality of the media effectively breaks time-reversal symmetry synonymous with QH states.

In analogy to electrons in traditional TIs, electromagnetic waves in photonic TIs propagate along the edge with very little backscattering, even in the presence of disorders such as missing site(s) on the edge of a photonic lattice [192, 113, 160]. The theoretical existence of the one-way photonic edge states was solidified experimentally by Wang et al [192] at microwave frequencies, where they considered a gyromagnetic square lattice and subjected it to a uniform magnetic field to break $\mathcal{T}$-symmetry. The interface permitting unidirectional states was formed adjacently to the lattice by using non-magnetic metallic walls. As expected from QH analogous states, they found the chiral electromagnetic states to 'ignore' defects/impurities of the crystal in the form of metallic scatterers.

The development of Floquet PTIs that exhibit edge states in the optical frequency range was a huge step forward in broadening the analysis on robust photon transport [160]. This work of Rechtsman et al explicitly showed the topological protection of photonic edge states on a honeycomb photonic lattice, effectively realising the Haldane model in an optical setting. The key difference to previous photonic analogues of QH is that there is no external field needed for the edge states to present themselves. The lattice is set up as an array of optical waveguides where the propagation in 'time' is along the z-axis in 3-dimensional space forming a pseudo-electric field. Inversion symmetry is broken along this dimension and chiral edge states may be found in the transverse plane (x, y) [146]. The diffraction of light in the transverse plane of waveguides, propagating in z, is akin to electron propagation in 2D arrays with rotating atoms. Such a system is governed by a lattice linear Schrödinger equation and inversion symmetry of z is explicitly broken when one replaces straight waveguides with helical ones [160]. It was subsequently shown by Rechtsman et al that

imposing the helical electric field effectively opens up the band gap, breaking the Dirac cones of the band spectrum, allowing the propagation of chiral edge states like in the Haldane model. It was also found that the deformation of the photonic lattice, from perfect honeycomb arrays, has an impact on the topology of the band spectrum [10]; see also [11] for further insight into the band spectrum of the honeycomb lattice. In particular, deformation of the honeycomb lattice can cause a transition between regular and QH states. For an extensive review on the subject of topological photonics, we refer to [129, 146] and the references therein.

We previously remarked that the existence of photonic Floquet topological insulators is a significant discovery with huge implications on robust photon transport. This is more so apparent, and with extreme relevance to the work presented in this thesis, when ***nonlinear*** topological edge states were reported in these type of TIs [7, 10, 125]. By considering the honeycomb lattice with a nonlinear Kerr effect (lattice NLS), one can reduce the governing equation to a 2D discrete system in the tight-binding approximation [11]. By assuming that the pseudo-electric field varies rapidly, one can introduce a multiple scale analysis where, in the case where anomalous dispersion is present and balances with nonlinearity, the scalar focusing NLS equation governs the envelope of nonlinear edge modes on the edge of the lattice [7]. As we discussed previously, in Sec. 1.1, the NLS equation permits soliton solutions so we expect that topologically protected edge solitons will exist on the edge of the honeycomb lattice in the topologically non-trivial regime. The existence of these edge solitons was presented in [7], with extensions to different edge types under the topologically trivial/non-trivial regimes in [10]. The analysis was also extended to include a slowly-varying electric field with weak nonlinearity [8]. Topologically protected edge solitons were subsequently shown experimentally in a helical waveguide array organised into a 2D rectangular lattice [125]. The repercussions of wave dynamics in the field of topological physics has proven to be a key insight into robust translations of photonic excitation around the edges of PTIs [7, 10], as well as for nonlinear optical switching and filtering [125]. We also remark that nonlinear topologically protected edge states have also been found in polariton TIs [108, 79, 126] and classical optical networks [168].

1.2.2 Mechanical (phononic) topological insulators (MTIs)

The emerging field of topological mechanics utilises topological principles to reveal new collective excitations in classical mechanical (phononic) systems [93, 130]. The definitive achievement in this field is the discovery of topologi-

cal acoustic metamaterials including, in particular, MTIs. The metamaterials in topological mechanics can be classified into two families depending on whether the topological edge modes appear at zero frequency or high frequencies [93]. In the zero frequency case, these edge modes are identified as floppy modes and self-stress states in Maxwell frames [102]. We are generally interested in, and thus streamline our focus to, the high frequency case, where topologically protected transport via phonons is enabled. Seminal work in this direction includes analogues of the QH state using a lattice of hanging gyroscopes [142, 190], and the QSH state using lattices of coupled pendula [177] or bilayered lattices of disks and springs [147]. Important steps have also been taken to formulate topologically non-trivial materials utilising continuous media, such as recent proposals on magnetic solitons [115] and water waves [195]. Though these materials are more favourable, in practice, the full analysis on discrete models is still missing some vital components, such as the full effects of nonlinearity, dissipation [198], and forcing [148], which is surely to present interesting directions of research and a greater understanding of MTIs.

The major, distinguishing difference between the two types of high-frequency metamaterials exhibiting the QH/QSH states is the presence of $\mathcal{T}$-symmetry. Metamaterials consisting of active matter are constructed using non-reciprocal components that actively break this symmetry, for instance by using spinning gyroscopes, which permit chiral edge states. In contrast, passive materials with time-reversal symmetry left intact, by using reciprocal components, will permit the helical edge states. Topological phonons are subsequently fully classified based on local symmetries [178]. In particular, the classification depends on three fundamental symmetries; $\mathcal{T}$-symmetry, particle-hole symmetry $(\mathcal{C})$, and chiral symmetry $(\mathcal{S})$. The two cases of zero and high frequency topological mechanics are further categorised by whether reciprocal or non-reciprocal components are implemented. Within these four categories there are distinct symmetry classes of topological mechanics which are described in Tables 1-4 in [178]. The work presented in this thesis focuses on models of symmetry class AII, with $\mathcal{T}$-symmetry always present and no $\mathcal{C}/\mathcal{S}$-symmetry present, which permits the existence of the QSH state in 2D.

In particular, we will focus on, and subsequently take as the basis of the work of this thesis, the first documented mechanical implementation of the QSH effect; this system is the one proposed by Süsstrunk and Huber [177]. The model consists of two copies of a Chern insulator, one for each spin, where the magnetic field acting on each insulator is opposite. Hence, the Chern number for the spin-up insulator is opposite to that of the spin-down insulator. There are an equivalent number of chiral edge states in the 2 spins, but with opposing

propagation, which are precisely the components that make up the helical edge states one expects from a QSH insulator. The proposed model is explicitly written as two independent copies of the Hofstadter model (1.21) on the 2D square lattice indexed by (r, s):

$$\hat{H} = \sum_{\alpha=\pm} \hat{H}_\alpha,$$
$$\hat{H}_\alpha = f_0 \sum_{r,s} \left(\hat{a}^\dagger_{r,s,\alpha} \hat{a}_{r,s+1,\alpha} + e^{i\alpha\Phi s} \hat{a}^\dagger_{r,s,\alpha} \hat{a}_{r+1,s,\alpha} + \text{H.c.} \right).$$

Here α is a spin index that labels the two copies, f_0 is the magnitude of the hopping amplitude, $\hat{a}^\dagger_{r,s,\alpha}$ and $\hat{a}_{r,s,\alpha}$ are respectively the creation and annihilation operators of a particle with spin α at site (r, s), $\Phi = 2\pi/3$ is the magnetic flux, and H.c. denotes Hermitian conjugacy. This choice of Φ makes $\hat{H}$ periodic on a 1×3 unit cell, so the Hamiltonian matrix takes the form

$$H = \begin{pmatrix} H_+ & 0 \\ 0 & H_- \end{pmatrix}, \tag{1.25}$$

where $H_\pm$ are 3×3 matrices that represent the opposing spins. As is mentioned in [177] , the two blocks are related via complex conjugacy $H_- = H_+^*$ and the matrix (1.25) is symmetric under time-reversal, which is key for the formation of the QSH states. The existence of three doubly-degenerate bulk bands, separated by non-zero gaps, is associated with the $\mathbb{Z}_2$ topological invariant formed for the QSH effect [104]. The description of this invariant, and the definition of $\mathcal{T}$-symmetry, is presented in Appendix B-C of [177], but we explain this briefly here. The matrix (1.25) is invariant under the action of $\mathcal{T}$-symmetry when $\mathcal{T} = i\sigma_2\mathcal{K}$, where we recall σ_2 as the second Pauli matrix and $\mathcal{K}$ as the action of complex conjugation. The system then falls under symmetry class AII [178], which permits the QSH state in 2D. Since there are no cross-couplings between the two Bloch Hamiltonians $H_\pm$, spin is conserved, and we may denote the two spins by the separate Chern numbers $C_\pm$. Recall that, for such a time-invariant system, one can formulate a related spin Hall conductance, defined by Eq. (1.23), which allows us to define a topological invariant (1.24). As stated in [177], the Chern number for the lower gap is given as $C_+ = 1$ and $C_- = -1$ for the upper gap, therefore, the invariant is given as $\nu = 1$ and the material is topologically non-trivial. Each spin is accompanied by two edge modes, corresponding to the conduction states connecting the bulk bands in each of the two gaps.

The key idea presented in [177, 178] is that one can directly compare the quantum mechanical problem, governed by Eq. (1.25), to the dynamical matrix,

D, of a lattice of undamped classical harmonic oscillators. This is possible since the edge states of each system are dynamically governed by the eigenfunctions of the respective matrix and nothing else. As shown in [177], the comparison can be formulated in the following way. The quantum-mechanical problem on the lattice can be written as the linear Schrödinger equation,

$$i\hbar\dot{\psi}_i = H_{ij}\psi_j \tag{1.26}$$

where ψ_i are the wavefunction amplitudes for an electron with given spin $\alpha = \pm$ at the lattice site i, and $\hbar$ is the reduced Planck's constant. The quantum-mechanical matrix H encodes the QSH state; see, for instance, an example formulation of H describing the QSH state in HgTe quantum wells in the work of Bernevig et al [28]. The problem described by Eq. (1.26) is a time-dependent equation that is solved explicitly for the wavefunction amplitudes ψ, with information on the dynamics of the system stored in these wavefunctions. In contrast, the equation for the classical oscillators is given by Newton's equation of motion,

$$\ddot{x}_i = -D_{ij}x_j \tag{1.27}$$

where x_i are coordinates of the pendula, and D_{ij} is the real, symmetric, positive-definite dynamical matrix governing the couplings between them. Since H represents a matrix allowing QSH states, the main idea is to present a dynamical matrix D that incorporates the same properties as H. The quantum matrix H is complex by definition but one can apply a similarity transform, due to the time-reversal symmetry of Eq. (1.25), to make the matrix real and symmetric. We can transform to a real basis by considering the Kramers pairs,

$$\begin{bmatrix} \psi^+_{r,s} \\ \psi^-_{r,s} \end{bmatrix} = \frac{1}{\sqrt{2}} \begin{bmatrix} 1 & -i \\ 1 & i \end{bmatrix} \begin{bmatrix} x_{r,s} \\ y_{r,s} \end{bmatrix}, U = u \otimes \mathbf{1}_{lattice} \tag{1.28}$$

where u is the transformation matrix shown, and U is defined by the number of sites of the lattice. This transformation gives an explicit relationship for the two matrices, given by

$$D = U^\dagger H U = \begin{bmatrix} \mathcal{R}\mathrm{e}H_+ & \mathrm{Im}H_+ \\ \mathrm{Im}H_- & \mathcal{R}\mathrm{e}H_+ \end{bmatrix}, \tag{1.29}$$

which can easily be made positive-definite by the addition of a diagonal term corresponding to self-interactions of a lattice site. The blocks of Eq. (1.29) encode the couplings between the $x_{r,s}$ and $y_{r,s}$ pendula.

The diagonal blocks govern the $x - x$ and $y - y$ connections, with the

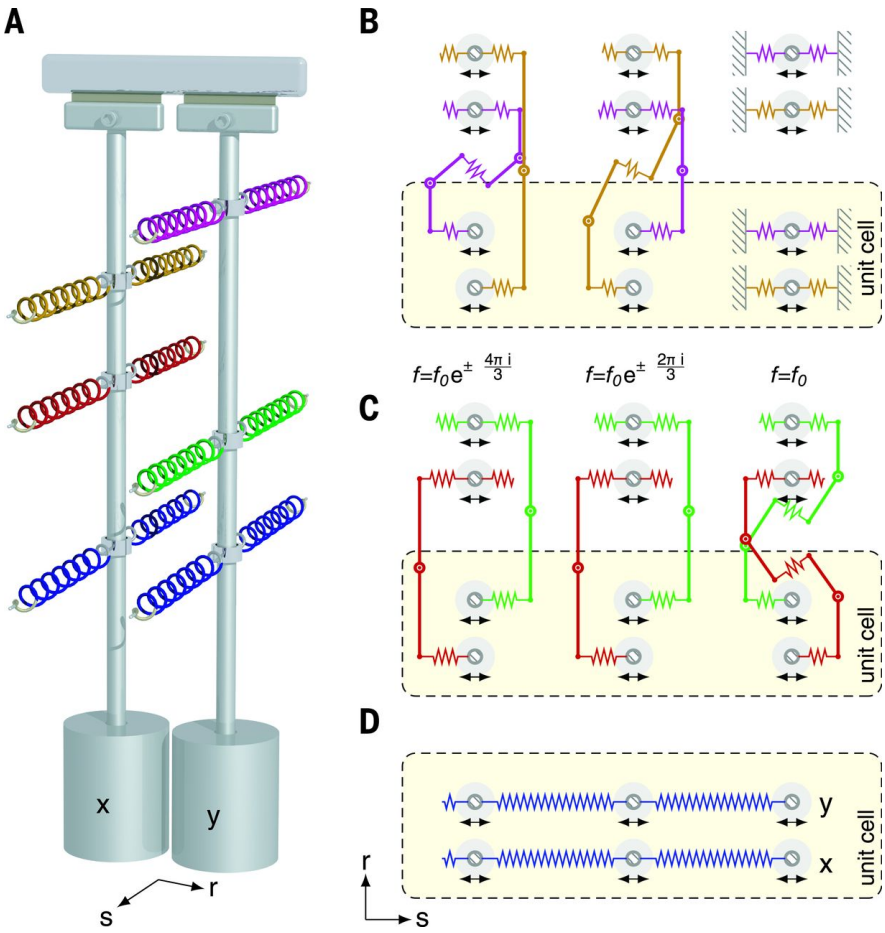

Figure 1.2: Figure and caption reproduced from [177] with permission from the American Association for the Advancement of Science (AAAS). (A) Illustration of two one-dimensional pendula, x and y, making up one effective site of our lattice model. (B) Schematic top view of the couplings perpendicular to the direction of motion of the pendula. The top two layers of springs (magenta and brown) implement the cross-coupling between x and y pendula. One lever arm yields a negative coupling, whereas two lever arms give rise to a positive coupling. The spring constants are chosen to give rise to the desired effective coupling strength $\mathrm{Im}(f)$. Note that there are three sites in one unit cell owing to the three different phases on the transverse couplings. (C) The next two layers of springs (green and red) implement the $x-x$ and $y-y$ couplings $\mathrm{Re}(f)$ in the transverse direction. (D) The bottom springs (blue) couple $x-x$ or $y-y$ springs with strength f_0 in the longitudinal direction.

off-diagonal blocks describing the cross-couplings between x and y pendula. These transverse connections are explicitly given by the periodicity of the magnetic flux $\Phi = 2\pi/3$. The first row of pendula, $x^{(0)}$ and $y^{(0)}$, are connected via the coupling strength $f = f_0$, which subsequently tells us that there is no cross coupling terms between x and y for this row. The secondary row of pendula, $x^{(1)}$ and $y^{(1)}$, are connected by the coupling strength $f = f_0 \exp\{i\Phi\}$. From the formation of the dynamical matrix (1.29), we know that the $x-x$ and $y-y$ connections are given by $\mathcal{R}\mathrm{e}(f) = -f_0/2$ and cross couplings with strength $\mathrm{Im}(f) = \pm\sqrt{3}f_0/2$, depending on the direction of the connection. The final row of pendula $x^{(2)}$ and $y^{(2)}$, are connected by the couplings $f = f_0 \exp\{i2\Phi\}$. This gives an $x-x$ and $y-y$ coupling strength of $\mathcal{R}\mathrm{e}(f) = -f_0/2$ and a cross

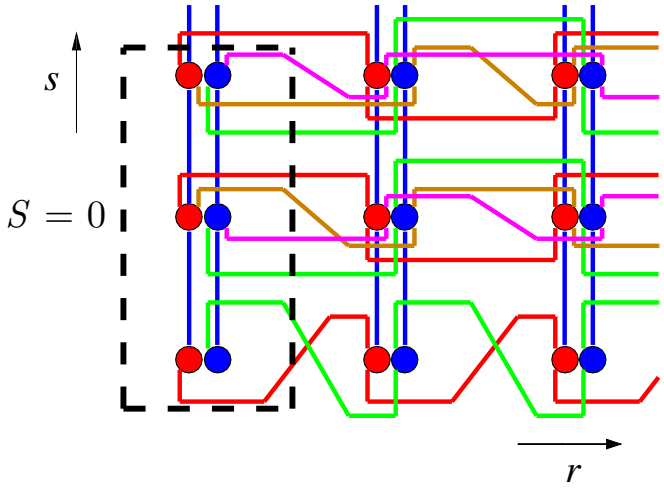

Figure 1.3: Schematic view of the first unit cell $S = 0$ consisting of three sites on a generic lattice. The first, second, and third rows respectively represent $(x^{(0)}_{r,S}, y^{(0)}_{r,S})$, $(x^{(1)}_{r,S}, y^{(1)}_{r,S})$, and $(x^{(2)}_{r,S}, y^{(2)}_{r,S})$. Each site hosts an x (red) and a y (blue) pendulum carrying a mass. Simple springs in the s-direction connecting pendula are shown as blue lines. Couplings between pendula in the r-direction are shown as red and green lines. Cross couplings between the x and y pendula of neighbouring sites are shown as brown and magenta lines. The edges are implemented by replacing the outside sites by solid walls. These walls are not shown for clarity.

coupling strength of $\text{Im}(f) = \mp\sqrt{3}f_0/2$. Rows of sites beyond this are periodic w.r.t these row descriptions and each row is connected longitudinally by simple springs with strength $f = f_0$.

The experimental setup of a mechanical lattice described by Eq. (1.29) is depicted in Fig. 1.2, reproduced from the original work of Süsstrunk and Huber [177]. This system is realised on a 2D rectangular lattice where each site contains the two pendula $x_{r,s}$ and $y_{r,s}$ that are hinged to swing only in the s-direction, with linear springs attached to the pendula to achieve couplings in both s- and r-directions. The negative connections are realised by one lever arms, with positive connections by two lever arms. In the following, we group the sites in the s-direction into unit cells, indexed by S, with each cell consisting of the three sites $(x^{(j)}_{r,S}, y^{(j)}_{r,S})$, $j = 0, 1, 2$. Figure 1.3 shows a schematic, top-down view of the couplings on a generic lattice with the first unit cell ($S = 0$) emphasised. Moving forward, to visualise any changes to the connections of the mechanical lattice, we will use the schematic viewpoint which can always be related back to the original experimental setup in Fig. 1.2. We will briefly analyse this MTI in the next section and show the existence of the helical linear edge modes through numerical simulations of the lattice.

1.3 Linear analysis of MTIs

The key proposition of classical mechanical systems, which are governed by Newton's equations of motion, is that the second time-derivative may be recast to form a Hermitian eigenvalue problem for the frequencies of the system [178]. In this form, the linear analysis of the system becomes akin to that of the linear Schrödinger equation in quantum mechanics, where the dispersion relation related to the Bloch states provides a band structure to analyse with appropriate symmetries defining classes of topological systems. The Hermitian eigenvalue problem may be solved accordingly along an infinite 1D edge, using analytical or numerical techniques, to produce the band structure formed by the Bloch eigenvalues.

The particular MTI that we will focus on, and present the explicit linear analysis for, is that of the spring-mass system proposed by and implemented experimentally in [177]. Linear equations of motion are presented for this system which yields

$$\begin{aligned}
\ddot{x}^{(0)}_{r,S} =& -(\omega_0^2 + A_s f)x^{(0)}_{r,S} \\
&+ f(x^{(0)}_{r+1,S} + x^{(0)}_{r-1,S} + x^{(1)}_{r,S} + x^{(2)}_{r,S-1}), && (1.30)\\
\ddot{y}^{(0)}_{r,S} =& -(\omega_0^2 + A_s f)y^{(0)}_{r,S} \\
&+ f(y^{(0)}_{r+1,S} + y^{(0)}_{r-1,S} + y^{(1)}_{r,S} + y^{(2)}_{r,S-1}), && (1.31)\\
\ddot{x}^{(1)}_{r,S} =& -(\omega_0^2 + A_s f)x^{(1)}_{r,S} \\
&+ f(x^{(0)}_{r,S} + x^{(2)}_{r,S}) - \frac{f}{2}(x^{(1)}_{r+1,S} + x^{(1)}_{r-1,S}) \\
&+ \frac{\sqrt{3}f}{2}(y^{(1)}_{r+1,S} - y^{(1)}_{r-1,S}), && (1.32)\\
\ddot{y}^{(1)}_{r,S} =& -(\omega_0^2 + A_s f)y^{(1)}_{r,S} \\
&+ f(y^{(0)}_{r,S} + y^{(2)}_{r,S}) - \frac{f}{2}(y^{(1)}_{r+1,S} + y^{(1)}_{r-1,S}) \\
&+ \frac{\sqrt{3}f}{2}(-x^{(1)}_{r+1,S} + x^{(1)}_{r-1,S}), && (1.33)\\
\ddot{x}^{(2)}_{r,S} =& -(\omega_0^2 + A_s f)x^{(2)}_{r,S} \\
&+ f(x^{(0)}_{r,S+1} + x^{(1)}_{r,S}) - \frac{f}{2}(x^{(2)}_{r+1,S} + x^{(2)}_{r-1,S}) \\
&+ \frac{\sqrt{3}f}{2}(-y^{(2)}_{r+1,S} + y^{(2)}_{r-1,S}), && (1.34)
\end{aligned}$$

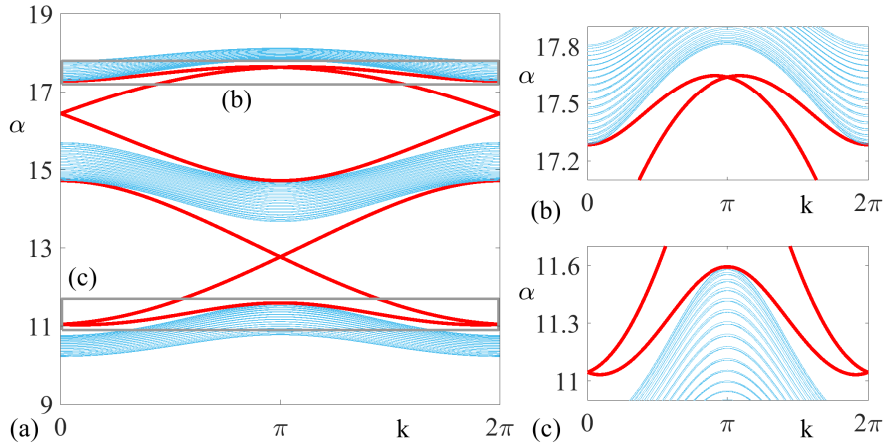

Figure 1.4: The dispersion relation $\alpha(k)$ computed on the left/right edge of a rectangular lattice with $N_r = 60$ sites in the r-direction. The bulk spectrum is shown in blue and the edge spectrum is shown in red. In the latter, each eigenvalue corresponds to a pair of edge states localised respectively on the left and on the right.

$$\begin{aligned}\ddot{y}^{(2)}_{r,S} =& -(\omega_0^2 + A_s f) y^{(2)}_{r,S} \\ &+ f(y^{(0)}_{r,S+1} + y^{(1)}_{r,S}) - \frac{f}{2}(y^{(2)}_{r+1,S} + y^{(2)}_{r-1,S}) \\ &+ \frac{\sqrt{3}f}{2}(x^{(2)}_{r+1,S} - x^{(2)}_{r-1,S}).\end{aligned} \tag{1.35}$$

Here $A_s = 3 + \sqrt{3}$ is the self-coupling coefficient, f describes the linear restoring forces of the springs, and ω_0 and describes the linear restoring forces of the pendula. These restoring forces are considered in [177] to be fixed as $\omega_0 = 3\pi/2$ and $f = 4.16\pi^2$. The equations of motion can be written in the compact matrix form as

$$\ddot{\boldsymbol{X}}_{r,S}(t) = (\boldsymbol{\mathcal{L}}\boldsymbol{X})_{r,S} \tag{1.36}$$

where $\boldsymbol{X} = [x^{(0)}, y^{(0)}, x^{(1)}, y^{(1)}, x^{(2)}, y^{(2)}]^T$, t denotes time, $\cdot$ denotes time derivative, and $\boldsymbol{\mathcal{L}}$ is the linear operator encoding the couplings of the system.

In the linear problem, to describe an edge state of a specific boundary, say along S, we take the Fourier transform $\boldsymbol{X}_{r,S}(t) = e^{i\theta}\boldsymbol{X}^E_r + c.c$, $c.c$ denoting complex conjugacy, where the exponent $\theta = Sk - t\alpha(k)$, with k being the wavenumber in S (along the edge), $\alpha(k)$ being the dispersion relation, and $\boldsymbol{X}^E_r$ being the 1D edge state that decays in r (perpendicular to the edge). This reduces Eq. (1.36) to the eigenvalue problem

$$\boldsymbol{\mathcal{L}}(k)\boldsymbol{X}^E_r = -\alpha(k)^2\boldsymbol{X}^E_r, \tag{1.37}$$

where $\boldsymbol{\mathcal{L}}(k)$ denotes the 1D linear operator after the Fourier transform, and $\boldsymbol{X}^E_r$ is normalised such that $\|\boldsymbol{X}^E_r\|_2^2 = \sum_j |\boldsymbol{X}^E_j|^2 = 1$.

The dispersion relation $\alpha(k)$, $k \in [0, 2\pi)$, numerically computed by solving

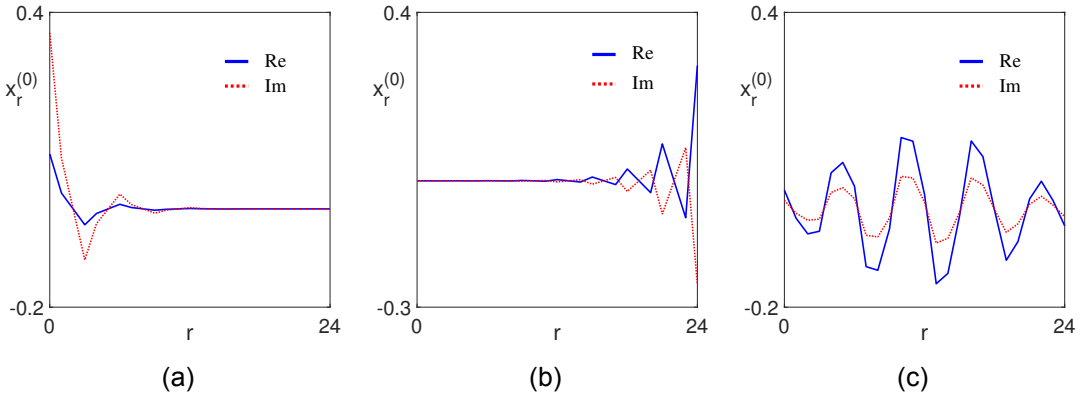

Figure 1.5: Example $x_r^{(0)}$ component of eigenmodes with $N_r = 25$. Edge modes are shown in the (a) lower bulk-band gap with carrier wavenumber/frequency $(9\pi/10, 12.506)$ and (b) upper bulk-band gap with carrier wavenumber/frequency $(\pi/10, 16.221)$. (c) Bulk mode between the lower and upper bulk-band gaps with carrier wavenumber/frequency $(9\pi/10, 13.740)$. Real and imaginary parts are shown as blue-solid (red-dashed) lines.

Eq. (1.37) on a finite 1D domain, is shown in Fig. 1.4. The bulk (continuous) spectrum consists of three bands (blue), and the edge (point) spectrum exist in the two gaps (red). Thus, for each wavenumber k there are precisely six point eigenvalues, three in either gap, whose corresponding eigenfunctions are the edge states that decay in r. The topologically protected edge states are those in the bulk band gap, or more precisely the range of α where the only permissible states are the pair of counter-propagating helical edge states. Examples of a particular component, say x_r^0, of the eigenmodes are shown for the system, according to the solution of Eq. (1.37), in Fig. 1.5. Note that similar figures could be formed for any of the 6 cell components, though the magnitudes of $x_r^{(i)}, y_r^{(i)}$, for $i = 0, 1, 2$, are different due to intra-cell variation of the eigenmodes. We first show two topologically protected modes in the lower and upper band-gaps respectively in Fig. 1.5(a–b). As one would expect, there is a clear exponential decay into the bulk for both modes, which signifies the conduction on the edge of the lattice imposed by the bulk-edge correspondence of the system. Note that, due to the lattice being finite, there is a degeneracy which indicates two modes localised on the left and right edges. This is reflected in the two edge mode panels of the figure, where we have utilised this freedom to implement a left- and right-localised mode respectively. Note that edge modes closer to the bulk-bands decay more slowly into the bulk. For comparison, we also include a bulk mode from the band between the two band gaps in Fig. 1.5(c).

1.3.1 Helical edge modes

As discussed in Sec. 1.2, the quantum Hall state produces unidirectional propagation of excitation along the edge of the material due to the physical mechanism of bulk-edge correspondence, described by Eq. (1.20). The edge modes that correspond to this propagation are commonly referred to as chiral edge modes, since their propagation exists in a singular direction with no state exhibiting a counter-propagation [88, 17]. In contrast, materials that form analogues of the quantum spin Hall state produce two counter-propagating chiral edge modes which travel in a clockwise and anti-clockwise manner. These edge modes exhibit a helical property, where the two states with opposite spin polarisation counter-propagate along the edge, with topological protection ensured by the $\mathcal{T}$-symmetry [1, 28, 122]. The helical edge modes form a Kramer's pair that are orthogonal and are found at the same energy level of the band spectrum/dispersion relation. The corresponding helical edge modes of the system imposed by Eq. (1.37) can be classified as those states found on the two symmetric branches, within the band-gaps, that have reversed group velocities $\pm\alpha_0'$ and equivalent frequency α_0. These edge modes are orthogonal such that if one defines the Kramer's pair $\boldsymbol{X}_r^{\alpha(k_0)}$ and $\boldsymbol{X}_r^{\alpha(2\pi-k_0)}$, with the superscript denoting the edge mode at the particular carrier wavenumber-frequency combination, then the edge modes satisfy $\langle \boldsymbol{X}_r^{\alpha(k_0)}, \boldsymbol{X}_r^{\alpha(2\pi-k_0)} \rangle = 0$, where the inner product is defined generically as $\langle \boldsymbol{g}, \boldsymbol{h} \rangle = \sum_j g_j^* h_j$ [1]. Note that the corresponding carrier frequencies of the two edge modes are equivalent as expected, i.e. $\alpha(k_0) = \alpha(2\pi - k_0)$, but they are located on the two distinctly different helical branches corresponding to group velocities with opposing signs. i.e. $\alpha'(k_0) = -\alpha'(2\pi - k_0)$. Due to the QSH effect and the inherent orthogonality, these conductive states propagate unidirectionally and should exhibit little to no backscattering at the corners of the lattice on the full domain. In general, one would expect no dynamical differences in the way that the excitation propagates around the boundary of the lattice, other than an obvious reversal of the group velocity.

We show, in Fig. 1.6, direct numerical simulations of these topologically-protected modes in the 2D linear system. Firstly, in Fig. 1.6(a–b), we implement the edge mode obtained from the lower bulk-band gap in Fig. 1.5(a) and its Kramer's partner found at $(k_0, \alpha_0) = (11\pi/10, 12.505)$ respectively. To portray the mechanical excitation we introduce an excitation variable $z_{r,S}^{(i)} = \sqrt{(x_{r,S}^{(i)})^2 + (y_{r,S}^{(i)})^2}$, for $i = 0, 1, 2$, that represents the intensity of each site in the lattice. Formally, we provide the edge modes with an arbitrary sech envelope and both directional envelopes experience an equivalent dispersion of the pro-

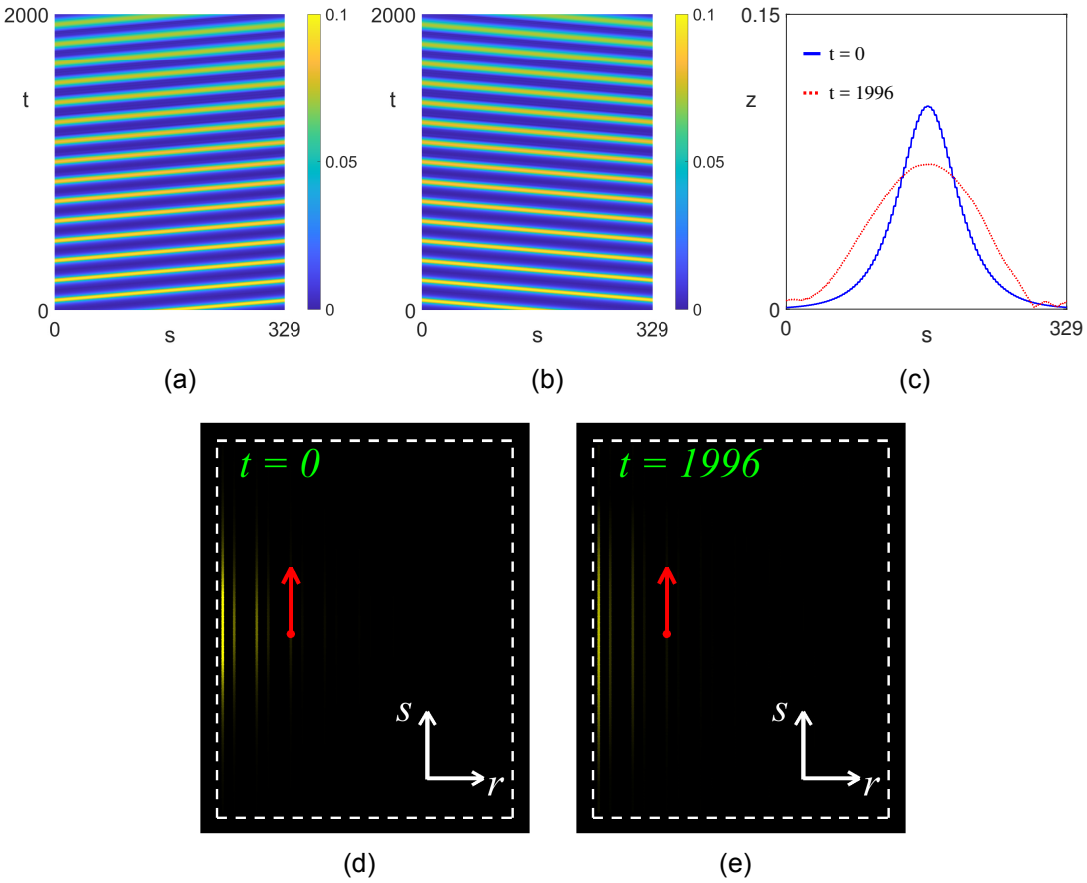

Figure 1.6: Numerical simulations of the 2D linear lattice, with an initialised sech envelope on the left edge, on an $s-$periodic domain. (a,b) The two helical edge modes with (a) $(k_0, \alpha_0) = (9\pi/10, 12.505)$ and (b) $(k_0, \alpha_0) = (11\pi/10, 12.505)$. (c) Profile of the left edge corresponding to the evolution of (a). (d,e) Snapshots of the evolution of (a) on the 2D lattice (d) initially and at (e) $t = 1996$. The white lines represent the border of the lattice and the red arrow indicates direction of envelope propagation.

file over a long time-frame in the linear system. This dispersion is seen more clearly in Fig. 1.6(c). It is also immediately obvious that energy is not lost from the edge to the bulk, but rather distributed amongst the sites on the edge, inferring the topological protection of the mode. This is shown in Fig. 1.6(d–e) where a top-down view of the 2D lattice for the evolution of Fig. 1.6(a) is depicted initially and after a long timeframe ($t = 1996$). The white border indicates the edge of the mechanical lattice and the yellow indicates the excitation at a given site corresponding to the variable z. The red arrow shows the location of the centre of the envelope and indicates the direction of propagation. There is a clear dispersion of the envelope along the edge sites as expected according to the profiles shown in Fig. 1.6(c). The topologically protected behaviour of the envelope is a physical property associated to the unique design of the mechanical lattice, however, the dispersion of the envelope over time is also associated to the linear model of this lattice. It remains whether an envelope that exhibits

a more-robust edge propagation is achievable in such a MTI system, which is a key question that we aim to explore in the forthcoming work.

Chapter 2

Introduction

2.1 Aims and objectives

The question of what additional dynamics one may expect when a mechanical TI system, such as Eq. (1.36), exhibits nonlinear terms is generally ignored in the literature of mechanical TIs and it remains largely an open question how to effectively harness the nonlinearity present in such systems. This is reflected in the very last statement in the work of S. Huber [93],

"Finally, nonlinear effects, which are ubiquitous in mechanical systems, will surely surprise us with interesting features beyond the simple linear theory of topological phonons."

The existing literature on nonlinear topological mechanics notably includes establishment of topological solitons as the nonlinear mechanism for zero-frequency floppy modes to propagate through the bulk of a 1D Maxwell frame [45], and the effect of nonlinearity on the resonant characteristics of high-frequency edge modes in both 1D and 2D mechanical TIs [148]. However, the possibility of nonlinear wave propagation remains open in the high-frequency case, such as the mechanical TI described by Eq. (1.36). We aim to address these nonlinear effects in the work presented here. In particular, we consider nonlinearity that is on-site only and imposed explicitly due to the type of mechanical component used in the discrete model of Eq. (1.36). The on-site nonlinearity is a property of the discrete element itself, with simple gravity-pendula exhibiting a sinusoidal nonlinearity far from the small-angle approximation. Since the pendula and connective springs are viewed as discrete elements here, we expect no extra nonlinear terms in the system providing that a rigid rod is used for the hanging pendula. We note that if one instead considers the response of the connective springs from the perspective of continuum mechanics, then geometric

and/or material nonlinearities may be present; seminal work on this topic studies phononic crystals, which may be viewed as nonlinear spring networks [191]. With the prospect of these additional nonlinearities available in mechanical TIs we expect more complicated models to appear with additional nonlinear edge solutions available, however, for the purpose of the current analysis we focus purely on the coupled pendula being viewed as discrete elements. Coupled pendula have been extensively studied in terms of synchronisation and destabilisation [153], while coherent structures therein such as breathers continue to capture considerable interest [56, 200, 149]. We also note that nonlinear elastic metamaterials known as granular crystals have attracted much recent attention [51], with topological effects already demonstrated [44].

The main objective of this work is to incorporate the concepts of nonlinear waves into the metamaterial designs, with a specific focus on TIs in 2-dimensions with the work presented here including aspects of condensed matter physics, nonlinear dynamics, and classical mechanics.. This idea has already been implemented for photonic TIs [10, 125], but our work will represent a first step into the mechanical (phononic) world. Most importantly we aim to discover, for what we believe to be the first time, topologically protected edge solitons (TPES) in mechanical TIs, which are nonlinear edge waves that inherit the topological protection of the linear system. We will aim to form a generalised mathematical framework to describe the underlying, nonlinear excitation dynamics of the edge modes, thus allowing a multitude of nonlinear phenomena to be found in the original 2D mechanical TI described by Eq. (1.36). The nonlinear analysis is considered to balance the dispersion seen in the edge mode propagation of Fig. 1.6, and produce more robust structures inheriting the topological protection of the full linear system. Applications of MTIs include, but are not limited to, the design of acoustic delay lines using reconfigurable, topological phononic crystals [212, 48, 190] and sound manipulation using topological acoustic polaritons [205]. With nonlinear effects enabled, there is also the distinct possibility that the phononic conduction propagating around the edge/surface of a mechanical TI will maintain its profile regardless of the domain shape. Therefore, the MTI could perform as an acoustical cloak in a similar manner to cloaks proposed in the optical setting [169].

Using the same framework as the single edge mode case, a key aim that we also propose is to study how two edge modes (bimodal dynamics) will interact nonlinearly in the mechanical TI. The dynamics should be significantly different from that of the singular edge mode (unimodal dynamics) propagation. There has already been considerable progress made on bimodal dynamics in the photonic case [96], but our work will form a basis for the phononic

case. This proposition will allow the formation of topologically protected ***vector*** edge solitons (TPVES), which will extend the allowed nonlinear solutions beyond standard, scalar soliton propagation. The existence of TPVES provides a framework that permits the possibility of energy transfer between the two modes which is a concept that is yet to appear, to the extent of our knowledge, in the current literature.

2.2 An overview of methodology

In this section, we will briefly outline the key methods presented throughout this thesis. In general, we explore and analyse both ordinary differential equations (ODEs) and partial differential equations (PDEs).

2.2.1 Asymptotic methods

One particular analytical method that we use throughout is the method of multiple scales [23]. If one assumes that the underlying dynamics of a PDE are well-separated into different spatio-temporal scales, then we are able to substitute a multiple-scale ansatz (sometimes referred to as a weakly-nonlinear ansatz) into the PDE itself. The multiple-scale ansatz is chosen to represent the generic field variable, u, as an asymptotic series of the small expansion parameter ϵ, where $|\epsilon| \ll 1$. The space, x, and time, t, variables are also expanded in terms of this small parameter to enforce the slow and fast behaviour of each dimension, i.e.

$$X_n = \epsilon^n x, \quad T_n = \epsilon^n t, \quad \text{for } n = 1, 2, 3, \cdots, \tag{2.1}$$

where the X_n, T_n represent slow variations in space/time, and x, t represent the fast variation. Formally, the field expansion then looks like the following,

$$u(x, X_1, X_2, t, T_1, T_2, \ldots) = \sum_{n=0}^{\infty} \epsilon^n u_n = u_0 + \epsilon u_1 + \epsilon^2 u_2 + \cdots, \tag{2.2}$$

where the coefficients u_n at each order are functions of the slow and fast variables. In practice, the linear terms of the PDE give an idea on what slow variables need to be included in the ansatz. Each order of ϵ then produces an equation which may be solved accordingly and the conditions on the variables u_n that allow these PDEs to be solved are the *solvability conditions* of the prob-

lem. The general form of these equations, at each order, may be written as

$$\mathcal{L}u_n = \mathcal{N}_n, \tag{2.3}$$

where $\mathcal{L}$ is the linear operator of the original PDE and $\mathcal{N}$ is a nonlinear function involving space and time derivatives, as well as the field variables u_m of lower orders ($m < n$). In most cases, the solvability condition on u_1 usually describes this function as a linear combination of the eigenfunction(s) of the linear operator $\mathcal{L}$, with an accompanying amplitude function, $\mathcal{A}$, describing the variation on slow scales [131].

Through correct implementation of the ansatz and solvability conditions one usually stops the analysis of the orders when the lowest non-trivial order is obtained. This non-trivial order should be apparent from the highest-order nonlinearity of the PDE and the equation obtained at this order is known as the amplitude equation. The amplitude equation is, in general, a nonlinear PDE involving an amplitude function, $\mathcal{A}$, where the nonlinear terms will yield some similarity to the nonlinearity of the original PDE. In practice, one usually truncates the expansion (2.2) to a leading order term, with higher-order terms omitted, that provides small residuals in the analysis and are often deemed negligible relative to the solution. Asymptotic solutions of the original PDE are then found by substituting the solution of the amplitude equation, obtained analytically or numerically, back into the expansion (2.2). The solutions obtained through this multiple-scale ansatz may be numerically evolved in the original PDE, or experimentally observed, to show how well the truncated form defines the solution. If there are irregularities in the evolved solution, then one may wish to include higher-order terms back into the analysis to remove residual terms. Weakly-nonlinear analysis of this kind has been proven to be fundamental in many research areas including, but not limited to, deep water waves [9], mathematical biology [66, 37], and fluid mechanics [203, 196].

2.2.2 Numerical solutions of ODEs/PDEs

Throughout the thesis we will consider the solutions of the proposed systems numerically using the software MATLAB (recently used version: R2020b). Discrete, nonlinear lattice problems that we will consider can be written in the general form,

$$\ddot{u}_i = M_{ij}u_j + N(u_i) \tag{2.4}$$

where M_{ij} denotes the linear connections between the lattice variables, u, and $N(u_i)$ is a nonlinear on-site function. The $\cdot$ denotes the time derivative and

the connection matrix M is typically sparse. This problem can be cast into a solvable form by making the denotation $v = \dot{u}$ and writing the system as a collection of first order ODEs,

$$\dot{u}_i = v_i, \tag{2.5}$$

$$\dot{v}_i = M_{ij}u_j + N(u_i). \tag{2.6}$$

The system of equations (2.5-2.6) forms a non-stiff problem which may be solved, with an appropriate initial condition, using the in-built MATLAB solver `ode45`. This solver is a single-step solver utilising the Runge-Kutta (4,5) formula (Dormand-Prince method), and more information on this method can be found in the MATLAB documentation or equivalently in [62]. We note that to remove any numerical/artificial dissipation of the solution we decrease the tolerance of the solver, in the `ode45` options, to be fixed as 10^{-5} for the relative tolerance and 10^{-8} for the absolute tolerance. As defined in MATLAB, the relative tolerance defines a measure estimate of the allowable error in each integration step relative to the size of each solution component, whereas the absolute tolerance is used as a measure estimate of the error when the solution component approaches zero. One is usually constrained by the allowable array size in MATLAB which, for the sparse matrix M, is an array of approximately $43,000 \times 43,000$ elements for the hardware specifications we are using. To enable a greater freedom of domain sizes, one must use hardware with greater computational power, and thus greater physical memory for MATLAB to utilise, or more specialised software. This is only a minor problem which doesn't directly affect the work presented in this thesis and we choose to limit our domain sizes so that the numerical simulations may be replicated on the average hardware. We note that the numerical simulations displaying the evolution of the edge modes in Fig. 1.6 were achieved by recasting the MTI equation of motion (1.36), which follows the general form of Eq. (2.4) with $N(u_i) = 0$, into a collection of first order ODEs like Eqs. (2.5–2.6) and applying the above solver.

As one would expect, the numerical solutions of PDEs are more complicated than that of the above ODE problem due to the addition of a secondary, spatial variable. There is no difference, however, when one considers the major issue of temporal stability of the numerical profile; the profile should be stable to perturbations if the solution is to be comparable to what one could expect from experiments. In general, we will define a solution stable if it has a linearly stable background field and if it propagates stably throughout the numerical evolution for a sufficiently long time frame. The stability of the background will be considered analytically, where conditions for stability will be presented, and may

be checked against numerical computation of the eigenvalues through the in-built MATLAB function `eigs`. A more precise definition of stability, for coherent structures, requires the thorough analysis of the point spectrum which usually requires numerical techniques. One may compute the point spectrum of these solutions by discretising the linear operator using a finite-difference scheme [78], with appropriate boundary conditions, and using the `eigs` function. Since a numerical method such as this may produce spurious point eigenvalues, this is only used as a rough guide for the overall stability of the solution. This suffices for our analysis since we will be ensuring a stable propagation via direct numerical simulations of the problem. If the solution is stable then any small noise/perturbations will decay away, but unstable solutions will exhibit an exponential growth of the perturbation related to the unstable eigenvalues. Any instability should present itself in finite-time during the numerical simulations.

To numerically solve the PDEs on a spatially periodic domain we will once again impose a solver in the MATLAB software. When we attempt to solve a PDE of the form

$$u_t = \mathcal{L}(u, u_x, u_{xx}, \ldots) + N(u), \tag{2.7}$$

where $u = u(x,t)$ and $\mathcal{L}, N$ represent linear and nonlinear functions respectively, we utilise spectral methods on the periodic domain [182]. The purpose of this method is to discretise the spatial dimension, using a Fourier transform on an appropriately chosen mesh grid, so that the PDE is transformed into a system of ODEs for the Fourier mode amplitudes. The ODE system may then be separated into the linear and nonlinear terms. According to [54], the spectral discretisation causes the problem to be stiff, because the time scale associated with the n^{th} mode scales as $O(n^{-m})$ for large n, where m is the order of the highest spatial derivative. Consequently, the highest modes then evolve on short time scales. Due to the stiffness of the problem one can no longer numerically solve the ODE system using the in-built MATLAB solver `ode45`, as this is only applicable to non-stiff problems. Generally, one will instead use a preferred time-stepping scheme, such as exponential time differencing (ETD) [54], where an exact integration of the governing ODE system is computed and followed by an approximation of the integral involving the nonlinear terms prescribed by the chosen scheme. The nonlinear terms are usually evaluated, at a given time point, by transforming the solution into the physical space via an inverse Fourier transform, evaluating the terms on the mesh grid, and then transforming back into the Fourier space. One then discretises the solution in time and solves the ODE system through the multiplication of an integrating factor. In doing so, the solution at a given time step is a summation of a linear

term and a nonlinear term that are both governed by the solution at the previous time step. The linear term is exact, and may be computed explicitly, where as the nonlinear term is a numerical approximation that is obtained through the chosen numerical scheme; we use the exponential time differencing-2 (ETD2) algorithm [54]. In general, we consider the time-step of the discretisation to be sufficiently small, between 10^{-4} and 10^{-3}, and the number of mesh points N is chosen to appropriately model any initial condition that we impose.

As a final note, we briefly mention numerical solutions of PDEs where the system now includes a secondary time derivative, i.e.

$$u_{tt} = \mathcal{L}(u, u_x, u_{xx}, \ldots) + N(u). \tag{2.8}$$

Though Eq. (2.8) is similar in construction to Eq. (2.7), the addition of the secondary time derivative has a significant impact on the way we numerically solve such a problem. When applying the spectral discretisation to the spatial variable in Eq. (2.7) the chosen ETD2 scheme involves multiplying the first order ODE system by an integrating factor to explicitly solve the linear part of the problem [54]. Since the ODE system after the spectral discretisation of Eq. (2.8) is a second order system, the integration factor does not apply here in general. Instead, one usually writes the second order equation as a system of first order ODEs in time: see, for instance, the use of spectral methods when numerically solving the 1D linear wave equation [180]. The recast system is then a nondiagonal problem and looks similar to that of Eqs. (2.5-2.6), only now being solved for the Fourier mode amplitudes which forms a stiff problem. As discussed in [54], the computation of the integration factor matrix associated with the nondiagonal problem is non-trivial to calculate for the ETD scheme and whether the linear problem exhibits zero eigenvalues plays a huge role in this numerical method. We note that the recasting into first order equations also doubles the number of variables that are needed to evolve, which impacts the overall computational cost of the simulations and may be a significant increase in general. It is important to note at this stage that our main priorities for these numerical simulations are efficiency and simplicity of implementation in MATLAB, providing that the accuracy of the solution is not fully sacrificed. This is, of course, subjective and the utilised solver is generally down to preference, with each numerical solver presenting certain advantages/disadvantages: see [179] for a review of numerical schemes solving nonlinear PDEs. Since we recast Eq. (2.8) into a system of equations that are first order in time, it is efficient, for the purpose of our work, to keep the numerical analysis similar to that of Eqs. (2.5-2.6) so that we may adapt the MATLAB code slightly and utilise

the in-built ODE solver `ode45`. In order to do this, we must first discretise the spatial derivative using a centred finite-difference scheme [78], opposed to the spectral discretisation when solving Eq. (2.7), so that a non-stiff ODE system is proposed. Using this spatial discretisation, the ODE system is then exactly Eqs. (2.5-2.6), where the indexes i, j refer to the mesh points representing the discretised 1D spatial domain. This system is then solved as described earlier in this section using `ode45`. We note that, in this work, the initial conditions used in the numerical simulations of Eq. (2.8) are imposed such that we know, in general, how the solution should propagate according to the equation, so one can make an informed decision whether the solver is providing an accurate solution.

2.2.3 Numerical continuation of ODEs

In general, we will consider stationary, coherent structures of PDEs by reducing the equation down to a dynamical system of ODEs with real-valued field variables dependent on space only. This system can then be thought of as a spatial-analogue of Eqs. (2.5-2.6) on one lattice site, where the derivative is now in space. One may also have multiple components, higher-order spatial derivatives, or an extension to the complex space which subsequently increases the dimension of the ODE system. The major problem with nonlinear ODE equations like Eqs. (2.5-2.6) is that there is a small likelihood of analytical solutions present, especially for systems extended to the complex-space and higher-dimensional/coupled systems. Due to this, one may choose to seek out numerical solutions permitted by a given set of rules. In this instance we utilise methodology developed for dynamical systems, in particular bifurcation theory [55], to compute branches of numerical solutions related via a continuation parameter of the system. The types of problems we will consider in this thesis can be generalised to the form of

$$\boldsymbol{u}' = f(\boldsymbol{u}, p), \qquad \boldsymbol{u}(\cdot),\ f(\cdot,\cdot) \in \mathbb{R}^n \tag{2.9}$$

where $\boldsymbol{u} = \boldsymbol{u}(x)$, p is a real-scalar continuation/bifurcation parameter, and f is a collection of linear and nonlinear terms. The system (2.9) is an autonomous, n-dimensional spatial ODE and the dynamics are affected by a particular choice of boundary conditions.

To compute numerical solutions of Eq. (2.9), we use the numerical software `AUTO-07p` (AUTO) [61]. AUTO continues solutions to boundary-value problems of this type by numerically continuing, in the control parameter p, via a pseudo-arclength method. An initial solution to the problem (2.9) may be denoted by

$\boldsymbol{U}_0 = (\boldsymbol{u}_0, p_0)$ and a solution branch is a set of solution points $\boldsymbol{U}_n = (\boldsymbol{u}_n, p_n)$, that also solve the system (2.9), which are connected to the initial point $\boldsymbol{U}_0$ via some path in the $(\boldsymbol{u}, p)$ space. Numerical continuation is a technique which details this path and produces a set of points on this solution branch. Given the initial guess $\boldsymbol{U}_0$, the next point on the solution curve is predicted by the type of numerical continuation one uses. A prediction of the next point using the pseudo-arclength method is taken by considering a sufficiently small step-size along the tangent vector of the given point. Since the numerical scheme is a predictor-corrector method, one then refines the predicted point using Newton's method, for a set number of iterations, followed by the chord (secant) method. Note that convergence is usually met, for our problems, within the Newton iterations. This process is then restarted a set number of times, defined by the user in the relevant AUTO file. The pseudo-arclength method is used by AUTO to incorporate simple folds/saddle-node bifurcations (turning of the branch with an increase/decrease of p), which the natural parameter continuation method may have problems with.

Providing that the initial solution is sufficiently far away from any singular points (points with a rank deficient Jacobian), we may continue the solution in AUTO forming a solution branch in the $\boldsymbol{U}$ space. In general, as one continues in the parameter p, the solution branch only encounters singular points in the form of simple folds so the full picture of the $\boldsymbol{U}$ solution branch(es) may be computed. For the purpose of our analysis, we are purely interested in using AUTO to compute these local solution branches, rather than the detection of bifurcation points and branch switching that AUTO is also widely used for. The key reasoning behind the dismissal of secondary branches in our work is due to our main aim of translating the numerical profiles obtained in AUTO back into the mechanical TI to produce topologically protected (vector) edge solitons, as discussed in Sec. 2.1. Therefore, the objective here is not to define every plausible nonlinear solution to Eq. (2.9) using AUTO, but rather to define, numerically, examples of spatially localised solutions that are most-often utilised in literature as robust translations of energy, i.e. solitons [207, 112] and fronts (domain walls) [197, 204, 101]. Such solutions have shown to be applicable to a wide-array of physical disciplines including, but not limited to, the fields of nonlinear optics [138, 158, 170, 120], Bose-Einstein condensates [21, 26, 193], water waves [5, 184], collision-based computing [159], and photorefractive materials [213]. The primary solution branches that we form in AUTO then provide a description, numerically, on how these localised solutions are related to each other through a single bifurcation parameter p, as well as their relation to the uniform states. Though we expect secondary branches, and branches stem-

ming from bifurcation points of higher co-dimension, to exist and fully describe, numerically, whole families of nonlinear solutions to Eq. (2.9), they are not necessary to consider in the grand scheme of this work on edge solitons in mechanical topological insulators.

To run a particular problem in AUTO one requires two necessary files; the function file implemented in `FORTRAN` language and a constants file enclosing all user inputs for AUTO. We run the problem through a script file and, in our case, we will always provide a data file that provides AUTO with numerical data of a guess solution. The problems we consider are boundary-value problems, with appropriate boundary conditions paired to the specific problem/desired solution, and the equation file encodes the ODE system and these boundary conditions. We note that the ODE problem must be rescaled to be solved on the truncated domain $x \in [0, 1]$, which is achievable by multiplying the right-hand side of the ODE system by the domain size L. The data file then includes the guess solution on the original domain size L. A typical AUTO output is depicted using the definition of the L^2-norm, as described in the AUTO manual [61], and is plotted against the continuation parameter p. For a particular value of p, the L^2-norm is written as,

$$\sqrt{\int_0^1 \sum_{k=0}^{DIM} U_k(x)^2 \, \mathrm{dx}} \tag{2.10}$$

where $U_k(x)$ is the solution to the k^{th} coupled differential equation and DIM is the number of equations. We fix the number of mesh points in AUTO to 10^3 for all problems, but note that the continuation of a solution branch with more complicated profiles may require more mesh points to truly measure any sudden variations. One usually chooses an appropriate pseudo-arclength step-size, `DS`, for the problem at hand, depending on how quickly we wish to compute the solution branch and how many points on the branch we wish to compute. In general, `DS` may be positive or negative, depending on the required direction of continuation, and we implement a value of `DS`$= \pm 10^{-3}$. However, AUTO yields the opportunity to alter this value after a number of iterations have been computed, providing that the lower (`DSMIN`) and upper (`DSMAX`) step-size limits are imposed such that `DSMIN`$\leq$|`DS`|$\leq$`DSMAX`. If no convergence is met at the current choice of `DS`, then AUTO will try the computation again with `DS`/2, and this process will continue until the step-size reaches the limit `DSMIN`. We fix this limit to be `DSMIN`$= 10^{-7}$ for all of the problems we will face, but one may wish to fine-tune this value for other systems/desired solutions. In contrast, if there is a rapid convergence of the Newton iterations then the step-size is increased, to remove unnecessary computation time, but not beyond the limit `DSMAX`. This

limit is fixed, for all of our problems, to DSMAX$= 10^{-2}$. In practice, if there are any obscure jumps/sharp curvatures of the solution branch then one should run the problem with more accurate/smaller AUTO constants imposed.

2.3 Outline of the thesis

Chapter 3 presents the nonlinear extension of the mechanical topological insulator described by Eq. (1.36), where we add an inherent on-site nonlinearity into the dynamical problem. We then formulate and present the existence of topologically protected edge solitons in this nonlinear mechanical topological insulator. Note that a large portion of this chapter is taken from our published work [171].

Chapter 4 presents an extension of the Chapter 3 analysis, from the underlying unimodal dynamics to the now bimodal dynamics. We discuss conditions in which the bimodal dynamics are well-governed by a mathematical reduction to the CNLS, and present ways of enforcing the condition by adapting the connections of the mechanical lattice and utilising mechanical properties.

Chapters 5-7 focus on solutions to the non-integrable CNLS equation. We first, in Chapter 5, formulate front solutions and provide criteria for the linear stability of the connecting background fields, as well as produce conservation equations describing some nonlinear interactions of fronts with grey solitons. Chapter 6 focuses on vector soliton solutions. The soliton solutions include both numerical and analytical profiles of bright-bright, bright-dark, dark-bright, and dark-dark solitons. A qualitative analysis of the inelastic collisions of vector solitons in non-integrable CNLS systems is also considered. Chapter 7 analyses the formation of more 'exotic' solutions, including travelling periodic and localised patterned states, that arise from the weakly-nonlinear analysis near a Turing bifurcation in the reduced spatial ODE system. We compare these states to similarly-formed patterned states of the Swift-Hohenberg equation [34].

Chapter 8 presents the implementation of the derived CNLS solutions, from Chapters 5-7, as topologically protected, nonlinearly interacting edge modes of a newly-designed mechanical topological insulator. We discuss the validity of these underlying solutions and analyse the topological protection of the bimodal dynamics.

Finally, we discuss and conclude the work in Chapter 9. We consider potential applications of this work, mention some possible improvements/considerations to the methodology, and discuss future directions/extensions of the work.

Chapter 3

Unimodal behaviour of a nonlinear MTI

In this chapter, we use the theory of nonlinear waves to describe nonlinear interactions between high-frequency edge modes in a 2D mechanical TI. The primary aim is to discover topologically protected edge solitons (TPES), which are nonlinear travelling edge waves that inherit the topological protection of the corresponding linear system. We formulate the problem by adding an inherent, on-site Duffing nonlinearity to the MTI, and utilise mathematical techniques to describe nonlinear solutions in the weakly nonlinear regime. Using dimension reduction and asymptotic analysis, the original 2D nonlinear system is reduced to the classical 1D nonlinear Schrödinger (NLS) equation (1.3), which is a well-studied integrable equation. The NLS admits a plethora of soliton and rogue wave solutions, all of which correspond to TPES in the original system. We also propose a 2D edge reconstruction method to efficiently initialise nonlinear structures embedded on a non-zero background.

Theoretical predictions obtained by the NLS equation are compared to numerical simulations on relatively large domains and over long time-frames, with excellent agreement. Different domain shapes are also proposed to enforce the topological protection of the nonlinear structures, and we analyse any scattering of the energy at the defects of the different domain types. The evolution of soliton amplitudes described by the NLS are compared to non-NLS amplitudes, enforcing the validity of the NLS as the underlying, governing envelope equation. The proposal of TPES practically enables robust transport of a mechanical state from one location to another on the edge of a generic 2D lattice, which is shown by the numerical simulations of the nonlinear MTI.

3.1 Reduction to the NLS equation

The MTI that we will consider for our analysis is the system proposed by Süsstrunk and Huber [177], governed by Eqs. (1.30-1.35). To study the propagation of nonlinear edge waves we will add an on-site nonlinearity into the system in the form of an additional cubic (Duffing) term that is inherent to simple gravity-pendula. It is assumed that the addition of this cubic term does not cause a nonlinear response from the connective springs in the model since we will consider a small amplitude response of the pendula, i.e. the nearest neighbour connections in the system remain linear. As mentioned previously, the system is composed of springs and pendula that are modelled as discrete elements, therefore we do not expect any further nonlinearity (geometric or material) in the lattice problem. The linear ODE system is then extended to incorporate this on-site nonlinearity with the ODEs involving the 6 cell variables now written as

$$\begin{aligned}
\ddot{x}^{(0)}_{r,S} =& -(\omega_0^2 + A_s f)x^{(0)}_{r,S} + \sigma(x^{(0)}_{r,S})^3 \\
&+ f(x^{(0)}_{r+1,S} + x^{(0)}_{r-1,S} + x^{(1)}_{r,S} + x^{(2)}_{r,S-1}), && (3.1)\\
\ddot{y}^{(0)}_{r,S} =& -(\omega_0^2 + A_s f)y^{(0)}_{r,S} + \sigma(y^{(0)}_{r,S})^3 \\
&+ f(y^{(0)}_{r+1,S} + y^{(0)}_{r-1,S} + y^{(1)}_{r,S} + y^{(2)}_{r,S-1}), && (3.2)\\
\ddot{x}^{(1)}_{r,S} =& -(\omega_0^2 + A_s f)x^{(1)}_{r,S} + \sigma(x^{(1)}_{r,S})^3 \\
&+ f(x^{(0)}_{r,S} + x^{(2)}_{r,S}) - \frac{f}{2}(x^{(1)}_{r+1,S} + x^{(1)}_{r-1,S}) \\
&+ \frac{\sqrt{3}f}{2}(y^{(1)}_{r+1,S} - y^{(1)}_{r-1,S}), && (3.3)\\
\ddot{y}^{(1)}_{r,S} =& -(\omega_0^2 + A_s f)y^{(1)}_{r,S} + \sigma(y^{(1)}_{r,S})^3 \\
&+ f(y^{(0)}_{r,S} + y^{(2)}_{r,S}) - \frac{f}{2}(y^{(1)}_{r+1,S} + y^{(1)}_{r-1,S}) \\
&+ \frac{\sqrt{3}f}{2}(-x^{(1)}_{r+1,S} + x^{(1)}_{r-1,S}), && (3.4)\\
\ddot{x}^{(2)}_{r,S} =& -(\omega_0^2 + A_s f)x^{(2)}_{r,S} + \sigma(x^{(2)}_{r,S})^3 \\
&+ f(x^{(0)}_{r,S+1} + x^{(1)}_{r,S}) - \frac{f}{2}(x^{(2)}_{r+1,S} + x^{(2)}_{r-1,S}) \\
&+ \frac{\sqrt{3}f}{2}(-y^{(2)}_{r+1,S} + y^{(2)}_{r-1,S}), && (3.5)\\
\ddot{y}^{(2)}_{r,S} =& -(\omega_0^2 + A_s f)y^{(2)}_{r,S} + \sigma(y^{(2)}_{r,S})^3 \\
&+ f(y^{(0)}_{r,S+1} + y^{(1)}_{r,S}) - \frac{f}{2}(y^{(2)}_{r+1,S} + y^{(2)}_{r-1,S}) \\
&+ \frac{\sqrt{3}f}{2}(x^{(2)}_{r+1,S} - x^{(2)}_{r-1,S}). && (3.6)
\end{aligned}$$

where σ is the strength of the Duffing nonlinearity, found by expanding the restoring force of the pendulum, i.e. $-\omega_0^2 \sin(\theta) \approx -\omega_0^2\theta + \frac{\omega_0^2}{6}\theta^3$, which gives $\sigma = \frac{\omega_0^2}{6}$. This extends the matrix linear problem (1.36) to the nonlinear compact matrix problem

$$\ddot{\boldsymbol{X}}_{r,S}(t) = (\boldsymbol{\mathcal{L}}\boldsymbol{X})_{r,S} + \sigma\boldsymbol{\mathcal{N}}_{r,S} \tag{3.7}$$

where $\boldsymbol{\mathcal{N}} = \boldsymbol{X}^3$. On a 1D domain with $\mathcal{L}$ chosen as the discrete Laplacian, Eq. (3.7) reduces to the 1D nonlinear Klein-Gordon equation with a cubic nonlinearity [76], from which the 1D NLS equation can be derived using the method of multiple scales [5]. Here, we will combine this procedure with dimension reduction to derive a 1D amplitude equation from the general 2D system given by Eq. (3.7).

The linear problem ($\sigma = 0$) has already been considered and yields the solvability condition (1.37), which produces the dispersion relation that we will use throughout the nonlinear analysis. In the nonlinear problem ($\sigma \neq 0$), similarly to [7, 10], we aim to construct a weakly nonlinear edge mode. Since Eq. (3.7) does not have a small parameter, we must introduce the small parameter in the initial condition. This is achieved by considering the spectral envelope with a narrow width $0 < \epsilon \ll 1$ at a carrier wavenumber $k = k_0$ and carrier frequency $\alpha_0 \equiv \alpha(k_0)$, in the reference frame co-moving with the group velocity of the envelope $\alpha_0' \equiv \alpha'(k_0)$. Specifically, we choose a multiple scale ansatz for the weakly nonlinear edge mode of the form

$$\boldsymbol{X}(r, S, \tilde{S}, t, \tau) = \epsilon\left\{C(\tilde{S}, \tau)e^{i(Sk_0 - t\alpha_0)}\boldsymbol{X}_r^E + c.c\right\} + O(\epsilon^2), \tag{3.8}$$

where $C(\tilde{S}, \tau)$ is the scalar envelope function and evolves in the slow variables $\tilde{S} \equiv \epsilon(S - \alpha_0' t)$ and $\tau \equiv \epsilon^2 t$. Thus, the time and space differential operators are now written as $\partial_t = \epsilon^2\partial_\tau - \epsilon\alpha_0'\partial_{\tilde{S}} - \alpha_0 i$ and $\partial_S = \epsilon\partial_{\tilde{S}} + k_0 i$ respectively.

One can then substitute the ansatz (3.8) directly into Eq. (3.7) and expand asymptotically in ϵ. In particular, we expand the dispersion relation $\alpha(k)$ around the carrier wavenumber k_0 in operator form as

$$\alpha(k) = \alpha_0 - i\alpha_0'\epsilon\partial_{\tilde{S}} - \frac{1}{2}\alpha_0''\epsilon^2\partial_{\tilde{S}\tilde{S}} + O(\epsilon^3), \tag{3.9}$$

where $\alpha_0'' \equiv \alpha''(k_0)$. We note that we have utilised the relationship $\tilde{k} = k - k_0 = -i\epsilon\partial_{\tilde{S}}$ here and the physical envelope width is related to the spectral envelope width via reciprocity, i.e. the physical envelope is expected to have a width of ϵ^{-1}. At $O(\epsilon)$ and $O(\epsilon^2)$ the equations are trivial due to the solvability condition and the shift into the co-moving frame of reference. To leading nontrivial order, at $O(\epsilon^3)$, taking the inner product of both sides of the equation with $\boldsymbol{X}_r^E$,

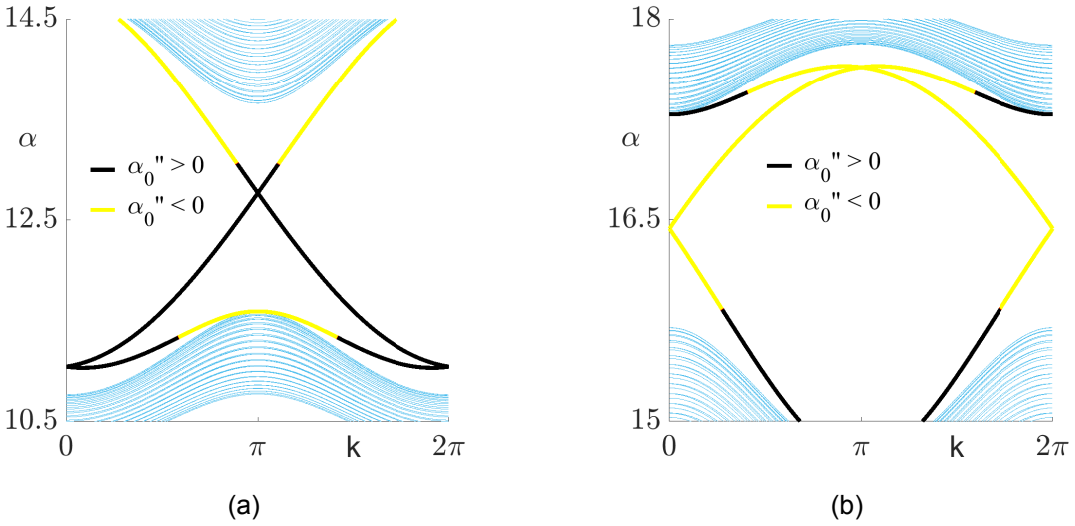

(a) (b)

Figure 3.1: Dispersion sign for the edge modes. The sign of α_0'' is shown for each of the edge modes in the (a) lower bulk-band gap and (b) upper bulk-band gap. The edge mode is shown as black (yellow) if the second-derivative is positive (negative).

where the inner product is defined generically as $\langle \boldsymbol{g}, \boldsymbol{h} \rangle = \sum_j g_j^* h_j$, then the 1D classical second-order NLS equation appears in canonical form:

$$iC_\tau + \frac{\alpha_0''}{2} C_{\tilde{S}\tilde{S}} + \frac{3\tilde{\sigma}}{2\alpha_0} |C|^2 C = 0, \tag{3.10}$$

where $\tilde{\sigma} = \sigma \|\boldsymbol{X}_r^E\|_4^4 \equiv \sigma \sum_j |\boldsymbol{X}_j^E|^4$. Residual terms can be removed by considering higher-order ϵ terms in the ansatz (3.8), but we deem the residual negligible here in the presence of small amplitudes.

The NLS equation is a maximally balanced equation and is focusing or defocusing if $\alpha_0''\alpha_0/\tilde{\sigma} > 0$ or $\alpha_0''\alpha_0/\tilde{\sigma} < 0$ respectively. Since the quantity $\tilde{\sigma}$ is strictly positive, and we restrict the carrier frequency to $\alpha_0 > 0$, the dispersive term directly governs whether the regime of the NLS is focusing or defocusing. Therefore, if one calculates the second-derivative α_0'' for the edge modes shown in Fig. 1.4, then we can determine carrier wavenumber-frequency combinations that produce focusing/defocusing parameters. The edge modes of the lower and upper bulk-band gaps are shown in Fig. 3.1(a) and Fig. 3.1(b) respectively. The carrier (k_0, α_0) combinations that provide focusing (defocusing) NLS parameters of the edge modes are shown as black (yellow); there is a wide range of chosen dispersion parameters that exhibit focusing or defocusing NLS. We will use this observation to embed different nonlinear structures into the original MTI lattice.

3.2 Numerical Simulations

The propagation of different types of edge solitons around the boundaries of the mechanical lattice can now be investigated by numerically solving Eq. (3.7) with the following initial condition resulting from the ansatz (3.8)

$$\boldsymbol{X}_{r,S}(t=0) = \epsilon C(S) e^{iSk_0} \boldsymbol{X}_r^E + c.c, \tag{3.11}$$

where $C(S)$ represents the initial envelope needed to produce the desired soliton solution to Eq. (3.10). Note that the initial velocity $\dot{\boldsymbol{X}}_{r,S}$ is then written as

$$\dot{\boldsymbol{X}}_{r,S}(t=0) = -\epsilon\alpha_0 i C(S) e^{iSk_0} \boldsymbol{X}_r^E + c.c,$$

where only the greatest contribution of the time derivative is considered and higher-order terms are omitted. Unless otherwise specified, the 2D domain is taken to be rectangular with N_r sites in the r-direction, $r = 0, 1, 2, \cdots, N_r - 1$, and N_S unit cells in the S-direction, $S = 0, 1, 2, \cdots, N_S - 1$. Note that the envelope $C(S)$ quantifies the inter-cell variation of the pulse shape along the edge, whilst the eigenstate $\boldsymbol{X}_r^E$ quantifies both the decay of the pulse shape into the bulk and the intra-cell variation between the three sites forming the unit cell. Hereafter we take $\epsilon = 0.1$, unless specified otherwise, and explore different choices of the carrier wave as specified by (k_0, α_0) with different types of nonlinear envelope $C(S)$.

3.2.1 Travelling Edge Solitons

First, we consider the focusing case where Eq. (3.10) admits a two-parameter family of bright solitons described by Eq. (1.11), where the two parameters can be taken as k_0 and ϵ. The bright soliton is a classical solution of the 1D NLS equation that can be obtained directly from the inverse scattering transform [166]. The focusing condition implies that bright solitons exist only for a finite interval of k_0; at each value of k_0, fixing the spectral width ϵ fixes the amplitude of the wave packet. The 2D bright edge soliton can be obtained by considering the initial condition (3.11) with the scalar envelope function

$$C_B(S) = \Lambda \text{sech}\left(\epsilon(S - S_0)\right), \tag{3.12}$$

where $\Lambda = \sqrt{2\alpha_0\alpha_0''/3\tilde{\sigma}}$ and S_0 represents the initial location of the wave packet. According to the theory, since the evolution is asymptotically governed by the 1D NLS equation, the bright edge soliton should persist at least until $t \sim O(\epsilon^{-2})$.

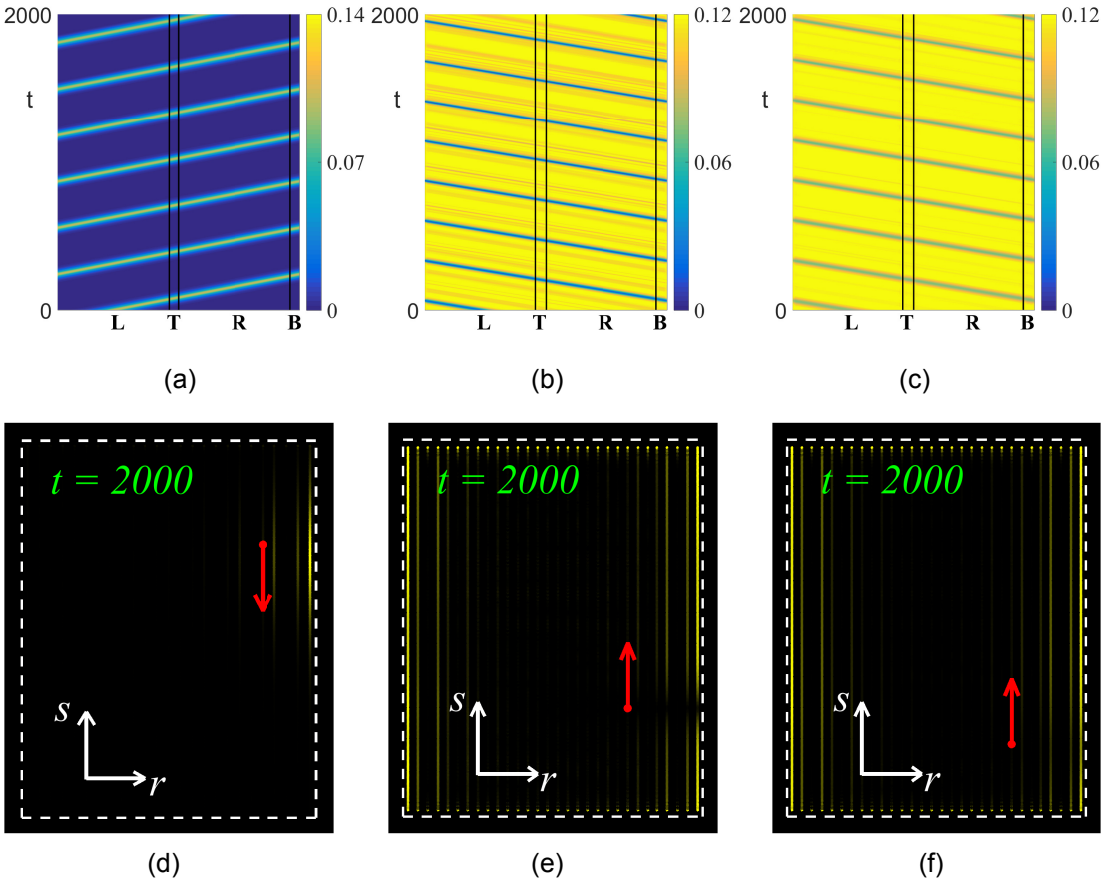

Figure 3.2: Propagation of bright, dark, and grey edge solitons on a rectangular lattice. The 2D domain consists of N_r sites in the r-direction and N_S unit cells in the S-direction. (a) A bright edge soliton on a lattice of size $N_r \times N_S = 30 \times 120$. The carrier wavenumber and frequency are $(k_0, \alpha_0) = (2.827, 12.506)$, which leads to soliton amplitude $\Lambda = 1.376$ in Eq. (3.12). (b) A dark edge soliton on a lattice of size $N_r \times N_S = 30 \times 101$. The carrier wavenumber and frequency are $(k_0, \alpha_0) = (2.146, 13.616)$, which leads to soliton amplitude $\Lambda = 1.705i$ in Eq. (3.13). (c) A grey soliton with the same setup as the dark soliton of (b), only with the parameter $\Phi_G = \pi/3$, and profile given by Eq. (3.14). L, T, R and B correspond respectively to left, top, right, and bottom edges of the 2D lattice. Panels (d,e,f) show 2D snapshots of the mechanical lattice. (d) Bright soliton from the evolution of (a). (e) Dark soliton from the evolution of (b). (f) Grey soliton from the evolution of (c).

At a large time scale, the asymptotic theory may produce errors that eventually destroy the soliton profile.

To visualise these edge solitons we use the same $z_{r,S}^{(i)}$ as in Sec. 1.3.1. The propagation of a bright edge soliton at $(k_0, \alpha_0) = (2.827, 12.506)$ is shown in Fig. 3.2(a) where we plot the intensity on the four edges of the rectangular lattice. Figure 3.2(d) shows a snapshot of the full 2D rectangular lattice with the bright edge soliton located on the opposite edge to initialised. The nonlinear wave traverses the boundaries of the mechanical lattice clockwise with almost no energy loss at the corners, which showcases both the topological protection of the travelling wave and the robustness of the soliton profile.

One can also initialise two bright solitons on the same edge of the MTI and

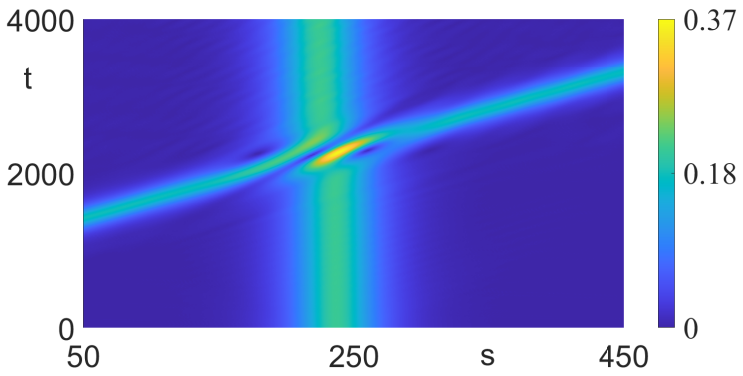

Figure 3.3: The interaction of two bright solitons on the left edge of a rectangular lattice of 9×350 cells, with periodic boundary conditions on the top and bottom edges. The co-moving soliton has carrier wavenumber and frequency $(k_0, \alpha_0) = (2.1, 11.941)$, which leads to soliton amplitude $\Lambda = 1.856$ in Eq. (3.12), whilst the interacting soliton has $(k_0, \alpha_0) = (2.5, 12.241)$ and $\Lambda = 1.597$. The small parameter is chosen as $\epsilon = 0.15$ to facilitate initialisation on the edge.

allow them to collide. For this we move to an S-periodic domain and transfer to the co-moving frame of one of the waves to best visualise the dynamics of the collision. Since the waves are nonlinear we expect that the interaction should not be a simple linear superposition of the two waves. Figure 3.3 shows the interaction of the two bright solitons on a periodic domain of $N_r \times N_S = 9 \times 350$ cells. Here we allow both waves to travel along the periodic edge with one wave having a greater group velocity, thus catching up with the other wave some time after initialising. The slower soliton has a wavenumber $k_0 = 2.1$ and corresponding frequency $\alpha_0 = 11.941$, whilst the faster soliton has a wavenumber $k_0 = 2.5$ and frequency $\alpha_0 = 12.241$. Here we transfer into the co-moving frame of the slower wave and the small parameter is chosen as $\epsilon = 0.15$ to facilitate initialisation of both solitons on the edge. The figure shows that immediately after the collision has occurred, the faster wave has passed through the slower with both structures intact, with a small amount of radiation, and with the similar amplitude and group velocity to before the collision. The only visible change is that the waves exhibit a clear positional shift as a direct consequence of the nonlinear collision. The nonlinear interaction here is permitted due to a spectral overlap of the two wavenumbers.

Akin to bright solitons in focusing NLS, there exists dark soliton solutions to the defocusing NLS given by Eq. (1.13), i.e. the $\alpha_0'' \alpha_0 / \tilde{\sigma} < 0$ regime in Eq. (3.10). Whereas a bright soliton is a localised elevation of energy on a zero background, a dark soliton is a localised depression in the energy of a non-zero background. The initial condition for a dark edge soliton is then given as Eq. (3.11) with the envelope function

$$C_D(S) = \Lambda \tanh(\epsilon(S - S_0)). \tag{3.13}$$

Such a dark edge soliton described by NLS also exists in, for example, polariton TIs [79, 126], but its propagation around a non-periodic 2D domain has not been explicitly demonstrated due to the difficulty of initialising the non-zero background. Here, we realise in Fig. 3.2(b) a dark edge soliton at $(k_0, \alpha_0) = (2.146, 13.616)$ travelling on a rectangular domain with little energy loss over a long time interval. A 2D snapshot of the dark edge soliton on the rectangular lattice is also shown in Fig. 3.2(e).

A generalised form of the dark soliton, which is not limited to a dip of zero intensity, is the grey soliton given by Eq. (1.12); the term 'dark' often incorporates both the grey and dark soliton profiles. The grey soliton envelope takes a form similar to that of the dark soliton and is given explicitly as

$$C_G(S; \Phi_G) = \Lambda \left[\cos\psi + i \sin\Phi_G \tanh\tilde{\Phi}_G \right], \tag{3.14}$$

with $\tilde{\Phi}_G = \epsilon(S - S_0)\sin\Phi_G$ and Φ_G an arbitrary real parameter. We see that the dip in energy is then described by the $\sin\Phi_G$ term and choosing $\Phi_G = \pi/2$ recovers the dark envelope (3.13). Figure 3.2(c) shows the space-time evolution of a grey soliton initialised with wavenumber $k_0 = 2.146$, frequency $\alpha_0 = 13.616$, and $\Phi_G = \pi/3$ on a rectangular domain. Figure 3.2(f) depicts the grey edge soliton after a long timeframe on the 2D mechanical lattice. As expected, the evolution of the grey soliton is in fact similar to the dark soliton for the same wavenumber-frequency pairing, with a primarily undistorted profile throughout the evolution and little decay in the background field after a long time interval. The slight difference in group velocity between the two solitons is also expected since the group velocity of the structure is related to the depression in the energy in the NLS, as shown by Eq. (1.12). The disturbance of the uniform background and small distortion of the profile in the dark and grey evolution is primarily down to our methodology of constructing the non-zero background of the profile. We will outline the rationale behind the construction of the initial condition, which also reveals the origin of the topological protection of edge solitons.

3.2.2 Topological Protection

Assume that a finite 2D domain is dominated by a particular type of edge, e.g. the left and right edges in Fig. 3.2(a–c). Near a topologically protected frequency, the eigenfrequencies and the corresponding eigenfunctions on this 2D domain should match up well with those on a semi-infinite 2D periodic stripe with this type of edge. In the presence of weak nonlinearity, the envelope equa-

tion for the edge solitons on such a finite 2D domain should then be well approximated by the NLS equation on the corresponding 1D periodic domain. Thus, a unidirectionally travelling 1D NLS soliton corresponds to a unidirectionally looping 2D edge soliton insensitive to the details of the 2D domain. The detailed method to construct the edge soliton is described as follows.

To facilitate initialisation of the non-zero background one must compute the full 2D profile, which is a linear combination of 2D eigenfunctions $\boldsymbol{X}^i_{r,S}$, based on the criterion that the left edge contains precisely the initial condition Eq. (3.11). Formally, given the 1D soliton profile, take $C_D(S)$ for example, and a set of wavenumbers k_i, we need to use an inverse discrete Fourier transform (IDFT) to find the coefficients X_i such that

$$C_D(S)e^{ik_0S} = \sum_i X_i e^{ik_iS}. \tag{3.15}$$

For each 2D eigenvalue there exists a set of 2 orthogonal 2D eigenfunctions that we may restrict to the left edge $(r = 0)$ and write in the form $\boldsymbol{u}_1 = \cos(k_iS + \theta)$ and $\boldsymbol{u}_2 = \sin(k_iS + \theta)$, each with the dual harmonics $\pm k_i$. We can isolate the $\pm k_i$ harmonic by forming the linear combination $\boldsymbol{u}_1 \pm i\boldsymbol{u}_2$. The 2D eigenfunctions are then normalised to make the left edge of the form e^{ik_iS} by finding a scaling factor $g_i\boldsymbol{X}^i_{r,S} = \boldsymbol{X}^E_r$ such that the values of all 6 variables in the central cell $(S = S_0)$ agree with the 1D eigenfunction in the least squares sense. The 2D eigenfunctions are now recast into a form most compatible with the initial condition Eq. (3.11).

We then compute the IDFT to find the multiplicative coefficients. Multiplying Eq. (3.15) by e^{-ik_jS} and summing over S gives us the following,

$$\begin{aligned}\sum_S C_D(S)e^{ik_0S}e^{-ik_jS} &= \sum_i X_i \sum_S e^{ik_iS}e^{-ik_jS} \\ &= \sum_i X_i L_S \delta_{ij} \\ &= L_S X_j,\end{aligned}$$

where we have used the properties of the Kronecker delta and L_S is the number of cells. This allows us to write the equation for the coefficients, given as

$$X_j = \frac{1}{L_S}\sum_S C_D(S)e^{ik_0S}e^{-ik_jS}. \tag{3.16}$$

For each 2D eigenfunction its coefficient is obtained by a convolution between the initial profile $C_D(S)e^{ik_0S}$ and the wavenumbers k_j. The wavenumber k_j can be determined accurately by utilising the following relationship between neigh-

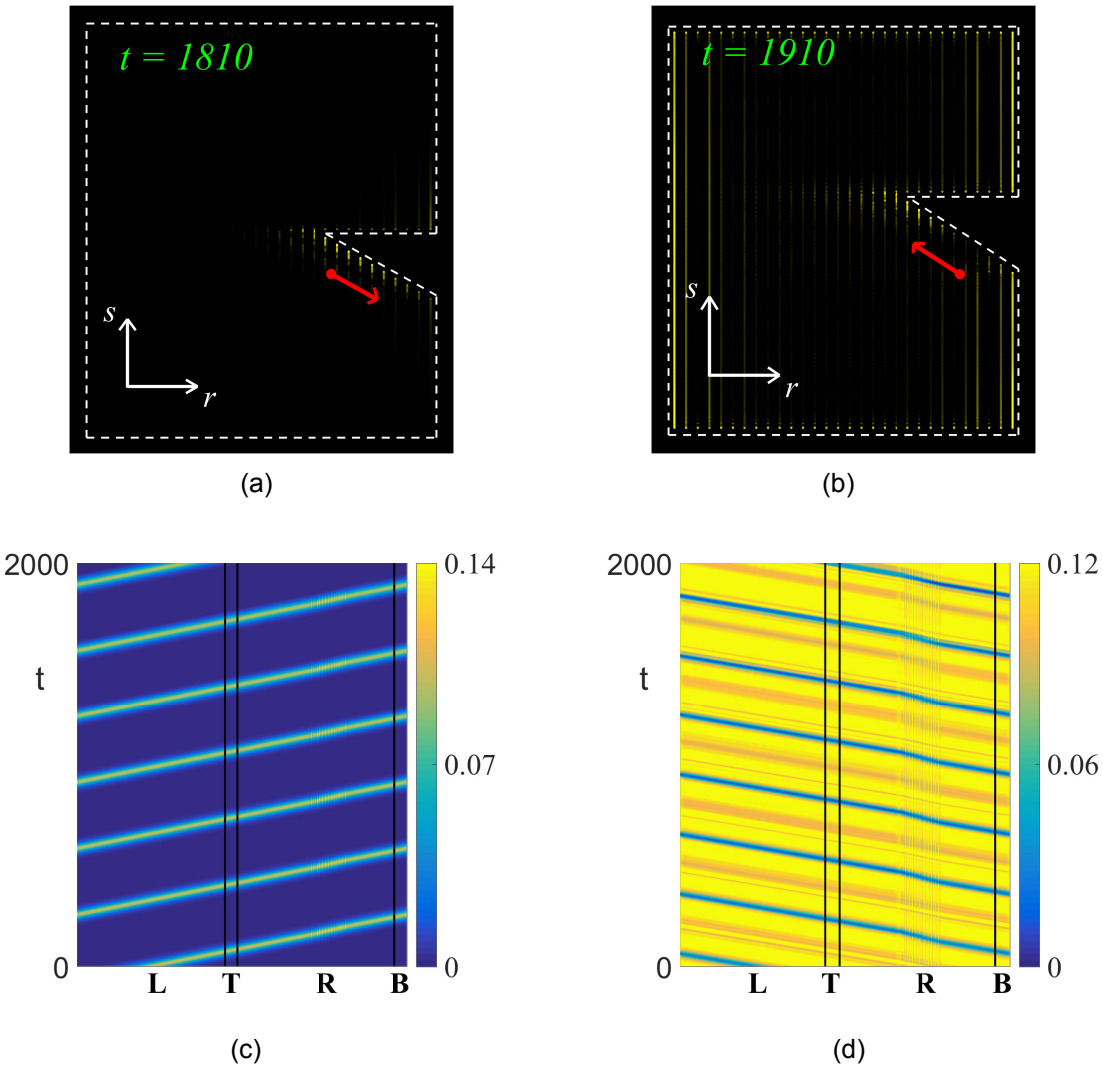

Figure 3.4: Propagation of bright and dark edge solitons on domain with a wedge structure. Panels (a,b) show snapshots of a respective bright (a) and dark (b) edge soliton on a rectangular domain with a sharp turn cut out of the right edge; red arrows indicate the centre of the soliton envelope and its direction of travel. Panels (c,d) show space-time plots along the edges of the irregular domain, where L, T, R and B correspond respectively to left, top, right, and bottom edges of the 2D lattice. The bright and dark solitons are given by the parameters of Fig. 3.2(a,b) respectively.

bouring cells of a particular component, say $x^{(0)}_{r=0,S}$:

$$x^{(0)}_{r=0,S=n+1} = e^{ik_j} x^{(0)}_{r=0,S=n}, \tag{3.17}$$

where n is a cell location sufficiently far enough away from the corners of the lattice. Rearranging Eq. (3.17) allows us to explicitly write the wavenumbers as

$$k_j = \mathcal{R}e(-i \log_e(x^{(0)}_{r=0,S=n+1}/x^{(0)}_{r=0,S=n})).$$

Finally, we need to choose L_S such that the wavenumbers on the left edge, extracted from the 2D eigenfunctions, agree with the wavenumbers on the 1D

periodic domain. The wavenumbers for successive 2D eigenfunctions are approximately equally spaced whilst, on a 1D periodic domain of length L_S, the spacing between the wavenumbers of successive eigenfunctions is $2\pi/L_S$. The equality of the two wavenumber spacings determines L_S, which generally may not be an integer. The value of L_S is approximately proportional to the number of perimeter sites $N_p/3$. The non-integer value of L_S is an inherent imperfection of the method that may be improved upon in future. This is also the explicit reasoning why we see small fluctuations that develop in the non-zero background of the opposing edge of the lattice; see Fig. 3.2(b). The 2D profile can then be constructed as the linear combination of the normalised 2D eigenfunctions:

$$X_{r,S}(t=0) = \sum_j X_j \boldsymbol{X}^j_{r,S} + c.c. \tag{3.18}$$

This construction method was used in the formation of the initial condition for the dark solitons in Fig. 3.2(b–c) and future NLS solutions with a non-zero background field.

Due to topological protection, we are not limited to domains that allow simple propagation, such as a rectangle, so let us consider irregular domains. For instance, by carving a sharp turn into the right edge of the lattice (the edge opposite the initial condition), we may evolve the system using the same bright and dark edge soliton initial conditions as in Fig. 3.2(a–b). Since the carrier wave is topologically protected, we expect that the nonlinear structures will traverse the domain with little to no backscattering regardless of the boundary type. This is seen in Fig. 3.4(a–b) where snapshots of the 2D domain show the edge solitons traverse the irregular domain in their last cycle before $t = 2000$. The space-time plots in Fig. 3.4(c–d) also show the edge solitons passing through the sharp turn of the right edge multiple times with little change in the pulse shape.

The same is found to occur for rough boundaries with finer length scales, such as a Cantor-like function carved into the right edge. Figure 3.5 shows the propagation of bright and dark edge solitons around the domain with finer length scales. Notably we see that both types of soliton traverse the irregular domain with little change in the structure of the initial pulse. This is expected from TPES as, regardless of the edge shape, we expect such robust nonlinear waves to pass through irregular edges without major backscattering of the energy. We do however note the appearance in Fig. 3.5(d) of an extra grey soliton stemming from the initial condition on the right edge of the lattice. This grey soliton appears due to the imperfection in the 2D reconstruction method but we note that this extra soliton is also topologically protected, showing ex-

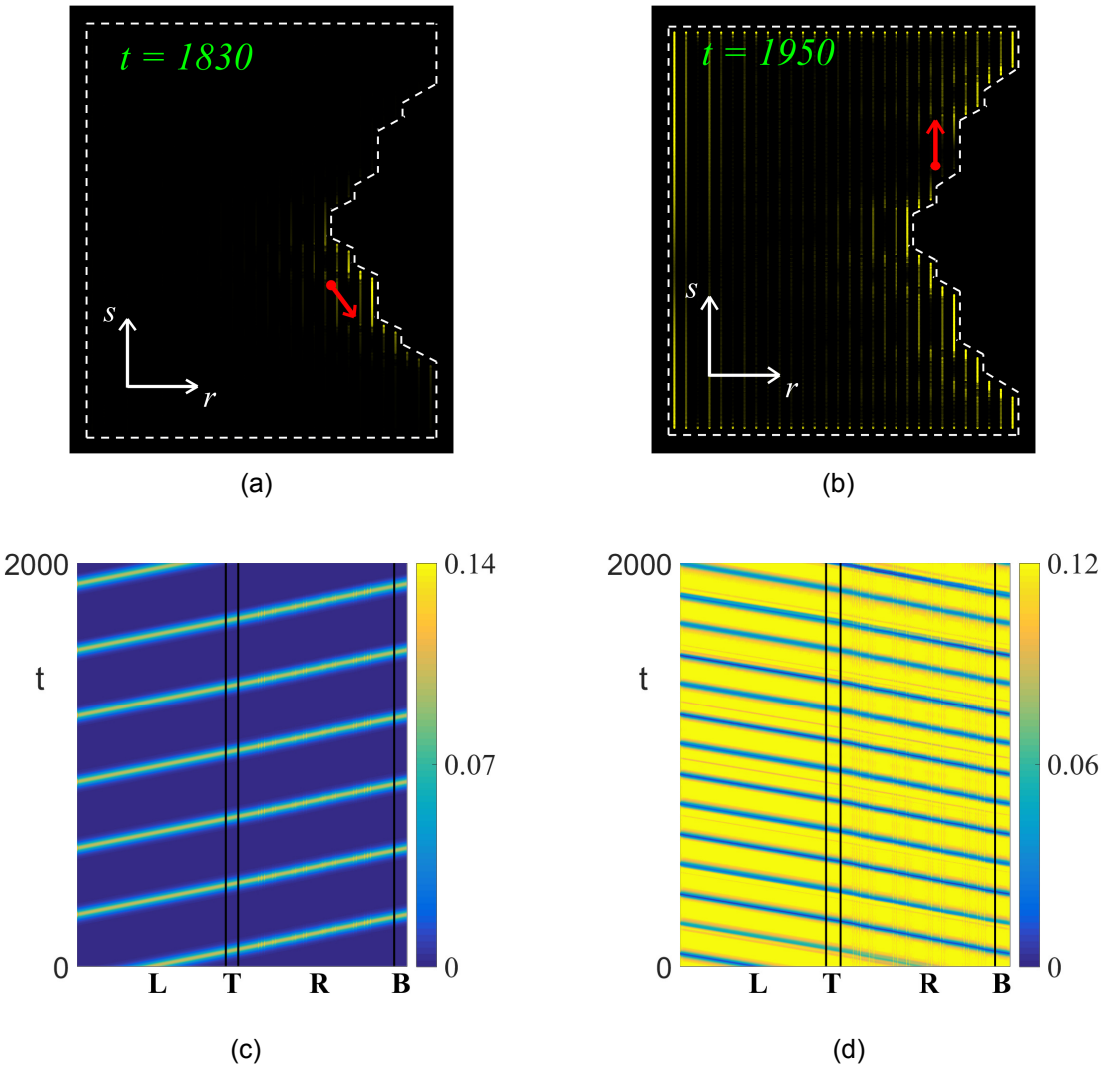

Figure 3.5: Propagation of bright and dark edge solitons on a domain with a Cantor edge. The same setup as in Fig. 3.4, only now with finer length scales introduced to the right edge.

actly the robust nature of TPES when generated. These numerical experiments all but confirm the general principle that weakly nonlinear edge solitons inherit the topological protection of linear edge modes.

To further show the topological protection of edge solitons around different types of corners, we can perform a numerical scattering analysis on bright solitons propagating on the above two types of domains over a long time period, say $t \in [0, 1 \times 10^4]$. Since the two parameters characterising the bright solitons are k_0 and ϵ, we consider varying them away from those in Fig. 3.2(a), i.e. $k_0 = 2.827$ and $\epsilon = 0.1$.

Firstly, we fix $k_0 = 2.827$ and compare the three cases $\epsilon = 0.05$, $\epsilon = 0.1$, and $\epsilon = 0.2$. Figure 3.6(a,b) respectively show the relative energy (the L^2-norm of z on the left edge relative to its initial value) and the maximum amplitude (the L^∞-norm of z on the left edge) over 25 propagation cycles on the rectangular

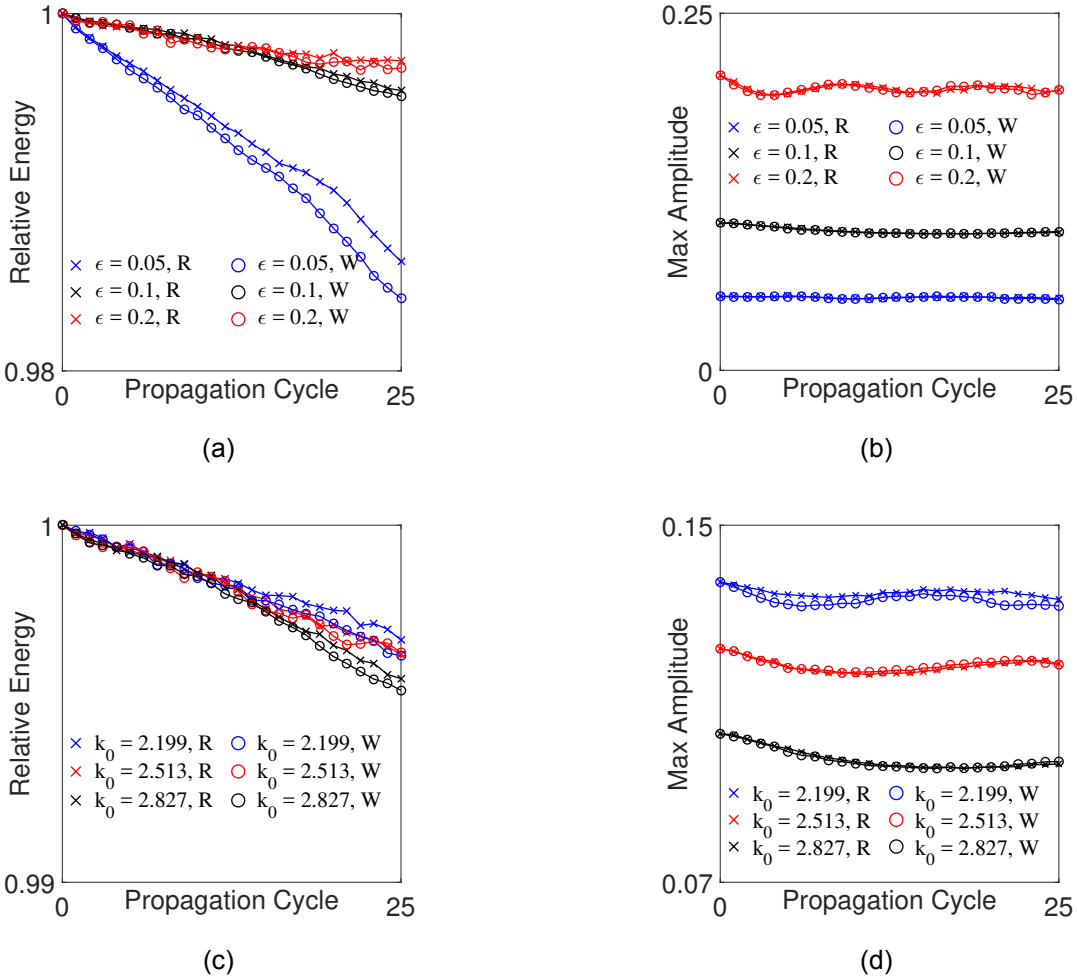

Figure 3.6: Numerical scattering analysis for bright solitons. Panels (a,b) show the effect of fixing $k_0 = 2.827$ and varying $\epsilon = 0.05$ (blue), $\epsilon = 0.1$ (black), $\epsilon = 0.2$ (red) over multiple propagation cycles on two different domains. Domain R is the fully rectangular domain, whilst domain W is the domain with a wedge carved into the right edge. (a) Total energy of the solitons at each cycle relative to the initial value. (b) The maximum amplitude of the solitons at each cycle. Similarly, panels (c,d) show the effect of fixing $\epsilon = 0.1$ and varying $k_0 = 2.199$ (blue), $k_0 = 2.513$ (red), $k_0 = 2.827$ (black) on the two different domains.

domain (R) and the domain with a wedge carved into the right edge (W). The most remarkable feature is that neither the energy nor the amplitude changes significantly, regardless of the domain shape. Thus, although these edge solitons are formally derived on the $O(\epsilon^{-2})$ time scale, they persist much longer in practice. It can also be seen that a larger ϵ causes the amplitude to oscillate more, while a smaller ϵ causes the energy to decay more. To explain these, we recall that ϵ is the spectral width and ϵ^{-1} is the physical width of the soliton. A larger ϵ causes greater interference between the two spectral envelopes centred at k_0 and $2\pi - k_0$ that form the soliton. This is a unique property of mechanical systems as opposed to optical systems, which will be further explored in future work. On the other hand, a smaller ϵ makes the soliton more spatially

extended and thus causes the energy to spread more onto the other edges.

Next, we fix $\epsilon = 0.1$ and vary k_0 with the stipulation that it belongs to the topologically protected and focusing regime. In this band gap, the topologically protected set of wavenumbers is $k \in [1.573, 4.178]$ and the focusing set of wavenumbers is $k \in [0, 3.483]$. As such, in Fig. 3.6(c,d) we compare the three cases $k_0 = 2.199$, $k_0 = 2.513$, and $k_0 = 2.827$ on the two types of domains. The soliton can be seen to propagate very well as long as its carrier wavenumber lies in the interior of the allowable set of wavenumbers. The wavenumbers closer to the bulk appear to be more sensitive to the irregularity of the domain shape, as seen in Fig. 3.6(d).

Remarkably, linear edge modes disperse differently depending on the deformity shape, but nonlinear edge solitons maintain their profiles independent of the deformity shape. The system thus functions as a nonlinear acoustic cloak; see [169] for a similar proposal of a nonlinear optical cloak.

3.2.3 The NLS amplitude

One would expect the nonlinear structures governed by the NLS to propagate significantly better than those that are initialised with no governance. In particular, the edge soliton should maintain its shape better at the theoretically predicted amplitude in comparison to smaller or greater amplitudes. Firstly, let us take the bright edge soliton in Fig. 3.2(a), with wavenumber $k_0 = 2.827$, frequency $\alpha_0 = 12.506$, and theoretically predicted NLS amplitude $\Lambda = 1.376$, as a case study for the varied amplitudes. The nonlinear wave travels clockwise around the domain, completing a full cycle with a period of about 300. The longtime profile of this edge soliton shows little decay as seen in Fig. 3.7(a): at $t \approx 2000$ ($t \approx 4000$), the soliton has completed about 6 (12) cycles of the domain and the soliton amplitude has only decayed to approximately 96% (93%) of its initial theoretically predicted value.

Taking a smaller amplitude than the theoretically predicted results in a compelling amount of decay of the bright soliton profile. This is seen in Fig. 3.7(b) where we have considered an amplitude that is approximately half of the predicted, i.e. $\Lambda = 0.7$. Here, the peak of the soliton has decayed to 61% of its original value long after the initial time (≈ 4000 time units), which is a significant decrease in comparison to the 93% seen before in Fig. 3.7(a). Moreover, the Gaussian profile has dispersed out to the point where the tail ends of the bright soliton are cut off by the corners of the 2D rectangular domain. This is equivalent to decreasing the strength of the nonlinearity, which causes a similar effect to the propagation of pulses in the linear system, like that of Fig. 1.6 . In

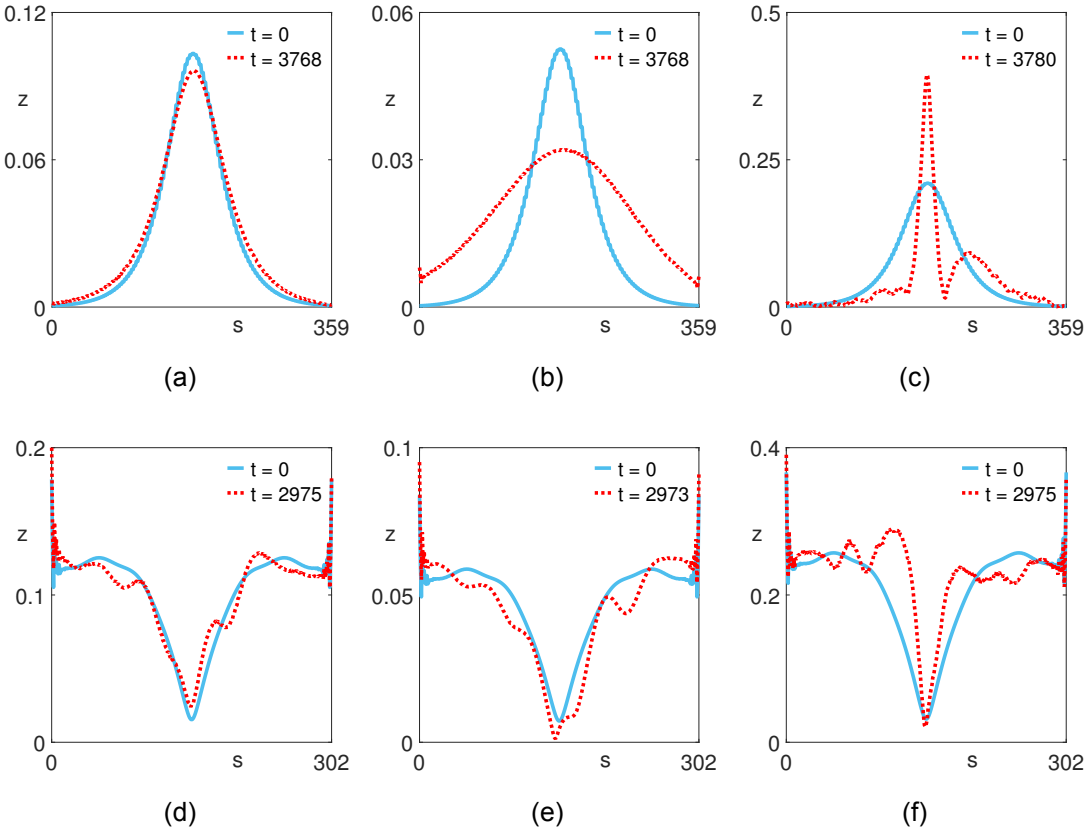

Figure 3.7: Propagation of solitons with differing amplitudes. (a,b,c) Bright solitons on a rectangular lattice of size $N_r \times N_S = 30 \times 120$ with carrier wavenumber and frequency $(k_0, \alpha_0) = (2.827, 12.506)$, and soliton amplitudes (a) $\Lambda = 1.376$; (b) $\Lambda = 0.7$; (c) $\Lambda = 2.8$. (d,e,f) Dark solitons on a rectangular lattice of size $N_r \times N_S = 30 \times 101$ with carrier wavenumber and frequency $(k_0, \alpha_0) = (2.146, 13.616)$, and soliton amplitudes (d) $\Lambda = 1.705i$; (e) $\Lambda = 0.8i$; (f) $\Lambda = 3.5i$. Profiles are taken initially (blue-solid) and after a long time interval (red-dashed). Solitons (a) and (d) are precisely the solitons with theoretically predicted NLS amplitudes seen in Fig. 3.2(a,b) respectively.

contrast to this, Fig. 3.7(c) shows the effect of initialising a larger amplitude, where we have considered approximately double the theoretically predicted, i.e. $\Lambda = 2.8$. We see that this has a severe consequence on the structure of the bright soliton and the crest of the initial Gaussian curve has almost doubled in size; the remainder of the soliton has a somewhat random structure to it. This phenomenon is down to an overfocusing effect, from an overpowering nonlinearity, where the energy to the immediate left and right of the initial peak has been redistributed to the peak itself. We remark that linear edge modes correspond to the limit $\Lambda \to 0$, which exhibits even more dispersion than Fig. 3.7(b).

The dark soliton can be explored in a similar manner by initialising an amplitude of half and double the theoretically predicted, seen in Figures 3.7(e) and 3.7(f) respectively. These two profiles are comparable to the dark soliton profile in Fig. 3.7(d) with the predicted amplitude $\Lambda = 1.705i$, wavenumber $k_0 = 2.146$, and corresponding frequency $\alpha_0 = 13.616$. As shown in Fig. 3.7(d), at $t \approx 4000$

the general structure of the dark soliton has not altered much at all and the fluctuations in the carrier wave are caused by the imperfectly constructed initial condition. Taking an amplitude which is less than that of the theoretically predicted, we see that the trough of the dark soliton widens. Contrary to this, taking an initial amplitude which is greater than that of the theoretically predicted causes a narrowing and distortion in the envelope itself; sporadic fluctuations are also produced in the carrier wave. Therefore, we see once again that the NLS amplitude is the best amplitude for the evolution of the dark soliton.

Overall, it is clear that the amplitude theoretically predicted by the NLS equation (3.10), which governs the envelope of these nonlinear travelling waves, is truly the best amplitude for the formation of solitons in this MTI. If one considers an initial amplitude other than this then the nonlinear and dispersive terms are no longer balanced causing effects such as overfocusing and severe profile distortion as the soliton evolves in time.

3.2.4 Rogue Edge Solitons

Due to the integrable nature of the NLS, one can have many solutions beyond the standard solitons. An example of such a solution to the classical 1D NLS equation are rational solutions, commonly known as rogue waves as they have recently proven to be very promising contenders for modelling waves with abnormally large heights [114, 38, 65, 30]. Let us explore the implementation of these rogue solutions as TPES in the MTI lattice. We first consider the famous Peregrine soliton [151] which is the prototypical example of a rogue wave solution. For visualisation purposes, we require the maximum amplitude to appear at some $t > 0$, say $t_0 = 1200$. Therefore we shift the temporal variable by t_0 and consider the initial condition (3.11) with the envelope function given by

$$C_P(S) = \Lambda \left[1 - \frac{4(1 - 2i\tilde{t}_0)}{1 + 4\epsilon^2 (S - S_0)^2 + 4\tilde{t}_0^2} \right] e^{i\tilde{\theta}}, \tag{3.19}$$

where $\tilde{\theta} = \alpha_0 t_0 - \tilde{t}_0$ and $\tilde{t}_0 = \epsilon^2 \alpha_0'' t_0$. Figure 3.8(a) shows the appearance of the Peregrine edge soliton with the carrier wavenumber and frequency $(k_0, \alpha_0) = (2.334, 12.113)$. A top-down view of the Peregrine soliton forming on the right edge of the 2D lattice is shown in Fig. 3.8(d). The red arrow indicates direction of Peregrine envelope propagation around the perimeter of the domain. We note that the peak does indeed appear at $t \approx t_0$ according to the numerics. As discussed in Sec. 1.1, the uniform background of the NLS in the focusing regime may exhibit modulational instability, which is expected for these particular rogue wave solutions to exist [151]. The breakup of the non-zero back-

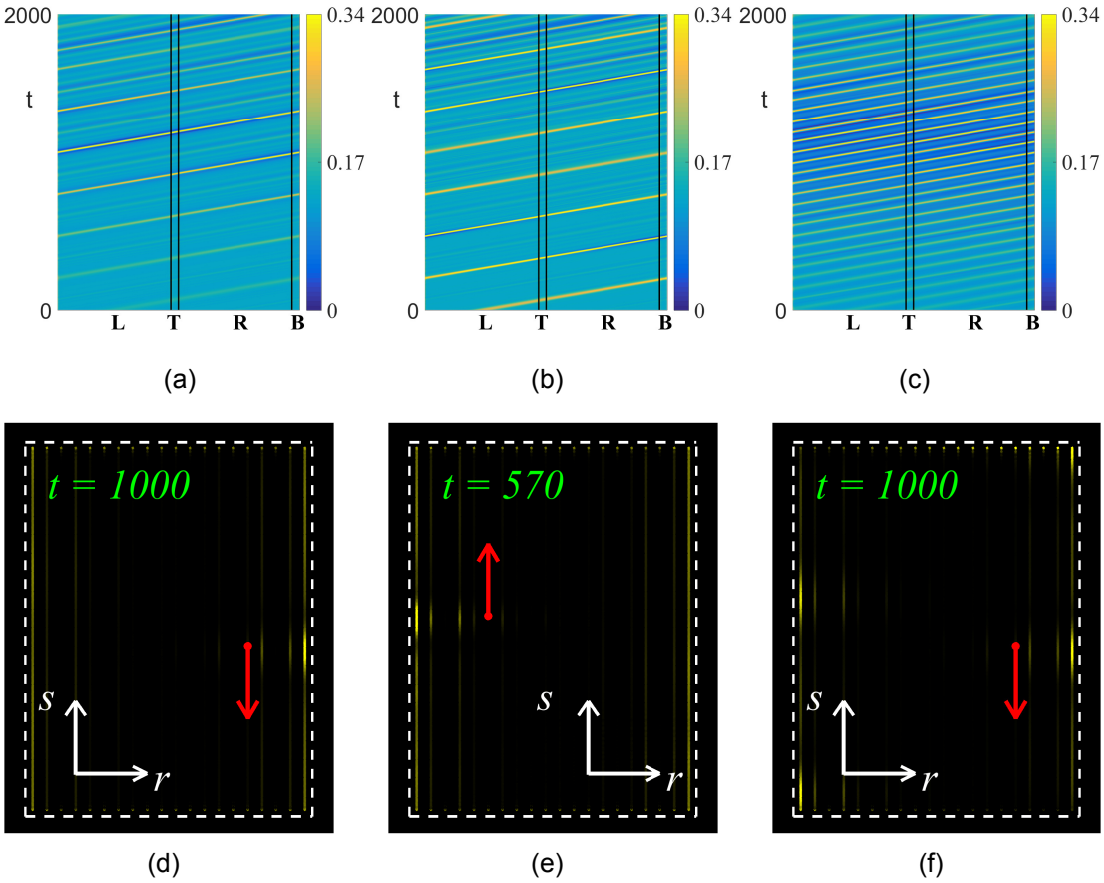

Figure 3.8: Propagation of rogue edge solitons. Panel (a) shows a space-time plot of a Peregrine soliton described by Eq. (3.19) that peaks at $t \approx 1200$. Panel (b) shows a Kuznetsov-Ma edge soliton described by Eq. (3.20), peaking at $t_0 = 500$ with modulation parameter $\phi = 1$, with a breathing period of ≈ 1000. (c) An Akhmediev breather described by Eq. (3.21) that peaks at $t \approx 1200$ with modulation parameter $\phi = 0.6$. The carrier wavenumber and frequency of all three rogue waves are $(k_0, \alpha_0) = (2.334, 12.113)$, and the size of the rectangular domain is $N_r \times N_S = 20 \times 100$. Panels (d,e,f) show snapshots of the 2D mechanical lattice. (d) Peregrine soliton from the evolution of (a). (e) Kuznetsov-Ma soliton from the evolution of (b). (f) Akhmediev breather from the evolution of (c).

ground in Fig. 3.8(a) for longer timeframes is once again a consequence of the profile reconstruction method using the 2D eigenfunctions rather than the modulational instability of the NLS background. Typically, any unstable behaviour of the solution in the NLS is reflected in the MTI system and the presence of any temporal instability can be checked via direct numerical simulations of the NLS equation with an appropriate initial condition. The Peregrine edge solitons are also topologically protected in their propagation on the MTI lattice, which shows again the robust nature of these edge solitons.

Let us also consider the Kuznetsov-Ma (K-M) soliton, which was first derived by Ma [132] as a breathing wavepacket in time embedded in a plane wave solution. To generate a K-M edge soliton, we replace the envelope function in

the initial condition (3.11) by the K-M expression seen in [65], i.e.

$$C_{KM}(S;\phi) = \Lambda \left[\frac{\cos(\Omega \tilde{t_0} + 2i\phi) - \cosh\phi \cosh\bar{S}}{\cos(\Omega \tilde{t_0}) - \cosh\phi \cosh\bar{S}} \right] e^{i\tilde{\theta}}, \tag{3.20}$$

where $\bar{S} = P\epsilon(S - S_0)$, $P = 2\sinh\phi$, $\Omega = \sinh 2\phi$, and ϕ is the real modulation parameter defining the breathing period. Figure 3.8(b) shows the appearance of a K-M edge soliton with $\phi = 1$ and $(k_0, \alpha_0) = (2.334, 12.113)$. Figure 3.8(e) provides a top-down snapshot of the 2D lattice right after the peak of the KM soliton has formed on the left edge of the lattice. The breathing period of ≈ 1000 agrees with the analytical prediction described by the envelope equation (3.20).

Finally, we explore another rogue wave solution known as the Akhmediev breather [15]. In contrast to the K-M soliton which is time-periodic, the Akhmediev breather is a spatially periodic solution that is localised in time. The scalar envelope function is given by the Akhmediev expression in [65], i.e.

$$C_A(S;\phi) = \Lambda \left[\frac{\cosh(\Omega \tilde{t_0} + 2i\phi) - \cos\phi \cos\bar{S}}{\cosh(\Omega \tilde{t_0}) - \cos\phi \cos\bar{S}} \right] e^{i\tilde{\theta}}, \tag{3.21}$$

where $\tilde{\theta} = \alpha_0 t_0 - \tilde{t}_0$, $\tilde{t}_0 = \epsilon^2 \alpha_0'' t_0$, $\bar{S} = P\epsilon(S - S_0)$, $P = 2\sin\phi$, and $\Omega = \sin 2\phi$. As with the Peregrine soliton, we initialise the time-localised structure well before its maximum amplitude, which is designed to appear at time $t_0 = 1200$. Note that one can recover the K-M solution (3.20) from the Akhmediev expression by using the parameter transformation $\phi \to i\phi$. Figure 3.8(c) shows the appearance of an Akhmediev breather and Fig. 3.8(f) provides a snapshot of the 2D domain where the spatially periodic structure of four peaks is shown to propagate around the domain edge. It is clear to see the spatially periodic nature of the breather and all peaks form their maximum amplitude at $t \approx t_0$, decaying away beyond this time which is consistent with the analytic solution in Eq. (3.21). The Peregrine soliton (3.19) is in fact the limiting case ($\phi \to 0$) of both the K-M soliton and the Akhmediev breather.

Note that since the carrier wave belongs to the topologically nontrivial regime, the propagation of these rogue edge solitons in the mechanical lattice is topologically protected, just like the travelling edge solitons presented earlier. There are similarly derived rogue waves in the FPUT lattice and granular crystals through reduction to NLS [43].

3.3 Discussion

To summarise this chapter, we have realised edge solitons theoretically and numerically in a 2D nonlinear mechanical topological insulator exhibiting the QSHE. These edge solitons inherit the topological protection of the linear system which enables robust transport of mechanical excitation on arbitrary domains. In experiments, any waveform such as Eqs. (3.12–3.14) and Eqs. (3.19–3.21) can be generated at a single site and propagated around the finite domain [177]. The required experimental setup is no different from that in the original experiment [177], only on a suitably larger domain to accommodate the narrow spectral envelope. The straightforward nature of the mechanical system, in comparison to its photonic counterpart, allows the formation of table-top experiments that will exhibit TPES on a directly observable scale. Though we truncate the on-site nonlinearity to the cubic order in Eq. (3.7) we note that, since we assume a weakly-nonlinear ansatz in Eq. (3.8), the amplitudes of the pendula response are small and the inclusion of higher-order nonlinear terms of the sine expansion does not have a significant effect on the propagation of the envelopes. Numerical simulations of the nonlinear system with the full, on-site sinusoidal nonlinearity exhibits little to no visible difference between the propagation of the NLS envelopes in this system and the propagation in the cubic system imposed throughout this chapter.

We note that the mechanism of topologically protection in this proposed nonlinear system is equivalent to the linear system presented in Eq. (1.36), where the construction of the Hamiltonian using mechanical components achieves a mechanical QSH analogue, with topologically protected edge modes arising due to the existence of the non-trivial Chern number, shown in Eq. (1.19). The robustness of the propagating edge modes is a direct consequence of the type of component used in forming the mechanical TI system, with the pendula exhibiting an inherent on-site nonlinearity. Recently, the study of robust edge modes in QH/QSH systems has led to attempts to generalise the Berry phase to 2D nonlinear, quantum-mechanical TIs [31]. In this work of Bomantara et al, a nonlinear extension of a spinless, two-band Chern insulator model is considered with a mean-field nonlinearity that may be tuned accordingly through a scalar parameter. As the nonlinear strength is tuned, there may be nonlinearity-induced quantum phase transitions where self-crossing Dirac cones (nonlinear Dirac cones) emerge in the band spectrum that are robust to local perturbations. The key difference between the robust edge modes presented in [31] and those presented here is that the nonlinearity, and therefore robustness of the edge modes, in our system stems directly from the mechanical component

used in constructing the mechanical analogue of the QSH Hamiltonian. In contrast, the work of [31] attempts to formalise a nonlinear extension of the QH model itself in the original quantum mechanical setting. As further research is carried out on the generalisation of the Berry phase in nonlinear quantum mechanical models, this may provide alternative indicators for the existence of robust topologically protected edge modes, which could also be of fundamental interest when constructing photonic or mechanical analogues.

We also briefly note a comprehensive study of stability of the QSH state in the quantum mechanical setting [199]. In this work of Xu and Moore, regions of stability for models exhibiting even or odd numbers of Kramer's pairs are obtained, where phase transitions may be driven between the QSH state and the regular insulator. In our nonlinear system, deforming the lattice remains the simplest way to explore the stability of the edge modes; a deeper analysis of the stability, like in [199], may yield a better understanding of the physical behaviour of these robust edge modes.

In addition to the envelope solutions shown in this chapter, there is also the possibility of more 'exotic' envelopes. Since the NLS equation is integrable, a plethora of solutions are available, beyond those already discussed, via different mathematical descriptions. An example of these are higher-order rogue wave solutions, which have been shown in the scalar NLS equation [73, 80]. The NLS equation also allows the formation of dispersive shock waves [53], which then permits the possibility of soliton tunnelling [173]. Though, in practice, the particular nature of the structures may prove difficult to implement in the nonlinear MTI due to the construction of the non-zero background, higher-order interference, and the derived $O(\epsilon^{-2})$ time scale of evolution.

Future applications of TPES to logic devices may benefit from the possibility for collision-based computing provided by such nonlinear coherent structures [12]. For this to be realised, one must consider the consequence of nonlinearly interacting edge modes and their collision behaviour dynamically. This concept can be summarised by the bimodal behaviour of the nonlinear MTI. To study how two edge modes interact at a certain carrier wavenumber, one can propose a reduction similar to the unimodal case, only now with two envelopes corresponding to different edge modes that will interact nonlinearly. We will explore this reduction in the next chapter and analyse under what constraints this nonlinear interaction is a possibility.

Chapter 4

Bimodal behaviour of a nonlinear MTI

If the scalar NLS equation governs the envelope of single edge modes, then a natural continuation of this would be to question if multiple, nonlinearly interacting edge modes could be governed in a similar fashion. The key comparison one can make is to that of birefringent optical fibres, where one has a particular version of the coupled NLS equation that governs the nonlinear pulse propagation [138]. Recent developments of PTIs also shows that one may expect bimodal behaviour of weakly-nonlinear TIs to be governed by CNLS-type equations [96].

In this chapter we develop the analytical theory behind the bimodal behaviour of the same nonlinear MTI that we considered in the previous chapter. Initially, the spring constants and pendula remain unchanged from the NLS analysis and we develop conditions for when the CNLS appears as the governing equation for the envelope of the edge modes. The analysis imposes strict criteria on the dispersion relation of the linear problem. This motivates a brief discussion on when said criteria are satisfied and leads us to a specific adaptation of the edge sites of the mechanical lattice. Finally, with an appropriate mechanical lattice, we show what type of CNLS equation one may expect, which dictates the kind of envelope solutions that may arise as nonlinear edge modes in the MTI.

4.1 Reduction to the Coupled NLS equation

Consider again the set of nonlinear MTI differential equations in the compact matrix form given by Eq. (3.7). We may impose a multiple-scale ansatz, consisting of two generic edge modes around a chosen carrier wavenumber k_0,

that takes the form

$$\boldsymbol{X} = \epsilon \left\{ A(\tilde{S},\tau)e^{i(Sk_0 - t\alpha_0)}\boldsymbol{X}_r^{(1)} + B(\tilde{S},\tau)e^{i(Sk_0 - t\beta_0)}\boldsymbol{X}_r^{(2)} + c.c \right\}, \tag{4.1}$$

where we have omitted higher-order terms $O(\epsilon^2)$ and $\boldsymbol{X} = \boldsymbol{X}(r, S, \tilde{S}, t, \tau)$ as before. It is assumed that the only modes present in the excitation, at the chosen wavenumber k_0, are the two interacting edge modes corresponding to the carrier frequencies α_0 and β_0. In the bimodal ansatz, we now have two envelopes A and B that are assumed to evolve purely in the slow space and time variables, given by $\tilde{S} \equiv \epsilon(S - V_g t)$ and $\tau \equiv \epsilon^2 t$ respectively. Note that the spatial variable is co-moving with a generic, currently unknown, group velocity V_g. We now have two distinct 1D edge states $\boldsymbol{X}_r^{(1)},\ \boldsymbol{X}_r^{(2)}$ that decay perpendicular to the edge and correspond to the eigenvalues α and β respectively. Both $\alpha(k)$ and $\beta(k)$ solve the linear eigenvalue problem (1.37), i.e.

$$\boldsymbol{\mathcal{L}}(k)\boldsymbol{X}_r^{(1)} = -\alpha(k)^2\boldsymbol{X}_r^{(1)}, \tag{4.2}$$

$$\boldsymbol{\mathcal{L}}(k)\boldsymbol{X}_r^{(2)} = -\beta(k)^2\boldsymbol{X}_r^{(2)}. \tag{4.3}$$

Recall that the chosen values of the carrier frequencies $\alpha_0 \equiv \alpha(k_0)$ and $\beta_0 \equiv \beta(k_0)$ correspond to topologically protected edge states when they are found in a bulk-band gap of the dispersion relation, where the only permissible states are the edge states.

One can then substitute the bimodal ansatz (4.1) into the MTI equation (3.7), expanding asymptotically in ϵ, and utilise the solvability conditions (4.2-4.3). If we expand $\alpha(k)$ and $\beta(k)$ around the carrier wavenumber k_0 in operator forms then $O(\epsilon)$ is trivial. At the next order $O(\epsilon^2)$, we may extract the equations for each of the harmonics to get $V_g = \alpha_0' = \beta_0'$, which means that the group velocity of each edge mode must be equivalent. Leading order terms for the analysis are then given at $O(\epsilon^3)$. If one extracts the equations at each of the harmonics, specifically $\theta_1 = (Sk_0 - t\alpha_0)$ and $\theta_2 = (Sk_0 - t\beta_0)$, then we get two coupled nonlinear equations, for the envelopes A and B, given as

$$\begin{aligned} &2i\alpha_0 A_\tau \boldsymbol{X}_r^{(1)} + \alpha_0\alpha_0'' A_{\tilde{S}\tilde{S}}\boldsymbol{X}_r^{(1)} + 3\sigma A\boldsymbol{X}_r^{(1)}(|A\boldsymbol{X}_r^{(1)}|^2 + 2|B\boldsymbol{X}_r^{(2)}|^2) = 0 \\ &2i\beta_0 B_\tau \boldsymbol{X}_r^{(2)} + \beta_0\beta_0'' B_{\tilde{S}\tilde{S}}\boldsymbol{X}_r^{(2)} + 3\sigma B\boldsymbol{X}_r^{(2)}(|B\boldsymbol{X}_r^{(2)}|^2 + 2|A\boldsymbol{X}_r^{(1)}|^2) = 0. \end{aligned}$$

The remaining harmonics produce residual terms that can be removed by considering higher-order terms in the original ansatz (4.1); the residuals are deemed negligible moving forward. If one then divides each equation through by its corresponding carrier frequency, α_0 and β_0 respectively, and take the inner-product

with the relevant eigenmode, then the final equation is written as

$$iA_\tau + \frac{\alpha_0''}{2} A_{\tilde{S}\tilde{S}} + 3A(\tilde{\sigma}_1|A|^2 + 2\tilde{\sigma}_2|B|^2) = 0, \tag{4.4}$$

$$iB_\tau + \frac{\beta_0''}{2} B_{\tilde{S}\tilde{S}} + 3B(\tilde{\sigma}_3|B|^2 + 2\tilde{\sigma}_4|A|^2) = 0, \tag{4.5}$$

where $\tilde{\sigma}_1 = \frac{\sigma}{2\alpha_0}\|\boldsymbol{X}_r^{(1)}\|_4^4$, $\tilde{\sigma}_2 = \frac{\sigma}{2\alpha_0}\|\boldsymbol{X}_r^{(1)}\boldsymbol{X}_r^{(2)}\|_2^2$, $\tilde{\sigma}_3 = \frac{\sigma}{2\beta_0}\|\boldsymbol{X}_r^{(2)}\|_4^4$, $\tilde{\sigma}_4 = \frac{\sigma}{2\beta_0}\|\boldsymbol{X}_r^{(1)}\boldsymbol{X}_r^{(2)}\|_2^2$, and $\|\boldsymbol{X}_r^{(1)}\|_2^2 = \|\boldsymbol{X}_r^{(2)}\|_2^2 = 1$ normalized.

The coupled, nonlinear equation (4.4)-(4.5) is precisely the coupled NLS equation with generic dispersion and nonlinear coefficients. Therefore, providing that the carrier frequencies are chosen to be at the same carrier wavenumber k_0 and with equal group velocities $\alpha_0' = \beta_0'$, then the CNLS governs the envelope of nonlinearly interacting edge modes in the MTI. The nonlinear terms involving $\tilde{\sigma}_1$ and $\tilde{\sigma}_3$ describe the self-phase modulation (SPM) and are equivalent to the nonlinear terms of the decoupled NLS analysis seen previously. This is expected since the CNLS equation with $A = 0$ or $B = 0$ narrows down to the scalar NLS by definition. The cross-modulation terms (XPM) describe the nonlinear interaction of one envelope with the other and must be non-zero to avoid trivial decoupling.

Due to the criterion of equal group velocity (EGV), one may not have CNLS edge modes in general. In fact, the dispersion relation shown in Fig. 1.4 does not yield an EGV set of topologically protected edge modes, which is expected due to the finite, small number of edge modes per k_0 and the particular nature of the criterion. In order to produce an EGV wavenumber k_0, we must introduce the process of adapting the original mechanical lattice.

4.2 Adapting the nonlinear MTI

The simple structure of the mechanical lattice, in comparison to its photonic counterpart, allows for a multitude of ways to adapt the lattice and produce EGV points from the dispersion relation. The strength of the connective springs, as well as the pendula themselves, may be altered so that one can achieve a specific EGV carrier wavenumber and force the two carrier frequencies to be fully in the bulk-band gap. There are many ways in which one may impose these changes to the lattice, but we will choose to alter the coupling strength of the wall springs connected to the left and right edge sites. We adopt this method due to there being no consequence on the dynamical connections of the neighbouring sites to the edges. These wall springs were not depicted in the previous site layout of Fig. 1.3 but, for clarity of the adaptation, we show

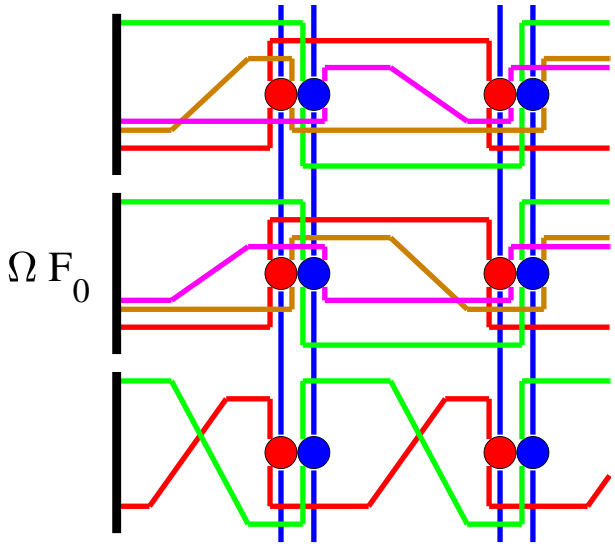

Figure 4.1: Two unit cells of the MTI lattice with the same schematic setup as in Fig. 1.3; wall-edge site connections are visualised. Experimentally, the sites represent the pendula in the same manner as Fig. 1.2, but the explicit connections of sites on the perimeter of the lattice to solid walls is also shown here. The connective strength between any edge pendulum and the wall, given by F_0, is increased/decreased proportionally by a scaling factor of Ω.

these wall springs are in Fig. 4.1. Note that we show specifically how the process affects the leftmost edge; one may picture the same process being applied to the right edge also. The experimental setup of the lattice is the same as before in Fig. 1.2, with r and s the horizontal and vertical axes respectively. If we consider a general connection between an edge pendulum and the wall, with strength F_0, then we alter this strength by a factor Ω. This modification is implemented for every left and right edge connection to the walls. Note that F_0 differs depending on which site connection one considers. Each value of F_0 is given specifically by the connections in Eqs. (1.30-1.35) relating r and $r-1$ for the left edge, and r and $r+1$ for the right edge. For instance, $F_0 = f$ for the $x^{(0)}$ and $y^{(0)}$ wall connections, but $F_0 = -f/2$ for the $x^{(1)}$-$x^{(1)}$ and $y^{(1)}$-$y^{(1)}$ connections.

The key reason behind altering the wall-edge connections is that this involves the least amount of alterations to the dynamical matrix $\mathcal{L}$. One is also free to impose a different Ω for each of the variables $x^{(j)}$, $y^{(j)}$, $j = 0, 1, 2$ that allows more freedom for the system, and would be analysed accordingly using matrix perturbation theory; see [20] for example. For the purpose of our analysis, and henceforth, we will consider a fixed Ω that alters each connection proportionally. Mathematically, this alteration only changes the value of the self-interaction term, A_s, in the original set of equations (1.30-1.35). This term will then become $A_1 = A_s + (\Omega - 1)$ for $x^{(0)}$ and $y^{(0)}$ sites, and $A_2 = A_s + (\Omega - 1)(1 + \sqrt{3})/2$ for $x^{(1)}$, $y^{(1)}$, $x^{(2)}$, and $y^{(2)}$ sites on both the left and right edges. For physical reasons we limit the choice of Ω to the interval

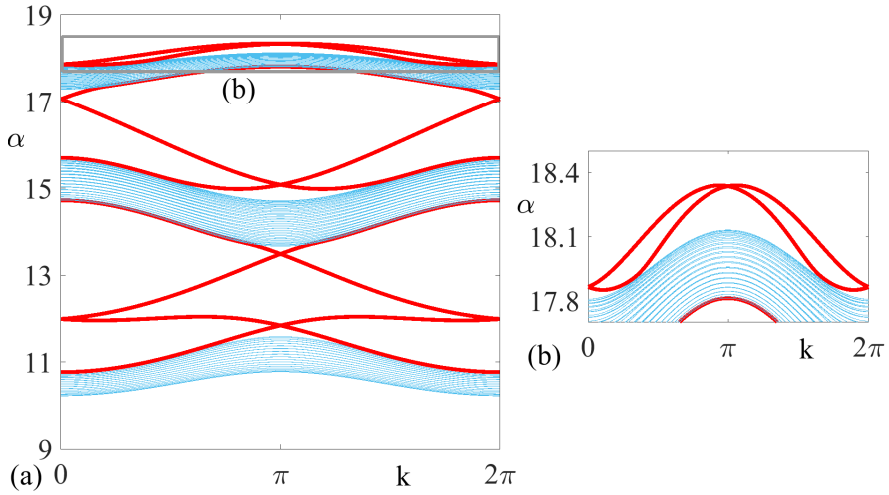

Figure 4.2: The dispersion relation $\alpha(k)$ computed on the left/right edge of a rectangular lattice with $N_r = 60$. The left and right wall-edge connections are scaled proportionally by a factor of $\Omega = 1.5$.

$\Omega \geq 0$. If one were to choose a negative value of Ω then this would be unphysical in the context presented, representing negative spring constants, therefore we neglect this case. We recover the original system when $\Omega = 1$ and $\Omega > 1$ corresponds to increasing the connection strength, and subsequently the self-interaction term. Values in the range $1 > \Omega > 0$ have weaker connections than the original system but are still physically viable using the same mechanical components. Since the only sites that are affected are the sites on the edge of the lattice, the dominant effect will be on the edge modes of the dispersion relation and will give more control over the possibility of EGV wavenumbers being found.

4.3 Points of equal group velocity

Adapting the dynamical connections is a definitive way of finding topologically protected EGV wavenumbers in the dispersion relation. The linear problem is now different since $\mathcal{L}$ has different entries, thus the dispersion relation will be modified depending on the particular strength of Ω. An example of a typical dispersion relation one may expect is seen in Fig. 4.2, where we have considered a value of $\Omega = 1.5$. The general description of the dispersion relation can be explained by the behaviour of Ω. As Ω increases, all of the left/right edge modes are simultaneously 'pushed' upwards and into the upper bulk-band of each gap. Left/right edge modes also appear out of the lower bulk band of the gaps creating a winding-structure within the bulk-band gaps. If one increases Ω further, then we get edge modes that lie above the upper-most bulk-band like those depicted in panel (b) of Fig. 4.2. This is expected since a significant

Table 4.1: Examples of topologically protected EGV points with edge mode parameters.

Ω	k_0	α_0	β_0	α_0''	β_0''	$\alpha_0' = \beta_0'$
2	0.403	12.756	17.298	0.112	-1.457	-0.111
2.2	2.838	12.310	16.099	-0.173	0.225	-0.567
2.4	2.701	12.464	16.447	-0.163	0.162	-0.599
2.7	2.292	12.821	17.088	-0.185	-0.046	-0.605

increase in the wall-edge strength will increase the eigenfrequency of these particular modes beyond the frequencies of the bulk modes, that are obviously less-impacted by our alteration method. These modes are physical, however the edge modes that fall in the bulk-band gaps are of greater interest to us so we will only consider these particular modes. When the connection strength is decreased below the regular value of $\Omega = 1$ we get a reversed effect where the edge modes are shifted downwards into the lower bulk-bands. Generally, the bulk bands are also shifted up/down as Ω increases/decreases, but this is only because of the finiteness of the domain used.

Since we are now familiar with the general qualitative changes to the dispersion relation as Ω varies, we can search numerically for topologically protected EGV points. Examples of points that satisfy our criteria are tabulated in Table. 4.1. In each case the two modes that are classified as EGV are found in different bulk-band gaps, i.e. the α mode is in the lower gap with the β mode in the upper gap. One advantage of these prototypical EGV points is that we may find a new EGV at a particular wavenumber near these values of Ω, providing that the point is still topologically protected and not close to the crossing points at $k_0 = 0, \pi$. This is useful when imposing periodic domains. As a case study let us consider the EGV found at $(\Omega, k_0) = (2.4, 2.701)$ and shift in the parameter Ω to find a new EGV point at $(\Omega, k_0) = (2.168, 10\pi/11)$. This allows us to impose a domain that is periodic with respect to the wavenumber k_0, given by $N_r \times N_S = 25 \times 110$. The nature of the CNLS parameters is generally governed by the signs of the second derivatives $\alpha_0'',\ \beta_0''$, since the values $\alpha_0,\ \beta_0$ and the 4-norm of the eigenvectors are strictly positive. Thus, the envelopes of these nonlinearly interacting edge modes are governed by the CNLS system (4.4-4.5) with system parameters

$$\alpha_0'' = -0.176,\ \tilde{\sigma}_1 = 0.013,\ \tilde{\sigma}_2 = 0.006,$$
$$\beta_0'' = 0.235,\ \tilde{\sigma}_3 = 0.014,\ \tilde{\sigma}_4 = 0.005.$$

We immediately see the non-integrable nature of the system. If the modes are decoupled, i.e. either $A = 0$ or $B = 0$, then one recovers the NLS system for the remaining edge mode within the newly adapted system. In particular, this CNLS

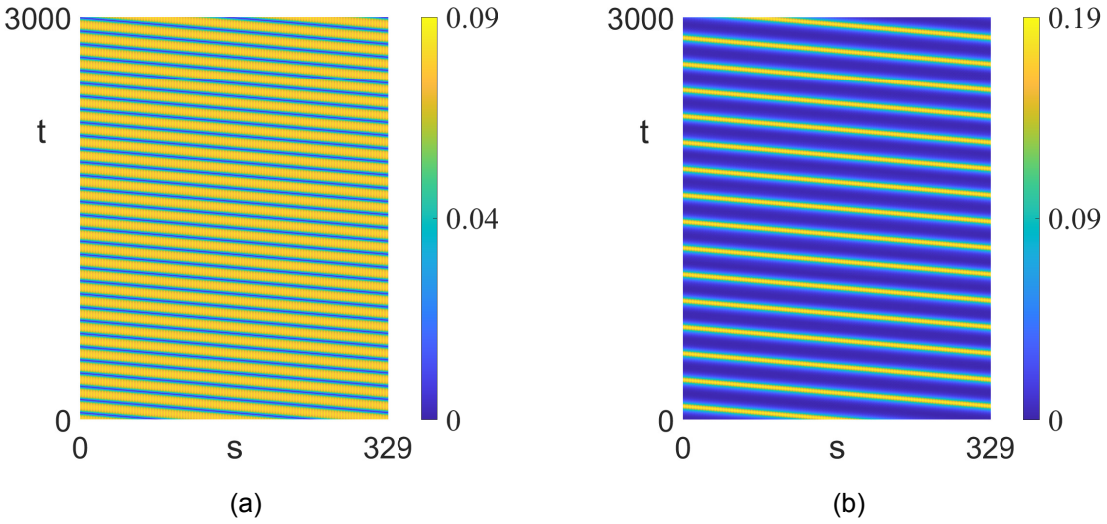

Figure 4.3: Scalar soliton solutions for edge modes of the adapted MTI lattice with parameter $\Omega = 2.168$. Solitons are evolved on the rectangular, periodic domain of $N_r \times N_s(N_S) = 25 \times 330(110)$. (a) Two dark solitons with carrier wavenumber and frequency $(k_0, \alpha_0) = (10\pi/11, 12.286)$. (b) Bright soliton with carrier wavenumber and frequency $(k_0, \alpha_0) = (10\pi/11, 16.046)$.

system decouples into a focusing and a defocusing NLS equation. We already know that the envelope of these edge modes will propagate as expected by Eq. (3.10). This is reinforced by Fig. 4.3 where we see the propagation of a dark soliton and a bright soliton, given by the α and β modes respectively. The carrier wavenumber and frequencies of the solitons are $(k_0, \alpha_0) = (10\pi/11, 12.286)$ and $(k_0, \beta_0) = (10\pi/11, 16.046)$, with the group velocity $\alpha_0' = \beta_0' = -0.56$. Note that, to facilitate the periodic initial condition for the dark soliton, we have implemented two copies of the soliton as seen in Fig. 4.3(a). The alteration of the wall-edge spring constants clearly has little effect on the general behaviour of the MTI as there still exists edge modes that will propagate unidirectionally and with an immunity to backscattering at boundary defects. In terms of the nonlinear edge waves, one has different parameters in the governing NLS/C-NLS equation but there is significant freedom when designing the MTI. We will consider the type of solutions one may have in such a non-integrable CNLS equation in later chapters. For now, we discuss a more robust method for locating EGV points and analyse the type of CNLS coefficients one can expect.

The main problem with adapting the strength of the wall-edge connections is that one is still required to find the EGV points by eye. This process is tedious numerically and the number of points found is sparse. Though one can make a qualitative connection between the parameter Ω and the behaviour of the dispersion relation, it is difficult to predict which edge modes will gain EGV points and if the points are still topologically protected. As well as this, as mentioned

previously, the two modes tend to be in different bulk-band gaps. Therefore, if one wishes to consider two modes in the same bulk-band gap then it is very unlikely that an EGV point can be found by trial and error.

There are more efficient methods for finding EGV points that one can utilise. One property, that is unique to mechanical TIs, is the existence of a negative solution to the linear eigenvalue problem (4.2-4.3), given by the $-\alpha(k)$ and $-\beta(k)$. This is a consequence of the matrix differential equation (3.7) being a second-order system of ODEs opposed to a first-order system, like in the photonic case. We can use this to our advantage by recognising certain symmetries and periodicities of the dispersion relation when looking for EGV points. Consider an edge mode and its negative partner $\pm\alpha(k)$, and perform a Taylor expansion around a fixed carrier wavenumber k_0, giving

$$\alpha(k) = \alpha_0 + \alpha_0'(k-k_0) + \frac{\alpha_0''}{2}(k-k_0)^2 + \cdots,$$
$$-\alpha(k) = -\alpha_0 - \alpha_0'(k-k_0) - \frac{\alpha_0''}{2}(k-k_0)^2 - \cdots.$$

The group velocity of the edge mode and its negative partner are then negatively related as one would expect. This is a significant observation in our search for points of EGV since we are no longer restricted to $\alpha_0' = \beta_0'$, but we may now have $|\alpha_0'| = |\beta_0'|$.

Another useful property, which can be paired with the negative frequency, is the periodicity and symmetry of the dispersion relation with respect to the carrier wavenumber k. The helical edge modes of the MTI guarantees that there will always exist two edge modes that travel with opposite velocities, located at k_0 and $2\pi - k_0$ respectively. The periodicity of the dispersion relation also allows us to write $\alpha(k) = \alpha(k+2\pi)$ and $\alpha(2\pi - k) = \alpha(-k)$. Therefore, it is advantageous for us to write the following Taylor expansions,

$$\alpha(-k) = \alpha_0 - \alpha_0'(k-k_0) + \frac{\alpha_0''}{2}(k-k_0)^2 + \cdots,$$
$$-\alpha(-k) = -\alpha_0 + \alpha_0'(k-k_0) - \frac{\alpha_0''}{2}(k-k_0)^2 + \cdots.$$

Note that α_0' takes the same sign for both $\alpha(k)$ and $-\alpha(-k) = -\alpha(2\pi - k)$. We can then manipulate the edge modes of a particular bulk-band gap to our liking using the symmetry and periodic properties of the dispersion relation. These properties are portrayed geometrically in Fig. 4.4. Two modes that cross in a particular bulk-band gap, with reversed velocities, have certain relationships with each-other and their negative partners. The circular and square points typically have different group velocities to each other and the non-filled points

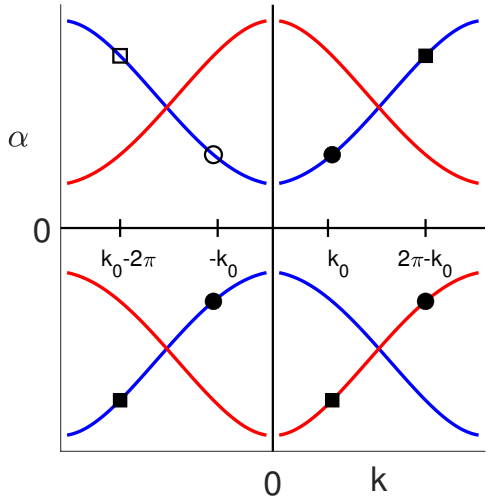

Figure 4.4: Symmetry/Periodicity of the dispersion relation. The two crossing edge modes, α and β, of a particular bulk-band gap are depicted in blue and red respectively. The square and circular points, in general, have different group velocities and the filled points have reversed velocity to the non-filled points.

have reversed velocity to their filled counterparts. If we denote the blue edge mode by α and the red by β, then we notice that the relationship $\alpha'(2\pi - k_0) = -\beta'(k_0)$ will always hold true. This observation means that one can have an EGV point at the carrier wavenumber k_0 if the group velocity of the square and circular points are equal, or equivalently $\alpha'(k_0) = \alpha'(2\pi - k_0)$. In order to satisfy this, one must consider how $\alpha'(k)$ changes as the parameter Ω is varied.

4.3.1 Bifurcation of crossing edge modes

Due to symmetry of the helical edge modes, there will always be crossing points of the two modes located at either $k_c = 0, 2\pi$ or $k_c = \pi$. This is a property shown in both of the previous dispersion relations for $\Omega_0 = 0$ (Fig. 1.4) and $\Omega_0 = 1.5$ (Fig. 4.2). There may also be other crossing points but these are irrelevant to us. As discussed before, these crossing edge modes may yield EGV points either side of the crossing point providing that $\alpha'(k_0) = \alpha'(2\pi - k_0)$. To study the points where this equation is satisfied, let us consider the symmetries of Fig. 4.4 and write the following first-derivative functions as a Taylor expansion around the crossing wavenumber, k_c,

$$\alpha'(k) = \alpha'_c + \alpha''_c(k - k_c) + \frac{\alpha'''_c}{2}(k - k_c)^2 + \cdots,$$
$$-\alpha'(-k) = \alpha'_c - \alpha''_c(k - k_c) + \frac{\alpha'''_c}{2}(k - k_c)^2 + \cdots,$$

where $\alpha_c' = \alpha'(k_c)$ etc. The difference between these two functions, given by

$$\alpha'(k) - \alpha'(-k) = 2\alpha_c''(k-k_c) + \frac{\alpha_c^{(4)}}{3}(k-k_c)^3 + \frac{\alpha_c^{(6)}}{60}(k-k_c)^5 + \cdots, \qquad (4.6)$$

is a polynomial function in $(k-k_c)$. If we alter α_c'' by varying the bifurcation parameter Ω then critical values of the polynomial may be found, consequently yielding criteria for extra EGV points. Since the polynomial is of odd order, we expect pitchfork or saddle-node bifurcations at critical values of the bifurcation parameter when the magnitudes and signs of the coefficients of the polynomial satisfy certain constraints. For instance, one such critical point, assuming higher-order terms are negligible, may be the value of Ω_c that produces $(\alpha_c^{(4)})^2/9 - 4\alpha_c''\alpha_c^{(6)}/30 = 0$. This critical value may determine whether certain roots of Eq. (4.6) become complex and therefore not physically viable. The key point to make here is that altering the bifurcation parameter beyond critical values of Ω_c can yield real roots of the polynomial beyond the trivial crossing mode solution of $k = k_c$. If one has a real solution to Eq. (4.6), say $\tilde{k}$, then we can find a new EGV carrier wavenumber k_{EGV} by writing $k_{EGV} = \tilde{k} + k_c$, with k_c the wavenumber of the crossing mode. We note that the eigenmodes of the crossing points correspond to degenerate eigenvalues so we omit this particular case and focus on those k_{EGV} away from the crossing point.

Since the dominant term for small $(k-k_c)$ in Eq. (4.6) is the linear term, this is a good quantity to consider in relation to the bifurcation. A sensible choice is to find a particular value of $\Omega = \Omega_c$ which yields $\alpha_c'' = 0$ at the crossing point k_c, and vary the parameter around this critical Ω_c. An example of this process can be seen in Fig. 4.5(a), where we have considered two edge modes crossing through $k_c = 0$ in the lower bulk-band gap. The critical value of $\Omega_c \approx 2.682$ yields $\alpha_c'' = 0$ and as one transitions through $(\Omega = \Omega_c)$, we have a pitchfork bifurcation that produces two extra roots in the polynomial Eq. (4.6). Similarly, pitchfork bifurcations are also viable from crossing points in the upper bulk-band gap, as apparent from Fig. 4.5(b) where a critical value of $\Omega_c \approx 3.31$ provides two extra EGV points, either side of $k_c = \pi$, for values of $\Omega < \Omega_c$. More complicated bifurcation diagrams with combinations of pitchfork and saddle-node bifurcations are also expected due to the 5$^{\text{th}}$-degree polynomial. One such crossing point that reflects this is seen in Fig. 4.5(c), where we find EGV points bifurcating from the $k_c = \pi$ crossing point in the lower bulk-band gap. In this particular instance, the first critical value $\Omega_c^{(1)} \approx 3.028$ yields a pitchfork bifurcation from the $k = \pi$ branch, producing two extra roots in the interval $\Omega > \Omega_c^{(1)}$. The four roots corresponding to branches where $k \neq \pi$ then coalesce and vanish at the secondary, double saddle-node bifurcation at $\Omega_c^{(2)} \approx 3.031$, where

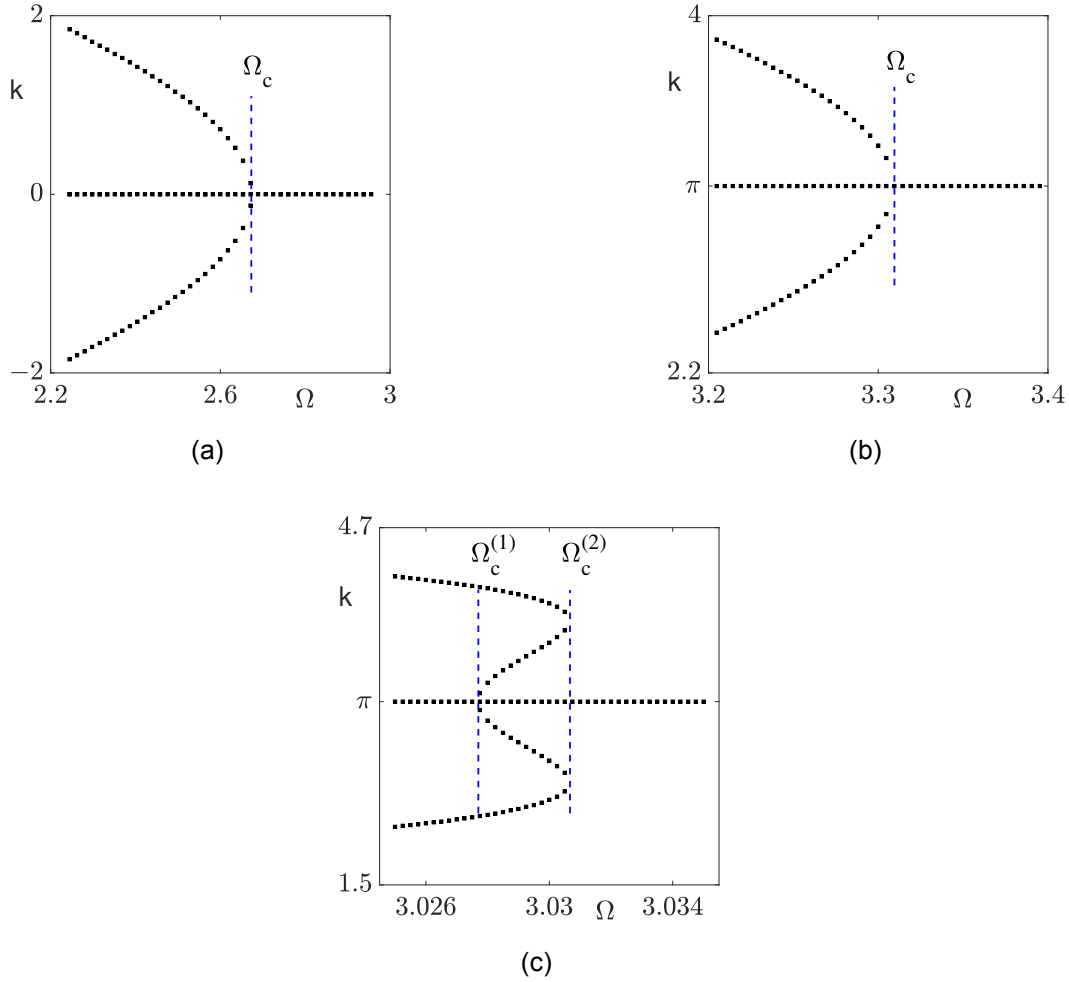

Figure 4.5: Bifurcation diagrams of EGV from crossing modes, with each point representing a point of EGV. (a) Pitchfork bifurcation of the 0 crossing point, in the lower bulk-band gap, at $\Omega_c = 2.682$. (b) Pitchfork bifurcation of the π crossing point, in the upper bulk-band gap, at $\Omega_c = 3.31$. (c) Pitchfork bifurcation of the π crossing point, in the lower bulk-band gap, at $\Omega_c^{(1)} = 3.028$ with a double saddle-node bifurcation at $\Omega_c^{(2)} = 3.031$.

only the trivial $k_c = \pi$ remains to the right of this value. As we have shown, finding EGV points of edge modes stemming from the same bulk-band gap is a relatively simple process when one utilises the symmetries of the mechanical dispersion relation. If we choose an example EGV point within the interval $\Omega_c^{(2)} > \Omega > \Omega_c^{(1)}$ of Fig. 4.5(c), say $(\Omega, k_{EGV}) = (3.03, 14\pi/11)$, then we get the following CNLS parameters,

$$\alpha_0'' = 0.145,\ \tilde{\sigma}_1 = 0.016,\ \tilde{\sigma}_2 = 0.015,$$
$$\beta_0'' = 0.144,\ \tilde{\sigma}_3 = -0.014,\ \tilde{\sigma}_4 = -0.014.$$

We see that the XPM terms are approximately twice the magnitude of the SPM terms, with a difference in sign for the nonlinear terms of each equation. The dispersion coefficients are similar in magnitude and take the same

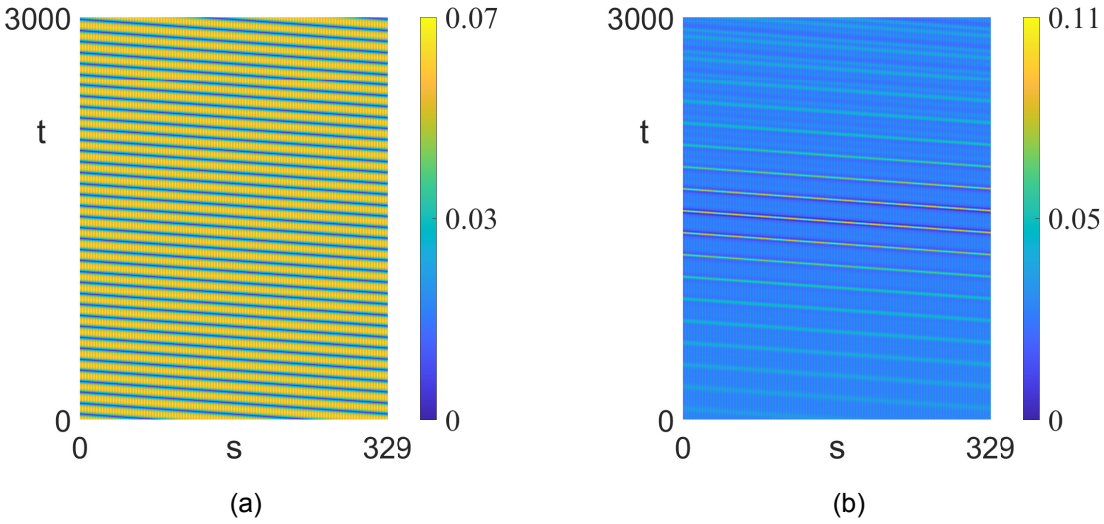

Figure 4.6: Scalar soliton solutions for crossing edge modes of the adapted MTI lattice with parameter $\Omega = 3.03$. Solitons are evolved on the rectangular, periodic domain of $N_r \times N_s(N_S) = 25 \times 330(110)$. (a) Two dark solitons with carrier wavenumber and frequency $(k_0, \alpha_0) = (14\pi/11, 11.708)$. (b) Peregrine soliton with carrier wavenumber and frequency $(k_0, \alpha_0) = (14\pi/11, -12.933)$.

sign in this particular case. Note also that the symmetric, bifurcating value of $k_{EGV} = 8\pi/11$ yields the same CNLS parameters but with an opposite sign of the velocity α_0', therefore one only needs to consider half of the set of EGV points. Similarly to before, when the edge modes are decoupled, a scalar NLS governs the mode which is focusing ($B = 0$) or defocusing ($A = 0$) respectively. Due to this, we may find scalar edge and rogue edge solitons like those seen in Fig. 4.6, where we have showcased focusing and defocusing solutions to the decoupled NLS modes. Two dark solitons are shown in Fig. 4.6(a) propagating on a periodic domain with a carrier wavenumber and frequency $(k_0, \alpha_0) = (14\pi/11, 11.708)$, and a Peregrine soliton is shown in Fig. 4.6(b) to appear at a theoretically chosen $t_0 = 1500s$, with a carrier wavenumber and frequency $(k_0, \alpha_0) = (14\pi/11, -12.933)$. The type of solutions one may expect to the full CNLS equation will be explored in later chapters. We note that the dispersion parameters α_0'' and β_0'', after appropriate scaling of A and B, are typically of different signs near the bifurcating crossing points. This is expected since the Taylor expansion of the second derivative $\alpha(k)''$ is dominated by the linear α_0''' term when $0 < |\alpha_0''| << 1$. This consequently means that $\alpha''(k_0) \sim -\alpha''(-k_0) = -\beta''(k_0)$. There will be a narrow band of values very close to the crossing point which will yield the same sign of the dispersion term but they are generally very small in this range, and therefore unfavourable.

4.4 Discussion

We have considered methodology to efficiently locate points of EGV in the dispersion relation of the MTI, which is a necessary condition for edge modes to be governed by the coupled NLS equation. It has subsequently been shown that the coefficients of the dispersion and nonlinear terms yield a non-integrable CNLS with different signs and magnitudes of the terms throughout. Solutions to such an equation are generally unknown and a slight variation in the chosen carrier wavenumber and frequency, or parameter Ω, can yield a relatively large difference in the coefficients. Therefore, motivated by the reduction of the MTI equations to the two-component CNLS equation with cubic nonlinearity, one may question the type of solutions that we can obtain in the non-integrable regime of Eqs. (4.4-4.5). Recall that, as first introduced in Eqs. (1.4–1.5), the CNLS equation with arbitrary, real-valued coefficients takes the following form:

$$iA_t + d_1 A_{xx} + A(g_1|A|^2 + g_2|B|^2) = 0, \tag{4.7}$$

$$iB_t + d_2 B_{xx} + B(g_3|B|^2 + g_4|A|^2) = 0, \tag{4.8}$$

where we have defined the complex envelopes $A,\ B$ that are dependent on both space, x, and time, t, variables.

In the forthcoming chapters we will consider analytical and numerical techniques to explore and produce nonlinear structures as solutions of Eqs. (4.7-4.8) that can then be utilised and translated back into the original MTI system. For now, we put the MTI lattice in the back of our minds and focus purely on the CNLS equation. Once we have explored the available solutions of the non-integrable CNLS, we will then return to and focus on the MTI lattice in Chapter 8. The solutions that we search for are those that are coherent structures, where the governing envelope has no time-dependence in a co-moving frame of reference such as front solutions and vector solitons.

Chapter 5

Travelling front solutions in the non-integrable coupled NLS equation

In this chapter we will pay particular attention to front solutions of Eqs. (4.7-4.8) and derive necessary conditions for their existence. Front solutions are a non-linear connection of two plane-waves, that propagates with a fixed shape and velocity, and are commonly seen in dissipative systems [134, 197]. They have various applications to pattern forming systems, such as biochemical [204] and degradation [69] processes. They are also commonly found in one-component 1D conservative systems such as the sine-Gordon equation [95] and scalar 1D and 2D NLS-type equations [120, 184].

Since the front is a heteroclinic connection of two plane-waves, we will begin by reducing the full CNLS system to a spatially dynamical system (coupled ODEs) and consider uniform states of this system. These uniform states (equilibria) translate to plane-waves of the CNLS and we will explore the conditions that allow spatial hyperbolicity and temporal stability of such plane-waves. We then consider the existence of a real-valued conserved quantity in the ODE system so that a heteroclinic connection of two uniform states may exist. The existence of fronts is well studied in the optics setting and in the context of Bose-Einsten condensates (BECs), where fronts are often referred to as domain walls. In these settings, fronts are often sought after under certain parameter simplifications such as the symmetrical CNLS [82, 101], where one imposes $d_1 = d_2$, $g_1 = g_3$, and $g_2 = g_4$, and often with trapping potential and/or linear interconversion terms added [63, 83, 58, 172]. More recently, effort has been made to generalise the front solutions further by requiring less restrictions on the system parameters; see [16] where fronts were found in the CNLS

system with $d_1 = d_2 = -1$, $g_2 = g_4$, and $g_{1-4} > 0$, with the added condition of $g_2 > \sqrt{g_1 g_3}$. We will show in this chapter the minimum number of criteria for the existence of travelling fronts with respect to our ODE reduction of Eqs. (4.7-4.8).

Finally, we briefly study the interaction of the fronts with wave turbulence and scalar grey solitons. Conservation equations are shown to partially explain the particle-like behaviour of the grey soliton in certain parameter regimes of the CNLS. There is very little literature on excitation-front transport in non-integrable CNLS systems, but we note that some progress has been made on the subject in regards to linear excitations in the symmetrically-coupled case [193].

5.1 ODE reduction

In order to search for structures of the coherent type, one may apply a transformation of variables and reduce Eq. (4.7-4.8) to a system of ODEs, much like the standard procedure in the commonly studied complex Ginzburg-Landau Equation [18]. We will utilise the gauge invariance of the system and apply a travelling wave ansatz of variables in the following manner,

$$A = \phi(\zeta, t) e^{i(k_A x - \omega_A t)}, \tag{5.1}$$

$$B = \psi(\zeta, t) e^{i(k_B x - \omega_B t)}, \tag{5.2}$$

where ϕ, ψ are complex envelopes dependent on the co-moving variable $\zeta = x - C_g t$, with $C_g \in \mathbb{R}$ the group velocity of the envelope. k_A, k_B and ω_A, ω_B are the respective, real-valued plane-wave wavenumbers and frequencies. Nonlinear solutions are often categorised into coherent structures that are time-independent in the co-moving frame or those with an envelope time-dependence like breathers. We focus here on the stationary solutions where $\phi,\ \psi$ are functions of ζ only, i.e. $\phi(\zeta, t) = \phi(\zeta),\ \psi(\zeta, t) = \psi(\zeta)$. Applying the above transformation of variables to the CNLS system (4.7-4.8) yields the following travelling wave ODE,

$$d_1 \phi'' + i(2 d_1 k_A - C_g)\phi' + (\omega_A - d_1 k_A^2)\phi + g_1 |\phi|^2 \phi + g_2 |\psi|^2 \phi = 0, \tag{5.3}$$

$$d_2 \psi'' + i(2 d_2 k_B - C_g)\psi' + (\omega_B - d_2 k_B^2)\psi + g_3 |\psi|^2 \psi + g_4 |\phi|^2 \psi = 0, \tag{5.4}$$

where the superscript $'$ now refers to the derivative w.r.t the variable ζ. Note that the ODE is reversible under the action $R(\phi, \psi, \phi', \psi') = (\phi^*, \psi^*, -\phi^{*'}, -\psi^{*'})$ and $\zeta \longrightarrow -\zeta$, where $*$ denotes complex conjugation. One can reduce the ODE to a system with purely real coefficients by considering a further transformation

of variables,

$$\phi = \Phi(\zeta)e^{i(\frac{C_g}{2d_1}-k_A)\zeta}, \tag{5.5}$$

$$\psi = \Psi(\zeta)e^{i(\frac{C_g}{2d_2}-k_B)\zeta}, \tag{5.6}$$

where we now have an ODE in the new dependent variables Φ, Ψ given by

$$d_1\Phi'' + ((2k_Ad_1 - C_g)^2/4d_1 + \omega_A - d_1k_A^2)\Phi + g_1|\Phi|^2\Phi + g_2|\Psi|^2\Phi = 0, \tag{5.7}$$

$$d_2\Psi'' + ((2k_Bd_2 - C_g)^2/4d_2 + \omega_B - d_2k_B^2)\Psi + g_3|\Psi|^2\Psi + g_4|\Phi|^2\Psi = 0. \tag{5.8}$$

We will show in Chapter 6 that this system of equations is important when considering vector soliton solutions to the coupled NLS system but we will simplify the current analysis by allowing $C_g = 2d_1k_A = 2d_2k_B$. This assumption then removes the need for the transformation (5.5-5.6) and one has a final travelling wave ODE to analyse,

$$d_1\phi'' + (\omega_A - d_1k_A^2)\phi + g_1|\phi|^2\phi + g_2|\psi|^2\phi = 0, \tag{5.9}$$

$$d_2\psi'' + (\omega_B - d_2k_B^2)\psi + g_3|\psi|^2\psi + g_4|\phi|^2\psi = 0, \tag{5.10}$$

with solutions dependent on the 3D parameter space $(C_g, \omega_A, \omega_B)$ and the six coupled CNLS system parameters $d_{1,2},\ g_{1-4}$.

5.1.1 Plane-wave solutions

The simplest CNLS solution that one may consider is the plane-wave which is given as a uniform state in the system (5.9-5.10). The number of equilibria of the ODE is dependent on the number of components in the system; since there are two components we have $2^2 = 4$ equilibria that we may denote by ZZ, ZN, NZ, and NN, where $Z(N)$ correspond to zero (non-zero) components. The equilibria are then given as

$$ZZ: \quad |\phi_0|^2 = 0, \quad |\psi_0|^2 = 0, \tag{5.11}$$

$$ZN: \quad |\phi_0|^2 = 0, \quad |\psi_0|^2 = \frac{(C_g^2 - 4d_2\omega_B)}{4d_2g_3}, \tag{5.12}$$

$$NZ: \quad |\phi_0|^2 = \frac{(C_g^2 - 4d_1\omega_A)}{4d_1g_1}, \quad |\psi_0|^2 = 0, \tag{5.13}$$

$$NN: \quad |\phi_0|^2 = \frac{(4\omega_Ad_1 - C_g^2)d_2g_3 - (4\omega_Bd_2 - C_g^2)d_1g_2}{4d_1d_2(g_2g_4 - g_1g_3)},$$

$$|\psi_0|^2 = \frac{(4\omega_Bd_2 - C_g^2)d_1g_1 - (4\omega_Ad_1 - C_g^2)d_2g_4}{4d_1d_2(g_2g_4 - g_1g_3)}. \tag{5.14}$$

Note that we have a circle of equivalent equilibria, for each non-zero component, in the complex plane that satisfy Eqs. (5.11-5.14) and these expressions can not be negative for the considered equilibria to exist, which directly imposes conditions on the parameters. For example, the defocusing Manakov system, $d_{1,2} = -1$ and $g_{1-4} = 2$, gives a negative denominator for Eqs. (5.12-5.13) and thus imposes the conditions $C_g^2 < 4d_2\omega_B$ and $C_g^2 < 4d_1\omega_A$ respectively. Both of the conditions are reversed for the focusing Manakov system, $d_{1,2} = 1$ and $g_{1-4} = 2$, with only one of the conditions reversed for each of the mixed Manakov systems, $d_{1,2} = 1$, $g_{1,4} = \pm 2$, and $g_{2,3} = \mp 2$. We note that this formulation of the NN plane-wave can not exist within any regime of the Manakov system since the term $g_2g_4 - g_1g_3 = 0$. It is also clear to see that the trivial solution ZZ exists regardless of parameters.

Since we will consider the most general case of system parameters we have general conditions that must be satisfied for the equilibria to exist. The ZN plane wave does not rely on the secondary equation of the CNLS and as such the criterion for a physical equilibrium depends only on the relative signs of the numerator and the denominator, imposing $\text{sgn}(C_g^2 - 4d_2\omega_B) = \text{sgn}(d_2g_3)$. By symmetry, the existence of NZ depends only on the criterion $\text{sgn}(C_g^2 - 4d_1\omega_A) = \text{sgn}(d_1g_1)$. The NN plane-wave is slightly more complicated but there exist certain criteria to ensure physicality by considering two separate cases. One may recognise from Eq. (5.14) that the denominator of the two components are equivalent and thus enforces both of the numerators to have the same sign. Therefore, assuming that $d_1d_2(g_2g_4 - g_1g_3) > 0$, the criteria for physical NN are then written as

$$(4\omega_A d_1 - C_g^2)d_2g_3 - (4\omega_B d_2 - C_g^2)d_1g_2 > 0,$$
$$(4\omega_B d_2 - C_g^2)d_1g_1 - (4\omega_A d_1 - C_g^2)d_2g_4 > 0,$$

with reversing the sign of the assumption consequently causing a reverse of sign in both of the criteria. Moving forward, travelling wave parameters must be chosen to preserve the physicality of these equilibria and we will always suggest parameters that satisfy the relevant criteria unless stated otherwise.

5.1.2 Spatial eigenvalues

As well as conditions to preserve physicality of the uniform solution, for nonlinear solutions to arise one also needs to ensure spatial hyperbolicity such that the dynamics in the vicinity of the equilibria behave similarly in the nonlinear system to the linearised system. This is equivalent to requiring spatial

eigenvalues to have non-zero real part which then implies structural stability in the neighbourhood of the given equilibrium point. To find the spatial eigenvalues of Eq. (5.9-5.10) we first separate the real and imaginary parts by defining $\phi(\zeta) = p(\zeta) + iq(\zeta)$ and $\psi(\zeta) = r(\zeta) + is(\zeta)$. One then writes the system (5.9-5.10) as a set of first-order ODEs by defining the real variables $z_1 = p$, $z_2 = q$, $z_3 = r$, $z_4 = s$, $z_5 = p'$, $z_6 = q'$, $z_7 = r'$, and $z_8 = s'$ which yields the following 8D coupled nonlinear ODE

$$
\begin{aligned}
z_1' &= z_5, \\
z_2' &= z_6, \\
z_3' &= z_7, \\
z_4' &= z_8, \\
z_5' &= -\frac{(4d_1\omega_A - C_g^2)}{4d_1^2} z_1 - \frac{g_1}{d_1}(z_1^2 + z_2^2)z_1 - \frac{g_2}{d_1}(z_3^2 + z_4^2)z_1, \\
z_6' &= -\frac{(4d_1\omega_A - C_g^2)}{4d_1^2} z_2 - \frac{g_1}{d_1}(z_1^2 + z_2^2)z_2 - \frac{g_2}{d_1}(z_3^2 + z_4^2)z_2, \\
z_7' &= -\frac{(4d_2\omega_B - C_g^2)}{4d_2^2} z_3 - \frac{g_3}{d_2}(z_3^2 + z_4^2)z_3 - \frac{g_4}{d_2}(z_1^2 + z_2^2)z_3, \\
z_8' &= -\frac{(4d_2\omega_B - C_g^2)}{4d_2^2} z_4 - \frac{g_3}{d_2}(z_3^2 + z_4^2)z_4 - \frac{g_4}{d_2}(z_1^2 + z_2^2)z_4,
\end{aligned}
$$

with uniform solution $[z_1, z_2, z_3, z_4, z_5, z_6, z_7, z_8]^T = [p_0, q_0, r_0, s_0, 0, 0, 0, 0]^T$, and superscript T denoting transposition. The uniform solution is a point on the circle of equilibria in one of the distinct cases and satisfies $p_0^2 + q_0^2 = |\phi_0|^2$ and $r_0^2 + s_0^2 = |\psi_0|^2$ respectively.

If one then considers a small perturbation to the uniform states and linearise around each equilibria, looking for perturbation solutions proportional to $\epsilon e^{\lambda\zeta}$ with $\epsilon \ll 1$, then the relevant Jacobian matrix yields the spatial eigenvalues, λ. The Jacobian matrix is written as

$$
\mathbf{J} = \begin{pmatrix} \mathbf{0}_{4,4} & \mathbf{I}_4 \\ \mathbf{A} & \mathbf{0}_{4,4} \end{pmatrix} \tag{5.15}
$$

where $\mathbf{0}_{4,4}$ and $\mathbf{I}_4$ are the zero and identity matrices respectively in $\mathbb{R}^{4\times4}$ space. The matrix $\mathbf{A} \in \mathbb{R}^{4\times4}$ can be simplified due to the gauge invariance of the system as one may suggest that the equillibria (5.11-5.14) be defined on the non-negative, real axis such that $\phi_0,\ \psi_0 \geq 0 \in \mathbb{R}$ without loss of generality. This is due to the circle of equilibria yielding similar Jacobians, where the eigenvalues are equivalent but the eigenvectors differ. We can then write the simplified

matrix **A** as

$$\mathbf{A} = \begin{pmatrix} D_1 & 0 & -\frac{2g_2}{d_1}\phi_0\psi_0 & 0 \\ 0 & D_2 & 0 & 0 \\ -\frac{2g_4}{d_2}\phi_0\psi_0 & 0 & D_3 & 0 \\ 0 & 0 & 0 & D_4 \end{pmatrix} \tag{5.16}$$

with,

$$\begin{aligned} D_1 &= \frac{1}{d_1}\left[\left(\frac{C_g^2}{4d_1} - \omega_A\right) - 3g_1\phi_0^2 - g_2\psi_0^2\right], \\ D_2 &= \frac{1}{d_1}\left[\left(\frac{C_g^2}{4d_1} - \omega_A\right) - g_1\phi_0^2 - g_2\psi_0^2\right], \\ D_3 &= \frac{1}{d_2}\left[\left(\frac{C_g^2}{4d_2} - \omega_B\right) - g_4\phi_0^2 - 3g_3\psi_0^2\right], \\ D_4 &= \frac{1}{d_2}\left[\left(\frac{C_g^2}{4d_2} - \omega_B\right) - g_4\phi_0^2 - g_3\psi_0^2\right]. \end{aligned}$$

Generally, the spatial eigenvalues are given by an 8th degree characteristic polynomial governed by $\det(\mathbf{J} - \lambda\mathbf{I}_8) = 0$, however we recognise that the Jacobian takes the form of a simple anti-diagonal block/partitioned matrix. The Schur complement states that for a generic matrix **M**, written in block form as

$$\mathbf{M} = \begin{pmatrix} \mathbf{P} & \mathbf{Q} \\ \mathbf{R} & \mathbf{S} \end{pmatrix}$$

with $\mathbf{P},\ \mathbf{Q},\ \mathbf{R},\ \mathbf{S} \in \mathbb{R}^{n\times n}$ matrices, the determinant of the full matrix can be written as $\det(\mathbf{M}) = \det(\mathbf{S})\det(\mathbf{P} - \mathbf{Q}\mathbf{S}^{-1}\mathbf{R})$, providing that **S** is invertible [211]. Using this property, one may write the spatial eigenvalues as the solution to

$$\begin{aligned} \det(\mathbf{J} - \lambda\mathbf{I}_8) &= 0, \\ \det(-\lambda\mathbf{I}_4)\det(\mathbf{A}(\lambda\mathbf{I}_4)^{-1} - \lambda\mathbf{I}_4) &= 0, \\ \left[\frac{4g_2g_4}{d_1d_2}\phi_0^2\psi_0^2 - D_1D_3 + (D_1 + D_3)\lambda^2 - \lambda^4\right]\left[D_4 - \lambda^2\right]\left[\lambda^2 - D_2\right] &= 0. \end{aligned} \tag{5.17}$$

We can now substitute each of the equilibria (5.11-5.14) into the above expression to show the conditions for spatial hyperbolicity of each case for general travelling wave and CNLS system parameters. Since we assume that the equilibria are physical, we may write these expressions in terms of $\phi_0,\ \psi_0$ and we then analyse the condition on the parameters that gives $\mathcal{R}\mathrm{e}(\lambda_{1-8}) \neq 0$.

Case (i) : ZZ

As one would expect, with ZZ substituted into the Jacobian matrix there is a significant simplification to the spatial eigenvalues. Namely, the quantities D_{1-4} are now written as $D_1 = D_2 = \left(C_g^2/4d_1 - \omega_A\right)/d_1$ and $D_3 = D_4 = \left(C_g^2/4d_2 - \omega_B\right)d_2$, with the eigenvalues then given as

$$\lambda_{1,2} = \sqrt{\frac{1}{d_1}\left(\frac{C_g^2}{4d_1} - \omega_A\right)}, \quad \lambda_{3,4} = -\sqrt{\frac{1}{d_1}\left(\frac{C_g^2}{4d_1} - \omega_A\right)},$$
$$\lambda_{5,6} = \sqrt{\frac{1}{d_2}\left(\frac{C_g^2}{4d_2} - \omega_B\right)}, \quad \lambda_{7,8} = -\sqrt{\frac{1}{d_2}\left(\frac{C_g^2}{4d_2} - \omega_B\right)}. \tag{5.18}$$

It can be seen from the above expressions that λ_{1-8} may only be purely real or imaginary with double degeneracy. These repeated eigenvalues are expected due to the structure of **J** for ZZ and the decomposition into the real and imaginary parts of the equations. For ZZ there is no interaction between the real and imaginary equations within a component and thus there are two copies of the same equation acting independently on separate variables. The consequence of this is that we get 4 sets of 2×2 system of equations, decoupled from one another, that are readily solvable, e.g. the system of $z_1' = z_5$ and $z_5' = (C_g^2/4d_1^2 - \omega_A/d_1)z_1$. Similar systems of equations can be formed for the variable sets (z_2, z_6), (z_3, z_7), and (z_4, z_8); the eigenvalues of these systems are precisely (5.18). We note that the eigenvectors are linearly independent and, as such, the eigenspace is well-defined and the eigenvalues are not degenerate.

The configuration of the eigenvalues depends on the signs of the dispersion quantities d_1 and d_2, and the travelling wave relationships $\left(C_g^2/4d_1 - \omega_A\right)$ and $\left(C_g^2/4d_2 - \omega_B\right)$. It is clear that, regardless of system parameters, there is the opportunity for spatially hyperbolic equilibria providing that the travelling wave parameters are chosen in the correct manner to counteract any sign changes of the dispersion. For instance, the defocusing Manakov system imposes $d_1 = d_2 = -1$ and $g_1 = g_2 = g_3 = g_4 > 0$, which would then provide a spatially hyperbolic ZZ as long as $\omega_A > C_g^2/2d_1$ and $\omega_B > C_g^2/2d_2$. The focusing Manakov reverses both conditions and mixed Manakov reverses one condition depending on which equation yields the positive dispersion constant. The choice of nonlinear system parameters has no effect on whether a ZZ equilibrium point is hyperbolic, which is expected.

Case (ii) : ZN

Similarly to above one may allow $\phi_0 = 0$, only now with a generic real,

positive ψ_0 given by Eq. (5.12), and reduce the expression (5.17) to find the spatial eigenvalues of this uniform state. In this case, we may simplify D_{1-4} by recognising that $D_1 = D_2$ and $D_4 = 0$. The eigenvalues are then given as

$$\lambda_{1,2} = \sqrt{\frac{1}{d_1}\left(\frac{C_g^2}{4d_1} - \omega_A - g_2\psi_0^2\right)}, \quad \lambda_{3,4} = -\sqrt{\frac{1}{d_1}\left(\frac{C_g^2}{4d_1} - \omega_A - g_2\psi_0^2\right)},$$
$$\lambda_{5,6} = \pm\sqrt{-\frac{2g_3}{d_2}\psi_0^2}, \qquad \lambda_{7,8} = 0, \tag{5.19}$$

where we note that λ_{1-8} are, once again, restricted to configurations involving purely real or imaginary values. λ_{1-4} are shown to have multiplicity 2, like in the ZZ case, due to the decoupling of equations involving the real and imaginary parts of the first component. $\lambda_{5,6}$ depend on the sign of the quantity $d_2 g_3$ which will add an extra criterion for spatial hyperbolicity in this particular case. The remaining eigenvalues $\lambda_{7,8}$ are always zero regardless of system and travelling wave parameters. These two zero values, corresponding to one eigenvector, are unavoidable when one has a reversible system with a 1D set of equivalent equilibria. Due to this, we focus our attention on the non-zero eigenvalues. The first condition, to ensure $\mathcal{R}\mathrm{e}(\lambda_{5,6}) \neq 0$, states that one must have $d_2 g_3 < 0$. For Manakov systems this is only possible in the defocusing and mixed cases, which is a reason why dark soliton components are only found in these particular regimes. For the remaining eigenvalues λ_{1-4}, the purely real configuration depends on the signs of the system parameter $d_1 > (<)\ 0$ and the travelling wave relation

$$\frac{C_g^2(d_2 g_3 - d_1 g_2)}{4 d_1 d_2 g_3} - \omega_A + \frac{g_2}{g_3}\omega_B > (<)\ 0,$$

found by substituting Eq. (5.12) into Eq. (5.19). One can therefore impose travelling wave parameters that enforce spatial hyperbolicity of this uniform state, depending on the magnitude of the system parameters.

Case (iii) : NZ

Due to certain parameter symmetries of Eqs. (4.7-4.8) we recognise that the spatial eigenvalues of the NZ uniform state are given by

$$\lambda_{1,2} = \pm\sqrt{-\frac{2g_1}{d_1}\phi_0^2}, \qquad \lambda_{3,4} = 0,$$
$$\lambda_{5,6} = \sqrt{\frac{1}{d_2}\left(\frac{C_g^2}{4d_2} - \omega_B - g_4\phi_0^2\right)}, \quad \lambda_{7,8} = -\sqrt{\frac{1}{d_2}\left(\frac{C_g^2}{4d_2} - \omega_B - g_4\phi_0^2\right)}. \tag{5.20}$$

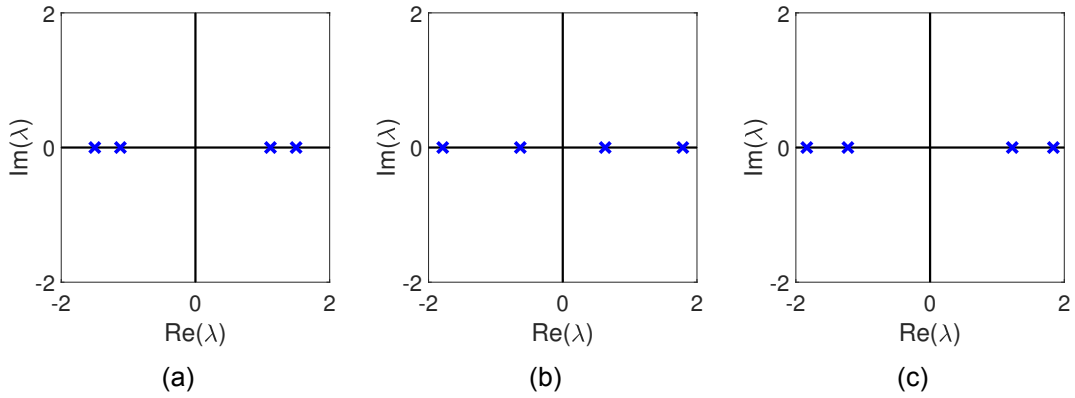

Figure 5.1: Hyperbolic ZZ/ZN/NZ in CNLS with system parameters $d_{1,2} = -1$, $g_{1-3} = 2$, and $g_4 = 3$. (a) ZZ with travelling wave parameters $(C_g, \omega_A, \omega_B) = (1, 1, 2)$. (b) ZN with travelling wave parameters $(C_g, \omega_A, \omega_B) = (2, 2, -1.2)$. (c) NZ with travelling wave parameters $(C_g, \omega_A, \omega_B) = (1, -1, 2)$.

As with the case of ZN, we see that two eigenvalues, $\lambda_{3,4}$, are always zero regardless of parameters and we get some eigenvalues with multiplicity 2. Similarly, we may focus on the conditions that allow the non-zero values to be purely real. Spatial hyperbolicity is then found for this equilibrium point only when $d_1 g_1 < 0$ and also with dependence on the relative signs of $d_2 > (<)\ 0$ and the travelling wave relation

$$\frac{C_g^2(d_1 g_1 - d_2 g_4)}{4 d_1 d_2 g_1} - \omega_B + \frac{g_4}{g_1}\omega_A > (<)\ 0.$$

Note that the hyperbolic condition in the mixed Manakov regime for ZN opposes the condition for NZ, therefore if both uniform states of the Manakov system are to be hyperbolic then this can only be satisfied in the defocusing regime. Since we do not limit ourselves to the Manakov parameters, we can have different signs of the dispersion parameters d_1 and d_2 that may allow both ZN and NZ to be spatially hyperbolic simultaneously. An example of a coupled NLS equation that exhibits spatially hyperbolic equilibria is seen in Fig. 5.1. The system with parameters $d_{1,2} = -1$, $g_{1-3} = 2$, and $g_4 = 3$ may have any of ZZ, ZN, or NZ be hyperbolic with correctly chosen travelling wave parameters. The repeated and zero eigenvalues are omitted from the figures, depicting the four eigenvalues of interest from the three distinct cases (5.18-5.20). We note that it is not possible to simultaneously allow both ZZ and NZ or ZN to be spatially hyperbolic under the same travelling wave parameter choice.

Case (iv) : NN

The final case is that of the uniform state given by Eq. (5.14) where the characteristic equation for the spatial eigenvalues (5.17) can not be simplified further and thus provides the richest dynamics of the four cases. The eigenvalues in this situation are written as,

$$\lambda_{1,2} = \pm\sqrt{-\frac{g_1\phi_0^2}{d_1} - \frac{g_3\psi_0^2}{d_2} + \sqrt{\left(\frac{g_1\phi_0^2}{d_1} - \frac{g_3\psi_0^2}{d_2}\right)^2 + 4\frac{g_2g_4}{d_1d_2}\phi_0^2\psi_0^2}},$$
$$\lambda_{5,6} = \pm\sqrt{-\frac{g_1\phi_0^2}{d_1} - \frac{g_3\psi_0^2}{d_2} - \sqrt{\left(\frac{g_1\phi_0^2}{d_1} - \frac{g_3\psi_0^2}{d_2}\right)^2 + 4\frac{g_2g_4}{d_1d_2}\phi_0^2\psi_0^2}},$$
$$\lambda_{3,4,7,8} = 0, \tag{5.21}$$

where, since the diagonal terms $D_2 = D_4 = 0$, we have 4 guaranteed zero eigenvalues and non-zero configurations involving real, imaginary or complex values. The configuration involving complex values is unique to this uniform state and conditions can be determined if we re-write the eigenvalues as $\lambda_{1,2} = \sqrt{C_1 + \sqrt{C_2}}$ and $\lambda_{5,6} = \sqrt{C_1 - \sqrt{C_2}}$ respectively. If $C_2 < 0$, then the configuration is that of a complex quartet which is only possible when the condition

$$4\frac{g_2g_4}{d_1d_2}\phi_0^2\psi_0^2 < -\left(\frac{g_1\phi_0^2}{d_1} - \frac{g_3\psi_0^2}{d_2}\right)^2, \tag{5.22}$$

is satisfied. Note that when this inequality becomes equal, a Turing bifurcation arises under certain conditions that we will discuss and analyse in Chapter 7. It is obvious that $\lambda_{1,2}$ and $\lambda_{5,6}$ have non-zero real parts when they are a complex quartet or when they are purely real, i.e. $C_1 > \sqrt{C_2} \geq 0$ with $C_2 \geq 0$, thus we have spatial hyperbolicity in either of these cases.

There is often interest in the impact of imposing different dispersion coefficients, d_1 and d_2, which play the role of inverse masses in BECs [42]. We will analyse the case(s) of choosing same/opposing signs of these system parameters, corresponding to positive and negative mass. We focus first on the two cases of positive mass, $d_1d_2 > 0$, where we may have $d_1,\ d_2 < 0$ or $d_1,\ d_2 > 0$. It is assumed in the forthcoming analysis that the NN equilibria exist as given by Eq. (5.14), i.e. $\phi_0^2,\ \psi_0^2 > 0$. For the regime of $d_1,\ d_2 > 0$ we have $C_1 > 0$ providing that the relationship $g_1d_2\phi_0^2 + d_1g_3\psi_0^2 < 0$. We see instantly that at least one of g_1 or g_3 must be negative in order for this to be satisfied. Then, assuming that Eq. (5.22) isn't satisfied, so that $C_2 \geq 0$, one can impose $C_1 > \sqrt{C_2}$ by forcing the relation $g_1g_3 - g_2g_4 > 0$. To ensure no change in the sign of C_2, one can satisfy this relation by allowing both g_1 and g_3 to be negative with their product larger than g_2g_4. Then, providing NN exists, the eigenvalues will be

purely real and therefore spatially hyperbolic. Alternatively, there is also the possibility of a complex quartet for $d_1,\ d_2 > 0$ if Eq. (5.22) is satisfied. This can only happen if g_2 or g_4 is negative but also depends on the magnitude of system and travelling wave parameters. An example of a non-integrable coupled NLS system, with $d_1, d_2 > 0$, that exhibits an equilibrium point with a complex quartet of eigenvalues is seen in Fig. 5.2(a).

The regime with $d_1,\ d_2 < 0$ is similar where $C_1 > 0$ given that $g_1 d_2 \phi_0^2 + d_1 g_3 \psi_0^2 < 0$, however, the reversed sign of the dispersion coefficients now enforces at least one of $g_1,\ g_3$ to be positive. Assuming that the product of the cross-nonlinearity terms $g_2 g_4$ is positive then C_2 is guaranteed to be positive and the inequality $C_1 > \sqrt{C_2}$ holds, once again, when $g_1 g_3 - g_2 g_4 > 0$. Providing travelling wave parameters that allow NN to exist, the eigenvalues will then be purely real. A complex quartet may exist if one imposes the product of the cross-nonlinearity terms $g_2 g_4$ to be negative and depends on the magnitude of all parameters. An example of an equilibrium point with purely real eigenvalues, in a coupled NLS equation with negative dispersion parameters, is seen in Fig. 5.2(b).

The two cases of negative mass yield similar analysis due to equation symmetry of Eqs. (4.7-4.8), so we can choose to analyse one particular case, e.g. $d_1 < 0,\ d_2 > 0$. Within this regime, the quantity C_1 is now positive only when $g_1 d_2 \phi_0^2 + d_1 g_3 \psi_0^2 > 0$, where we note that this inequality is now reversed from previous due to the product of $d_1 d_2 < 0$. Assuming the existence of Eq. (5.14) and $C_2 \geq 0$, then the inequality $C_1 > \sqrt{C_2}$ is satisfied providing that $g_1 g_3 - g_2 g_4 < 0$. This then ensures that the eigenvalues are purely real. The complex quartet arises when Eq. (5.22) is satisfied, which can occur here without any change in the sign of g_2 and g_4, but also depends on the magnitude of the parameters. This condition enforces sign$(g_2) =$ sign(g_4), but we may have any combination of g_1 and g_3 positive/negative. An example of a spatially hyperbolic NN, in the regime with negative mass, that exhibits purely real eigenvalues is seen in Fig. 5.2(c). Note that, though the systems seen in Fig. 5.1 and Fig. 5.2 have dispersion coefficients that are positive/negative unity, we are not limited to those coupled NLS systems with $|d_{1,2}| = 1$. One is free to impose more generalised parameters, with different magnitudes of dispersion parameters, and check the above conditions which allow spatially hyperbolic $ZZ/ZN/NZ/NN$.

It is important to note that the equilibria being spatially hyperbolic doesn't directly affect the time evolution of the plane-wave solution in the CNLS, but hyperbolicity is a vital condition for the existence of nonlinear structures homoclinic/heteroclinic to the equilibria that we will consider in the forthcoming sections and chapters.

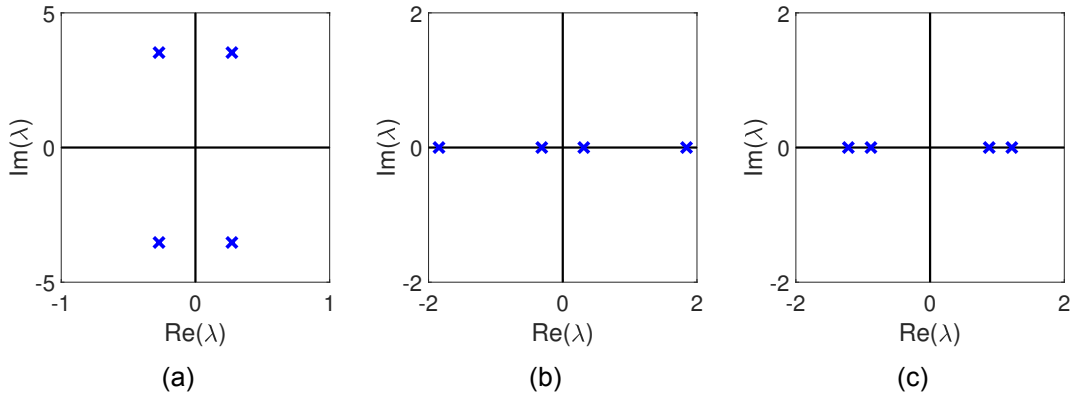

Figure 5.2: Spatial eigenvalues of NN for positive and negative masses. (a) Positive dispersion parameters with $d_1 = d_2 = 1$, $g_1 = 5$, $g_2 = -4$, $g_3 = 3$, $g_4 = 1$, and travelling wave parameters $(C_g, \omega_A, \omega_B) = (3, -2, -3)$. (b) Negative dispersion parameters with $d_1 = d_2 = -1$, $g_1 = g_4 = 4$, $g_2 = 2$, $g_3 = 5$, and travelling wave parameters $(C_g, \omega_A, \omega_B) = (1, -1, -2)$. (c) Mixed dispersion parameters with $d_1 = -1$, $d_2 = 1$, $g_1 = g_2 = 4$, $g_3 = 2$, $g_4 = 5$, and travelling wave parameters $(C_g, \omega_A, \omega_B) = (1, -1.83, -1.5)$.

5.1.3 Temporal Stability

For a plane-wave solution to persist in the CNLS, one must ensure temporal stability of the uniform state in the dynamical system. The temporal (Roskes) stability of a plane-wave in the CNLS is a topic well-studied for interacting modes with similar group velocity [162]. In [162] the linear stability of NN solutions is considered when $k_{A,B} = C_g = 0$, $\omega_A = \omega_A(\phi_0, \psi_0)$, and $\omega_B = \omega_B(\phi_0, \psi_0)$. Generally, the temporal stability is computed by considering the complex growth rate S of a small, spatial perturbation of wavenumber K in the co-moving variable. To analyse the linear stability of equilibria, one first needs to include the temporal terms back into the ODE, i.e. adding $i\phi_t$ and $i\psi_t$ to the respective component of Eqs. (5.9-5.10). Similarly to the spatial eigenvalues, one then perturbs the chosen real, positive uniform state $[p, q, r, s]^T = [\phi_0, 0, \psi_0, 0]^T$ and looks for solutions proportional to $\epsilon e^{iK\zeta + St}$, linearising in $\epsilon << 1$. The full temporal Jacobian is given by

$$\mathbf{J}_S = \begin{pmatrix} 0 & E_1 & 0 & 0 \\ E_2 & 0 & 2g_2\phi_0\psi_0 & 0 \\ 0 & 0 & 0 & E_3 \\ 2g_4\phi_0\psi_0 & 0 & E_4 & 0 \end{pmatrix} \tag{5.23}$$

with

$$E_1 = K^2 d_1 + \left(\frac{C_g^2}{4d_1} - \omega_A\right) - g_1\phi_0^2 - g_2\psi_0^2,$$
$$E_2 = -K^2 d_1 - \left(\frac{C_g^2}{4d_1} - \omega_A\right) + 3g_1\phi_0^2 + g_2\psi_0^2,$$
$$E_3 = K^2 d_2 + \left(\frac{C_g^2}{4d_2} - \omega_B\right) - g_3\psi_0^2 - g_4\phi_0^2,$$
$$E_4 = -K^2 d_2 - \left(\frac{C_g^2}{4d_2} - \omega_B\right) + 3g_3\psi_0^2 + g_4\phi_0^2.$$

We have considered the positive, real equilibria, but it is important to note that if one considers the complex equilibria instead, $\phi_0 = p_0 + iq_0$, and $\psi_0 = r_0 + is_0$, then the temporal eigenvalues remain unchanged due to gauge invariance of the dynamical system. The temporal eigenvalues S_{1-4} of the full Jacobian can be derived, once again, by utilising the Schur Complement. Following the same procedure as Eq. (5.17), one can write the temporal eigenvalues as the solution to $\det(\mathbf{J}_S - S\mathbf{I}_4) = 0$ which yields the temporal characteristic equation

$$S^4 - (E_1E_2 + E_3E_4)S^2 + E_1E_2E_3E_4 - 4g_2g_4E_1E_3\phi_0^2\psi_0^2 = 0. \tag{5.24}$$

The real part of the temporal eigenvalues, $\mathcal{R}\mathrm{e}(S)$, corresponds to the growth rate of the perturbation whilst the imaginary part, $\mathrm{Im}(S)$, is the oscillation frequency of the perturbation. Both are described as functions of the perturbation wavenumber, K, and temporal instability corresponds to some $\mathcal{R}\mathrm{e}(S) > 0$ for $K^2 \geq 0$. If one substitutes $S = 0$ and $K = i\lambda$ into this equation then the characteristic equation for the spatial eigenvalues (5.17) is recovered. To analyse the temporal stability of the four uniform states (5.11-5.14), we substitute each one into the characteristic equation (5.24) and consider the repercussions of differing system and travelling wave parameters on the stability of each particular case.

Case (i) : ZZ

As with the spatial eigenvalues, the ZZ uniform state significantly simplifies the description of the temporal eigenvalues when one substitutes $\phi_0 = 0,\ \psi_0 = 0$ into the characteristic equation. Since the two components are decoupled, the temporal eigenvalues are governed by the product of the terms E_1E_2 and E_3E_4. These terms are further simplified due to the relationships $E_1 = -E_2$ and

$E_3 = -E_4$, thus we may write the eigenvalues for ZZ as

$$S_{1,2} = \pm\sqrt{-\left(K^2 d_1 + \frac{C_g^2}{4d_1} - \omega_A\right)^2},$$
$$S_{3,4} = \pm\sqrt{-\left(K^2 d_2 + \frac{C_g^2}{4d_2} - \omega_B\right)^2}. \tag{5.25}$$

The eigenvalues are always purely imaginary, independent of the choice of K^2. Therefore the ZZ plane-wave is temporally stable, to small perturbations, for any choice of system and travelling wave parameters.

Case (ii) : ZN

For the ZN uniform state, the temporal eigenvalues are again governed by the products E_1E_2 and E_3E_4. The relationship of $E_1 = -E_2$ still remains but now we have simplifications to $E_3,\ E_4$ that take the form $E_3 = K^2 d_2$ and $E_4 = 2g_3\psi_0^2 - K^2 d_2$. The eigenvalues for the ZN state can then be written as

$$S_{1,2} = \pm\sqrt{-\left(K^2 d_1 + \frac{C_g^2}{4d_1} - \omega_A - g_2\psi_0^2\right)^2},$$
$$S_{3,4} = \pm\sqrt{K^2 d_2\left(\frac{C_g^2}{2d_2} - 2\omega_B - K^2 d_2\right)}. \tag{5.26}$$

The eigenvalues $S_{1,2}$ are purely imaginary no matter the choice of system and travelling wave parameters, therefore temporal stability of this uniform state relies entirely on whether $\mathcal{R}\mathrm{e}(S_{3,4}) \leq 0$ for $K^2 \geq 0$. Due to the symmetry of these eigenvalues, one can only guarantee this criterion providing that $S_{3,4}$ are purely imaginary. By fixing K^2 positive, one sees that we have differing criteria depending on the sign of the dispersion parameter d_2. It can be shown that, if $d_2 > 0$ then temporal stability of ZN is obtained when $(C_g^2/4d_2 - \omega_B) < 0$; the reverse is true for $d_2 < 0$. This also imposes conditions on the parameter g_3 since the equilibrium point (5.12) only exists when the quantities $(C_g^2/4d_2 - \omega_B)$ and g_3 take the same sign.

Case (iii) : NZ

Due to the component parameter symmetries of the coupled NLS equation, one can readily write $E_3 = -E_4$, $E_1 = K^2 d_1$, and $E_2 = 2g_1\phi_0^2 - K^2 d_1$. The

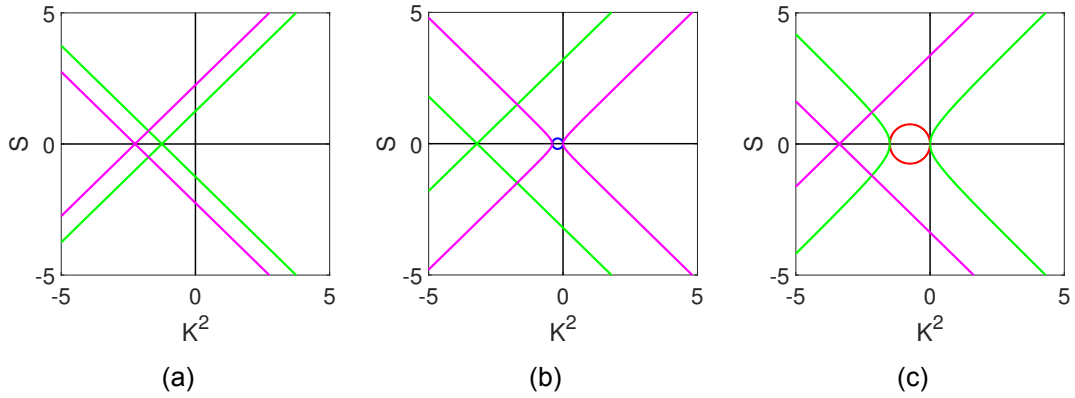

Figure 5.3: Dispersion relation $S_{1-4}(K^2)$ for $ZZ/ZN/NZ$ uniform states. Red (green) curves indicate $\mathcal{R}\text{e}(S_{1,2})$ and $\text{Im}(S_{1,2})$ respectively, whilst blue (magenta) curves indicate $\mathcal{R}\text{e}(S_{3,4})$ and $\text{Im}(S_{3,4})$ respectively. (a) ZZ with parameters from Fig. 5.1(a). (b) ZN with parameters from Fig. 5.1(b). (c) NZ with parameters from Fig. 5.1(c).

temporal eigenvalues of NZ are therefore given as

$$S_{1,2} = \pm\sqrt{K^2 d_1 \left(\frac{C_g^2}{2d_1} - 2\omega_A - K^2 d_1\right)},$$
$$S_{3,4} = \pm\sqrt{-\left(K^2 d_2 + \frac{C_g^2}{4d_2} - \omega_B - g_4\phi_0^2\right)^2}. \tag{5.27}$$

In this instance, $S_{3,4}$ are always purely imaginary with the configuration of $S_{1,2}$ inferring temporal stability of the NZ uniform state. Once again, fixing K^2 positive, if $d_1 > 0$ then this imposes the condition for stability as $(C_g^2/4d_1 - \omega_A) < 0$, and consequently $g_1 < 0$ for the equilibrium point to exist as given by Eq. (5.13). The criteria are then reversed when one considers a swap in the sign of dispersion parameter $d_1 < 0$.

Figure 5.3 shows the dispersion relation for each of the spatially hyperbolic equilibrium points $ZZ/ZN/NZ$ from Fig. 5.1. In these particular cases the uniform state is temporally stable as well as spatially hyperbolic, which is apparent from the figures since there are no red or blue segments in the first quadrants. Geometrically, the non-zero component yields temporal eigenvalues that form an ellipse, and two rays along the K^2 axis, in the plot of the corresponding $\mathcal{R}\text{e}(S)$ vs K^2. The plot of $\text{Im}(S)$ vs K^2 yields a pair of hyperbolas connected via a line segment along the K^2 axis for the eigenvalues of the non-zero component. The eigenvalues of the zero component, that are always imaginary, will appear as a set of lines with positive and negative gradient in the plot of $\text{Im}(S)$ vs K^2; the lines intersect at $(C_g^2/4d_2^2 - \omega_B/d_2)$ for NZ and $(C_g^2/4d_1^2 - \omega_A/d_1)$ for ZN. Therefore, for the uniform states ZN/NZ, as long as the ellipse is located in the half-plane $K^2 < 0$ then temporal stability is guaranteed by our definition

for the uniform state.

Case (iv) : NN

Due to non-zero components for the uniform state NN, the temporal characteristic equation can not be simplified further. We can only write the full eigenvalues as the solution to the generic dispersion relation (5.24), which are

$$S_{1,2} = \pm\sqrt{K^2F_1 + \frac{\sqrt{K^4F_2}}{2}}, \quad S_{3,4} = \pm\sqrt{K^2F_1 - \frac{\sqrt{K^4F_2}}{2}} \tag{5.28}$$

where

$$F_1 = \frac{-K^2(d_1^2 + d_2^2)}{2} + d_1g_1\phi_0^2 + d_2g_3\psi_0^2,$$
$$F_2 = \left[2(d_1g_1\phi_0^2 - d_2g_3\psi_0^2) + K^2(d_2^2 - d_1^2)\right]^2 + 16d_1d_2g_2g_4\phi_0^2\psi_0^2.$$

Though the configurations of the temporal eigenvalues are not immediately obvious, we can consider the properties of the functions F_1 and F_2 in the half plane $K^2 > 0$. Recall that temporal instability is inferred geometrically from the first quadrant in the plot of $\mathcal{R}\mathrm{e}(S)$ vs K^2. This quadrant is empty, and thus imposes temporal stability of the uniform state, if the eigenvalues are purely imaginary for $K^2 > 0$. This is only a possibility if $F_2 \geq 0$, $F_1 \leq 0$, and $|F_1| \geq \sqrt{F_2}/2$ within this interval. When $K^2 = 0$, the eigenvalues S are all zero by definition so we need not consider this unique case.

The function $F_2(K^2)$ takes a parabolic form and can be analysed according to the signs of the coefficients in the quadratic equation. The first thing to note is that the coefficient $(d_2^2 - d_1^2)^2 \geq 0$, regardless of the signs of the dispersion parameters, therefore the parabola always has a minimum located at

$$K_a^2 = \frac{-2(d_1g_1\phi_0^2 - d_2g_3\psi_0^2)}{d_2^2 - d_1^2}.$$

The sign of the function $F_2(K^2)$ then depends on this minimum and the solution to $F_2(K^2) = 0$, which we will denote by $K_{b,c}^2$, given explicitly as,

$$K_{b,c}^2 = K_a^2 \pm \frac{4\sqrt{-d_1d_2g_2g_4\phi_0^2\psi_0^2}}{d_2^2 - d_1^2}.$$

Firstly, if the minimum is located in the interval $K_a^2 \geq 0$ then one can not have $F_2 \geq 0$, for all $K^2 > 0$, unless $K_{b,c}^2$ are complex-valued. This amounts to the system parameters having the product sign of $d_1d_2g_2g_4 > 0$. In con-

trast, if the minimum is located in the interval $K_a^2 < 0$, then we must have sgn$(d_1 g_1 \phi_0^2 - d_2 g_3 \psi_0^2) =$ sgn$(d_2^2 - d_1^2)$ and $F_2 > 0$ is guaranteed if $d_1 d_2 g_2 g_4 > 0$, or if $d_1 d_2 g_2 g_4 < 0$ and $(d_1 g_1 \phi_0^2 - d_2 g_3 \psi_0^2)^2 > -4 d_1 d_2 g_2 g_4 \phi_0^2 \psi_0^2$. In the unique case that the parameters chosen enforce $d_1^2 = d_2^2$, the analysis above does not hold since the parabola simplifies to a constant for all K^2. In this instance, the function $F_2 \geq 0$ providing that $(d_1 g_1 \phi_0^2 - d_2 g_3 \psi_0^2)^2 > -4 d_1 d_2 g_2 g_4 \phi_0^2 \psi_0^2$, which is always possible by imposing $d_1 d_2 g_2 g_4 > 0$. If one has $d_1 d_2 g_2 g_4 < 0$ then the magnitude of the parameters has an effect on whether this criterion is fully satisfied.

The function $F_1(K^2)$ takes a much simpler form being a linear equation in K^2, with a gradient $-(d_1^2 + d_2^2)/2$ that is always negative. We note that the function takes the sign of $F_1 \leq 0$, for $K^2 > 0$, providing that the vertical intercept is taken to be negative in the interval of interest, i.e. $d_1 g_1 \phi_0^2 + d_2 g_3 \psi_0^2 < 0$.

The final inequality to ensure is $|F_1| \geq \sqrt{F_2}/2$, where we know F_2 is only defined positively, which guarantees that both sets of the temporal eigenvalues, $S_{1,2}$ and $S_{3,4}$, are purely imaginary in the interval $K^2 > 0$. Since we know the signs of both sides, and are only interested in the magnitude of the quantity, we may instead consider the inequality $F_1^2 \geq F_2/4$. This inequality then produces the criterion,

$$d_1^2 d_2^2 K^4 - 2 d_1 d_2 (d_1 g_3 \psi_0^2 + d_2 g_1 \phi_0^2) K^2 + 4 d_1 d_2 (g_1 g_3 - g_2 g_4) \phi_0^2 \psi_0^2 > 0, \qquad (5.29)$$

which is a quadratic in K^2 and can be analysed accordingly for $K^2 > 0$. Since $d_1^2 d_2^2 > 0$, the quadratic will always form a parabola with a minimum located at the K^2 point

$$K_d^2 = \frac{d_1 g_3 \psi_0^2 + d_2 g_1 \phi_0^2}{d_1 d_2},$$

and K^2-intercepts at

$$K_{e,f}^2 = K_d^2 \pm \frac{\sqrt{(d_1 g_3 \psi_0^2 - d_2 g_1 \phi_0^2)^2 + 4 d_1 d_2 g_2 g_4 \phi_0^2 \psi_0^2}}{d_1 d_2}.$$

We can split the analysis into two distinct cases, when $K_d^2 \geq 0$ and $K_d^2 < 0$. If the minimum is located in the interval $K_d^2 \geq 0$, then the only possibility for the condition (5.29) to be satisfied, for all $K^2 > 0$, is when $K_{e,f}^2$ are not defined in purely real space. This is equivalent to the condition $(d_1 g_3 \psi_0^2 - d_2 g_1 \phi_0^2)^2 < -4 d_1 d_2 g_2 g_4 \phi_0^2 \psi_0^2$, which is only possible if $d_1 d_2 g_2 g_4 < 0$, but also relies on the magnitude of the parameters. In contrast, if $K_d^2 < 0$, then we can once again have $K_{e,f}^2$ not defined in purely real space, which guarantees Eq. (5.29) to be satisfied for $K^2 > 0$, or we also have the possibility of allowing both $K_{e,f}^2 \leq 0$. Assuming that $K_{e,f}^2$ are defined in the purely real space, the criterion for these

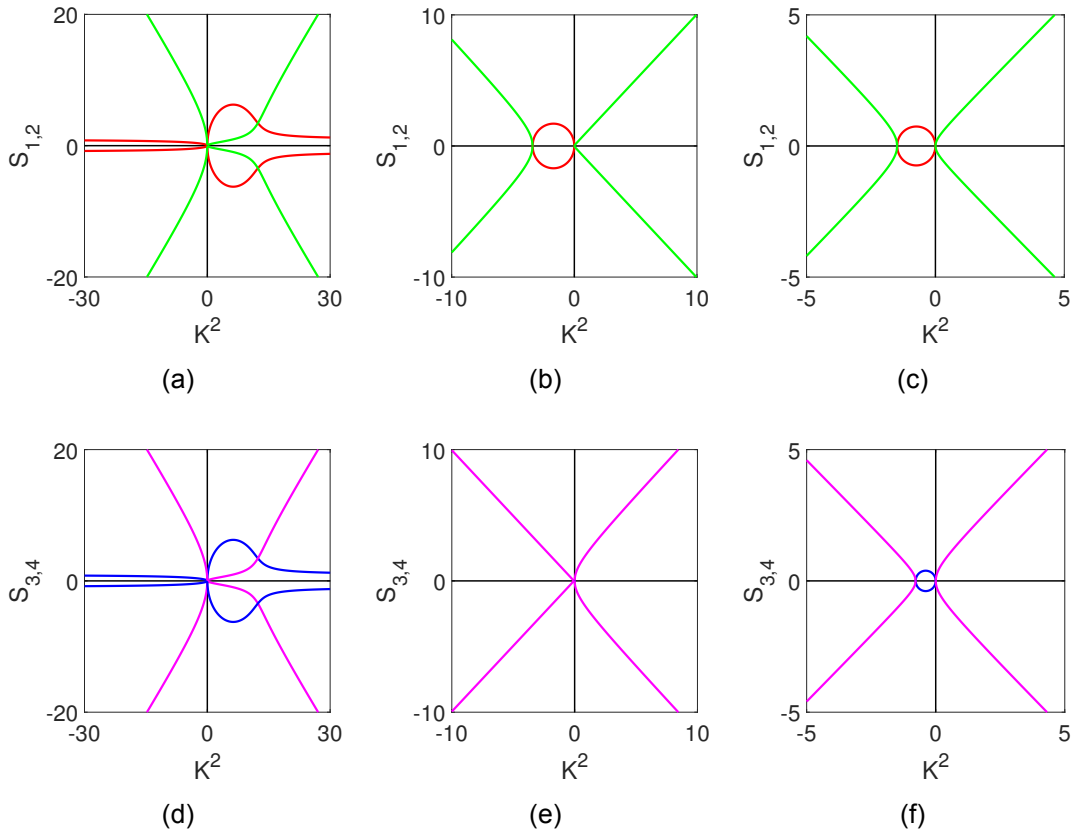

Figure 5.4: Dispersion relation $S_{1-4}(K^2)$ for the NN uniform state with differing dispersion signs. Red (green) curves of (a-c) indicate $\mathcal{R}\text{e}(S_{1,2})$ and $\text{Im}(S_{1,2})$ respectively, whilst blue (magenta) curves of (d-f) indicate $\mathcal{R}\text{e}(S_{3,4})$ and $\text{Im}(S_{3,4})$ respectively. (a,d) Positive dispersion constants with parameters from Fig. 5.2(a). (b,e) Negative dispersion constants with parameters from Fig. 5.2(b). (c,f) Mixed dispersion constants with parameters from Fig. 5.2(c).

to be negative becomes $d_1 d_2 (g_1 g_3 - g_2 g_4) > 0$.

With all three of the inequalities, $F_2 \geq 0$, $F_1 \leq 0$, and $|F_1| \geq \sqrt{F_2}/2$ satisfied, one will have temporal stability of NN in the PDE. The key property to note is that the sign of the quantity $d_1 d_2 g_2 g_4$ plays a significant role in all of the criteria. Therefore if one wants to search for a particular set of parameters that produce temporally stable NN, then this is the first quantity one should consider.

Figure 5.4 shows the dispersion relation for the three sets of parameters seen previously in Fig. 5.2; the temporal eigenvalues for $S_{1,2}$ are depicted in panels (a-c) and $S_{3,4}$ are depicted in (d-f). The first observation we can make is that the cases of negative (Fig. 5.4(b) and Fig. 5.4(e)) and mixed (Fig. 5.4(c) and Fig. 5.4(f)) dispersion constants are temporally stable for the chosen parameter sets. One can easily see that this should be the case for these chosen parameters if the criteria are followed accordingly. Recall also that $|d_{1,2}| = 1$ was imposed for the chosen parameter sets, therefore the analysis is simpler in these cases since one has $d_1^2 = d_2^2$.

The considered case of positive dispersion coefficients is very different since

this particular uniform state is not temporally stable. The complex structure of the dispersion relation, seen in Fig. 5.4(a) and Fig. 5.4(d), is caused by a combination of the functions $F_2 < 0$ for all $K^2 > 0$, and $F_1 > 0$ for some $K^2 > 0$. Thus, the temporal eigenvalues form complex quartets as K^2 varies. This is an important observation since it shows that spatial hyperbolicity of NN does not guarantee temporal stability. We note that this statement does not hold true for all uniform states within the different cases of dispersion sign, but rather only for the particular states chosen from Fig. 5.2, i.e. we expect both temporally stable/unstable states in all three cases of different dispersive signs.

5.1.4 Non-integrable Focusing and Defocusing regimes

The Manakov system encases particular parameter regimes that can be classified as focusing, defocusing, or mixed. In particular, the type of regime considered depends on the relationship between the dispersion and nonlinearity signs of each component equation. We often call the focusing Manakov the equation in which all parameters take a positive sign after scaling; the defocusing Manakov system is similar only the nonlinear terms now have opposing signs to the dispersion parameters. The mixed Manakov regime is unique in that one considers opposing nonlinear signs for each component equation, i.e. $g_1 = -g_2 = -g_3 = g_4$. Distinguishing what type of regime the coupled NLS equation follows is important when considering the type of solutions that one may have in general. For instance, one expects the formation of bright-bright vector solitons in the focusing and mixed Manakov systems but not the defocusing regime, as reviewed in Sec. 1.1.2. In contrast, one expects vector solitons with a dark component (dark-dark, dark-bright, and bright-dark) in the defocusing and mixed regimes.

Whether the equation is in the focusing, defocusing, or mixed regime is well-defined for the Manakov-type systems, but recall that we wish to keep the analysis as general as possible. Therefore, we will define the regimes in the following way:

(i) We call a system, with given system and travelling wave parameters, **focusing** if the uniform state ZZ is Spatially Hyperbolic and Temporally Stable (SHATS).

(ii) We call a system, with given system and travelling wave parameters, **defocusing** if at least one of the uniform states ZN/NZ are Spatially Hyperbolic and Temporally Stable (SHATS).

By this definition the system may be focusing, defocusing, or neither (but not both simultaneously). Note that the NN state is deemed to be a non-classifier for the regime of the non-integrable CNLS. Each uniform state has a unique set of criteria that imposes SHATS, and the criteria for one state often disallows SHATS for another state, which is why we may suggest the definition of focusing and defocusing regimes above. A brief overlook of the conditions tells us that every spatially hyperbolic (SH) ZZ state is also temporally stable (TS), but TS does not guarantee SH. This is also true for the NZ and ZN states. The reverse can be said for NN, i.e. every state that is TS is also SH, however, SH does not guarantee TS.

In general, the pairs of uniform states that allow SHATS simultaneously are ZZ and NN, and NZ and ZN. Though it is not immediately obvious, one can check from the derived conditions in the previous sections why this is always the case. For the purpose of this brief analysis we will denote the following $G_1 = (C_g^2/4d_1 - \omega_A)$ and $G_2 = (C_g^2/4d_2 - \omega_B)$. If one considers the ZZ state then the conditions for SH are simply $d_2 G_2 > 0$ and $d_1 G_1 > 0$. These conditions directly contradict some conditions for SH in ZN and NZ, which are $d_2 G_2 < 0$ and $d_1 G_1 < 0$ respectively. Therefore, ZZ can not be SHATS with ZN or NZ simultaneously. In contrast, there is no contradiction between the conditions for ZZ and NN so it is possible to have SHATS here but not guaranteed. For example, one such system that allows this is $d_1 = d_2 = -5$, $g_1 = -1$, $g_2 = 1$, $g_3 = 4$, $g_4 = -5$, and the travelling wave parameter set $(C_g, \omega_A, \omega_B) = (0, 0.1, 0.7)$. Similarly, there is no contradiction for SHATS of ZN and NZ simultaneously so it is possible to satisfy all of the conditions of each state. An example of this is obtained if we consider the nearly-integrable system parameters from Fig. 5.1, with the travelling wave parameter set $(C_g, \omega_A, \omega_B) = (1, -1, -1.1)$.

We note certain constraints that appear when one considers ZN and NZ to be SHATS simultaneously. To impose SHATS, one must ensure that $d_1 g_1 < 0$ and $d_2 g_3 < 0$, which has already been discussed in the previous sections. Extra constraints, however, are imposed by the remaining SH conditions of each state. In order to enforce SH and physical equilibria, one must also have $d_1 g_2 < 0$ and $d_2 g_4 < 0$. Therefore, for ZN and NZ to be SHATS together, we are limited to the CNLS system of type $g_1 g_2 > 0$, $g_3 g_4 > 0$, $\text{sgn}(d_1) \neq \text{sgn}(g_{1,2})$, and $\text{sgn}(d_2) \neq \text{sgn}(g_{3,4})$. For $d_1 d_2 > 0$, the remaining parameters must satisfy $g_2 g_4 - g_1 g_3 > 0$, whereas the reverse is true for $d_1 d_2 < 0$. These relations are expected since the CNLS system can be scaled from $d_1 d_2 < 0$ to $d_1 d_2 > 0$ by applying conjugation to either the A or the B equation.

If one considers the SH conditions of the ZN state, then these contradict the conditions for SH of the NN state. Though it is not immediately obvious,

the spatial eigenvalues of both the ZN and NZ can not be purely real simultaneously because the ZN conditions, and the assumption of physical equilibria given by Eq. (5.12) and Eq. (5.14), force $d_1 d_2(g_1 g_3 - g_2 g_4) < 0$. This directly contradicts the condition for purely real NN eigenvalues, so we are then limited to complex eigenvalues. Recall that complex eigenvalues for NN are given when the condition (5.22) is satisfied, and can be more conveniently written as

$$\frac{1}{d_1^2 d_2^2}\left(g_1^2 d_2^2 \phi_0^4 + g_3^2 d_1^2 \psi_0^4 + 2d_1 d_2(2g_2 g_4 - g_1 g_3)\phi_0^2 \psi_0^2\right) < 0.$$

If we fix all of the system parameters then this function can be written in terms of the variable ϕ_0^2 or ψ_0^2, and takes the form of a 'U' shaped parabola. If we fix one of $\phi_0^2,\ \psi_0^2 > 0$, and consider the other as a variable, then the function can only take negative values when it crosses the ϕ_0^2 or ψ_0^2 axis, which is equivalent to the existence of a Turing bifurcation. In either case, the relationship between the two components that allows the function to be negative involves the quantity $\sqrt{g_2 g_4(g_2 g_4 - g_1 g_3)}$. The conditions for ZN to be SH, and the assumption of physical equilibria, force the quantity under the root to be negative; the relationship that allows the function to become negative can not be satisfied in real space. Therefore, a contradiction occurs and there is no CNLS system which allows Eq. (5.22) to be satisfied whilst simultaneously allowing ZN to be SH, and both ZN, NN physical. A very similar analysis can be performed with the NZ and NN states, with the same result of contradictory SHATS conditions.

5.2 Heteroclinic orbits

Coherent structures of the coupled NLS equation can be found by considering the existence of reversible homoclinic orbits, that translate to soliton solutions, or heteroclinic orbits (connections) that translate to front solutions. The former corresponds to a trajectory that connects a uniform state back to itself, forming a 'loop' in the phase space, whilst the latter is a trajectory that connects two uniform states in the phase space. See, for instance, [175] for information regarding such special trajectories. Formally, we say that a generic solution $\boldsymbol{X}(\zeta)$ is a homoclinic orbit if $\boldsymbol{X}(\zeta) \longrightarrow \boldsymbol{X}_0$ as $\zeta \longrightarrow \pm\infty$, where $\boldsymbol{X}_0$ is an equilibrium of the considered ODE. In contrast, the heteroclinic orbit is formally defined if $\boldsymbol{X}(\zeta) \longrightarrow \boldsymbol{X}_1$ as $\zeta \longrightarrow -\infty$ and $\boldsymbol{X}(\zeta) \longrightarrow \boldsymbol{X}_2$ as $\zeta \longrightarrow +\infty$ where $\boldsymbol{X}_{1,2}$ are equillibria of the considered ODE and $\boldsymbol{X}_1 \neq \boldsymbol{X}_2$. Further to this, a homoclinic orbit must be encompassed by both of the stable and unstable manifolds of $\boldsymbol{X}_0$, whereas the heteroclinic orbit is encompassed by the unstable manifold of $\boldsymbol{X}_1$ and the stable manifold of $\boldsymbol{X}_2$. This is precisely the reason why we pre-

viously derived conditions for the equilibria of Eqs. (5.9-5.10) to be SHATS, since spatial hyperbolicity guarantees that the stable and unstable manifolds to the equilibrium have the right dimensions to form transverse intersections. The remainder of this chapter will focus on the derivation of heteroclinic orbits connecting the uniform states, with homoclinic orbits considered in Chapter 6.

A necessary condition for heteroclinic orbits is the existence of a real-valued conserved quantity, which we denote $\mathcal{E}$, for the ODE system (5.9-5.10). This conserved value remains as a constant on the trajectory connecting two uniform states of the system. The quantity can be explicitly written as

$$\mathcal{E} = c_1|\phi'|^2 + c_2|\phi|^2 + c_3|\phi|^4 + c_4|\psi'|^2 + c_5|\psi|^2 + c_6|\psi|^4 + c_7|\phi|^2|\psi|^2, \qquad (5.30)$$

where, due to $\mathcal{E}$ being defined up to a multiplicative constant, we may suggest $c_7 = 1$ without loss of generality. The analysis is similar to that of [40]. By definition, the derivative of the quantity is given by $\mathcal{E}' = 0$ so we may say that the system (5.9-5.10) is conserved by the equivalence of the following,

$$\begin{aligned} &D_1(d_1\phi'' + (\omega_A - d_1k_A^2)\phi + g_1|\phi|^2\phi + g_2|\psi|^2\phi) \\ &\quad + D_2(d_2\psi'' + (\omega_B - d_2k_B^2)\psi + g_3|\psi|^2\psi + g_4|\phi|^2\psi) + c.c = \mathcal{E}', \end{aligned}$$

where the coefficients $D_{1,2}$ and c_{1-6} can be formally derived. Therefore, under the previous simplification $C_g = 2d_1k_A = 2d_2k_B$, the quantity (5.30) is given precisely by

$$\begin{aligned} \mathcal{E} =& \frac{d_1}{g_2}|\phi'|^2 + \frac{(\omega_A - C_g^2/4d_1)}{g_2}|\phi|^2 + \frac{g_1}{2g_2}|\phi|^4 + \frac{d_2}{g_4}|\psi'|^2 \\ &+ \frac{(\omega_B - C_g^2/4d_2)}{g_4}|\psi|^2 + \frac{g_3}{2g_4}|\psi|^4 + |\phi|^2|\psi|^2, \end{aligned} \qquad (5.31)$$

with $\mathcal{E}' = 0,\ \forall\ \zeta$, and depends explicitly on the system parameters $d_{1,2}$, g_{1-4}, and the travelling wave parameter set $(C_g, \omega_A, \omega_B)$.

Utilising the fact that $\mathcal{E}$ is constant on the trajectory, for an orbit to exist there must be a set of the real-valued parameter range $(C_g, \omega_A, \omega_B)$ that satisfies $\mathcal{E}^i = \mathcal{E}^j$, where $i,\ j$ are each one of $ZZ,\ ZN,\ NZ,\ NN$ and $\mathcal{E}^{i,j}$ corresponds to Eq. (5.31) with the relevant equilibria substituted. The first observation that we can make is that an orbit between the ZZ and the ZN or NZ uniform states can not exist, since the only set of $(C_g, \omega_A, \omega_B)$ that allows $\mathcal{E}^{ZZ} = \mathcal{E}^{ZN}$ or $\mathcal{E}^{ZZ} = \mathcal{E}^{NZ}$ is the same set that gives $ZZ = ZN$ or $ZZ = NZ$ respectively. That is, the non-zero components become zero at the respective parameter set. Thus, the orbit will reduce to a homoclinic orbit in these cases. A similar argument can be made for the NN and the ZN or NZ uniform states, where one of the non-zero

components become zero and the orbit reduces to a homoclinic orbit from ZN or NZ. Therefore, the only two heteroclinic orbits that are permitted, according to Eq. (5.31), are the orbits which connect the ZZ to NN and ZN to NZ. This result is no coincidence. We deduced in the previous sections precisely what combination of uniform states may be SHATS simultaneously, and these two combinations were the only two which were permitted.

Due to the large number of conditions permitting the uniform state NN to be SHATS, along with ZZ, we focus purely on the heteroclinic orbits connecting ZN and NZ. These fronts will also be useful in later chapters when imposing numerical continuation to find soliton solutions and are available in a large number of CNLS systems. To our knowledge, there is very limited literature on front solutions connecting ZZ and NN, especially in relation to the stability, which is why front solutions in the context of the CNLS (Gross-Pitaevskii), seemingly, always refer to ZN-NZ fronts. Therefore, to be consistent with current literature, and to make valid comparison to said literature, we deem travelling front solutions as the connection between ZN and NZ only. Numerically, we have found few simultaneous ZZ and NN SHATS states, and the further restrictions imposed by Eq. (5.31) dwindles the allowed parameters down further. We note that we are yet to find a stable ZZ to NN connection, but one can not rule out the existence of such structures on this basis. See Appendix A for a brief analysis of the heteroclinic connection between these two uniform states.

5.2.1 Travelling front condition

The existence of a heteroclinic orbit, in a particular CNLS system, depends on if there is a set of values in the travelling wave parameter space $(C_g, \omega_A, \omega_B)$ that provides a solution to $\mathcal{E}^{ZN} = \mathcal{E}^{NZ}$. If one substitutes the relevant equilibria into Eq. (5.31) and equates the two, then we can write this equality as a quartic equation in C_g with a fixed choice of $\omega_{A,B} \in \mathbb{R}$, given by

$$(d_1^2 g_1 g_2 - d_2^2 g_3 g_4) C_g^4 + 8 d_1 d_2 (d_2 g_3 g_4 \omega_A - d_1 g_1 g_2 \omega_B) C_g^2 + 16 d_1^2 d_2^2 (g_1 g_2 \omega_B^2 - g_3 g_4 \omega_A^2) = 0. \tag{5.32}$$

A physical solution is deemed possible when there exists a root to this equation such that the group velocity is defined in real space $C_g^2 \in \mathbb{R}$ and $C_g^2 \geq 0$. The

roots of the equation (5.32) are given explicitly by

$$C_{g\pm}^2 = \frac{4d_1d_2}{(g_1g_2d_1^2 - g_3g_4d_2^2)}\Big[\omega_B(d_1g_1g_2 \mp d_2\sqrt{g_1g_2g_3g_4}) + \omega_A(\pm d_1\sqrt{g_1g_2g_3g_4} - d_2g_3g_4)\Big]. \tag{5.33}$$

We note that the system parameters d_{1-2} and g_{1-4} are assumed to be always known and thus we have a simple relationship between the travelling wave parameter space of the form $C_{g\pm}^2 = \omega_B N_{1\mp} + \omega_A N_{2\pm}$. Firstly, we observe that the denominator of Eq. (5.33) is zero for the symmetrically coupled CNLS ($d_1 = d_2$, $g_1 = g_3$, $g_2 = g_4$), which is due to the vanishing C_g^4 term of Eq. (5.32). In fact, the condition for fronts in this type of system reduces to initially imposing $\omega_A = \omega_B$, for which the condition is satisfied for all C_g, or by imposing $C_g^2 = 2d_1(\omega_A + \omega_B)$. If one considers the relationship $C_g^2 = 2d_1(\omega_A + \omega_B)$, then the physicality of the equilibria (5.12-5.13) is broken as $|\phi_{ZN}|^2 = -|\psi_{NZ}|^2$, which always gives one nonphysical uniform state. Therefore, one is limited to imposing $\omega_A = \omega_B$ in this particular case and, since this is satisfied for all C_g, an abundance of fronts can be found in symmetrically-coupled CNLS-type systems. This is reflected in the literature where travelling fronts have been considered under this frequency equivalence [101, 193, 63].

We will remain in the most generalised regime of Eqs. (5.9-5.10), in which the condition (5.33) imposes $g_1g_2g_3g_4 > 0$ and, as mentioned previously, we require SHATS of the uniform states. At a minimum, the SHATS conditions impose restrictions on the system parameters of $g_1g_2 > 0$, $g_3g_4 > 0$, sgn$(d_1) \neq$ sgn(g_1), and sgn$(d_2) \neq$ sgn(g_3), which automatically satisfies the front condition $g_1g_2g_3g_4 > 0$. Recent effort has been made to analyse travelling fronts (synonym domain wall) under parameter regimes similar to this. The recent work of Alama et al [16] considers this setup of the parameters, only with the extra assumptions of $d_1 = d_2$, $g_2 = g_4$, and $g_2^2 - g_1g_3 > 0$. The last condition, in the context of Bose-Einstein condensates, is known as the immiscibility condition [112, 183] and describes the mixing of the two components. The conditions that we have developed generalises the work presented in [16, 183] beyond the case of equal masses $d_1 = d_2$. We note that the immiscibility condition is also present in our case in the form of $g_2g_4 - g_1g_3 > 0$. The only way in which ZN and NZ can be simultaneously SH when $g_2g_4 - g_1g_3 < 0$ is in the case of negative mass $d_1d_2 < 0$, which is outside the framework of [16], but this situation can be rescaled via conjugation of the equation with the positive dispersion coefficient, to be within the framework presented in the paper.

We will briefly note an important scaling of the CNLS system, which may be

achieved in a similar manner to the substitutions made for the NLS in Eq. (1.2) only with an extra transformation for the new component. By imposing the transformations, one can reduce the 6 free system parameters of $d_{1,2}$ and g_{1-4} down to 3 free parameters representing the dispersive and nonlinear coefficients. Therefore, the most general regime of the CNLS may be represented by 3 free parameters which adds an extra degree of freedom, due to unequal masses, in contrast to the 2 free parameters of [16]. Note that the symmetrically-coupled CNLS system can be represented by 1 free parameter, and the scalar NLS equation by 0 free parameters, as shown in Eq. (1.3).

The expression for the group velocity (5.33) guarantees that only one group velocity is physically viable and an analysis of this can be formulated fully. First, let us rewrite the equilibria (5.12-5.13) with the substitution of $C_{g\pm}^2$,

$$|\phi_+|^2 = \frac{(d_2\omega_B - d_1\omega_A)(d_1 g_1 g_2 - d_2\sqrt{g_1 g_2 g_3 g_4})}{g_1(d_1^2 g_1 g_2 - d_2^2 g_3 g_4)} \tag{5.34}$$

$$|\psi_+|^2 = \frac{(d_2\omega_B - d_1\omega_A)(d_2 g_3 g_4 - d_1\sqrt{g_1 g_2 g_3 g_4})}{g_3(d_1^2 g_1 g_2 - d_2^2 g_3 g_4)} \tag{5.35}$$

$$|\phi_-|^2 = \frac{(d_2\omega_B - d_1\omega_A)(d_1 g_1 g_2 + d_2\sqrt{g_1 g_2 g_3 g_4})}{g_1(d_1^2 g_1 g_2 - d_2^2 g_3 g_4)} \tag{5.36}$$

$$|\psi_-|^2 = \frac{(d_2\omega_B - d_1\omega_A)(d_2 g_3 g_4 + d_1\sqrt{g_1 g_2 g_3 g_4})}{g_3(d_1^2 g_1 g_2 - d_2^2 g_3 g_4)} \tag{5.37}$$

where the index $\pm$ relates to the corresponding $C_{g\pm}^2$. Note that all of the equilibria (5.34-5.37) have a common factor of $(d_2\omega_B - d_1\omega_A)/(d_1^2 g_1 g_2 - d_2^2 g_3 g_4)$ so the relative sign of the numerator and the denominator affects all of the equilibria simultaneously. Recall that for the equilibria to be physical, the value of C_g must give positive (5.12-5.13). Therefore, one may analyse the signs of the remaining terms of Eqs. (5.34-5.37) in order to recover the signs of the equilibria.

Let us compute the total product of all the quantities, i.e. $|\phi_+|^2|\psi_+|^2|\phi_-|^2|\psi_-|^2$. By recognising that $(d_2\omega_B - d_1\omega_A)^4/g_1^2 g_3^2 > 0$ for any set of parameters, then the remaining sign is governed only by the system parameters through the relation $-g_1 g_2 g_3 g_4$ which, since the condition for $C_g \in \mathbb{R}$ is sgn$(g_1 g_2 g_3 g_4) = 1$, is always negative. This means that either one or three of Eqs. (5.34-5.37) are negative for any parameter choice. If one of the equilibria is negative then we may say that one of $C_{g\pm}^2$ yields a physical solution, whereas if three are negative then both are nonphysical solutions.

The next step is to consider which of the equilibria have the same sign so that we can efficiently decide which of the two group velocities yields a physical solution. In order to determine the condition for physicality, let us look at the

individual products of the equilibria. If one computes $|\phi_+|^2|\psi_+|^2$ and $|\phi_-|^2|\psi_-|^2$ then we get the following expressions that determine the respective signs of the products,

$$\text{sgn}(|\phi_+|^2|\psi_+|^2) = \text{sgn}(V_1 - V_2),$$
$$\text{sgn}(|\phi_-|^2|\psi_-|^2) = \text{sgn}(V_1 + V_2),$$

where

$$V_1 = 2d_1g_2d_2g_4,\ V_2 = (\frac{d_1^2g_2}{g_3} + \frac{d_2^2g_4}{g_1})\sqrt{g_1g_2g_3g_4}.$$

Note that we may show $|V_2| > |V_1|$, regardless of parameter choice, by considering the assumption $V_2^2 > V_1^2$. When one computes this inequality, we arrive at the following condition $g_1g_2g_3g_4(d_1^2g_1g_2 - d_2^2g_3g_4)^2 > 0$ which is true for any set of system parameters. Following from this, it is easy to see from the formulation of V_2 that the decisive condition is $d_1^2g_2/g_3 + d_2^2g_4/g_1 > (<)\ 0$. If $V_2 < 0$ then $|\phi_+|^2$ and $|\psi_+|^2$ have the same sign and $|\phi_-|^2$ and $|\psi_-|^2$ have opposite signs. If $V_2 > 0$ then the opposite can be said.

The above condition only tells us which of the $C_{g\pm}^2$ can yield a physical solution, not whether there are one or three negative equilibria. We may determine a condition for the physicality of $C_{g\pm}^2$ by taking a closer look at the equilibria themselves. Let us first rewrite the equilibria (5.34-5.37) in the following way; $|\phi_+|^2 = r_{11}(d_2\omega_B - d_1\omega_A)$, $|\psi_+|^2 = r_{12}(d_2\omega_B - d_1\omega_A)$, $|\phi_-|^2 = r_{21}(d_2\omega_B - d_1\omega_A)$, and $|\psi_-|^2 = r_{22}(d_2\omega_B - d_1\omega_A)$. We will divide the formulation into four distinct cases for ease of analysis.

Cases 1(i) and 1(ii):

Assume that $V_2 > 0$, which means sgn$(|\phi_-|^2) =$ sgn$(|\psi_-|^2)$ and sgn$(|\phi_+|^2) \neq$ sgn$(|\psi_+|^2)$. This subsequently means that C_{g+}^2 may never yield physical equilibria whilst C_{g-}^2 can, depending on the signs of the travelling wave parameters. Since sgn$(r_{21}) =$ sgn(r_{22}), the two subcases of physical group velocity depend on the relative sign of either quantity and the remainder of the term. Thus, the physical conditions are

1(i): If $r_{21} > 0$, then $(d_2\omega_B - d_1\omega_A) > 0$;

1(ii): If $r_{21} < 0$, then $(d_2\omega_B - d_1\omega_A) < 0$.

Cases 2(i) and 2(ii):

Assume that $V_2 < 0$, which means sgn($|\phi_-|^2$) $\neq$ sgn($|\psi_-|^2$) and sgn($|\phi_+|^2$) = sgn($|\psi_+|^2$). We know from the prior definitions that sgn(r_{11}) = sgn(r_{12}), therefore if one computes the sign of either r_{11} or r_{12}, we arrive at the following subcases for physical equilibria,

2(i): If $r_{11} > 0$, then $(d_2\omega_B - d_1\omega_A) > 0$;

2(ii): If $r_{11} < 0$, then $(d_2\omega_B - d_1\omega_A) < 0$.

We see that travelling wave parameters need to be carefully chosen in order to preserve physicality of the equilibria. To summarise, at least one value of $C^2_{g\pm}$ will always give nonphysical equilibria. One may check, however, the above criteria in order to guarantee that one physical solution applies. This guarantees a physically viable travelling front, with the added conditions of SHATS for ZN and NZ already discussed, that will allow for the formation and propagation of the front.

5.2.2 Front structure

There are a couple of numerical methods one may use to find the particular structure of the nonlinear connection between the plane-waves. One way is to use numerical continuation software such as AUTO; see Sec. 2.2.3. A simpler method, which allows us to remain in MATLAB software, is to search for the profile by building a dissipative analogue of the CNLS. We adopt this method and construct a dissipative PDE that reduces down to the same ODE as the CNLS, given by Eqs. (5.9-5.10). This is done by adding $i\kappa_A\phi_t$, $i\kappa_B\psi_t$ to their respective component, where κ_A, κ_B are arbitrary, complex coefficients. The dissipative PDE is then given by

$$i\kappa_A\phi_t + d_1\phi_{\zeta\zeta} + (\omega_A - d_1k_A^2)\phi + g_1|\phi|^2\phi + g_2|\psi|^2\phi = 0, \tag{5.38}$$

$$i\kappa_B\psi_t + d_2\psi_{\zeta\zeta} + (\omega_B - d_2k_B^2)\psi + g_3|\psi|^2\psi + g_4|\phi|^2\psi = 0. \tag{5.39}$$

The conditions for dissipation are Im(κ_A)$d_1 > 0$ and Im(κ_B)$d_2 > 0$, so we will restrict the choice to κ_A = sgn(d_1)i and κ_B = sgn(d_2)i, where Eqs. (5.38-5.39) become a nonlinear extension of the heat equation. The mass and energy of such a system are no longer conserved and the nature of the dynamically open system allows us to evolve and locate the front solution as a steady state of the dissipative PDE. One evolves Eqs. (5.38-5.39) with the following initial

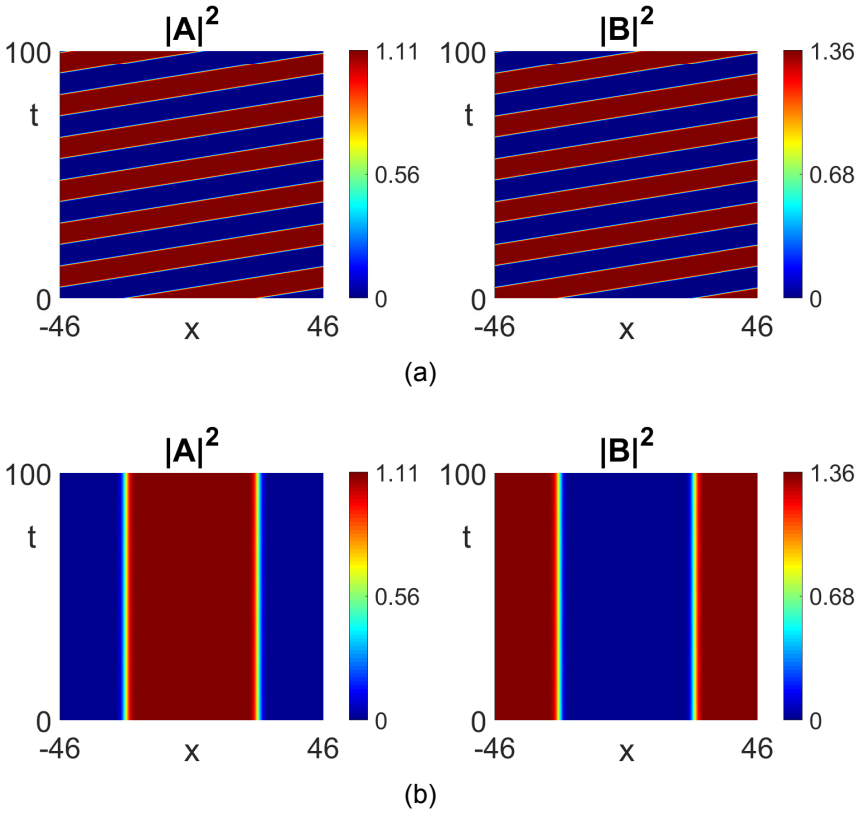

Figure 5.5: Travelling front solution obtained for the nearly-integrable CNLS equation with system parameters $d_1 = d_2 = -1$, $g_1 = g_2 = g_3 = 2$, $g_4 = 3$, and travelling wave parameters $(C_g, \omega_A, \omega_B) = (5.395, -9.5 - 10)$. Travelling wave parameters satisfy the heteroclinic relationship (5.33) and the evolution of both components A and B are shown in the (a) regular reference frame and (b) co-moving reference frame.

conditions

$$\phi = \frac{\phi_0}{1 + e^{\zeta - \zeta_0}} - \frac{\phi_0}{1 + e^{\zeta + \zeta_0}},$$

$$\psi = \frac{\psi_0}{1 + e^{\zeta + \zeta_0}} + \frac{\psi_0 e^{\zeta - \zeta_0}}{1 + e^{\zeta - \zeta_0}},$$

where ζ_0 is the front location and $\phi_0,\ \psi_0 > 0$ are given by the non-zero component of the ZN and NZ states respectively. After a long time period, say $t > 500$, the steady state will be found and we can then use this steady state as the initial condition for solving the CNLS system (4.7-4.8). The choice of $\kappa_A = \text{sgn}(d_1)i$ and $\kappa_B = \text{sgn}(d_2)i$ guarantees that the temporal eigenvalues are stable, providing that the ZN and NZ states are SHATS in CNLS.

We then have all of the information needed to construct these fronts in the most general form of the CNLS. Let us first showcase these fronts in the 'nearly-integrable' system that we previously considered in Fig. 5.1. This system will be the prototypical example that we will use throughout, unless specified otherwise, but we note that the analysis is no different from other CNLS system

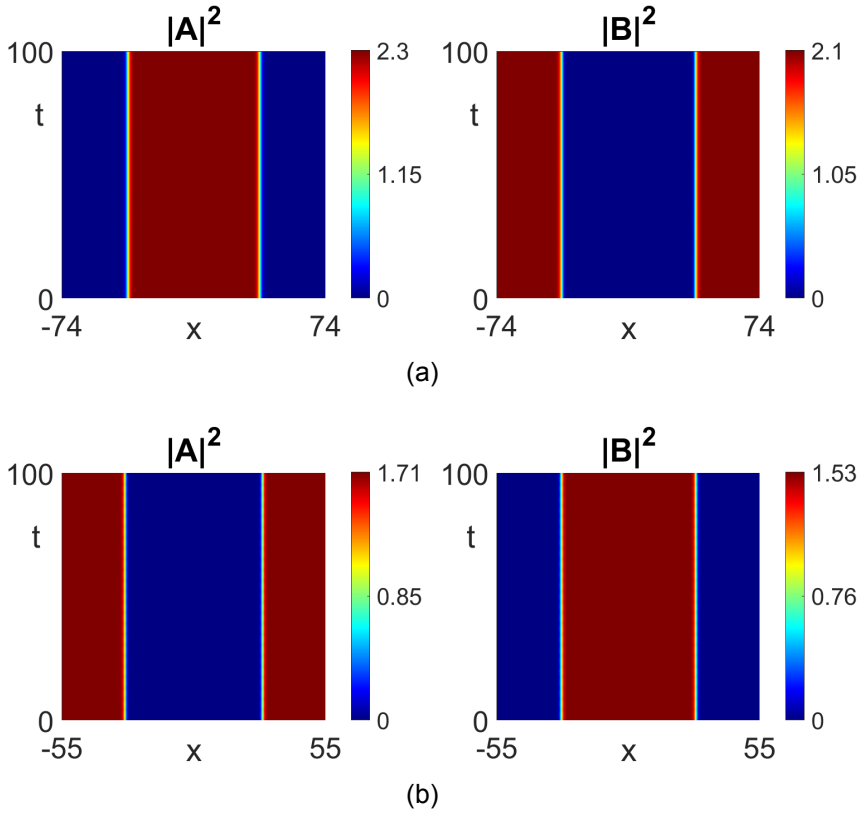

Figure 5.6: Travelling front solution obtained for CNLS systems with unequal masses. (a) $d_1 = -4$, $d_2 = -2$, $g_1 = 2$, $g_2 = 3$, $g_3 = 4$, $g_4 = 5$, and travelling wave parameters $(C_g, \omega_A, \omega_B) = (3.368, -5.3, -9.8)$. (b) $d_1 = -1$, $d_2 = -3$, $g_1 = 2$, $g_2 = 4$, $g_3 = 5$, $g_4 = 8$, and travelling wave parameters $(C_g, \omega_A, \omega_B) = (5.093, -9.9, -9.8)$. The front propagating in (b) is shifted along the X-axis.

parameter choices. By definition, a large proportion of the conditions for SHATS are already satisfied for the ZN and NZ simultaneously due to the system parameter choice. When one numerically explores the relationship (5.33) we find a plethora of solutions, providing that the travelling wave parameters also allow physical equillibria, physical C_g, and ensures the remaining SHATS conditions.

One particular example of a stable travelling front in this system arises when one considers the frequencies $\omega_A = -9.5$ and $\omega_B = -10$, which leads to a group velocity of $C_g = \pm 5.395$, as obtained from Eq. (5.33). This point in the parameter space provides a front that connects the equilibria $(\phi_0, \psi_0) = (1.055, 0)$ and $(\phi_0, \psi_0) = (0, 1.167)$, where both uniform states are SHATS. Figure 5.5(a) shows the propagation of this travelling front in the CNLS, and Fig. 5.5(b) shows the evolution where we have shifted into the reference frame co-moving with positive C_g. Note that there is an equivalent front that propagates with the reversed sign of the velocity. We will represent future fronts in the co-moving frame unless stated otherwise.

As mentioned previously, our analysis is not limited to the case of equivalent masses $d_1 = d_2$. To show this, we can consider CNLS systems where we

impose $|d_1| > \ (<) \ |d_2|$. Let us consider the former, where we explore the CNLS with system parameters $d_1 = -4$, $d_2 = -2$, $g_1 = 2$, $g_2 = 3$, $g_3 = 4$, $g_4 = 5$. Figure 5.6(a) shows an example of a front solution found with the chosen frequencies $\omega_A = -5.3$ and $\omega_B = -9.8$, which leads to a group velocity of $C_g = \pm 3.368$. We may consider the case of $|d_2| > |d_1|$ by imposing the CNLS system parameters $d_1 = -1$, $d_2 = -3$, $g_1 = 2$, $g_2 = 4$, $g_3 = 5$, $g_4 = 8$. By choosing the component frequencies as $\omega_A = -9.9$ and $\omega_B = -9.8$, the heteroclinic condition (5.33) imposes the group velocity $C_g = \pm 5.093$. Figure 5.6(b) shows the evolution of this front, where we have shifted the structure in X to clarify that the profile can be implemented with $(0, \psi_0)$ or $(\phi_0, 0)$ at $X = 0$. A generic width for the structure can also be imposed providing that the front location ζ is far away from the centre $\zeta = 0$ and there is a sufficient decay to the uniform state for $\zeta \longrightarrow \pm\infty$. The above CNLS systems show that we may find travelling fronts for unequal masses, but we note that in both of the systems we also considered vastly different nonlinear coefficients. In both systems we considered $|g_3 g_4| > |g_1 g_2|$, which shows that one can implement larger nonlinear terms for either component regardless of which dispersion term possesses the larger magnitude.

5.2.3 Stochastic pinning via wave turbulence

One may question whether the heteroclinic condition (5.33) is truly required to form the fronts in the CNLS, under the assumption $C_g = 2d_1 k_A = 2d_2 k_B$. To explore this, let us consider the front found in the nearly integrable system, shown in Fig. 5.5, and break the travelling front condition. We do this by allowing ω_A to vary by an incremental amount, ± 0.5, whilst fixing all other parameters. We produce the original front from the dissipative PDE as before, but the front amplitude in A is instead rescaled to the new amplitude, governed by the new value of ω_A. Doing so will keep the B-component the same, and the A-component will have the same front structure but a different amplitude. Figures 5.7(a) and 5.7(b) show what happens to the front when we decrease and increase the parameter ω_A respectively. In the early stages of the evolution we see two 'tilted' fronts, located to the left and right of the original front, propagating with a new amplitude that corresponds to a new point $(C_g, \omega_A, \omega_B)$ in the parameter space. These spontaneous tilted fronts also satisfy the heteroclinic condition (5.33); the left and right tilted fronts of Fig. 5.7(a) correspond to the parameter sets $(C_g, \omega_A, \omega_B) = (5.159, -9.110, -9.654)$ and $(C_g, \omega_A, \omega_B) = (5.630, -10.380, -10.924)$ respectively, whilst the left and right tilted fronts of Fig. 5.7(b) correspond to the parameter sets $(C_g, \omega_A, \omega_B) = (5.661, -9.986, -10.430)$

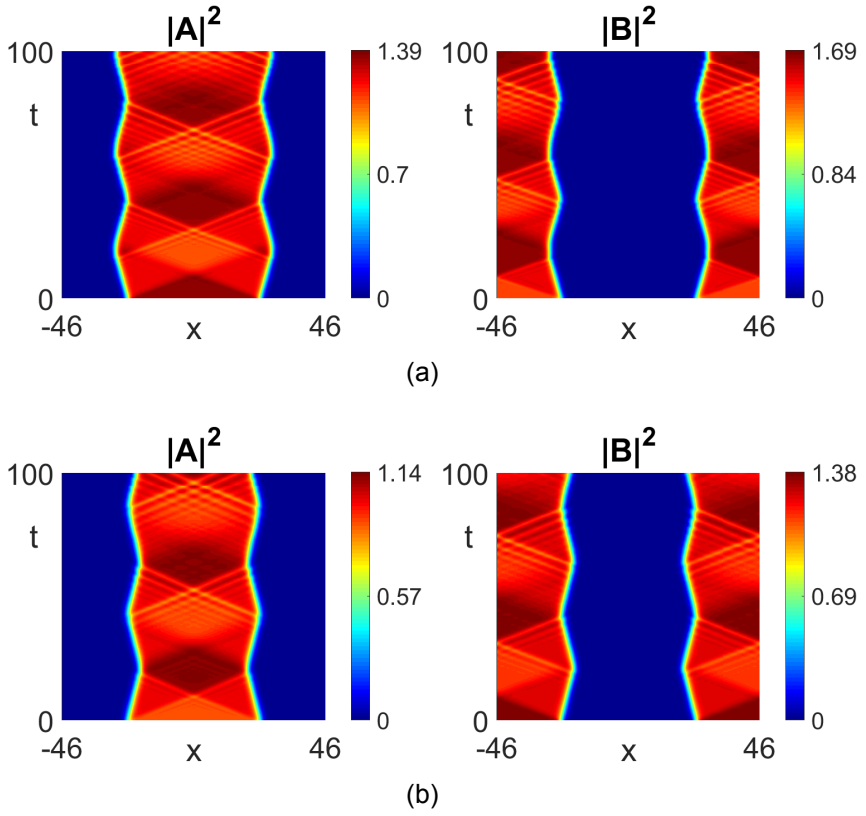

Figure 5.7: Propagation of the travelling front from Fig. 5.5 with shifted parameter $\omega_A = \omega_A \pm 0.5$. The new equilibria are defined by the points in the parameter space (a) $(C_g, \omega_A, \omega_B) = (5.395, -10, -10)$; (b) $(C_g, \omega_A, \omega_B) = (5.395, -9, -10)$. The plots are in the frame comoving with C_g.

and $(C_g, \omega_A, \omega_B) = (5.130, -8.559, -9.003)$ respectively. This is another reason why we mainly consider travelling fronts of the reduced parameter space $(C_g, \omega_A, \omega_B)$, since fronts that are formed via evolution often obey this reduction. There is also a clear fluctuation in the width of the structure caused by the tilted fronts propagating into the other component and forming a zero net polarity of the background. Finally, since the plane-waves connected by the tilted fronts do not match those in the initial condition, dispersive shock waves (DSWs) form, causing wave turbulence amongst the structure, and the velocity of these propagating DSWs should follow the universal description of DSWs [67, 53]. When one considers tracking the width of the total structure throughout a long-time evolution ($t = 1000$), we see unique behaviour of the interaction between the fronts and the wave turbulence. More specifically, for certain parameters away from the original front, the fluctuating width gathers itself such that there is some order from the turbulent interaction. Figure 5.8 shows a plot of the front width against time for each of the 3 fronts seen in Fig. 5.5 and Fig. 5.7. We note that, for the front with decreased parameter $\omega_A = -10$, there is a regathering of the front width fluctuation some time after $t \approx 500$; the $\omega_A = -9$

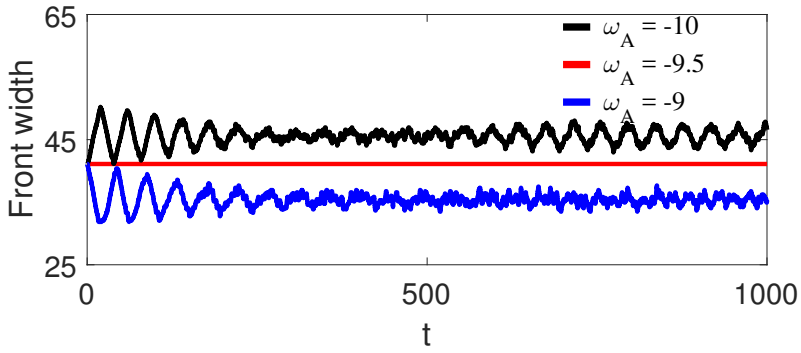

Figure 5.8: Plot of the front width vs time for the travelling fronts seen in Fig. 5.7 and the original travelling front in Fig. 5.5.

case does not see this width formation, showing a certain asymmetry of the regathering. This regathering of the front width to form a periodic fluctuation should be well described by a stochastic model such as [64], with an incorporation of dispersive shock wave dynamics, and hydrodynamic variables using the Madelung transform [144, 53]. Since we are purely interested in solutions of the CNLS, so that we may translate back to the original MTI problem, this observation will be explored in future work. The purpose of the above exercise was to demonstrate the importance of the heteroclinic condition (5.33) when initialising front solutions to the CNLS. One can not naively form a travelling front for an arbitrary choice of travelling wave parameters $(C_g, \omega_A, \omega_B)$.

5.2.4 Breaking the wavenumber-velocity relationship

We will briefly mention the extension of the fronts into the regime where the wavenumbers $k_{A,B}$ are no longer governed by the choice of C_g. If we break the original assumption of $C_g = 2d_1k_A = 2d_2k_B$ then we must look for heteroclinic orbits that connect the ZN and NZ equilibria in the full ODE system (5.3–5.4). Formally, we wish to address whether a front may be arbitrarily formed between two plane-waves governed by the parameters (k_A, ω_A) and (k_B, ω_B). To analyse this, we shift in a wavenumber, say k_A, to distinguish whether or not the CNLS will evolve the front connecting these two plane-waves. The process is similar to that of the previous section, only now we must take the initial front profile and rescale the amplitude to the new amplitude, as well as multiply by the shifted plane-wave wavenumber opposed to the original wavenumber $C_g/2d_1$.

As a baseline, let us once again consider the front from Fig. 5.5 and shift away from this solution by considering the parameters $C_g = 2d_2k_B = 5.395$, $(\omega_A, \omega_B) = (-9.5, -10)$, and $k_A = C_g/2d_1 \pm 0.1$. The evolution for these two sets of parameters are shown explicitly in Fig. 5.9. Note that the general be-

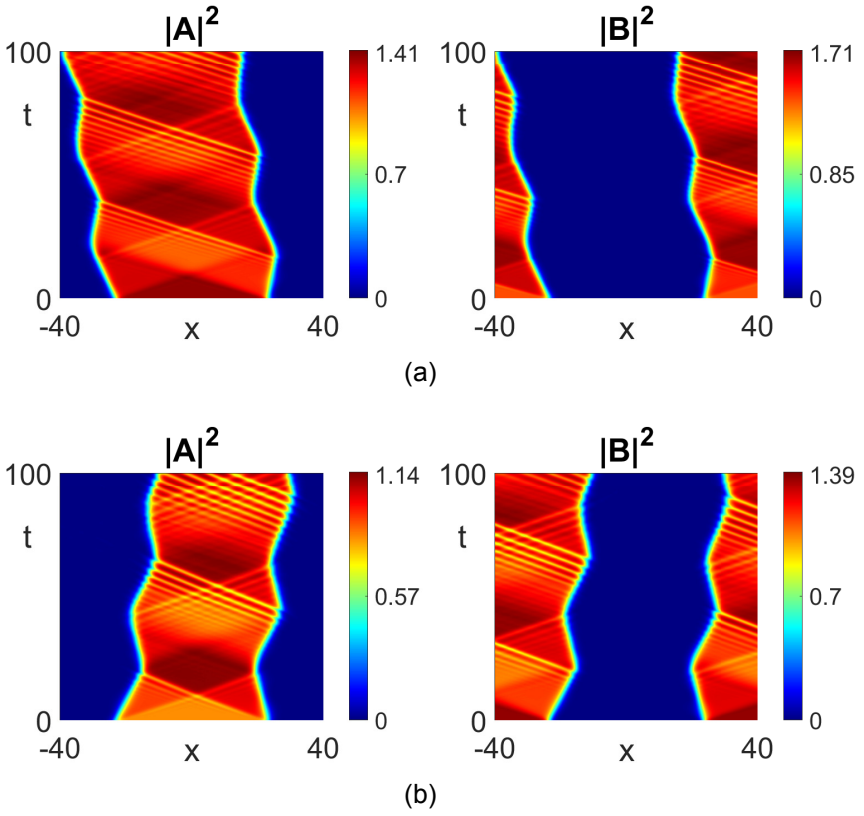

Figure 5.9: Propagation of the travelling front from Fig. 5.5 with shifted parameter $k_A = k_A \pm 0.1$, plotted in the frame co-moving with $C_g = 5.395$. The new initial amplitude for A is defined by the point in the parameter space (a) $(k_A, \omega_A) = (-2.597, -9.5)$; (b) $(k_A, \omega_A) = (-2.797, -9.5)$, where k_A has been shifted from the original wavenumber $k_A = C_g/2d_1 \pm 0.1$.

haviour is similar to that of Sec. 5.2.3, when we shifted in the parameter ω_A. There are, however, two vital differences here to that of the ω_A case. The first is the asymmetric amplitudes of the two tilted fronts that appear to the left and right of the original front. The second difference is the obvious drifting of the entire profile in the co-moving frame. In this instance, since the CNLS system is nearly-integrable, the full profile now moves with velocity $C_g = d_1(k_A + k_B)$, but this does not hold true away from the nearly-integrable regime. Both differences can be owed to the forced breaking of the wavenumber-velocity relationship of the initial condition. The key property of the tilted fronts is that they are, once again, governed by the heteroclinic condition (5.33) and they satisfy the original assumption $C_g = 2d_1k_A = 2d_2k_B$, despite the initialised front imposing $C_g \neq 2d_1k_A$. The left and right tilted fronts of Fig. 5.9(a) correspond to the parameter sets $(C_g, \omega_A, \omega_B) \approx (5.043, -8.930, -9.508)$ and $(C_g, \omega_A, \omega_B) \approx (5.542, -10.042, -10.572)$ respectively, whilst the left and right tilted fronts of Fig. 5.9(b) correspond to the parameter sets $(C_g, \omega_A, \omega_B) \approx (5.795, -10.253, -10.670)$ and $(C_g, \omega_A, \omega_B) \approx (5.205, -8.824, -9.285)$ respectively.

We note that directly searching for fronts in Eqs. (5.3–5.4) using the method

of the dissipative evolution, or numerical continuation software, produced no front structures when the velocity-wavenumber relationship was explicitly broken. The only way that we could impose a front solution without this governing relationship was by taking a profile governed by the relationship and then shifting in the parameter like we have done in Fig. 5.9. Due to this, we do not expect front solutions of Eqs. (5.3–5.4) unless the coefficient of the first derivative vanishes because of the initial assumption. This is also evident due to the fact that the spontaneously-formed tilted fronts also obey the heteroclinic condition (5.33), despite the initial condition breaking the relationship $C_g = 2d_1k_A = 2d_2k_B$. The above numerical analysis details the importance of the initial assumption between the group velocity and component plane-wave wavenumbers when searching for the front solutions.

5.3 Front-grey soliton interaction

We have shown that, when one shifts away from the parameters that satisfy Eq. (5.33), there is an expected formation of DSWs and the interaction of the fronts with these DSWs, leads to a natural questioning to the behaviour of soliton-front collisions. We are interested in said collisions since there is a possibility of other soliton-like structures propagating away from the collision. The collision behaviour will be explored by initially imposing a grey soliton in the A component of the front seen in the regime of Fig. 5.5, and evolving the CNLS as before. We have already shown the form of the grey soliton solution previously in Eq. (1.12) and Eq. (3.14), however, the profile is now adapted to be efficiently embedded in the background field, and is given by

$$G(x;\Phi_G,W_0) = W_0\left[\cos\Phi_G + i\sin\Phi_G\tanh\left(W_0\sin\Phi_G x\right)\right].$$

$\Phi_G \in [0,\pi/2]$ is the grey soliton parameter defining the depression/group velocity of the soliton and W_0 is defined by ϕ_0 or ψ_0 equilibria, depending on which component the grey soliton is in. In this particular system, the interaction produces 3 types of behaviour: singular refraction, double refraction and reflection. All 3 cases are seen in Fig. 5.10 on a sufficiently larger domain ($\times 4$) to previous.

Firstly, we note that the unidirectional shift of the fronts is related to the polarity of the background and there is also a small amount of radiation upon collision, that we deem negligible in comparison to the nonlinear structures, in this nearly-integrable CNLS system. The differing behaviour can be partially explained by considering conserved quantities of the CNLS (4.7-4.8). The major difference of this equation, in comparison to the Manakov systems or the

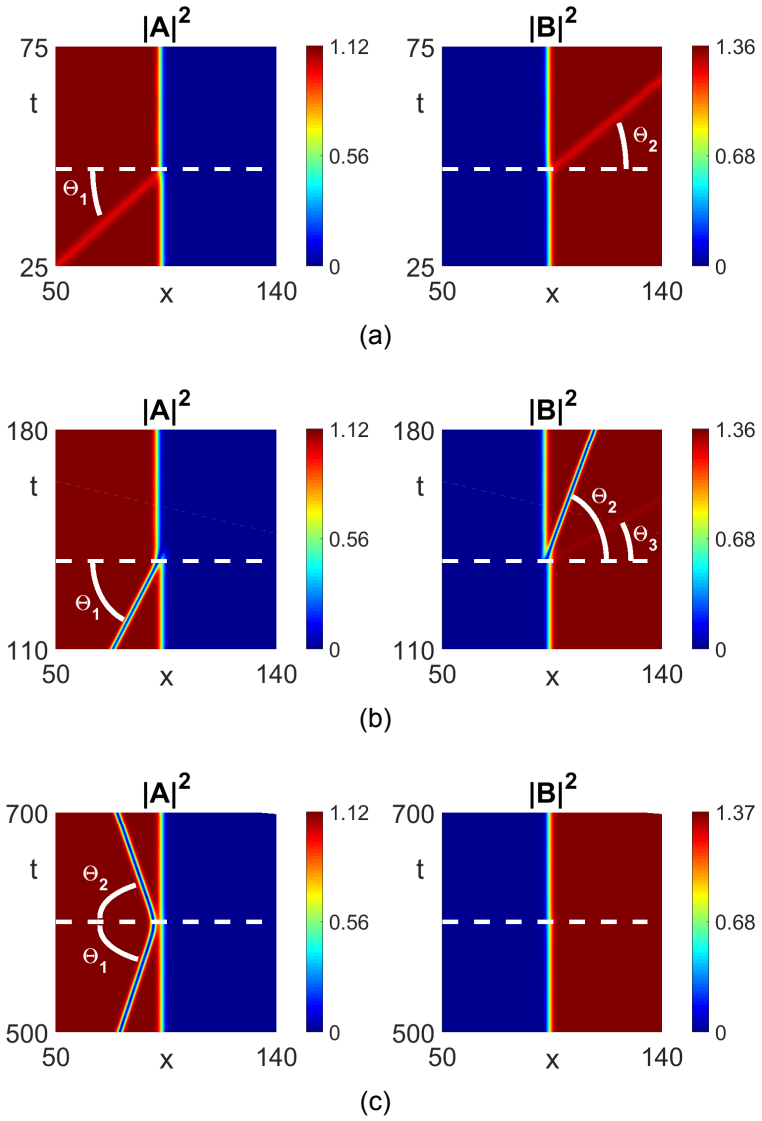

Figure 5.10: Front-grey soliton collisions. Different collision behaviour is shown for the front with system and travelling wave parameters seen in Fig. 5.5, with initialised grey soliton parameter (a) $\Phi_G = \pi/10$, (b) $\Phi_G = 1.25$, (c) $\Phi_G = 1.5$. Reflection/refraction angles are given in radians as (a) $(\Theta_1, \Theta_2) = (0.463, 0.426)$, (b) $(\Theta_1, \Theta_2, \Theta_3) = (0.984, 1.082, 0.405)$, (c) $(\Theta_1, \Theta_2) = (1.407, 1.423)$.

scalar NLS, is the non-integrable nature of the problem.

Integrable systems generally posses many conserved quantities that can be utilised to tell us more about the evolution of an initial condition; since our CNLS is non-integrable we do not have a large number of conserved quantities. The system does, however, conserve some quantities such as the component masses

$$\mathcal{H}_A = \int |A|^2 \mathrm{dx}, \tag{5.40}$$

$$\mathcal{H}_B = \int |B|^2 \mathrm{dx}, \tag{5.41}$$

as well as the energy

$$\mathcal{H} = \int |A|^2|B|^2 \mathsf{dx} - \frac{1}{g_2}\int d_1|A_X|^2 - \frac{g_1}{2}|A|^4 \mathsf{dx} - \frac{1}{g_4}\int d_2|B_X|^2 - \frac{g_3}{2}|B|^4 \mathsf{dx}, \quad (5.42)$$

which are extensions to those quantities obtained geometrically for the NLS equation [91]. By considering $\mathcal{H}_A^b = \mathcal{H}_A^a$, $\mathcal{H}_B^b = \mathcal{H}_B^a$, and $\mathcal{H}^b = \mathcal{H}^a$ where the superscripts refer to before (b) and after (a) the collision, one may suggest that a solution to all three equations must exist for the soliton to propagate through the front. The existence of these three quantities should be enough to predict the two grey soliton parameters after the collision, given the grey soliton parameter before collision.

5.3.1 Conservation equations

Assuming that the nonlinear structures are well separated before and after collision, we will use the following two qualitative properties from the evolution to formulate the equations:

1. The shape of the front, $A_f(x)$ and $B_f(x)$, is not altered upon collision, other than through some positional shift x_{shift}, and the functions A_f and B_f asymptotically approach the relevant plane-wave as $x \to \pm\infty$.
2. The most complex case of collision behaviour is the double refraction and thus we will assume that the grey soliton, defined by $G^{(1)}(x;\Phi_G^{(1)},\phi_0)$, splits into two grey solitons, defined by $G^{(2)}(x;\Phi_G^{(2)},\psi_0)$ and $G^{(3)}(x;\Phi_G^{(3)},\psi_0)$ respectively.

Providing that the front and the solitons are well separated, one can always write A and B as piece-wise functions of x, given as

$$A^{(b)} = \begin{cases} G^{(1)}e^{ik_A x} & L_- < x < x_-^{(b)}, \\ A_f e^{ik_A x} & x_-^{(b)} < x < x_+^{(b)}, \\ 0 & x_+^{(b)} < x < L_+, \end{cases}$$

and

$$B^{(b)} = \begin{cases} 0 & L_- < x < x_-^{(b)}, \\ B_f e^{ik_B x} & x_-^{(b)} < x < x_+^{(b)}, \\ \psi_0 e^{ik_B x} & x_+^{(b)} < x < L_+, \end{cases}$$

before the collision has taken place. The limits of $x_\pm^{(b)}$ are arbitrarily large such that the front and solitons decay to the relevant background field, and so the

structures are well separated. The boundary limits $L_\pm$ are set by an arbitrarily large domain. After the collision, the ansatz of double refraction provides us with the piece-wise functions,

$$A^{(a)} = \begin{cases} \phi_0 e^{ik_A x} & L_- < x < x_-^{(a)}, \\ A_f e^{ik_A x} & x_-^{(a)} < x < x_+^{(a)}, \\ 0 & x_+^{(a)} < x < L_+, \end{cases}$$

and

$$B^{(a)} = \begin{cases} 0 & L_- < x < x_-^{(a)}, \\ B_f e^{ik_B x} & x_-^{(a)} < x < x_+^{(a)}, \\ G^{(2)} e^{ik_B x} & x_+^{(a)} < x < x_0, \\ G^{(3)} e^{ik_B x} & x_0 < x < L_+, \end{cases}$$

where x_0 is the centre point of the two grey solitons that are well separated. The values of $x_\pm^{(a)}$ are different from $x_\pm^{(b)}$, and indicate the total distance that the front has shifted from the collision. One can substitute these piece-wise functions, and their derivatives, into the equations $\mathcal{H}_A^b = \mathcal{H}_A^a$, $\mathcal{H}_B^b = \mathcal{H}_B^a$, and $\mathcal{H}^b = \mathcal{H}^a$. Using property 1, we know that the front structure is equivalent between the boundaries $x_\pm^{(b)}$ or $x_\pm^{(a)}$, therefore any piece-wise integrals involving this quantity, or its derivative, will cancel in the equation. Since the front is shifted uniformally, we will define $x_+^{(b)} - x_+^{(a)} = x_-^{(b)} - x_-^{(a)} = x_{shift}$. As well as this, since we define the structures as well-separated, we know that $\tanh(x) = \pm 1$ at the upper and lower bounds respectively. Using this information, one can write the conservation equations explicitly to give us a relationship between the four structure parameters $\Phi_G^{(1)}$ (before collision), x_{shift}, $\Phi_G^{(2)}$, and $\Phi_G^{(3)}$ (after collision), given by the following three equations:

$$x_{shift} = \frac{2}{|\phi_0|} \sin \Phi_G^{(1)}, \tag{5.43}$$

$$x_{shift} = \frac{2}{|\psi_0|} \left(\sin \Phi_G^{(2)} + \sin \Phi_G^{(3)} \right), \tag{5.44}$$

$$C_1 x_{shift} = \sum_{i=1}^{3} D_{1i} \sin \Phi_G^{(i)} + D_{2i} \sin 2\Phi_G^{(i)} + D_{3i} \sin 3\Phi_G^{(i)} \tag{5.45}$$

where

$$D_{11} = \frac{3g_1 + 2d_1}{2g_2}|\phi_0|^3 - \frac{2d_1 k_A^2}{g_2}|\phi_0|, \quad D_{21} = \frac{2d_1 k_A}{g_2}|\phi_0|^2, \quad D_{31} = \frac{g_1 - 2d_1}{6g_2}|\phi_0|^3,$$
$$D_{12} = D_{13} = \frac{2d_2 k_B^2}{g_4}|\psi_0| - \frac{2d_2 + 3g_3}{2g_4}|\psi_0|^3, \quad D_{22} = D_{23} = -\frac{2d_2 k_B}{g_4}|\psi_0|^2,$$
$$D_{32} = D_{33} = \frac{2d_2 - g_3}{6g_4}|\psi_0|^3,$$
$$C_1 = \frac{g_1}{2g_2}|\phi_0|^4 + \frac{d_2 k_B^2}{g_4}|\psi_0|^2 - \frac{g_3}{2g_4}|\psi_0|^4 - \frac{d_1 k_A^2}{g_2}|\phi_0|^2.$$

A key property to note here is that for small values of $\Phi_G^{(1)}$, when we get singular refraction like those in Fig. 5.10(a), the grey soliton parameter after collision is well described by a 2-soliton analogue of Snell's law [89], i.e. considering the first two conservation equations (5.43-5.44) with $\Phi_G^{(3)} = 0$. There is also a clear relationship between the angle of reflection/refraction to the normal, which we will denote as Θ, and the soliton parameter that takes the form $\cot\Theta = 2|W_0|\cos(\Phi_G)$, where W_0 is the equilibrium of the component we are in. These conservation equations can be used to infer the type of collision behaviour one will expect for different initial values of the grey soliton parameter Φ_G.

5.3.2 Parameter prediction

Given an initialised grey soliton, with parameter $\Phi_G^{(1)}$, we have three variables governed by the three equations (5.43-5.45). Due to the trigonometric structure of these equations, an analytical solution is difficult to find, however, if one substitutes Eq. (5.43) into Eq. (5.44) and Eq. (5.45), to remove the variable x_{shift}, then we say a solution to these three equations exists when there is a set of $(\Phi_G^{(2)}, \Phi_G^{(3)})$ that numerically solves the two remaining equations simultaneously. The choice of the grey soliton parameter also directly imposes a value for x_{shift}, which increases as $\Phi_G^{(1)} \to \pi/2$. Slower, more depressed solitons will cause a greater shift of the front upon interaction in this particular CNLS system.

When $\Phi_G^{(1)} = \pi/10$, corresponding to Fig. 5.10(a), the evolution produces a singular refraction. This allows us to alter the ansatz and set $\Phi_G^{(3)} = 0$, subsequently considering the Snell's law-type conservation equations (5.43-5.44). These equations predict a value of $\Phi_G^{(2)} = 0.349$ rad and the measured space-time plot gives us a value of $\Phi_2 \approx 0.334$ rad. The shift of the front is also predicted as $x_{shift} = 0.586$, whereas the space-time plot shows a shift of $x_{shift} \approx 0.615$. Thus, there is an agreement of ≈ 95% accuracy for both predictions. As one increases $\Phi_G^{(1)}$ in this system, the behaviour is generally described by the existence of a solution to Eqs. (5.43-5.45). For the double refraction seen in Fig.

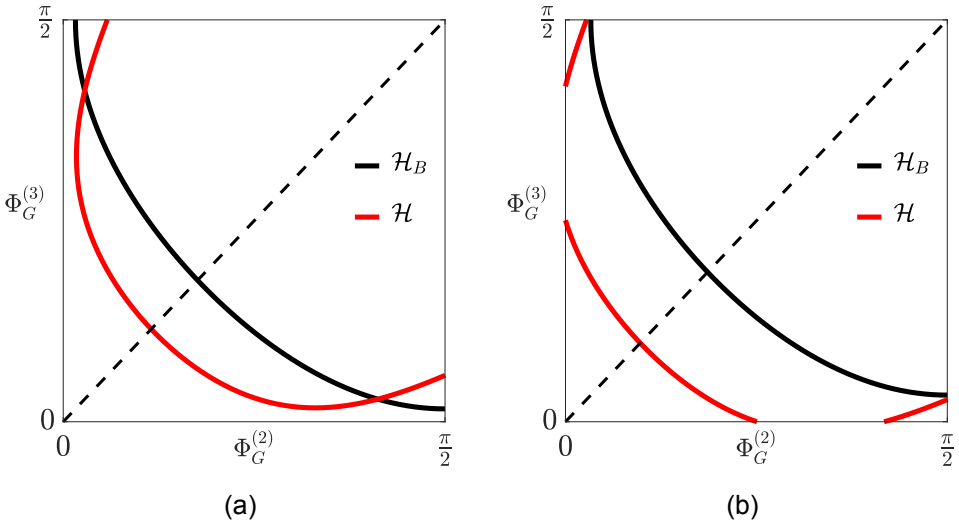

Figure 5.11: Solution plots of Eqs. (5.43-5.45) with (a) $\Phi_G^{(1)} = 1.25$ and (b) $\Phi_G^{(1)} = 1.5$. There is a reflection symmetry about the line $\Phi_G^{(2)} = \Phi_G^{(3)}$ due to interchangeability of the two variables.

5.10(b), we show that there is a solution to the conservation equations; the plot, Fig. 5.11(a), of these equations shows explicitly the overlapping solution. The figure is also symmetric about the line $\Phi_G^{(2)} = \Phi_G^{(3)}$, which is expected since these two variables are interchangeable in the conservation equations. The parameters are predicted from Eqs. (5.43-5.45) as $(\Phi_G^{(2)}, \Phi_G^{(3)}) = (0.088, 1.294)$, with the numerically-observed parameters being $(\Phi_G^{(2)}, \Phi_G^{(3)}) \approx (0.053, 1.341)$. The front shift is also given as $x_{shift} = 1.8$ analytically, and $x_{shift} = 1.899$ numerically. As a two-dimensional measure of accuracy, the Euclidean distance between the analytical and numerical points is $\approx 5\%$ of the magnitude of the numerically-observed point. Thus, along with x_{shift}, there is once again an agreement of $\approx 95\%$ for the parameter prediction. If there is no solution to Eqs. (5.43-5.45) then the general behaviour is that of Fig. 5.10(c), where the grey soliton can not propagate through the front. The corresponding solution plot, shown in Fig. 5.11(b), provides us with no overlap in the $(\Phi_G^{(2)}, \Phi_G^{(3)})$ space. The angle of reflection does not match up numerically with the perfect reflection that is expected from the conservation equations, but all of these discrepancies can be owed to the small radiation upon collision. Generally, as one moves further away from the integrable regime of the CNLS, more radiation is created upon collision and the conservation equations become less accurate in representing the qualitative nature of the collisions.

We note that we assumed there is a transmission of two grey solitons after the collision with the front, whereas in some cases a one transmission-one reflection ansatz may be needed. In contrast, the case of the two-reflection ansatz analytically narrows down to the form of one reflection and has already

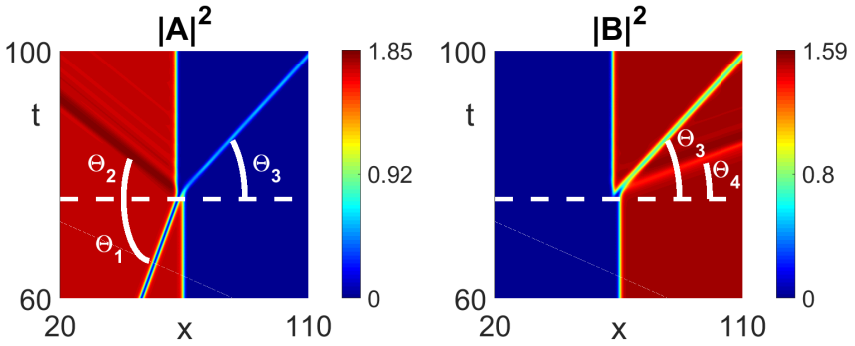

Figure 5.12: Grey-vector soliton refraction in the CNLS with system parameters $d_1 = -1,\ d_2 = -3,\ g_1 = 2,\ g_2 = 4,\ g_3 = 5,\ g_4 = 8$, travelling wave parameters $(C_g, \omega_A, \omega_B) = (5.093, -9.9, -9.8)$, and initialised grey soliton parameter $\Phi_G^{(1)} = 1.25$. The measured reflection/refraction angles are given as $(\Theta_1, \Theta_2, \Theta_3, \Theta_4) = (0.882, 0.337, 0.452, 0.159)$.

been discussed. We note that the conservation equations only allow us to estimate the grey soliton parameters given that we know the type of behaviour that will occur, e.g. a two-soliton refraction ansatz in the nearly integrable regime. As one moves further away from the defocusing Manakov system, the radiation is typically increased and we may also find the existence of a vector soliton (VS) refraction like that seen in Fig. 5.12; this refraction falls outside the framework of Eqs. (5.43-5.45). The figure shows the collision of a travelling front and an initialised grey soliton, with parameter $\Phi_1 = 1.25$, in the CNLS with system parameters $d_1 = -1,\ d_2 = -3,\ g_1 = 2,\ g_2 = 4,\ g_3 = 5$, and $g_4 = 8$. In contrast to the nearly integrable regime, there are 4 structures after collision and significantly larger radiation upon collision. The observation of the vector-soliton refraction is particularly important as it shows the propagation of a bright-dark (BD) soliton in this non-integrable system. Therefore, it should be possible to find such robust structures in general, which will allow us to impose said vector solitons into the MTI.

To summarise this chapter, we have reduced the non-integrable CNLS down to a system of nonlinear ODEs. This system permits the existence of heteroclinic orbits connecting two SHATS uniform states, which translates to a travelling front in the CNLS; either ZZ to NN, or ZN to NZ are permitted by SHATS conditions. We focus purely on the abundance of ZN to NZ fronts and orbits connecting said plane-waves are allowed only in the regime of parameters prescribed by $g_1 g_2 > 0$, $g_3 g_4 > 0$, sgn$(d_1) \neq$ sgn$(g_{1,2})$, and sgn$(d_2) \neq$ sgn$(g_{3,4})$. We have developed a condition that relates the group velocity of the front to the chosen carrier frequencies of the plane-waves, and provided constraints of the travelling wave parameters to guarantee both of the plane-waves exist for one of $C_{g\pm}$. A brief analysis on solutions away from a fixed parameter set $(C_g, \omega_A, \omega_B)$ has been considered and we have shown the importance of

the heteroclinic condition when imposing travelling fronts in the non-integrable CNLS. Finally, we considered the collision of our front solutions with a scalar grey soliton. The reflection/refraction properties of the collision, in those systems that do not exhibit large radiation, is well-predicted by conservation laws of the non-integrable system. The collision of the front and grey soliton, in a system far away from the defocusing Manakov system, yields a vector soliton refraction, which shows the ability to produce such robust structures in non-integrable regimes. We will discuss the derivation and propagation of these vector soliton solutions in the next chapter.

Chapter 6

Soliton solutions in the non-integrable coupled NLS equation

In this chapter we will consider techniques to derive numerical and analytical soliton profiles. In particular, we focus on vector solitons (VS) that are classified into three categories: bright-bright (BB), dark-dark (DD), and bright-dark/dark-bright (BD/DB). We first consider solitons in the weakly-nonlinear regime by considering localised states near codimension-1 pitchfork bifurcations of the ZZ/ZN/NZ uniform states. These solitons provide us with an estimated starting point for numerical continuation using AUTO, which allows us to numerically find BD/DB solitons, given certain parameter constraints.

These solitons can also be numerically continued from the travelling fronts, which will yield BD/DB soliton profiles, depending on the direction of continuation. Continuing from the travelling front solutions yield strongly nonlinear profiles and the solitons will propagate with the same group velocity as the fronts. One may numerically continue the vector soliton profiles in the parameter C_g to also give vector soliton profiles that are no longer purely-real solutions of the travelling wave ODE. We then briefly explore the collision dynamics of these VS in different CNLS systems, and consider the possibility of energy transfer between the two VS.

The final section of this chapter focuses on BB and DD solitons. Analytical solutions are presented for each of the BB and DD, and correspond to codimension-2 bifurcations of the ZZ and NN uniform states respectively. The solutions are presented in their simplest form, which accounts for the fewest number of free parameters that determine the exact structure of the VS. We show the evolution of each of BD/DB/BB/DD in CNLS systems with different,

non-integrable system parameters.

6.1 Pitchfork bifurcations of uniform states

In a similar fashion to the Ginzburg-Landau equation, one may consider the bifurcation of the uniform states and look for localised solutions near the bifurcation value [35]. The spatial eigenvalues, given by Eq. (5.17), tell us the story of where these bifurcation points are found for each uniform state. To search for these localised solutions we consider a weakly nonlinear expansion of the dependent variables ϕ and ψ. Note that we will always consider ω_A as the bifurcation parameter throughout this chapter and Chapter 7, in order to be consistent with all numerical continuations. This does not have to be the case, and the forthcoming analysis can be applied to any of the three remaining travelling wave parameters $(C_g, \omega_A, \omega_B)$. In general, we will formulate a multiple scale analysis with the assumption of $C_g = 2d_1k_A = 2d_2k_B$, to reduce the parameter space, and we will assume a purely real solution $\phi,\ \psi \in \mathbb{R}$. One then performs a multiple-scale expansion in the purely-real ODE (5.9-5.10) around a bifurcation point, which we will denote as ω_b, and collect terms of the expansion at the orders of the implemented small parameter $\epsilon << 1$. Note that this ϵ is different from that of the MTI problem and we refer to this parameter arbitrarily. We first write the ODE system in the operator form

$$(\mathcal{L} + \mathcal{N}) \begin{bmatrix} \phi \\ \psi \end{bmatrix} = \mathbf{0}, \tag{6.1}$$

where $\mathbf{0}$ is the zero vector and we recall $\phi,\ \psi \in \mathbb{R}$. The linear, $\mathcal{L}$, and nonlinear, $\mathcal{N}$, operators are given in a functional form as

$$\mathcal{L} = \begin{bmatrix} d_1\partial_{\zeta\zeta} + (\omega_A - \frac{C_g^2}{4d_1}) & 0 \\ 0 & d_2\partial_{\zeta\zeta} + (\omega_B - \frac{C_g^2}{4d_2}) \end{bmatrix}, \tag{6.2}$$

$$\mathcal{N} = \begin{bmatrix} g_1\phi^2 + g_2\psi^2 & 0 \\ 0 & g_3\psi^2 + g_4\phi^2 \end{bmatrix}. \tag{6.3}$$

The asymptotic expansion of the field variables will then be written as

$$\begin{bmatrix} \phi \\ \psi \end{bmatrix} = \begin{bmatrix} U \\ V \end{bmatrix} + \begin{bmatrix} u \\ v \end{bmatrix} \tag{6.4}$$

where we introduce a slow spatial variable $Z = \epsilon\zeta$, and we also expand around the bifurcation parameter as $\omega_A = \omega_b + \epsilon^2\delta$, with δ an $O(1)$ quantity. The constants U, V represent the uniform state approximation in the expansion, and $u(\zeta, Z),\ v(\zeta, Z)$ represent the spatially-dependent terms. These terms are expanded around the small parameter by the following;

$$\begin{bmatrix} U \\ V \end{bmatrix} = \begin{bmatrix} U_0 \\ V_0 \end{bmatrix} + \epsilon \begin{bmatrix} U_1 \\ V_1 \end{bmatrix} + \epsilon^2 \begin{bmatrix} U_2 \\ V_2 \end{bmatrix} + \cdots$$

$$\begin{bmatrix} u \\ v \end{bmatrix} = \epsilon \begin{bmatrix} u_1 \\ v_1 \end{bmatrix} + \epsilon^2 \begin{bmatrix} u_2 \\ v_2 \end{bmatrix} + \epsilon^3 \begin{bmatrix} u_3 \\ v_3 \end{bmatrix} + \cdots$$

where $U_0,\ V_0$ are the values of the uniform state that we are considering. By substituting this ansatz into the equation (6.1), and collecting the orders of ϵ, we may find the asymptotic expansions of localised solutions near critical values of ω_b, for each of the uniform states.

Throughout the analysis we will consider the expansion in terms of matrix operators. These operators are given in a functional form as,

$$\mathcal{L}_0 = \begin{bmatrix} d_1\partial_{\zeta\zeta} + (\omega_b - \frac{C_g^2}{4d_1}) & 0 \\ 0 & d_2\partial_{\zeta\zeta} + (\omega_B - \frac{C_g^2}{4d_2}) \end{bmatrix}, \tag{6.5}$$

$$\mathcal{L}_1 = \begin{bmatrix} 2d_1\partial_Z\partial_\zeta & 0 \\ 0 & 2d_2\partial_Z\partial_\zeta \end{bmatrix}, \quad \mathcal{L}_2 = \begin{bmatrix} d_1\partial_{ZZ} + \delta & 0 \\ 0 & d_2\partial_{ZZ} + \delta \end{bmatrix}, \tag{6.6}$$

$$\mathcal{N}_0(X, Y) = \begin{bmatrix} g_1X^2 + g_2Y^2 & 0 \\ 0 & g_3Y^2 + g_4X^2 \end{bmatrix}, \tag{6.7}$$

$$\mathcal{N}_1(X, Y) = \begin{bmatrix} 2g_1U_0X & 2g_2V_0X \\ 2g_4U_0Y & 2g_3V_0Y \end{bmatrix}, \tag{6.8}$$

$$\mathcal{N}_2(X, Y) = \begin{bmatrix} 3g_1U_0X + 2g_2V_0Y & g_2U_0Y \\ g_4V_0X & 3g_3V_0Y + 2g_4U_0X \end{bmatrix}, \tag{6.9}$$

$$\mathcal{N}_3(X, Y) = \begin{bmatrix} g_1U_0X + 2g_2V_0Y & g_2U_0Y - 2g_2V_0X \\ g_4V_0X - 2g_4U_0Y & g_3V_0Y + 2g_4U_0X \end{bmatrix} \tag{6.10}$$

where $X,\ Y$ are dummy variables that may take the values $X = U_0,\ (u_1 + U_1),\ (u_2 + U_2), \ldots$ and $Y = V_0,\ (v_1 + V_1),\ (v_2 + V_2), \ldots$. Higher order terms of $O(\epsilon^4)$ and above are also present, but we truncate the expansion at $O(\epsilon^3)$ since

this is sufficient to yield the leading-order localised solutions. Therefore, the analysis is similar to that of [35]. There are three distinct critical values of the parameter ω_A that produce a pitchfork bifurcation; one for each of the uniform states $ZZ/ZN/NZ$. From the ZZ eigenvalues (5.18), we see that four eigenvalues become zero at the value of $\omega_{ZZ} = C_g^2/4d_1$. At this critical value, these particular eigenvalues change stability and this bifurcation produces two new solutions that correspond precisely to positive and negative NZ. The uniform state ZN can not bifurcate from the ZZ branch since the bifurcation parameter ω_A does not alter the other four eigenvalues of Eq. (5.18); this can occur when ω_B and C_g are bifurcation parameters. Similar analysis of the ZN and NZ spatial eigenvalues (5.19-5.20) tells us that we also have pitchfork bifurcations at the critical values

$$\omega_{ZN} = \frac{C_g^2}{4d_1} - \frac{g_2}{g_3}\left(\frac{C_g^2}{4d_2} - \omega_B\right),$$
$$\omega_{NZ} = \frac{C_g^2}{4d_1} - \frac{g_1}{g_4}\left(\frac{C_g^2}{4d_2} - \omega_B\right),$$

which correspond to the NN uniform state bifurcating from ZN and NZ respectively. These points are also the codimension-1 critical values, which allow the branch of vector solitons, that we will see when numerically continuing the front solutions in Fig. 6.2. Whether $\omega_{ZZ},\ \omega_{ZN},\ \omega_{NZ}$ produce subcritical/supercritical bifurcations depends on the signs and magnitudes of the system and travelling wave parameters. Since we are considering pitchfork bifurcations, the appropriate expansion of the fields u, v allows us to further simplify by writing the functions $u_1,\ u_2,\ u_3,\ v_1,\ v_2,\ v_3, \ldots$ as functions of the slow variable Z only. One can now formally substitute the multiple-scale ansatz into the ODE (6.1) and consider the expansion around each of the critical values.

6.1.1 ZZ equilibria $(\omega_b = \omega_{ZZ})$

The simplest case to consider is that of the ZZ equilibrium point. Further simplifications can be made in this instance since we know that the expansion of the uniform state will be zero in the vicinity of the critical value, i.e. $U_0,\ U_1,\ U_2, \ldots = 0$ and $V_0,\ V_1,\ V_2, \cdots = 0$. At each order of ϵ, the analysis also tells us that the field v is always zero, i.e. $v_1,\ v_2, \ldots = 0$. The leading order expansion, at $O(\epsilon^3)$, then gives us a solvability condition involving u_1, written as

$$\delta u_1 + d_1 u_{1ZZ} + g_1 u_1^3 = 0, \tag{6.11}$$

that yields three spatially-homogeneous solutions given by

$$u_1 = 0, \quad u_1 = \pm\sqrt{\frac{-\delta}{g_1}}.$$

Since we know that $\delta = (\omega_A - \omega_{ZZ})/\epsilon^2$, we may write the full solutions as

$$\phi = 0, \quad \phi = \pm\sqrt{\frac{\omega_b - \omega_A}{g_1}},$$

which correspond to the ZZ and $\pm NZ$ states respectively and the NZ state exists only when $\text{sgn}(\omega_b - \omega_A) = \text{sgn}(g_1)$, in agreement with Eq. (5.13). The solvability equation (6.11) also admits spatially-dependent solutions depending on the signs of the parameters. Similarly to [35], one can obtain subcritical bifurcations to localised states, given by

$$\phi = \sqrt{\frac{-2(\omega_A - \omega_{ZZ})}{g_1}}\text{sech}\left(\sqrt{\frac{(\omega_A - \omega_{ZZ})}{-d_1}}\zeta\right) + \cdots, \tag{6.12}$$

and supercritical bifurcations to the front-like states

$$\phi = \sqrt{\frac{-(\omega_A - \omega_{ZZ})}{g_1}}\tanh\left(\sqrt{\frac{(\omega_A - \omega_{ZZ})}{2d_1}}\zeta\right) + \cdots, \tag{6.13}$$

with $\psi = 0$. These solutions are precisely the bright and dark soliton solutions to the scalar NLS equation, which is expected since this codimension-1 critical value bifurcates one component of the CNLS only. These are exact solutions, with carrier wavenumber $k_A = C_g/2d_1$ and frequency ω_A, and require no higher-order terms in the expansion. As one would expect from the criticality of the bifurcation, localised bright solitons can only be formed when $d_1 g_1 > 0$, with the dark soliton existing purely in the regime $d_1 g_1 < 0$. Since these solutions are simply solutions of scalar NLS, we do not consider them further, and now focus purely on the remaining pitchfork bifurcations.

6.1.2 ZN equilibria $(\omega_b = \omega_{ZN})$

The case of pitchfork bifurcations from ZN is more complicated as we must thoroughly analyse each order of ϵ to obtain the correct form of both of the fields u, v. We can make a simplification from the beginning since we know that the expansion of the zero component will always be zero, i.e. $U_0,\ U_1,\ U_2, \ldots = 0$, and the parameter ω_A does not affect ψ_0, i.e. $V_0,\ V_1,\ V_2, \ldots = 0$. When one

substitutes the multiple-scale ansatz (6.4) into the ODE, with the value of $\omega_b = \omega_{ZN}$, we can consider the solvability conditions at each of the ϵ orders. At $O(1)$, the leading equation is given by

$$(\mathcal{L}_0 + \mathcal{N}_0(U_0, V_0)) \begin{bmatrix} U_0 \\ V_0 \end{bmatrix} = \underline{0}, \tag{6.14}$$

where $\mathcal{L}_0,\ \mathcal{N}_0(U_0, V_0)$ are given by (6.5) and (6.7) respectively. This is solved non-trivially by virtue of the positive, real ZN uniform state (5.12), i.e.

$$U_0 = 0, \quad V_0 = \sqrt{\frac{(C_g^2 - 4d_2\omega_B)}{4d_2 g_3}}.$$

At the next order of $O(\epsilon)$, one has

$$(\mathcal{L}_0 + \mathcal{N}_0(U_0, V_0) + \mathcal{N}_1(U_0, V_0)) \begin{bmatrix} u_1 \\ v_1 \end{bmatrix} + \mathcal{L}_1 \begin{bmatrix} U_0 \\ V_0 \end{bmatrix} = \underline{0}, \tag{6.15}$$

where $\mathcal{L}_1,\ \mathcal{N}_1(U_0, V_0)$ are given by Eq. (6.6) and Eq. (6.8) respectively, and we may substitute $U_0,\ V_0$ in from the previous order. This equation simplifies down to the solvability condition of $v_1 = 0$. The next order of $O(\epsilon^2)$ yields,

$$\begin{aligned}(\mathcal{L}_0 + \mathcal{N}_0(U_0, V_0) + \mathcal{N}_1(U_0, V_0)) \begin{bmatrix} u_2 \\ v_2 \end{bmatrix} \\ + (\mathcal{L}_1 + \mathcal{N}_2(u_1, v_1)) \begin{bmatrix} u_1 \\ v_1 \end{bmatrix} + \mathcal{L}_2 \begin{bmatrix} U_0 \\ V_0 \end{bmatrix} = \underline{0},\end{aligned} \tag{6.16}$$

where $\mathcal{L}_2,\ \mathcal{N}_2(u_1, v_1)$ are given by Eq. (6.6) and Eq. (6.9) respectively. By substituting previous order quantities in, we get a relationship between the field variables u_1 and v_2, given as

$$v_2 = -\frac{g_4}{2g_3 V_0} u_1^2.$$

The final order that we will consider, $O(\epsilon^3)$, yields the equation

$$\begin{aligned}(\mathcal{L}_0 + \mathcal{N}_0(U_0, V_0) + \mathcal{N}_1(U_0, V_0)) \begin{bmatrix} u_3 \\ v_3 \end{bmatrix} + (\mathcal{L}_1 + \mathcal{N}_2(u_1, v_1)) \begin{bmatrix} u_2 \\ v_2 \end{bmatrix} \\ + (\mathcal{L}_2 + \mathcal{N}_0(u_1, v_1) + \mathcal{N}_1(u_2, v_2) + \mathcal{N}_3(u_2, v_2)) \begin{bmatrix} u_1 \\ v_1 \end{bmatrix} = \underline{0},\end{aligned} \tag{6.17}$$

where $\mathcal{N}_3(u_2, v_2)$ is given by Eq. (6.10). When one substitutes the information from previous orders into Eq. (6.17) there is a relationship between higher-order variables,

$$v_3 = -\frac{g_4}{g_3 V_0} u_1 u_2.$$

as well as the solvability condition for the field variable u_1, given by

$$d_1 u_{1ZZ} + \delta u_1 + (g_1 - \frac{g_2 g_4}{g_3}) u_1^3 = 0. \tag{6.18}$$

The solvability condition (6.18) admits three spatially-homogeneous solutions. One of these is the trivial, persistent state that corresponds to the ZN equilibria. The other solutions give an expansion of,

$$\begin{bmatrix} \phi \\ \psi \end{bmatrix} = \begin{bmatrix} 0 \\ \sqrt{\frac{(C_g^2 - 4d_2\omega_B)}{4d_2 g_3}} \end{bmatrix} + \begin{bmatrix} \pm\sqrt{\frac{g_3(\omega_A - \omega_{ZN})}{g_2 g_4 - g_1 g_3}} \\ 0 \end{bmatrix} + \begin{bmatrix} 0 \\ \frac{-\sqrt{d_2 g_3} g_4 (\omega_A - \omega_{ZN})}{(g_2 g_4 - g_1 g_3)\sqrt{C_g^2 - 4d_1\omega_B}} \end{bmatrix} + \cdots,$$

which corresponds to an approximate expansion of the NN equilibria, with $\pm\phi$ component. Note that we have set $u_2 = 0$ here, which is in agreement with higher-order solvability conditions. The ϕ component above is exactly the ϕ component of NN and thus there are no further non-zero values of $u_2,\ u_3, \ldots$. We have also excluded higher-order terms here, but as one extends the expansion beyond $O(\epsilon^2)$, the approximation of the ψ component becomes more accurate. In addition to the uniform solutions, there are also spatially-dependent solutions of Eq. (6.18). An example of these are subcritical bifurcations to localised states given by

$$u_1 = \sqrt{\frac{2g_3(\omega_A - \omega_{ZN})}{g_2 g_4 - g_1 g_3}} \text{sech}\left(\sqrt{\frac{(\omega_A - \omega_{ZN})}{-d_1}}\zeta\right), \tag{6.19}$$

which subsequently leads to

$$v_2 = \frac{-2\sqrt{d_2 g_3} g_4 (\omega_A - \omega_{ZN})}{\sqrt{(C_g^2 - 4d_2\omega_B)}(g_2 g_4 - g_1 g_3)} \text{sech}^2\left(\sqrt{\frac{(\omega_A - \omega_{ZN})}{-d_1}}\zeta\right). \tag{6.20}$$

The approximation is only valid when $\text{sgn}(d_1) \neq \text{sgn}(g_3(g_2 g_4 - g_1 g_3))$. Further to this, when $g_3 g_4 > 0$, the solution corresponds to a weakly-nonlinear BD soliton and the elevation of the ϕ component directly impacts the depression of the ψ

component nonlinearly. Note also that when $g_3 g_4 < 0$, the solution corresponds to a double-elevation of energy from the ZN state, i.e. a reversible homoclinic orbit (RHO) that increases in both $\phi,\ \psi$ before returning to ZN. Similarly to the ω_{ZZ} critical value, there also exists supercritical bifurcations to front-like states, given by

$$u_1 = \sqrt{\frac{g_3(\omega_A - \omega_{ZN})}{g_2 g_4 - g_1 g_3}} \text{tanh}\left(\sqrt{\frac{(\omega_A - \omega_{ZN})}{2d_1}}\zeta\right), \tag{6.21}$$

which subsequently leads to

$$v_2 = \frac{-\sqrt{d_2 g_3} g_4(\omega_A - \omega_{ZN})}{\sqrt{(C_g^2 - 4d_2\omega_B)}(g_2 g_4 - g_1 g_3)} \text{tanh}^2\left(\sqrt{\frac{(\omega_A - \omega_{ZN})}{2d_1}}\zeta\right). \tag{6.22}$$

In contrast to the subcritical bifurcation, this approximation is only valid when $\text{sgn}(d_1) = \text{sgn}(g_3(g_2 g_4 - g_1 g_3))$. When one has $g_3 g_4 > 0$, the solution corresponds to a weakly-nonlinear DD soliton which forms a depression in the energy of both the ϕ and ψ components; this corresponds to a heteroclinic orbit connecting the NN states with $\pm\phi$ components. If we instead have $g_3 g_4 < 0$, then the solution is that of a depression in the energy of the ϕ component and an elevation of energy in the ψ component of NN; this is, once again, a heteroclinic orbit only now with the orbit increasing in the ψ component.

Typical vector solitons, related to ZN and NZ, look like those of BD and DB variants, i.e. an elevation of energy from a zero component and a depression in the energy of a non-zero component. The other solutions are still valid and propagate well, as we will show later, however we wish to compare the solitons in the non-integrable regime to those of the integrable. Therefore, we focus mainly on those solutions formed as BD and DB vector solitons and are governed by Eqs. (6.19-6.20) and with $g_3 g_4 > 0$. We have only shown the BD soliton, but one may recognise that a DB soliton is likely to arise from pitchfork bifurcations of the NZ uniform state, which is what we will now consider.

6.1.3 NZ equilibria $(\omega_b = \omega_{NZ})$

The pitchfork bifurcation of NZ is slightly more complicated than that of ZZ and ZN. The key difference is that one can no longer set $U_0,\ U_1,\ U_2, \ldots = 0$, since the ϕ component is altered when one shifts in ω_A. We can still allow $V_0,\ V_1,\ V_2, \ldots = 0$, however, since the ψ component will remain zero within the vicinity of the critical value ω_{NZ}. The formation and analysis of the expansion then follows closely the case of $\omega_b = \omega_{ZN}$. We substitute the multiple-scale ansatz (6.4) into the system (6.1) and allow $\omega_b = \omega_{NZ}$.

At $O(1)$, the equation is precisely that of Eq. (6.14). The only difference is that we are now considering the uniform state of

$$U_0 = \sqrt{\frac{(C_g^2 - 4d_2\omega_B)}{4d_2 g_4}}, \quad V_0 = 0. \tag{6.23}$$

At the next order of $O(\epsilon)$ we have a solvability equation of Eq. (6.15), only now with the variable $u_1 + U_1$, i.e.

$$(\mathcal{L}_0 + \mathcal{N}_0(U_0, V_0) + \mathcal{N}_1(U_0, V_0)) \begin{bmatrix} u_1 + U_1 \\ v_1 \end{bmatrix} + \mathcal{L}_1 \begin{bmatrix} U_0 \\ V_0 \end{bmatrix} = \underline{0}. \tag{6.24}$$

When one substitutes Eq. (6.23) into Eq. (6.24), and extracts the spatially-dependent and independent terms, then this is only solved trivially by $u_1,\ U_1 = 0$, with no further information on the field variable v_1. The next order of $O(\epsilon^2)$ yields Eq. (6.16), with the equilibria expansion terms included, i.e.

$$\begin{aligned}(\mathcal{L}_0 &+ \mathcal{N}_0(U_0, V_0) + \mathcal{N}_1(U_0, V_0)) \begin{bmatrix} u_2 + U_2 \\ v_2 \end{bmatrix} \\ &+ (\mathcal{L}_1 + \mathcal{N}_2(u_1 + U_1, v_1)) \begin{bmatrix} u_1 + U_1 \\ v_1 \end{bmatrix} + \mathcal{L}_2 \begin{bmatrix} U_0 \\ V_0 \end{bmatrix} = \underline{0}.\end{aligned} \tag{6.25}$$

By substituting in all prior information, extracting the spatially-dependent and independent terms, we get two significant relationships for the equillibria expansion and the field variables. These are given as,

$$U_2 = -\frac{\delta}{2g_1 U_0}, \quad u_2 = -\frac{g_2}{2g_1 U_0} v_1^2.$$

The final order that we consider, $O(\epsilon^3)$, provides us with the solvability equation (6.17), with equilibria expansion terms included, i.e.

$$\begin{aligned}(\mathcal{L}_0 &+ \mathcal{N}_0(U_0, V_0) + \mathcal{N}_1(U_0, V_0)) \begin{bmatrix} u_3 + U_3 \\ v_3 \end{bmatrix} \\ &+ (\mathcal{L}_1 + \mathcal{N}_2(u_1 + U_1, v_1)) \begin{bmatrix} u_2 + U_2 \\ v_2 \end{bmatrix} \\ &+ (\mathcal{L}_2 + \mathcal{N}_0(u_1 + U_1, v_1) + \mathcal{N}_1(u_2 + U_2, v_2) \\ &+ \mathcal{N}_3(u_2 + U_2, v_2)) \begin{bmatrix} u_1 + U_1 \\ v_1 \end{bmatrix} = \underline{0}.\end{aligned} \tag{6.26}$$

Extracting the spatially-dependent and independent terms, gives the trivial value of $U_3 = 0$. The remaining terms impose a relationship between higher-order field variables of

$$u_3 = -\frac{g_2}{g_1 U_0} v_1 v_2$$

and provides us with the following solvability condition on the field variable v_1,

$$d_2 v_{1ZZ} - \frac{\delta g_4}{g_1} v_1 + (g_3 - \frac{g_2 g_4}{g_1}) v_1^3 = 0. \tag{6.27}$$

Similarly to the analysis of the critical value ω_{ZN}, we obtain three spatially-homogeneous solutions to Eq. (6.27). The trivial solution, given by $v_3 = 0$, corresponds to the persistent state after bifurcation, namely NZ. The remaining solutions give us an expansion of

$$\begin{bmatrix} \phi \\ \psi \end{bmatrix} = \begin{bmatrix} \sqrt{\frac{(C_g^2 - 4d_2\omega_B)}{4d_2 g_4}} \\ 0 \end{bmatrix} + \begin{bmatrix} 0 \\ \pm\sqrt{\frac{g_4(\omega_A - \omega_{NZ})}{g_1 g_3 - g_2 g_4}} \end{bmatrix} + \begin{bmatrix} -\frac{\sqrt{d_2 g_4} g_3 (\omega_A - \omega_{NZ})}{(g_1 g_3 - g_2 g_4)\sqrt{(C_g^2 - 4d_2\omega_B)}} \\ 0 \end{bmatrix} + \cdots,$$

which corresponds to the approximate expansion of the NN uniform state, with $\pm\psi$ component. Note that we have set the field variable $v_2 = 0$, which is in agreement with higher-order solvability conditions, and a higher-order expansion would also give a more accurate approximation of the ϕ component. The ψ component above is exactly the ψ component of NN and thus there are no further non-zero values of $v_2,\ v_3, \ldots$, which validates the imposed value of $v_2 = 0$.

Like with the previous critical values, the solvability equation also admits a branch of localised solutions, given by

$$v_1 = \sqrt{\frac{2g_4(\omega_A - \omega_{ZN})}{g_1 g_3 - g_2 g_4}} \text{sech}\left(\sqrt{\frac{g_4(\omega_A - \omega_{ZN})}{d_2 g_1}}\zeta\right), \tag{6.28}$$

which subsequently leads to

$$u_2 = \frac{-2g_2 g_4 \sqrt{d_2 g_4}(\omega_A - \omega_{ZN})}{g_1\sqrt{(C_g^2 - 4d_2\omega_B)}(g_1 g_3 - g_2 g_4)} \text{sech}^2\left(\sqrt{\frac{(\omega_A - \omega_{ZN})}{d_2 g_1}}\zeta\right). \tag{6.29}$$

The solution may exist providing that $\text{sgn}(d_2 g_1) = \text{sgn}(g_1 g_3 - g_2 g_4)$. Further to this, we get different behaviour of the ψ component depending on if $g_1 g_2 > 0$ is

satisfied. If this product is positive, then we get the structure of of D$^-$B soliton. If this quantity is negative, then we get an elevation of energy in both components corresponding to a D$^+$B solution from NZ. Note that the superscripts $\pm$ refer to a depression/elevation in the non-zero background field.

As expected, there is also a branch of front-like states, given by

$$v_1 = \sqrt{\frac{g_4(\omega_A - \omega_{ZN})}{g_1 g_3 - g_2 g_4}}\tanh\left(\sqrt{\frac{-g_4(\omega_A - \omega_{ZN})}{2d_2 g_1}}\zeta\right) \tag{6.30}$$

which subsequently leads to

$$u_2 = \frac{-g_2 g_4\sqrt{g_4}(\omega_A - \omega_{ZN})}{g_1\sqrt{(C_g^2 - 4d_2\omega_B)}(g_1 g_3 - g_2 g_4)}\tanh^2\left(\sqrt{\frac{-g_4(\omega_A - \omega_{ZN})}{2d_2 g_1}}\zeta\right). \tag{6.31}$$

In contrast to the localised branch, we see that these solutions may exist only when sgn$(d_2 g_1) \neq$ sgn$(g_1 g_3 - g_2 g_4)$. There is also considerably different profiles of these solutions when the sign of the product $g_1 g_2$ takes a positive or negative sign. In the positive case, one has an elevation of energy in the non-zero ϕ component and a depression in the energy of the ψ component, formed by a heteroclinic connection of the $\pm\psi$ amplitudes. In the negative case, one has the same depression of the energy in the ψ component, but there is now a depression of the energy in the ϕ component also. Similarly to be the ZN case, when looking for vector soliton solutions to the MTI, we will focus purely on the DB soliton solutions from this weakly nonlinear analysis, formally, the solutions obtained from Eqs. (6.28-6.29) that represent a depression in the energy of a non-zero ϕ and an elevation of energy from a zero ψ component.

6.2 Numerical continuation

The weakly nonlinear solutions obtained for the critical values of ω_{ZN} and ω_{NZ} will not propagate in the CNLS without some form of excess radiation. This is simply down to the solutions being approximated through an expansion. To obtain solutions that will propagate as expected, one can use numerical continuation in AUTO to continue these solutions to the the exact structure of the nonlinear profile. In order to find the vector soliton solutions numerically, we will impose our weakly nonlinear solutions in the right-half domain and numerically continue in the bifurcation parameter ω_A. To impose the correct structure, we allow reversible boundary conditions on $\zeta = 0$ and Neumann boundary conditions on $\zeta = L$, where L is a fixed value and is chosen appropriately

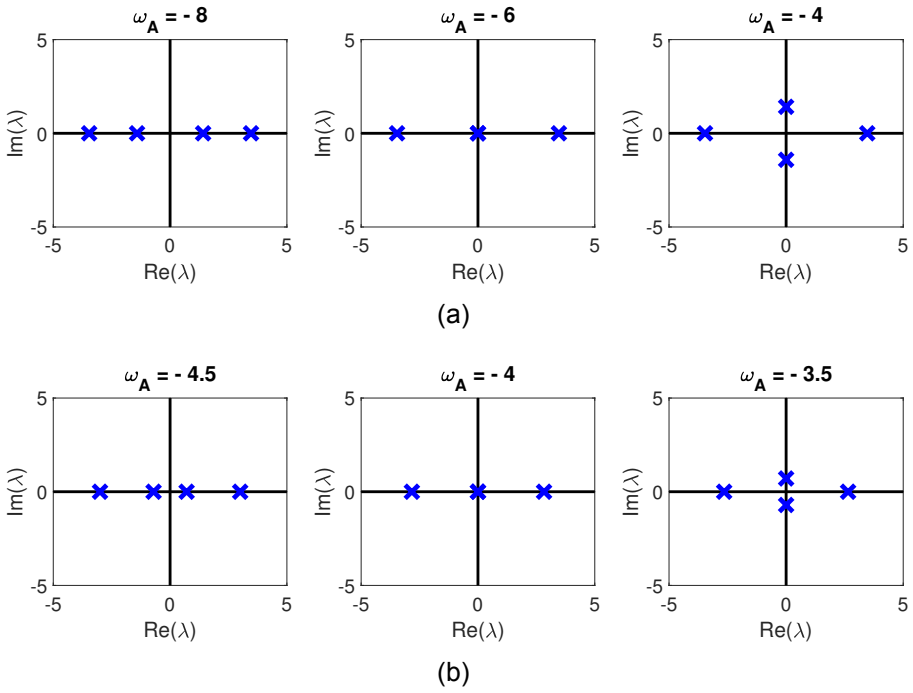

Figure 6.1: Transition of spatial eigenvalue configuration for the uniform state (a) ZN and (b) NZ. Subcritical pitchfork bifurcations occur in the middle-panel for both states at (a) $\omega_A = \omega_{ZN} = -6$ and (b) $\omega_A = \omega_{NZ} = -4$. System and remaining travelling wave parameters are given as (a) $d_1 = 1$, $d_2 = -1$, $g_2 = g_3 = g_4 = 2$, $g_1 = 3$, $(C_g, \omega_B) = (0, -6)$ and (b) $d_1 = d_2 = -1$, $g_1 = g_3 = g_4 = 2$, $g_2 = 3$, $(C_g, \omega_B) = (0, -4)$.

such that the full domain is periodic in the wavenumber of the non-zero component. The reversible boundaries are defined by the reversibility of the general ODE system (5.3–5.4). Recall that this system is reversible under the action of $R(\phi, \psi, \phi', \psi') = (\phi^*, \psi^*, -\phi^{*'}, -\psi^{*'})$ and $\zeta \longrightarrow -\zeta$, where $*$ denotes complex conjugation. The boundary conditions on $\zeta = 0$ are then $\mathrm{Im}(\phi(0), \psi(0)) = 0$ and $\mathcal{R}\mathrm{e}(\phi_\zeta(0), \psi_\zeta(0)) = 0$. After a branch of solutions is found in AUTO, we then take the solution profile on the right half-domain found in AUTO and use the reversible boundary conditions on $\zeta = 0$ to create the solution profile on the full domain of ζ.

To showcase how these bifurcations affect the configuration of the spatial eigenvalues, we allow subcritical bifurcations of ω_{ZN} and ω_{NZ} in Fig. 6.1. This figure encompasses plots of the eigenvalues at the critical value of ω_b (middle panel), as well as before (left panel) and after (right panel), to validate this change of stability. Note that repeated eigenvalues and eigenvalues that are always zero, just as before, are left out of the plots for clarity. The transition of the eigenvalue configuration is shown for the critical value of $\omega_{ZN} = -6$ in Fig. 6.1(a), where we see two eigenvalues approaching zero as we increase ω_A towards 0. These values collide at $\lambda = 0$, when $\omega_A = \omega_{ZN}$, before splitting along the imaginary axis and become unstable. For clarity, the CNLS system

parameters are given as $d_1 = 1$, $d_2 = -1$, $g_2 = g_3 = g_4 = 2$ and $g_1 = 3$ with remaining travelling wave parameters $(C_g, \omega_B) = (0, -6)$. Similarly, Fig. 6.1(b) shows the transition of the eigenvalue configuration through the critical value $\omega_{NZ} = -4$. The analysis is similar to the ω_{ZN} case in this instance, other than the observation that the non-colliding eigenvalues are also altered slightly by the shift in ω_A. These extra eigenvalues collide at the value of ω_{ZZ}, which is apparent from Eq. (5.20). System and travelling wave parameters for this transition are fixed as $d_1 = d_2 = -1$, $g_1 = g_3 = g_4 = 2$, $g_2 = 3$,and $(C_g, \omega_B) = (0, -4)$.

We now consider examples of CNLS systems that exhibit supercritical or subcritical bifurcations at the critical values of ω_{ZN} and ω_{NZ}. First, we show examples of these vector solitons propagating stably from the analysis of ω_{ZN}; these are seen in Fig. 6.11 at the end of this chapter. The standard BD$^-$ soliton solution (6.19-6.20) is shown in Fig. 6.11(a), where we have imposed $g_3 g_4 > 0$, with the same choice of system parameters as Fig. 6.1(a). By fixing $(C_g, \omega_B) = (0, -6)$, one can numerically continue up to the profile found at $\omega_A = -6.051$, and evolve the BD$^-$ profile in the CNLS system. We will keep the chosen value of $C_g = 0$, for all of the upcoming solutions, for consistency, however, we note that one can easily continue to $C_g \neq 0$ for any of the solutions to produce a travelling structure. In contrast to the above BD$^-$ solution, one can also impose the sech profile with $g_3 g_4 < 0$, that exhibits the BD$^+$ double elevation of energy from ZN, shown in 6.11(b). This solution takes the form of a bright soliton in the zero-component, with a soliton protruding from a non-zero background field in the other component. System parameters are given as $d_1 = 1$, $d_2 = -1$, $g_1 = 3$, $g_2 = g_4 = -2$, and $g_3 = 2$, with the travelling wave parameters $(\omega_B, \omega_A) = (-8, 7.949)$.

The tanh solutions, obtained from Eqs. (6.21-6.22), may also propagate stably in the CNLS. The chosen sign of the product $g_3 g_4 > 0$, shown in Fig. 6.11(c), produces a DD$^+$ solution where the background fields are equivalent to the uniform state NN, and there is an elevation of energy from the non-zero background ψ. The system parameters are given as $d_1 = 1$, $d_2 = -1$, $g_1 = g_3 = g_4 = 2$, and $g_2 = 3$, with travelling wave parameters $(\omega_B, \omega_A) = (-8, -11.949)$. In contrast, the enforced sign of terms $g_3 g_4 < 0$, shown in Fig.6.11(d), produces a DD$^-$ soliton in the bifurcated background field of NN. We choose the system parameters as $d_1 = 1$, $d_2 = -1$, $g_1 = g_3 = 2$, $g_2 = -3$, and $g_4 = -2$, along with the system parameters $(\omega_B, \omega_A) = (-8, 12.409)$.

One can also consider both the localised and front-like solutions found by the pitchfork bifurcation of the NZ uniform state, which are shown in Fig. 6.12 at the end of this chapter. There is a certain solitonic-component symmetry

to the ω_{ZN} solutions shown previously. For instance, the solution given by the numerical continuation of Eqs. (6.28-6.29), with product $g_1 g_2 > 0$, yields a D$^-$B soliton shown in Fig. 6.12(a). This is in contrast to the sech solution, with $g_3 g_4 > 0$, that produced a BD$^-$ soliton solution for ω_{ZN}. The D$^-$B solution of ω_{NZ} was found in the CNLS with system parameters $d_1 = d_2 - 1$, $g_1 = g_3 = g_4 = 2$, and $g_2 = 3$, with the travelling wave parameters $(\omega_B, \omega_A) = (-4, -4.052)$. A D$^+$B solution is formed from the NZ state when one considers $g_1 g_2 < 0$, and an example is shown in Fig.6.12(b). The CNLS parameters considered here are $d_1 = d_2 = 1$, $g_1 = g_3 = -2$, $g_2 = 2$, and $g_4 = 3$, with travelling wave parameters $(\omega_B, \omega_A) = (-6, 3.948)$. There is an elevation of energy in both the zero, and the non-zero components.

As expected, from the component symmetry, one finds D$^\pm$D solutions bifurcating from NZ in those systems that exhibit tanh solutions, given by Eqs. (6.30-6.31), with imposed $g_1 g_2 > 0$. An example of this is shown in Fig. 6.12(c), where we have considered the propagation of the structure in the CNLS with system parameters $d_1 = d_2 = -1$, $g_1 = 3$, and $g_2 = g_3 = g_4 = 2$, with imposed travelling wave parameters $(\omega_B, \omega_A) = (-6, -8.951)$. The ϕ component, in this instance, is exhibits an elevation of energy from the non-zero ϕ background field. Finally, when one considers the tanh solution with opposing $g_1 g_2 < 0$, there is a formation of a D$^-$D solution in the bifurcated background field of NN, shown in Fig. 6.12(d). Here, we have considered a CNLS with system parameters $d_1 = d_2 = -1$, $g_1 = g_3 = g_4 = 2$, and $g_2 = -3$, and travelling wave parameters $(\omega_B, \omega_A) = (-6, -5.885)$. For each of the tanh solutions we have multiplied the soliton bifurcating from the zero-component by a factor of i. This makes the component purely imaginary so that we can numerically continue in AUTO efficiently, as this allows us to keep the boundary conditions as reversible on $\zeta = 0$ and Neumann on $\zeta = L$. We have also initialised two tanh solitons, related via complex conjugacy, on the same domain, with peaks located at $x = \pm\frac{L}{2}$ respectively, to enforce periodic domains for the evolution of the CNLS equation. This is why some figures are represented in the positive x-axis only with a peak location at $x = \frac{L}{2}$; see, for instance, Fig. 6.11(c).

We note that all of these solutions represent those RHOs that are of small amplitudes away from the uniform states, thus the stability is closely represented by the SHATS formation we presented in Chapter 5. The heteroclinic orbits are also represented in the small amplitude case. When one continues into the strongly nonlinear regime, the stability of the solution itself must be considered. The spectrum of the CNLS [60], which can be obtained numerically via discretisation and the finite difference scheme [78], is used to check whether such structures are temporally stable. In our case, we only wish to seek so-

lutions that can be translated back into the MTI lattice. Therefore, as long as these structures are stable in the CNLS for a long time-frame, they will propagate well as nonlinear edge solutions of the MTI. As mentioned previously, we will mainly focus on the prototypical VS solutions of BD^{-} and $\mathrm{D}^{-}\mathrm{B}$, depicted in Fig. 6.11(a) and Fig. 6.12(a) respectively, which consist of a bright-soliton in the zero component and a dark-soliton in the non-zero component. These two VS are typically what is referred to when BD and DB are mentioned in the literature; see, for instance, [155, 188, 112]. Henceforth, we will drop the superscript and denote these two VS as BD and DB respectively.

We also briefly discuss these weakly nonlinear solutions as one breaks the assumption of $C_g = 2d_1k_A = 2d_2k_B$. In this case, one no longer bifurcates the uniform states of Eqs. (5.9-5.10), but rather the uniform states of Eqs. (5.3-5.4). The subsequent complex ansatz required for this analysis is outside of our current framework and will be considered in future work. We choose to keep the original assumption as the purpose of our analysis is to explore and search for these localised structures for the MTI evolution. Since a plethora of solutions exist in the reduced parameter space, as we have shown, it is more efficient for us to consider this regime for the MTI. This is because we can force $C_g = k_A = k_B = 0$ to provide a simpler initialisation and a more visual evolution of the vector edge solitons.

6.2.1 Continuation from the travelling front solution

Equivalently, the bifurcating BD/DB solutions, that can be found by continuing from the sech profiles of ZN and NZ uniform states respectively, can also be found in the strongly nonlinear regime by continuing from the travelling front solution. This shows that all of the solutions are connected through the shifting of a single parameter, say ω_A. When one continues in the bifurcation parameter, we expect a branch of localised vector soliton solutions to appear from the points ω_{ZN} and ω_{NZ}, providing that the parameters allow the localised states to exist. As one continues in the parameter further, there may exist a point in which the heteroclinic condition (5.33) is satisfied, where the front solution is found.

Let us consider the nearly-integrable regime, where we found a travelling front previously, portrayed in Fig. 5.5. Continuing in the parameter ω_A traces out the solution branch shown in Fig. 6.2(a), where we have plotted the L^2-norm, described by Eq. (2.10), against ω_A. The point at A_1 is precisely the travelling front found previously at $(C_g, \omega_A, \omega_B) = (-5.395, -9.5, -10)$ and, depending on the direction of continuation, one may find DB or BD solitons to either side of

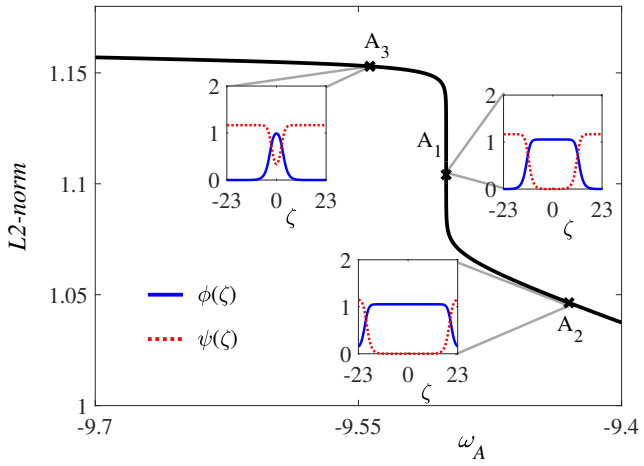

(a)

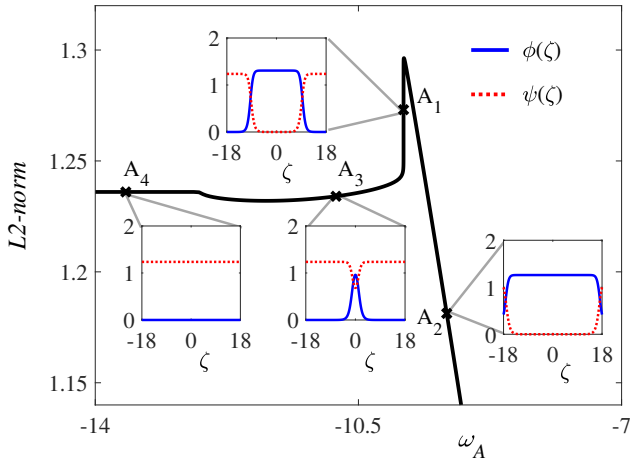

(b)

Figure 6.2: Bifurcation diagrams and subsequent profiles are shown for the bifurcation parameter ω_A. Profiles are shown as ϕ (blue-solid) and ψ (red-dashed). All other parameters k_A, k_B, ω_B, g_{1-4}, and d_{1-2} are fixed and the domain size is fixed to impose periodicity. Continuation has been proposed on the fronts that are portrayed in (a) Fig. 5.5 and (b) Fig. 5.6(b).

the front solution. Examples of these solitons are located at A_2 and A_3 respectively. Continuing along the branch, in the direction of A_2, one would find the DB branch merging with the branch containing the NZ state at the critical value of $\omega_{NZ} = -9.092$. DB solutions can't be found beyond this merging critical value. If one continues in the opposite direction, beyond A_3, then the branch of BD solutions meets the branch containing ZN at $\omega_{ZN} = -10$. BD solutions do not exist to the left of this value. The solution branch looks very similar for other system parameters, providing that the equilibria are physical and SHATS, and localised states are permitted. For instance, consider the solution branch that is shown in Fig. 6.2(b), where we have numerically continued the travelling front that we found previously in Fig. 5.6(b). Recall that the front, located at A_1, was found with the travelling wave parameters $(C_g, \omega_A, \omega_B) = (5.093, -9.9 - 9.8)$.

By numerical continuation of this front the structure of the solution branch is very similar to that of Fig. 6.2(a), only here the value of $\omega_{ZN} = -12.595$ is sandwiched between the profiles of A_3 and A_4, which is why the profile of A_4 is simply the ZN uniform state. Continuing in the parameter beyond the profile A_2 yields the critical value of $\omega_{NZ} = -8.394$, and the DB branch ceases to exist to the right of this value.

These purely real vector soliton solutions may propagate in the CNLS system they were derived in, providing that they are temporally stable. We know that the uniform states, which the orbit is formed from, are spatially hyperbolic (SH) on the whole branch by our definition; AUTO would struggle to admit these solutions if the uniform states were not SH. The temporal stability of the soliton itself can be explored by considering the spectrum of the CNLS and, since the front solutions are derived from SHATS states, one expects nearby stable VS solutions. Examples of strongly nonlinear BD and DB solitons are shown in Fig. 6.3. The evolution shown in Fig. 6.3(a) is precisely the profile of the DB soliton shown at the point A_2 in Fig. 6.2(a), only with the peak position shifted and centred to $x = 0$. Note that the bifurcation parameter is given as $\omega_A = -9.430$ at this point on the solution branch. In contrast, the evolution shown in Fig. 6.3(b) is precisely the profile of the BD soliton shown at the point A_3 in 6.2(b). The bifurcation parameter is given as $\omega_A = -10.798$ at this point on the solution branch. We see that it is relatively simple to find these VS solutions numerically, providing that we have a valid starting point in the travelling front solution. These solutions are available in a wide variety of CNLS systems and we, therefore, expect such real-valued profiles to appear in the CNLS system that is governed by the MTI parameters.

6.2.2 Complex soliton profiles

From previous collision analysis of fronts and grey solitons, we know that VS solutions which yield complex profiles are possible in the CNLS; one particular example has already been shown in Fig. 5.12. Measuring parameters of this VS solution, refracting in the front-grey soliton collision, we see that only ω_A and C_g are altered upon collision. One can use this information to find precisely the VS solution profile that is shown in this collision by numerically continuing in these parameters in AUTO. Let us consider the system where the VS refraction occurs and explore the precise structure of the complex VS profile that appears out of the collision, i.e. consider the system parameters $d_1 = -1$, $g_1 = 2$, $g_2 = 4$, $d_2 = -3$, $g_3 = 5$, and $g_4 = 8$. We have already produced the AUTO plot for the bifurcation of the travelling front in this system, shown in Fig. 6.2(b).

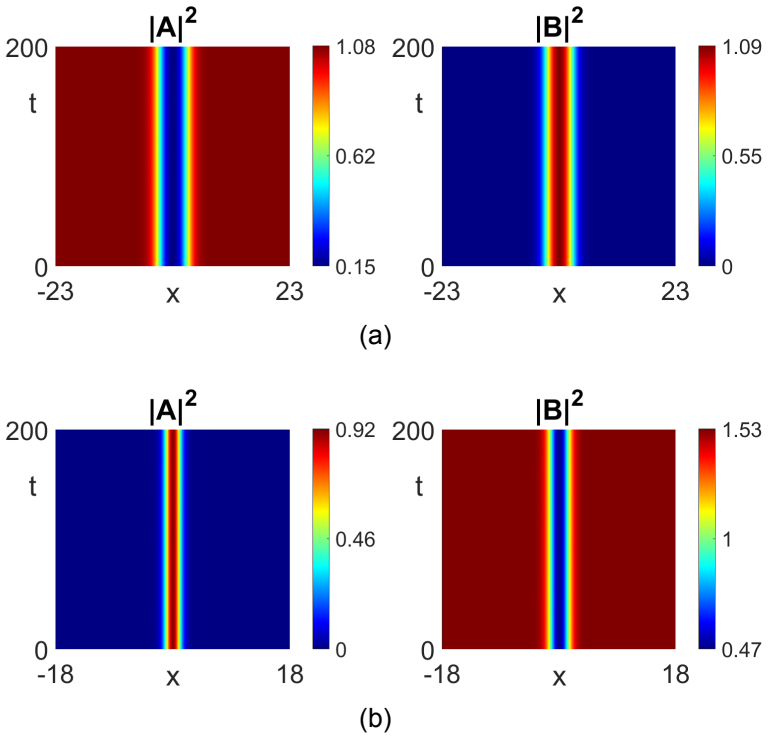

Figure 6.3: Purely real VS solutions in the comoving reference frame. Evolution is shown for the profile in their respective CNLS system and profiles are taken as (a) point A_2 from Fig. 6.2(a) and (b) point A_3 from Fig. 6.2(b).

By measuring the soliton profile, in the space-time plot of the refraction, one can approximate the value of the carrier frequency to be $\omega_A = -9.987$. We can extract the profile found by AUTO, on the solution branch, at this particular value of the continuation parameter. The profile of both ϕ and ψ components are shown in Fig. 6.4(a) at the point B_1. It has already been shown that the profiles on this solution branch take the form of purely real BD solutions, which is precisely what one expects since the refracting VS is precisely a BD soliton. Further to this, since we know that the group velocity of the BD is different from the original travelling front velocity, one has to break the original assumption of $C_g = 2d_1k_A = 2d_2k_B$ numerically. The problem that is now solved in AUTO is then extended to Eqs. (5.3-5.4), where complex coefficients are now included so complex profiles are expected.

When one measures the group velocity of the refracted VS the value is given as $C_g = 7.147$. If we numerically continue in the parameter C_g, from the purely real profile given at B_1, then we see a symmetric solution branch centred at the value of the travelling front group velocity $C_g = 5.093$. The solution branch is shown in Fig. 6.4(b). This complex conjugation symmetry is caused by the particular structure of the imaginary coefficients, $(2d_1k_A - C_g)$ and $(2d_2k_B - C_g)$ for ϕ and ψ respectively, as well as the reversible boundary condition on $\zeta = 0$. This is somewhat expected since the velocity-reversal $(C_g \to -C_g)$ of a grey

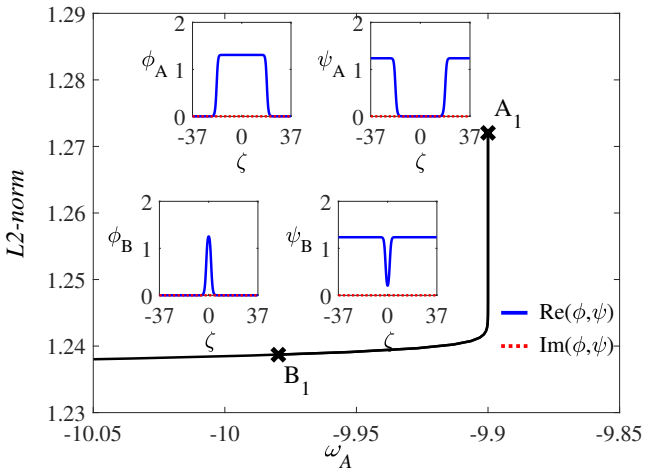

(a)

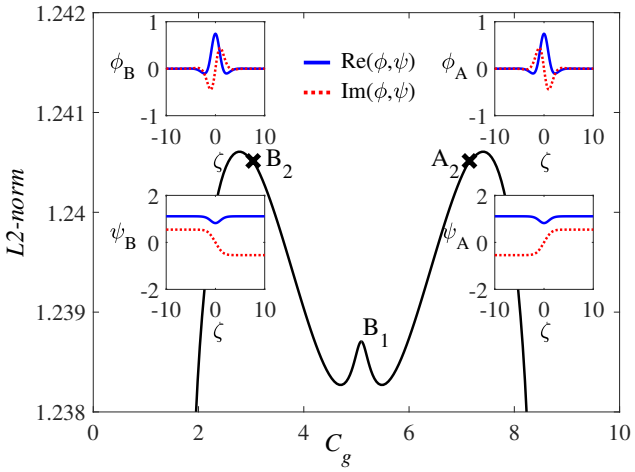

(b)

Figure 6.4: Bifurcation diagrams and subsequent profiles are shown for bifurcation parameter (a) ω_A followed by (b) C_g. Profiles are shown in terms of their real (blue-solid) and imaginary (red-dashed) parts. All other parameters k_A, k_B, ω_B, g_{1-4}, and d_{1-2} are fixed to those in Fig. 5.6(b); domain size is fixed as $L = 74.026$ to impose periodicity.

soliton in the scalar NLS equation is also the complex conjugate profile. The profile shown at the point A_2 is exactly that of the VS seen in the original space-time collision of Fig. 5.12, shown as a bifurcation of the original front structure. This observation is important since it shows that the collision of the front and grey soliton produced a VS structure that can be related back to the original front solution.

The numerical analysis presented above shows that VS solutions can be formulated, in the CNLS system, with different group velocities to the travelling fronts. In the grand scheme of the work, this allows more freedom when looking for solutions to the MTI lattice, since one can theoretically continue the solution to a nearby vector soliton with differing C_g. For our current analysis, this is important since we can now collide the vector solitons appropriately and

qualitatively discuss the dynamics of the collisions.

6.2.3 Qualitative BD collision dynamics

For the purpose of the collision analysis, it suffices to consider only one of the BD and DB type solutions; we will choose to collide BD solutions. This is permitted since we know that a DB soliton can be written as a BD soliton if we interchange the components A and B, whilst recognising that the system and travelling wave notation will now be also swapped around, e.g. $d_1 \leftrightarrow d_2$ etc. Let us first consider the particular system that produced the VS refraction and explore the collision behaviour of interacting BD solitons. We already know that the solution branch and subsequent profiles look like that of Fig. 6.4(b). Imposing a periodic initial condition is the major problem when considering the collision of these VS without any radiation or imperfections in the profile. One way around this problem is to consider the conjugate profiles A_2 and B_2 shown in Fig. 6.4(b). We see that implementing these two VS solutions side-by-side provides a periodic initial condition that can be evolved efficiently in the CNLS. To formulate this generally, let us denote any given group velocity on the right-continued branch $C_g^{(1)}$ with a symmetric point on the left-continued branch $C_g^{(2)}$, such that the average of the two is $(C_g^{(1)} + C_g^{(2)})/2 = C_g^{(0)}$, where $C_g^{(0)}$ is the real profile velocity of the initial front solution. It is recognised, through the solution branch symmetry, that the complex conjugate profile of the refracting VS from Fig. 5.12 will be given by the profile at B_2 with velocity $C_g^{(2)} = 3.038$. We can then impose the corresponding profiles of A_2 and B_2 and subsequently evolve them in the CNLS system. Figure 6.5(a) shows us the collision behaviour of the two VS solutions in the reference frame comoving with the original group velocity $C_g^{(0)}$. The vector solitons interact with each other, producing an obvious positional shift after the collision, and with radiating structures propagating away at differing velocities from the interaction point. The propagating radiation is expected from the interaction of nonlinear structures in non-integrable systems, which is also why large radiation was seen in the collision of the front and soliton in Fig. 5.12. The radiation is also symmetric, in reference to the comoving frame, which is expected since the profiles have equivalent amplitudes and only differ by complex conjugation. There is no energy transfer between the two VS profiles after the collision and both solitons lose equivalent energy to the radiation.

For comparison of different CNLS system parameters, via the same AUTO process, one may look for VS solutions that propagate in the nearly integrable system that we have considered throughout; see, for instance, Fig. 5.5. When

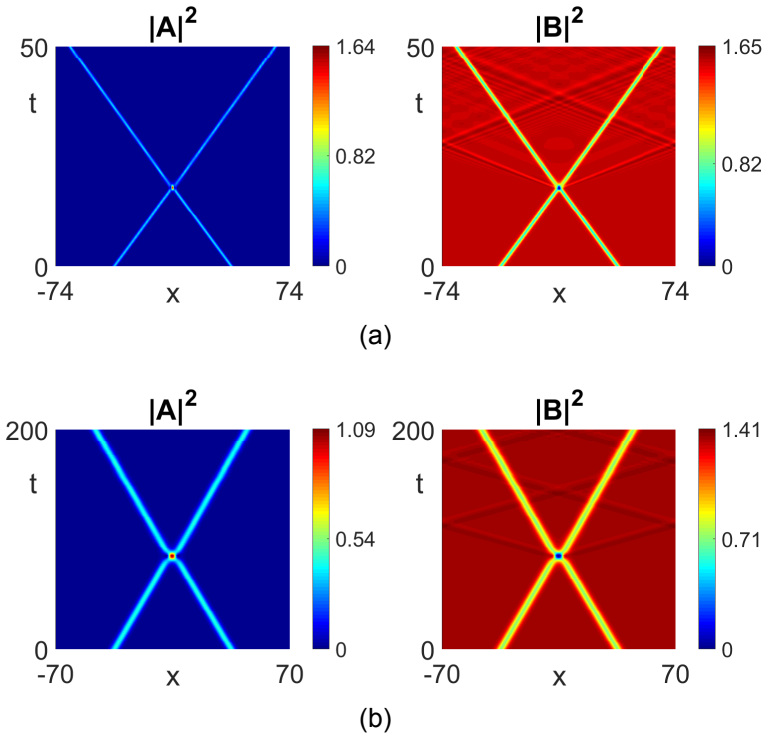

Figure 6.5: Collision of vector solitons in the non-integrable CNLS equation. (a) Collision of the two VS solutions B_1 and B_2, shown in Fig. 6.4(b), with corresponding soliton velocities $(C_g^{(1)}, C_g^{(2)}) = (7.147, 3.038)$. (b) Two solitons colliding in the nearly-integrable CNLS ($d_{1-2} = -1$, $g_{1-3} = 2$, and $g_4 = 3$) with wave parameters $(k_A, k_B, \omega_A, \omega_B) = (-2.697, -2.697, -9.7, -10)$, and soliton velocities $(C_g^{(1)}, C_g^{(2)}) = (5.789, 5)$.

one numerically continues in ω_A, followed by C_g, we can find complex conjugate VS solutions that are governed by the travelling wave parameter space $(\omega_A, \omega_B, k_A, k_B) = (-9.7, -10, -2.697, -2.697)$ and the symmetric velocities on the solution branch are chosen as $(C_g^{(1)}, C_g^{(2)}) = (5.789, 5)$. Figure. 6.5(b) shows a similar interaction of the VS to the previous system, only with less radiation originating from the collision point. This decrease in radiation size is expected since the system parameters here are much closer to the integrable, defocusing Manakov system.

It is also a possibility to initialise and collide VS solutions with different amplitudes. The process is very particular due to periodic boundary conditions of the evolution and the complex profile of the dark-soliton component. An efficient way to implement the two VS solutions is to ensure that they have the same complex uniform B state on the boundaries of their profiles in AUTO. If we first continue to two different values of the bifurcation parameter $\omega_A^{(1,2)}$, then we can find two purely real VS solutions of different amplitudes. Then, for each of these profiles, we continue in the group velocity C_g such that the amplitude of the imaginary parts of the B-component are equivalent on $\zeta = 0$ and $\zeta = L$. Finally, taking the complex conjugation of one of the profiles will allow the two

initialised VS to satisfy periodic boundary conditions. Figure 6.6(a) shows the collision of two vector solitons, imposed as described above, with different initial amplitudes. These solitons are found in the nearly integrable system numerically with the wave parameters $(k_A, k_B, \omega_B) = (-2.697, -2.697, -10)$, left soliton frequency/velocity $(\omega_A^{(1)}, C_g^{(1)}) = (-9.672, 6.070)$, and right soliton frequency/velocity $(\omega_A^{(2)}, C_g^{(2)}) = (-9.585, 5.425)$. The first observation to make here is that the radiation propagating away from the collision centre is now asymmetric. This causes less energy to be lost from the smaller, and faster, left soliton overall. Quantitatively, the left bright soliton decreases to 97.56% of its original amplitude, with the corresponding dark soliton decreasing its energy depression to 96.58% of the original. The right bright soliton amplitude decreases to 97.93% of the original, whilst the corresponding dark soliton depression becomes 92.89% of the original depression. Amongst the asymmetry of the collision, and therefore asymmetric energy loss, qualitatively there is also a key difference in the collision of solitons with non-equivalent amplitudes. This difference is the possibility of energy and polarisation (phase) transfer between the two structures during the collision.

An example of this energy transfer can be seen in the space-time plot shown in Fig. 6.6(b), as well as the corresponding profiles shown in Fig. 6.6(c). The VS collision here is proposed in the same system that exhibited the original VS refraction, i.e. from Fig. 5.12. We, once again, observe an asymmetric radiation propagating away from the collision of two VS with non-equivalent amplitudes. In this case, there is also a decrease (increase) of the amplitude for the left (right) bright solitons, with an associated decrease (increase) in the dark depression of energy. Quantitatively, the left bright soliton decreases to 92.19% of the original amplitude, whilst the left dark soliton decreases to 94.81% of the original depression. In contrast, the right bright soliton increases to 106.44% of the original amplitude, whilst the right dark soliton depression increases to 106.66%.

To find energy transfers between BD/DB solitons of similar amplitudes, like those in Fig. 6.5, we note that there is a particular freedom of multiplying the components of a VS by a constant arbitrary phase, $\exp\{i\Theta_{A,B}\}$. This phase freedom is only appropriate for bright components, since VS collisions require that the equilibria be unchanged after multiplication. This subsequently means that we may consider a free phase parameter Θ_A for BD solitons or Θ_B for DB solitons. The profiles will then have equivalent amplitudes (absolute) but yield the opportunity for different polarisation. The polarisation of a particular BD soliton is governed by the argument of the peak ratio of the two soliton components. By denoting the values of the bright and dark peaks by B_{Max} and

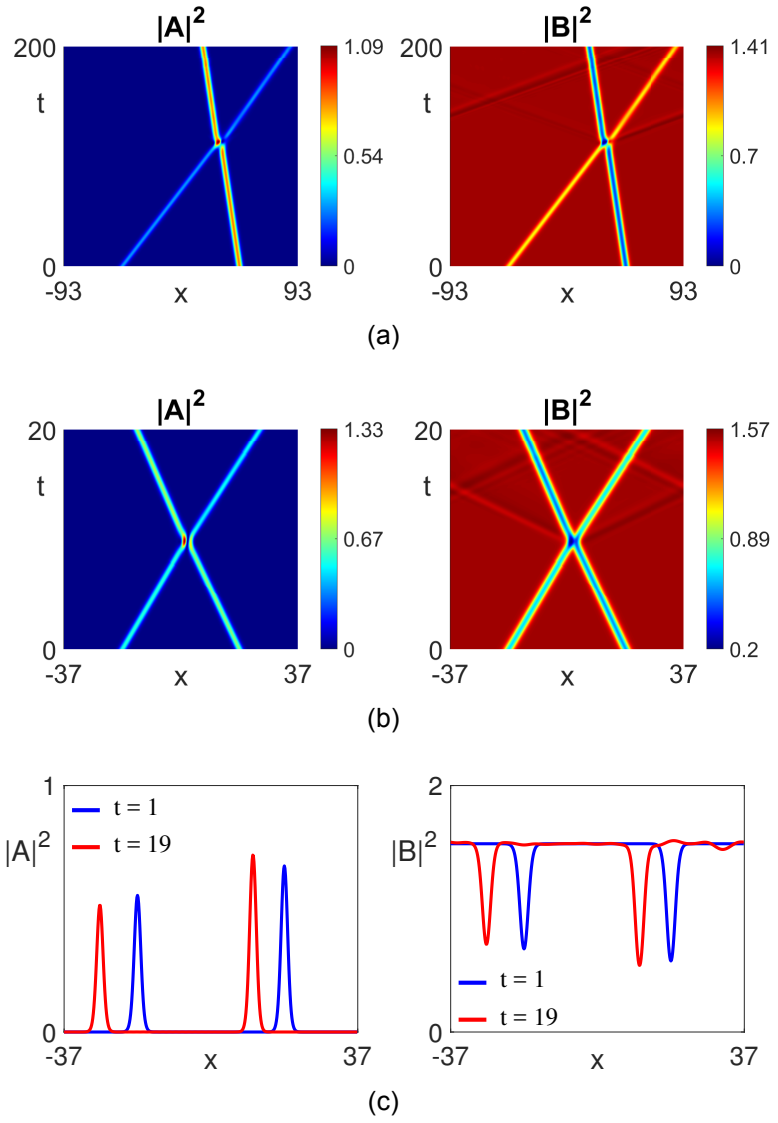

Figure 6.6: Collision of vector solitons with non-equivalent amplitudes. (a) CNLS system from Fig. 6.5(b) with wave parameters $(k_A, k_B, \omega_B) = (-2.697, -2.697, -10)$, and left soliton frequency/velocity $(\omega_A^{(1)}, C_g^{(1)}) = (-9.672, 6.070)$, right soliton frequency/velocity $(\omega_A^{(2)}, C_g^{(2)}) = (-9.585, 5.425)$. (b,c) CNLS system from Fig. 6.5(a) with wave parameters $(k_A, k_B, \omega_B) = (-2.546, -0.849, -9.8)$, and left soliton frequency/velocity $(\omega_A^{(1)}, C_g^{(1)}) = (-9.987, 7.147)$, right soliton frequency/velocity $(\omega_A^{(2)}, C_g^{(2)}) = (-10.2, 6.741)$. (b) Space-time plot. (c) Profiles before/after collision. For the profiles, the left VS are always shown in the domain $x < 0$, and the right VS are shown in the domain $x > 0$.

D_{Min}, we may define the argument of the ratio B_{Max}/D_{Min} by the quantity ρ. In general, the ratio is an arbitrary complex value which defines the polarisation $\rho \in [0, 2\pi)$ and, for the purposes of colliding VS, we will denote the polarisation of the left (right) initialised VS by ρ_L (ρ_R). We expect colliding VS with equivalent amplitudes and polarisations $\rho_L = \rho_R$ to yield no energy transfer, like those considered in Fig. 6.5. Numerically, it is found that the most prominent energy transfer between components happens when there is a $\pm\frac{\pi}{2}, \pm\frac{3\pi}{2}$ shift between the two polarisations, i.e. when $|\rho_L| - |\rho_R| = \pm\frac{\pi}{2}$. By altering the phase param-

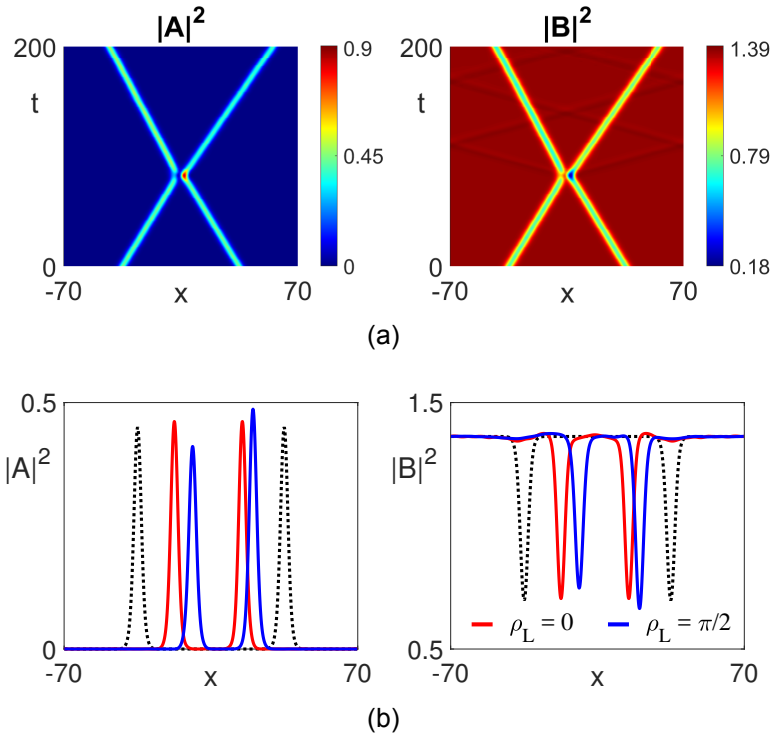

Figure 6.7: Energy transfer of BD solitons with different polarisation. (a) Space-time plot showing the collision of the VS from Fig. 6.5(b), with VS polarisation $\rho_L = \frac{\pi}{2}$ and $\rho_R = 0$. (b) Profiles after collision for the polarisation $\rho_L = 0$ (red) and $\rho_L = \frac{\pi}{2}$ (blue). The profile before collision (black-dotted) is shown to visualise energy transfer. The left soliton is always shown in the left-half plane, $x < 0$, with the right soliton in the right-half plane, $x > 0$.

eter Θ_A of one of the VS, say the left initialised soliton, then the polarisation of the VS is altered proportionally. If one chooses $\Theta_A = \frac{\pi}{2}$, then this gives $\rho_L = \frac{\pi}{2}$ for the left soliton, whilst the right soliton is unchanged with $\rho_R = 0$. Note that, since the only free phase parameter for BD solitons is Θ_A, there is no difference between the definition of Θ_A and ρ. However, when one has both $\Theta_{A,B}$ as free parameters, like for BB solutions, then $\Theta_A \neq \rho$.

The evolution of the VS collision from Fig. 6.5(b) is adapted by allowing this particular choice of $\Theta_A = \frac{\pi}{2}$, and the new evolution, with different left soliton polarisation, is portrayed in Fig. 6.7(a). It is immediately obvious that the radiation propagating away from the collision point is unchanged by this new polarisation. There is, however, a visible difference in the amplitudes of the two VS after collision. This difference is seen more clearly in Fig. 6.7(b), where the profiles are shown after the collision for the original evolution with $\Theta_A = 0$ (red) and for the evolution with $\Theta_A = \frac{\pi}{2}$ (blue). The initial profile, before collision, is shown in black as a baseline for amplitude change. There is a clear energy transfer during the inelastic collision of VS with different polarisations.

One key aspect of these collisions, that we are yet to mention explicitly, is the shift of the group velocity C_g after the collision. This shift is seen more clearly

when the polarisation is altered in Fig. 6.7. Due to the radiation propagating away from the collision point and the non-integrable nature of these CNLS systems, the profiles after the collision differ slightly from those before the collision, thus, they must be governed by a new set of parameters. There is an inherent difficulty when analytically predicting the amount of energy transferred during collision and subsequently when predicting the parameters governing the VS after collision. We note that the qualitative analysis presented is only valid for the collisions above, and solitons with different travelling wave parameters, or non-integrable CNLS with different system parameters, may provide different collision behaviour. The inelastic nature of the collisions tells us that the interaction of BD/DB solitons may yield more complicated dynamics like solitons merging together [128]. Since the profile of the outgoing solitons are different from those going in to the collision, paired with radiation, the state-transformation function is difficult to find here. We aim to study these inelastic collisions in more detail in future work, with the possibility of defining the state-transformation of these collisions, numerically or analytically, for specific choices of CNLS parameters.

6.3 Exact analytical solutions

We will now discuss the prospect of vector soliton solutions that possess the same type of soliton in each component, namely bright-bright (BB) and dark-dark (DD) solitons. In terms of weakly nonlinear bifurcations from the ZZ and NN uniform states, BB and DD solutions appear as codimension-2 bifurcations where two of the travelling wave parameters are related via some function of the remaining parameters. Some of these solutions, however, can be shown to be exact and their profile can be written down explicitly, with relevant conditions for their existence given. For both BB and DD solutions, we note that only three travelling wave parameters are needed to express a BB or DD profile, which is caused by the uniqueness of RHOs of the travelling wave ODE. For example, consider two separate reductions of the CNLS to the complex ODE given by Eqs. (5.3-5.4), with equation and parameters indexed by the superscript (1) and (2). A given VS of the CNLS system is represented by a RHO in each of the two reduced ODES, ODE$^{(1)}$ and ODE$^{(2)}$, but the two ODEs are related by multiplying the CNLS A component by exp$\{i(k_A^{(1)}-k_A^{(2)})x\}$ and the B component by exp$\{i(k_B^{(1)}-k_B^{(2)})x\}$. Assuming that each RHO is unique in each ODE then the RHOs of ODE$^{(1)}$ and ODE$^{(2)}$ must be equivalent, which eliminates $k_A,\ k_B$ as free parameter choices. Note that the parameters $\omega_A,\ \omega_B$, and C_g are essential

for removing time-dependence, so these are considered true free parameters. The parameters k_A and k_B are needed, however, to reduce a plane-wave to an equilibrium, so we can introduce these back in as free parameters when one has a RHO from a component with a non-zero background field.

Let us first focus on RHOs that form from the ZZ uniform state, which translates to a BB soliton solution of the CNLS system. To search for these solutions we consider the ansatz of

$$A = A_1 \text{sech}\,(W\zeta)\,\mathrm{e}^{i\theta_1\zeta - i\omega_A t}, \tag{6.32}$$

$$B = A_2 \text{sech}\,(W\zeta)\,\mathrm{e}^{i\theta_2\zeta - i\omega_B t}, \tag{6.33}$$

where $\zeta = x - C_g t$ as before, and the quantities $A_{1,2},\ W,\ \theta_{1,2}$ are calculated by subbing the ansatz into the CNLS (4.7–4.8). By definition, $W,\ \theta_{1,2}$ are strictly real parameters whilst $A_{1,2}$ may take complex values. For equivalence of the component widths, one must impose restrictions on one of the free parameters; we choose ω_B for simplicity. This parameter is then given by the following function of the free parameters,

$$\omega_B = \frac{C_g^2}{4}\left(\frac{d_2}{d_1^2} - \frac{1}{d_2}\right) + \frac{d_2}{d_1}\omega_A, \tag{6.34}$$

which gives an explicit formulation for the width of the soliton envelope as,

$$W^2 = \frac{-C_g^2 - 4d_1\omega_A}{4d_1^2}. \tag{6.35}$$

The remaining quantities are found simply by equating the terms of the equation, with the substituted ansatz, to yield

$$|A_1|^2 = \frac{2W^2(d_1 g_3 - d_2 g_2)}{g_1 g_3 - g_2 g_4},\quad |A_2|^2 = \frac{2W^2(d_2 g_1 - d_1 g_4)}{g_1 g_3 - g_2 g_4},$$
$$\theta_1 = \frac{C_g}{2d_1},\quad \theta_2 = \frac{C_g}{2d_2}. \tag{6.36}$$

We can see that there are explicit criteria for BB solitons to exist, assuming also that the ZZ state is itself SHATS. The formula for the width (6.35) tells us that the envelope is only defined when $C_g^2 + 4d_1\omega_A < 0$, so the free travelling wave parameters must be chosen to preserve this. The exponents $\theta_{1,2}$ are always defined by the parameter choice, whilst the amplitudes $A_{1,2}$ are only defined when $|A_{1,2}|^2 > 0$. Note that the deciding factors for whether the amplitude is physical, generically, come directly from the system parameters, so one can not choose travelling wave parameters that force the amplitude to exist. For

a physical BB soliton solution to exist, one must require $\text{sgn}(g_1 g_3 - g_2 g_4) = \text{sgn}(d_1 g_3 - d_2 g_2) = \text{sgn}(d_2 g_1 - d_1 g_4)$. If the system parameters produce $g_1 g_3 - g_2 g_4 = 0$, then we see that the amplitudes are undefined under this formation and there is no direct solution, other than the trivial case, if the numerators are zero. If one of the numerators is zero, with the denominator non-zero, then the only permitted solution is the scalar bright soliton presented in the NLS equation. For clarity, these scalar soliton solutions are given by one of,

$$|A_1|^2 = 0, \quad |A_2|^2 = \frac{2d_2 W^2}{g_3},$$
$$|A_1|^2 = \frac{2d_1 W^2}{g_1}, \quad |A_2|^2 = 0.$$

where each of the solutions represents the scalar bright soliton of the decoupled systems. The special case of the Manakov system permits BB solitons, due to its integrability, that are already described well in the context of their collision and the subsequent impact on collision-based computing [158, 97, 159, 174]. By appropriate substitutions, the ansatz (6.32-6.33), where the function (6.34) gives $\omega_A = \omega_B$, can be written in the same manner as the well-known Manakov BB solution [97, 174] with 6 free, real parameters governing the amplitude, width, and position of the VS. Generalising the system parameters further, to the regime of the symmetrically coupled CNLS, one finds that the amplitudes must be equivalent, given by $|A_{1,2}|^2 = 2W^2 d_1/(g_1 + g_2)$, and the relationship (6.34) is, once again, given simply as $\omega_B = \omega_A$. The relationship between the frequencies ω_A and ω_B relies purely on the dispersion coefficients $d_{1,2}$, and an equivalence of the two will always force an equivalence of the frequencies. We may consider $A_{1,2} > 0 \in \mathbb{R}$ without loss of generality.

Generically, the BB solutions (6.32-6.36) are represented by 2 free parameters (C_g, ω_A), however, we also have the freedom of multiplying each component by an arbitrary phase, $\exp\{i\Theta_A\}$ and $\exp\{i\Theta_B\}$ respectively. This produces a new solution with the same parameters, given by Eq. (6.36), but a new phase of the profile, and thus polarisation. The BB solutions we have proposed analytically are governed by a family of 4 free parameters $(C_g, \omega_A, \Theta_A, \Theta_B)$. Let us now explore explicit BB solutions in the non-integrable CNLS systems, where we will consider $\Theta_A = \Theta_B = 0$ unless specified otherwise.

The first observation to note is the lack of BB solutions in those systems that we have already proposed in earlier Chapters. This is because we have primarily considered equations that permit the ZN and NZ uniform states to be SHATS, which contradicts the existence of BB amplitudes (6.36) since $d_{1,2} < 0$ and $g_{1-4} > 0$ can not allow both $|A_1| > 0$ and $|A_2|^2 > 0$ simultaneously. Let us

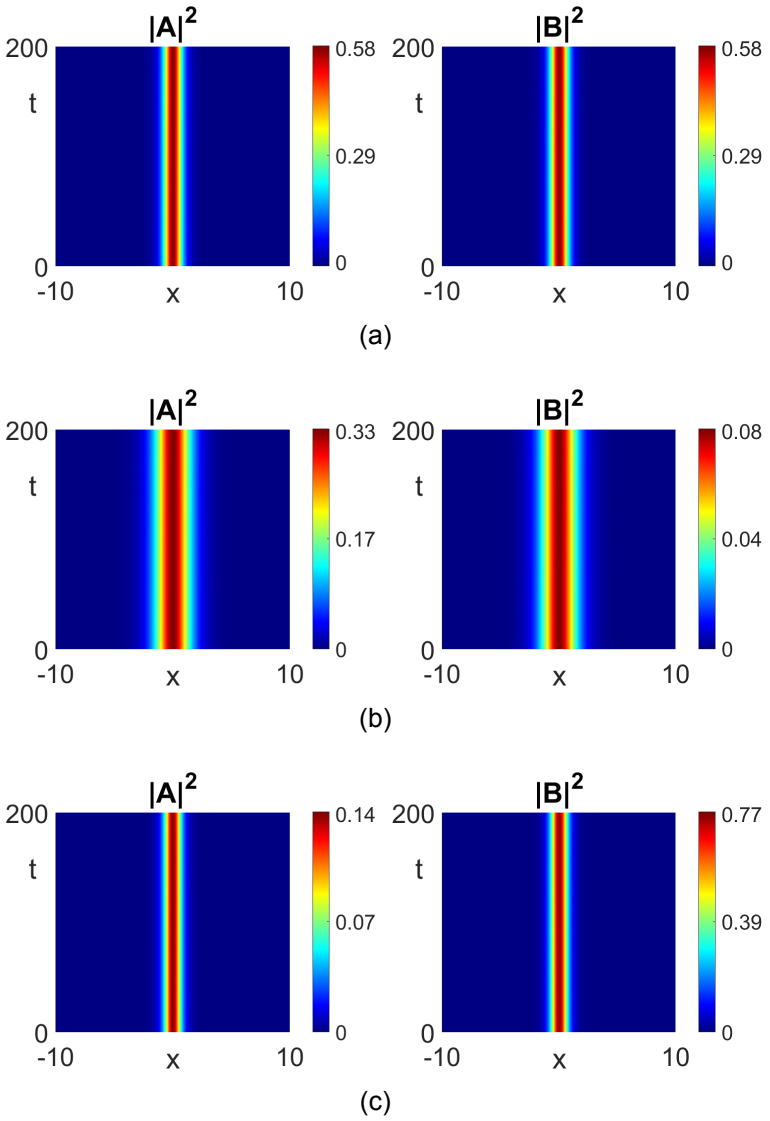

Figure 6.8: BB soliton solutions in a CNLS system with nonlinear parameters $g_1 = g_3 = 2$ and $g_2 = g_4 = 4$, and imposed phase parameters $\Theta_{A,B} = 0$. The remaining system and travelling wave parameters are given by; (a) $(d_1, d_2, C_g, \omega_A) = (1, 1, 1, -1)$, (b) $(d_1, d_2, C_g, \omega_A) = (1, 1.5, 2, -1.5)$, and (c) $(d_1, d_2, C_g, \omega_A) = (0.8, 0.5, 1, -2)$. All solutions are shown in the co-moving reference frame with appropriate C_g.

propose a nearly-integrable system related to the focusing Manakov system (FM1) by altering the XPM parameters away from the integrable regime. The non-integrable regime that we consider is that of the XPM parameters being double the SPM parameters, which we denote as FM2. Explicitly, the nonlinear parameters are written as $g_1 = g_3 = 2$ and $g_2 = g_4 = 4$, where we propose the cases of equal and unequal masses of $d_1,\ d_2$. The first case of equal masses ($d_1 = d_2 = 1$) is shown in Fig. 6.8(a) in the comoving reference frame, where we have imposed a BB soliton with frequency $\omega_A = -1$ and group velocity $C_g = 1$. This choice of the parameters leads to equal amplitudes $A_{1,2} = 0.764$, and equivalence of $\omega_A = \omega_B$. The width of the soliton is subsequently $W =$

1.323. Figures. 6.8(b–c) show the cases of unequal masses, with ($d_2 > d_1$) and ($d_1 > d_2$) respectively. The first, Fig. 6.8(b), shows a variation of only one dispersion parameter, $d_2 = 1.5$, from unity. The travelling wave parameters are chosen as $(C_g, \omega_A) = (2, -1.5)$, which leads to a pulse width of $W = 0.707$. The non-equivalence of the dispersion coefficients gives non-equivalent amplitudes $A_1 = 0.577$ and $A_2 = 0.289$, with a corresponding frequency parameter of $\omega_B = -1.417$. Lastly, the case of both dispersion parameters being non-unity, $d_1 = 0.8$ and $d_2 = 0.5$, is shown in Fig. 6.8(c). Here, we have imposed travelling wave parameters of $(C_g, \omega_A) = (1, -2)$, which leads to a pulse width of $W = 1.452$. Non-equivalent amplitudes are subsequently given by $A_1 = 0.375$ and $A_2 = 0.880$, with the frequency parameter $\omega_B = -1.555$. This case produces no differences from that of varying only one dispersion parameter, but showcases that the unequal masses is not limited to specific choices of one parameter, which is expected through scaling freedom of the CNLS.

The next VS solution that one may consider is that of a depression of energy in each component, corresponding to a dark-dark VS solution. These solutions form RHOs from the NN uniform state and we can search for the explicit form of these solutions by considering the ansatz

$$A = A_1 \mathrm{tanh}\,(W\zeta)\,\mathrm{e}^{i\theta_1\zeta - i\omega_A t}, \tag{6.37}$$

$$B = A_2 \mathrm{tanh}\,(W\zeta)\,\mathrm{e}^{i\theta_2\zeta - i\omega_B t}, \tag{6.38}$$

where $A_{1,2}$ are generally complex amplitudes and $\theta_{1,2},\ W$ are real-valued quantities. Similarly to the case of the BB analysis, one finds that the equivalent width of the component envelopes causes a direct relationship between the frequencies ω_A and ω_B, which is given explicitly by Eq. (6.34). The width of the envelopes is then written as,

$$W^2 = \frac{C_g^2 + 4d_1\omega_A}{8d_1^2}, \tag{6.39}$$

with the remaining quantities governed by,

$$|A_1|^2 = \frac{2W^2(d_2 g_2 - d_1 g_3)}{g_1 g_3 - g_2 g_4}, \quad |A_2|^2 = \frac{2W^2(d_1 g_4 - d_2 g_1)}{g_1 g_3 - g_2 g_4},$$

$$\theta_1 = \frac{C_g}{2d_1}, \quad \theta_2 = \frac{C_g}{2d_2}. \tag{6.40}$$

The DD solution then represents a π phase shift of the plane waves with wavenumbers $C_g/(2d_1)$ and $C_g/(2d_2)$ for each component respectively. From the definition of the pulse width (6.39), we see that a condition for existence is given by

the sign of the quantity $C_g^2 + 4d_1\omega_A > 0$, precisely the opposite of the condition for BB solitons. Further to this, one requires physical equilibria which requires $\text{sgn}(g_1g_3 - g_2g_4) = \text{sgn}(d_2g_2 - d_1g_3) = \text{sgn}(d_1g_4 - d_2g_1)$. Once again, we see that the amplitude being physically viable relies completely on the CNLS system parameters, so there are various CNLS systems that simply do not permit the existence of such VS solutions. The symmetrically coupled CNLS system yields a simplification to the amplitudes, where the two component background fields are governed equivalently by $|A_{1,2}|^2 = -2W^2d_1/(g_1 + g_2)$. The relationship between the two frequencies are, once again, reliant on the dispersion coefficients $d_{1,2}$ and the remaining free parameter C_g.

As with the BB solutions, one has the freedom to multiply the DD components by the arbitrary phases $\exp\{i\Theta_A\}$ and $\exp\{i\Theta_B\}$. Analytically we have 4 free parameters $(C_g, \omega_A, \Theta_A, \Theta_B)$ governing the structure of the DD solutions, which are unique in their description. The major difference with the DD solitons, in comparison to BB solitons, is the existence of the non-zero background field for each component. Since one can always multiply the uniform equilibria of each component by the spatial wavenumbers $\exp\{ik_Ax\}$ and $\exp\{ik_Bx\}$ respectively, to give a new solution embedded in a plane-wave, we have the extra free parameters $k_{A,B}$ that govern the uniquely defined DD family of solutions. We do not know analytically how these extra free parameters affect the profile itself, so we opt to numerically continue the analytical solutions in AUTO to find the numerical profiles of the DD family. For the benefit of the reversible boundaries in AUTO we implement the DD solutions with a purely imaginary, positive amplitude without loss of generality, i.e. $A_1 = \sqrt{|A_1|^2}i$ and $A_2 = \sqrt{|A_2|^2}i$. Let us now explore explicit DD solutions in the non-integrable CNLS system, where we will propose $\Theta_A = \Theta_B = 0$ for all upcoming profiles.

As a case study we impose the system parameters $d_1 = d_2 = -1$, $g_1 = 4$, $g_2 = 2$, $g_3 = 5$, and $g_4 = 3$, since this system exhibits a wide range of SHATS NN states and the parameters explicitly satisfy the amplitude criteria put forward by Eq. (6.40). One set of the remaining free parameters that exhibits a stably propagating DD solution is that of $(C_g, \omega_A, k_A, k_B) = (1, -5, 0, 0)$, where we know $\omega_B = -5$ and the profile width can be calculated as $W = 1.62$. The evolution of this DD solution can be seen in Fig. 6.9(a) in the frame comoving in C_g, with component amplitudes calculated as $A_1 = 1.061i$ and $A_2 = 0.612i$. Note that, due to periodic boundary conditions of the implemented PDE solver, we have initialised two DD solitons but have focused on a single profile in the right-half plane. We can then numerically continue this analytical DD profile in AUTO, with appropriate boundary conditions, to find profiles where $k_A \neq 0$. The result of this process is shown in Fig. 6.9(b), where we have considered the an-

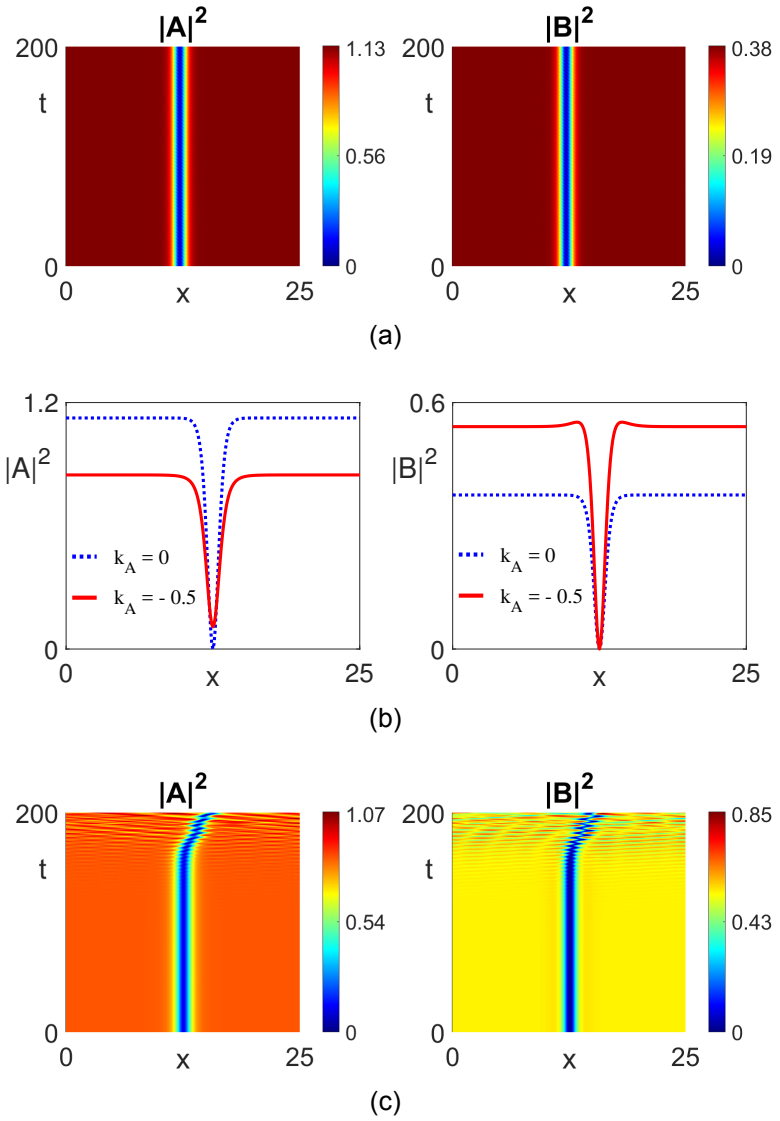

Figure 6.9: DD soliton solutions in the non-integrable CNLS equation with system parameters $d_1 = d_2 = -1$, $g_1 = 4$, $g_2 = 2$, $g_3 = 5$, and $g_4 = 3$. (a) Evolution of the profile with free parameters $(C_g, \omega_A, k_A, k_B) = (1, -5, 0, 0)$. (b) Profile obtained by AUTO continuation in the parameter k_A, from the profile of (a), to the profile governed by the free parameters $(C_g, \omega_A, k_A, k_B) = (1, -5, -0.5, 0)$. (c) Evolution of the new (red-solid) profile from (b).

alytical profile (blue-dashed) and continued along the branch of DD solutions to the profile found at the value of $k_A = -0.5$ (red-solid). We have explicitly chosen this value of $k_A = -0.5$ because the domain size L incorporates periodic solutions with respect to both wavenumbers $C_g/(2d_1) + k_A$ and $C_g/(2d_2)$, such that each component may propagate on this domain. Note that we have chosen to numerically continue in k_A only, but one could have easily chosen k_B to continue in, or even a combination of the two. In general, the structure of the profiles resembles that shown in Fig. 6.9(b), where the profiles may gain some energy in the background plane waves or the dip can be raised to resemble a grey soliton-like component. This example profile is evolved in the CNLS, as

seen in Fig. 6.9(c), and propagates stably for a long time period. Note, however, that at some point in finite-time ($t > 150$) temporal instability is shown and the profile breaks up despite the background field being SHATS. This is in direct contrast to the original $k_A = 0$ profile of Fig. 6.9(a) where the structure propagates for a large time frame ($t > 5000$).

We emphasise that the analytical BB and DD solutions, presented in Eqs. (6.32–6.33) and Eqs. (6.37–6.38) respectively, only cover a portion of the full solution set of BB and DD solutions. We have presented the number of free parameters required to represent the profiles analytically in this way, but it should be noted that there is also the freedom to numerically continue in ω_B and break the equal width assumption of the envelopes. The numerical profiles are then no longer guaranteed to be governed by simple sech and tanh envelopes, as was the case of DD solutions when we numerically shifted in the parameter k_A (Fig. 6.9(b–c)). Since this section focuses purely on exact analytical solutions, we only note this numerical freedom, and extension to the full family of BB/DD solutions, and focus on those BB/DD described by the analytical sech and tanh envelopes with equal width across both components.

The linear stability of solutions of the CNLS is well-described for the integrable, Manakov regime; see, for instance, the study of linear stability of plane-waves through the formation of a Lax pair [59, 60]. In the non-integrable regime, one can not form a Lax pair in this manner so we propose that the BB solution is linearly stable providing that the ZZ state is SHATS, and if the CNLS evolution of the BB exhibits no unstable behaviour over a long time-frame. Similarly for the NN uniform state and DD solutions. By this definition, we have seen both temporally stable and unstable evolution of these soliton profiles in the CNLS. One must be careful when numerically computing the CNLS spectrum of these structures as some methods, like the finite difference scheme, may yield spurious point eigenvalues despite no temporal instabilities being present in the evolution. This is precisely what we found for some BB and DD solitons, where weak noise added to the profile does not produce any unstable behaviour, despite unstable predictions from the spectrum. Therefore, more advanced techniques would be required to accurately portray the full stability for these solutions. Such methods include the use of Chebyshev spectral methods [33] and the construction of the Evans function [165, 74]. For the purpose of our current analysis, in relation to long-lasting MTI soliton solutions, the presented solutions are already viable as propagating nonlinear structures.

6.3.1 Qualitative BB collision dynamics

As a final note for this chapter we will briefly consider the collision dynamics of these analytical profiles. The family of BB solitons is governed by 5 free, real parameters $(C_g, \omega_A, \omega_B, \Theta_A, \Theta_B)$, so collisions are subsequently reliant on these 5 parameters of each soliton. Previously we stated that the DD solitons were governed by 7 free parameters $(C_g, \omega_A, \omega_B, \Theta_A, \Theta_B, k_A, k_B)$, however, we note that VS collisions require that the equilibria be unchanged after multiplication, so the phase freedom is not relevant for components with non-zero backgrounds. Due to this, the collisions of DD solitons are reliant on the 5 free, real parameters $(C_g, \omega_A, \omega_B, k_A, k_B)$ of each soliton. The velocity of the DD solitons is related explicitly to the wavenumber of the background field and, as such, difficulties are presented when one attempts to initialise two of these structures, with differing C_g, on the same background with periodic boundary conditions. We focus only on the collision of the BB solitons as these collisions are of greater interest to us; these collisions can be directly compared to Manakov solitons presented in the FM1 system that have been discussed with respect to collision-based computing [159]. Note also that we focus purely on the analytically-described BB solutions (6.32–6.33), where ω_B is no longer a free parameter and is governed explicitly by Eq. (6.34).

Recall that we previously analysed the effect of the initial polarisation on the energy transfer of BD solitons during collisions. The same process can be achieved for BB solitons, only now we have an extra degree of freedom by altering the phase of the B component. Initialising two BB solitons with arbitrary amplitudes/widths is significantly easier here, in comparison to BD/DB solitons, since we have a zero-background field. Let us consider the collision of BB solitons in the FM2 system with equal masses $d_1 = d_2 = 1$, where an example of a stably propagating solution is already shown in Fig. 6.8(a). We may collide this BB soliton by initialising it on the domain with its velocity-reversed partner, i.e. the solution governed by the free parameters $(C_g, \omega_A, \Theta_A, \Theta_B) = (-1, -1, 0, 0)$. We know, from the previous evolution, that this structure is stable so we need not worry about any instabilities developing from the propagation of the structure itself. The collision of the two BB solitons, with state variables $\rho_L = 0$ and $\rho_R = 0$, is depicted in Fig. 6.10(a). As expected from the interaction of the two zero-polarisation structures, one observes no energy transfer across the components or between solitons. The collision is near-elastic and the outgoing solitons have minimal change to the velocity C_g. These solitons are also capable of a cascade of collisions, with little radiation loss from the interaction.

When one alters the polarisation of either BB solution, there is an expected

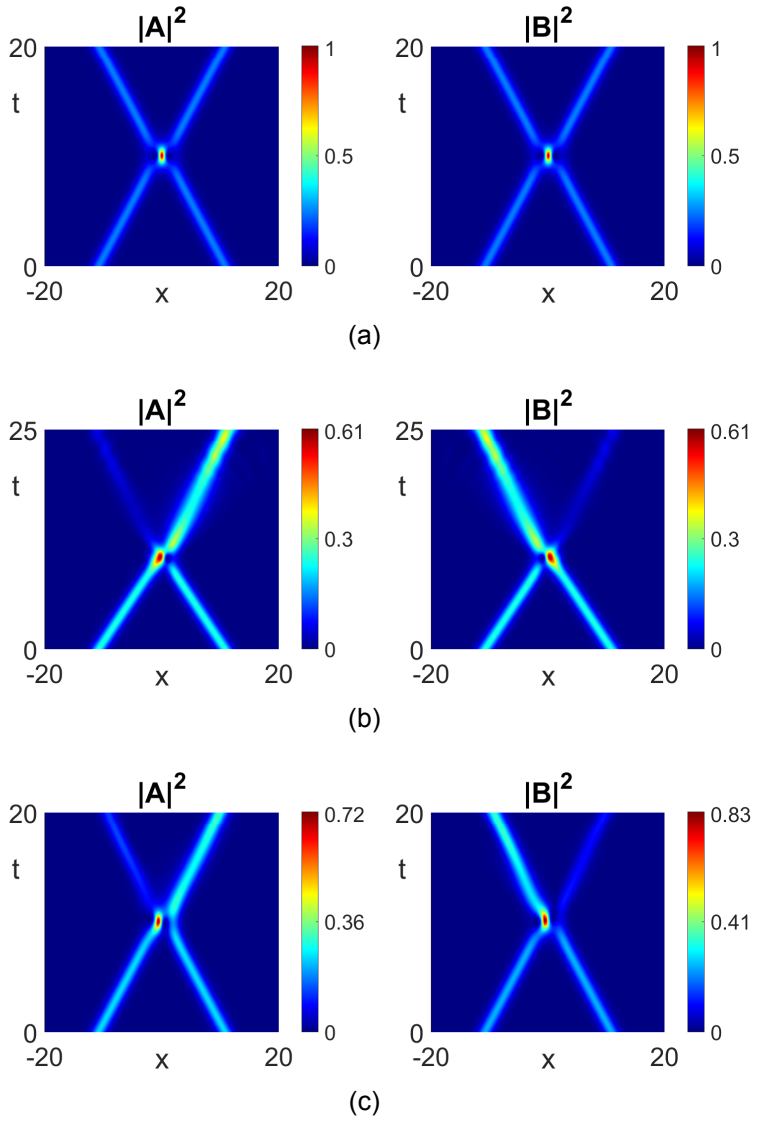

Figure 6.10: Collisions of BB solitons in the FM2 system. (a) Left soliton parameters $(C_g, \omega_A, \Theta_A, \Theta_B) = (1, -1, 0, 0)$ and right soliton parameters $(C_g, \omega_A, \Theta_A, \Theta_B) = (-1, -1, 0, 0)$. (b) Left soliton parameters $(C_g, \omega_A, \Theta_A, \Theta_B) = (1, -1, \frac{\pi}{2}, 0)$ and right soliton parameters $(C_g, \omega_A, \Theta_A, \Theta_B) = (-1, -1, 0, \frac{\pi}{2})$. (c) Left soliton parameters $(C_g, \omega_A, \Theta_A, \Theta_B) = (1, -1, \frac{\pi}{2}, \frac{\pi}{10})$ and right soliton parameters $(C_g, \omega_A, \Theta_A, \Theta_B) = (-1, -1, 0, 0)$.

transfer of energy through an inelastic interaction. Unlike the collisions of BD solitons, we may allow a polarisation shift of the A component, as well as the B component. Figure 6.10(b) depicts the collision of two solitons with equivalent widths/velocity to before, only now with a phase multiplication of the left soliton by $(\Theta_A, \Theta_B) = (\frac{\pi}{2}, 0)$ and $(\Theta_A, \Theta_B) = (0, \frac{\pi}{2})$ to the right soliton. This multiplication gives the new polarisations $\rho_L = \frac{\pi}{2}$ and $\rho_R = \frac{3\pi}{2}$. There is a distinct energy transfer between the two solitons during collision, as well as a polarisation shift that is not depicted here. The inelastic collision dictates a shift of the velocity after interaction with a considerable amount of radiation. Since the collision is inelastic, with inherent radiation as a consequence, the collisions may not cas-

cade like the near-elastic case and the profiles are lost over many interactions. We also showcase the effect of altering Θ_A for both left and right solitons in Fig. 6.10(c). Here, the phase multiplications are governed by $(\Theta_A, \Theta_B) = (\frac{\pi}{2}, 0)$ and $(\Theta_A, \Theta_B) = (\frac{\pi}{10}, 0)$ for the left and right solitons respectively. There is a clear energy transfer and a shift in the C_g parameter after collision. Though not shown explicitly here, BB solitons with different amplitudes/velocities may collide and produce energy transfer, with shifts of the parameters after collision like those in Fig. 6.10(b–c). Shifts of initial polarisation can also make this transfer less/-more prominent in these collisions as one would expect.

It is clear that the amount of energy transferred between the two conjugate, reversed-velocity profiles depends heavily on the polarisation of the two. This energy transfer is difficult to predict due to the excess radiation propagating from the collision point and, unlike collisions in FM1 [97, 174], one can not analytically produce the state-transformation function of the interaction. One major problem with the state-transformation is the fact that the width and velocity are not conserved for the general, non-zero polarised collision. We note also that the collisions shown in Fig. 6.10 are only valid for the particular parameter set $(C_g, \omega_A) = (\pm 1, -1)$, and only for the FM2 system. Collisions of general travelling wave parameters, and in CNLS systems with general system parameters, are not guaranteed to behave in the same way to above. These collisions rely on the stability of the two solitons and on how much radiation propagates from the interaction of the two structures. We aim to study these generalised collisions further in future work, and the possibility of describing the inelastic behaviour through numerical, or even analytical, state-transformations. For the purpose of the current work on MTI solitons, it suffices to say that many soliton solutions are a possibility and the energy transfer of these solitons will signify underlying CNLS dynamics.

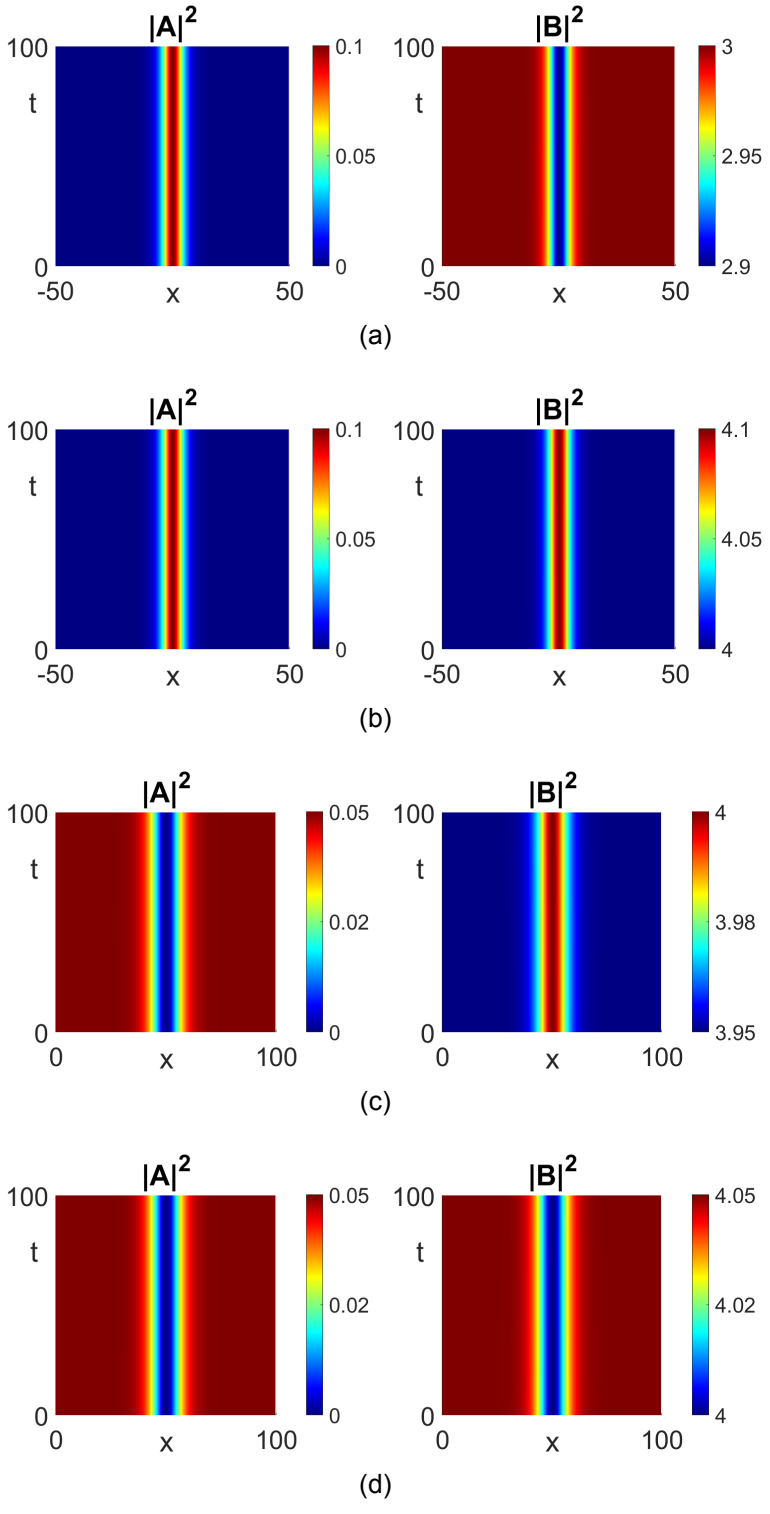

Figure 6.11: Weakly-nonlinear solutions bifurcating from ZN. Solutions are found by considering the asymptotic expansion and performing numerical continuation. (a,b) sech solutions governed by Eqs. (6.19-6.20), with the parameter product (a) $g_3 g_4 > 0$ and (b) $g_3 g_4 < 0$. (c,d) tanh solutions governed by Eqs. (6.21-6.22), with the parameter product (c) $g_3 g_4 > 0$ and (d) $g_3 g_4 < 0$.

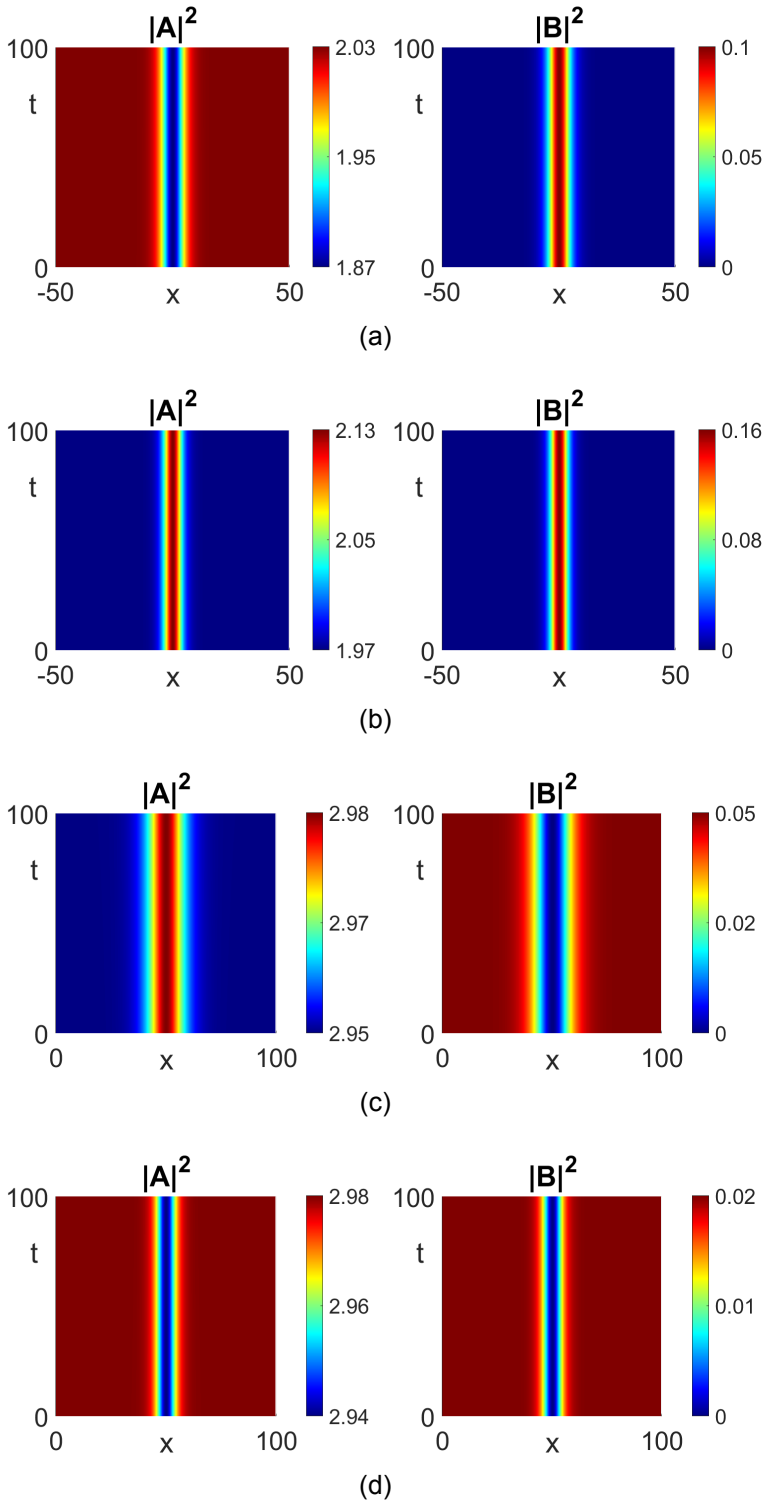

Figure 6.12: Weakly-nonlinear solutions bifurcating from NZ. (a,b) sech solutions governed by Eqs. (6.28-6.29), with the parameter product (a) $g_1 g_2 > 0$ and (b) $g_1 g_2 < 0$. (c,d) tanh solutions governed by Eqs. (6.30-6.31), with the parameter product (c) $g_1 g_2 > 0$ and (d) $g_1 g_2 < 0$.

Chapter 7

Turing bifurcations in CNLS

In this chapter we will discuss the possibility of non-pitchfork bifurcations that can occur in the system of (5.9-5.10). In particular, we notice that the eigenvalues of the NN uniform state can take a complex quartet configuration, as seen in Eq. (5.21). This leads to the possibility of a reversible double-Hopf bifurcation with 1:1 resonance [94] (Turing bifurcation in spatial dynamics), which may be supercritical or subcritical like in the previous pitchfork analysis. Comparisons can be drawn to the optics setting, where a Turing bifurcation corresponds to modulational instability [14]. Solution branches near the Turing bifurcation may be translated back to the CNLS equation to form periodic and localised states. We provide a weakly nonlinear analysis near the Turing value, analysing the conditions required for the value to exist, and produce a brief description of the dispersion relation near this value. We make a brief comparison of the derived travelling localised solutions to a conservative analogue of the Swift-Hohenberg equation, where the modulation equation and similar localised solutions are well studied in general [116, 34]. Finally, the chapter discusses the implication of these periodic and localised solutions, and we draw final conclusions in relation to the MTI.

7.1 Analysis of the Turing bifurcation

If one considers the real-valued ODE (5.9-5.10) and the eigenvalues of the NN uniform state, given by Eq. (5.21), then it is apparent that there is the opportunity for richer configurations of the values. In particular if one focuses on non-zero eigenvalues, so that we now have a real-valued 4D ODE in the dependent variables $(\phi, \phi_\zeta, \psi, \psi_\zeta) \in \mathbb{R}$, then we may have four different configurations of

the four remaining eigenvalues, which can be explicitly written as

(i): the eigenvalues form a complex quartet,

(ii): the eigenvalues are strictly real,

(iii): two values are strictly real, and the other two are purely imaginary,

(iv): the eigenvalues are purely imaginary.

As discussed in Sec. 5.1, the uniform state is only spatially hyperbolic with configurations (i) and (ii). The transition from (ii) to (iii) was discussed previously in Sec. 6.1, and corresponds to the pitchfork bifurcations, given by ω_{ZZ}, ω_{ZN} and ω_{NZ}. We see that there is the possibility of new codimension-1 bifurcations for NN, in comparison to the other uniform states, where transitions to and from (i) may take place. Transitions between configurations in such 4D reversible ODE systems have been well studied [40, 35] and the analysis is readily adaptable for us to utilise in our case. It is clear from the eigenvalues that transitions through the configuration (i) occurs when the discriminant of the spatial characteristic equation is zero. Formally, this is the same as allowing the inequality (5.22) to be equal, i.e.

$$\left(\frac{g_1\phi_0^2}{d_1} - \frac{g_3\psi_0^2}{d_2}\right)^2 + 4\frac{g_2g_4}{d_1d_2}\phi_0^2\psi_0^2 = 0. \tag{7.1}$$

To be consistent with the pitchfork bifurcations, we will keep the travelling wave parameter ω_A as the bifurcation parameter. By substituting NN into Eq. (7.1), we find that there are two critical values, which we will denote as

$$\omega_{\Delta_\pm} = \frac{C_g^2}{4d_1} + \frac{(4d_2\omega_B - C_g^2)(\mu_1 \pm \mu_2)}{4d_2\mu_3} \tag{7.2}$$

where

$$\mu_1 = d_2g_1^2g_3(d_1g_3 + d_2g_2) + d_1g_1g_3g_4(d_1g_3 - d_2g_2) - 2d_1d_2g_2^2g_4^2$$

$$\mu_2 = 2d_1d_2(g_1g_3 - g_2g_4)\sqrt{g_2g_4(g_2g_4 - g_1g_3)}$$

$$\mu_3 = g_3^2(d_2g_1 + d_1g_4)^2 - 4d_1d_2g_2g_3g_4^2.$$

The only obvious constraint on the CNLS system parameters that is imposed is $g_2g_4(g_2g_4 - g_1g_3) > 0$, since ω_A is restricted to the real space. By substituting the Turing values into the NN eigenvalues (5.21) we show the multiplicity-2 set of eigenvalues, that collide pair-wise, are governed by,

$$\lambda_{\Delta_{(\pm1,\pm2)}} = \pm\sqrt{\frac{g_3(C_g^2 - 4d_2\omega_B)\mu_4}{2d_2\mu_3}}, \tag{7.3}$$

where

$$\mu_4 = (d_1 g_4 + d_2 g_1)(g_2 g_4 - g_1 g_3) \pm (d_1 g_4 - d_2 g_1)\sqrt{g_2 g_4 (g_2 g_4 - g_1 g_3)},$$

and the subscripts ± 1, ± 2 refer to the first and second pair-wise eigenvalues, with ω_{Δ_+} and ω_{Δ_-} substituted in respectively. When Eq. (7.3) are strictly real the collision of eigenvalues occurs on the real-axis of the eigenvalue plane $(\mathcal{R}\mathrm{e}(\lambda), \mathrm{Im}(\lambda))$. In this case the configuration transitions from (i) to (ii), which corresponds to a Belyakov-Delaney bifurcation [39, 40]. We are not particularly interested in this case since the NN state remains hyperbolic through this transition, only changing type from a saddle to a saddle-focus. We are, instead, interested purely in the case of transitions from (i) to (iv) that corresponds to Eq. (7.3) being purely imaginary. This is precisely the Turing bifurcation, which has been studied in a wide array of systems such as the forced-complex Ginzburg-Landau equation (FCGLE) [35] and the Swift-Hohenberg equation [34]. Assuming that Eq. (7.3) is imaginary, let us re-write this as $\lambda_{\Delta_{(\pm 1,\pm 2)}} = \pm k_{\Delta_\pm} i$, where the quantities

$$k_{\Delta_\pm} = \sqrt{\frac{g_3(4d_2\omega_B - C_g^2)\mu_4}{2d_2\mu_3}} \tag{7.4}$$

are described as the Turing wavenumbers that govern the spatially-periodic oscillations of bifurcating solutions.

7.1.1 Existence conditions

We have already shown the criterion for the Turing value to exist, i.e. $g_2 g_4 (g_2 g_4 - g_1 g_3) > 0$, however another vital component is whether or not the NN itself exists at the given critical values of $\omega_A = \omega_{\Delta_\pm}$. In the upcoming analysis we will formulate criteria that must be implemented on the parameters for this to be true. As we know, depending on the direction of the pitchfork bifurcation, the NN state only exists due to the critical values of ω_{ZN} and ω_{NZ}. If these two values do not produce a pitchfork bifurcation, then the NN state does not exist for the fixed CNLS system parameters and fixed (ω_B, C_g). The first observation to make from Sec. 6.1 is that, for each of the pitchfork critical values, the parameters must satisfy

$$\omega_{ZN}: \ \frac{(C_g^2 - 4d_2\omega_B)}{4d_2 g_3} > 0, \quad \frac{g_3 \delta_{ZN}}{g_2 g_4 - g_1 g_3} > 0,$$

$$\omega_{NZ}: \ \frac{(C_g^2 - 4d_2\omega_B)}{4d_2 g_4} > 0, \quad \frac{g_4 \delta_{NZ}}{g_1 g_3 - g_2 g_4} > 0,$$

where we have denoted $\delta_{ZN} = \omega_A - \omega_{ZN}$ and $\delta_{NZ} = \omega_A - \omega_{NZ}$. If conditions are satisfied for both ω_{ZN} and ω_{NZ}, then the NN state bifurcates from both; if only one is satisfied then bifurcation is only permitted from that state and if neither are satisfied then NN is not permitted. We can see from the conditions above that there are four cases allowed by the choice of parameters. These are,

(a) Neither permit NN : $\quad \text{sgn}(g_3) = \text{sgn}(g_4) = -\text{sgn}(\frac{C_g^2}{4d_2} - \omega_B),$

(b) Only ω_{ZN} permits NN : $\quad \text{sgn}(g_3) = -\text{sgn}(g_4) = \text{sgn}(\frac{C_g^2}{4d_2} - \omega_B),$

(c) Only ω_{NZ} permits NN : $\quad -\text{sgn}(g_3) = \text{sgn}(g_4) = \text{sgn}(\frac{C_g^2}{4d_2} - \omega_B),$

(d) Both permit NN : $\quad \text{sgn}(g_3) = \text{sgn}(g_4) = \text{sgn}(\frac{C_g^2}{4d_2} - \omega_B),$

where the choice of travelling wave parameters may transition between cases (a) and (d), or (b) and (c). The remaining criterion, for each of the pitchfork values, depends on the relative sign of the quantity $g_2 g_4 - g_1 g_3$, and either g_3 or g_4. Case (a) is trivial and can not accommodate NN, so we ignore this case.

For the remaining cases, one must recall the condition imposed by the Turing value (7.2), i.e. $g_2 g_4 (g_2 g_4 - g_1 g_3) > 0$. Let us first consider case (b). If one assumes that the following quantity takes the sign of $g_4(g_2 g_4 - g_1 g_3) > 0$, then by deduction of the criteria, one must have $g_2 > 0$, $g_3(g_2 g_4 - g_1 g_3) < 0$, and subsequently $\delta_{ZN} < 0$. If we instead assume that $g_4(g_2 g_4 - g_1 g_3) < 0$, then the signs are reversed and this leads to $\delta_{ZN} > 0$. A very similar analysis can be formed for case (c). If we assume that $g_4(g_2 g_4 - g_1 g_3) > 0$, then $g_2 > 0$, and subsequently $\delta_{NZ} < 0$. If the reverse is assumed, then $g_2 < 0$, and $\delta_{NZ} > 0$. Finally, for case (d) one has both δ_{ZN} and δ_{NZ}, but they always have opposing signs. If we assume $g_4(g_2 g_4 - g_1 g_3) > 0$, then $g_2 > 0$ and $g_3(g_2 g_4 - g_1 g_3) > 0$. This forces $\delta_{ZN} > 0$ and $\delta_{NZ} < 0$. If the inequality signs of the parameters are flipped then this imposes $\delta_{ZN} < 0$ and $\delta_{NZ} > 0$. We now have explicit intervals for which $\omega_{\Delta_\pm}$ must be located for there to be a physically-viable Turing value. These intervals are summarised, for each case, in Table. 7.1.

7.1.2 Real-valued amplitude equation

To sufficiently analyse the periodic and localised states near the Turing bifurcation value, we impose a weakly nonlinear, multiple scale ansatz like we did for the pitchfork bifurcations in Sec. 6.1. The expansion takes the form of

Table 7.1: Existence intervals of the Turing values for the NN state, showing explicitly where the Turing value $\omega_{\Delta_\pm}$ must be located for each case of the parameters (b-d).

Case	sgn$(g_4(g_2g_4 - g_1g_3))$	Interval of existence
(b)	+	$\omega_{\Delta_\pm} < \omega_{ZN}$
(b)	-	$\omega_{\Delta_\pm} > \omega_{ZN}$
(c)	+	$\omega_{\Delta_\pm} < \omega_{NZ}$
(c)	-	$\omega_{\Delta_\pm} > \omega_{NZ}$
(d)	+	$\omega_{ZN} < \omega_{\Delta_\pm} < \omega_{NZ}$
(d)	-	$\omega_{NZ} < \omega_{\Delta_\pm} < \omega_{ZN}$

Eq. (6.4), only now we must write the variables $u_1,\ v_1,\ u_2,\ v_2, \cdots$ as functions of both the slow spatial variable $Z = \epsilon\zeta$ and the original variable ζ. The uniform state expansion terms $U_0,\ V_0,\ U_1,\ V_1, \cdots$ are constant. The bifurcation parameter expansion is explicitly given by $\omega_A = \omega_{\Delta_\pm} + \epsilon^2\delta$. We then, as before, substitute the multiple scale ansatz (6.4) into the ODE (6.1), restricting to the real variable space $(\phi, \psi) \in \mathbb{R}$, and consider the solvability conditions at each order of ϵ. The analysis then closely follows that of the FCGLE equation [35]. At $O(1)$, the equation is given by

$$(\mathcal{L}_0 + \mathcal{N}_0(U_0, V_0)) \begin{bmatrix} U_0 \\ V_0 \end{bmatrix} = \underline{0}, \tag{7.5}$$

where $\mathcal{L}_0,\ \mathcal{N}_0(U_0, V_0)$ are given by Eq. (6.5) and Eq. (6.7) respectively. This is solved by the NN uniform state itself, with the values of $\omega_A = \omega_{\Delta_\pm}$ substituted in. Explicitly, the variables $U_0,\ V_0$ are given by,

$$U_0 = \sqrt{\frac{(C_g^2 - 4d_2\omega_B)(\mu_3 g_2 - g_3(\mu_1 \pm \mu_2))}{4d_2\mu_3(g_2g_4 - g_1g_3)}}, \tag{7.6}$$

$$V_0 = \sqrt{\frac{(C_g^2 - 4d_2\omega_B)(g_4(\mu_1 \pm \mu_2) - g_1\mu_3)}{4d_2\mu_3(g_2g_4 - g_1g_3)}}. \tag{7.7}$$

At the next order of $O(\epsilon)$, one has

$$(\mathcal{L}_0 + \mathcal{N}_0(U_0, V_0) + \mathcal{N}_1(U_0, V_0)) \begin{bmatrix} u_1 + U_1 \\ v_1 + V_1 \end{bmatrix} + \mathcal{L}_1 \begin{bmatrix} U_0 \\ V_0 \end{bmatrix} = \underline{0}, \tag{7.8}$$

where $\mathcal{L}_1,\ \mathcal{N}_1(U_0, V_0)$ are given by Eq. (6.6) and Eq. (6.8) respectively. We may simplify this equation by substituting Eqs. (7.6-7.7) into Eq. (7.8), and extracting the Z, ζ-independent terms to deduce $U_1, V_1 = 0$. The critical Turing wavenumbers $k_{\Delta_\pm}$ are determined by the solvability of this equation, given precisely by our previous description in Eq. (7.4). With this satisfied, the solution at this

order can be written as,

$$\begin{bmatrix} u_1 \\ v_1 \end{bmatrix} = \begin{bmatrix} \aleph \\ 1 \end{bmatrix} \mathcal{A}(Z)\mathsf{e}^{ik_{\Delta_\pm}\zeta} + c.c., \tag{7.9}$$

where

$$\aleph = -\frac{2g_2U_0V_0}{2g_1U_0^2 - d_1k_{\Delta_\pm}^2},$$

and $\mathcal{A}(Z)$ is a complex envelope. Note that if $k_{\Delta_\pm}$ is purely imaginary then the spatial eigenvalues become real and the Turing analysis is not valid. This is expected since we mentioned previously that this is no longer a Turing bifurcation, but rather a Belyakov-Delaney bifurcation. Proceeding to the next order of $O(\epsilon^2)$, one obtains the equation

$$\begin{aligned}(\mathcal{L}_0 + \mathcal{N}_0(U_0, V_0) + \mathcal{N}_1(U_0, V_0)) \begin{bmatrix} u_2 + U_2 \\ v_2 + V_2 \end{bmatrix} \\ + (\mathcal{L}_1 + \mathcal{N}_2(u_1, v_1)) \begin{bmatrix} u_1 + U_1 \\ v_1 + V_1 \end{bmatrix} + \mathcal{L}_2 \begin{bmatrix} U_0 \\ V_0 \end{bmatrix} = \underline{0},\end{aligned} \tag{7.10}$$

where $\mathcal{L}_2,\ \mathcal{N}_2(u_1, v_1)$ are given by Eq. (6.6) and Eq. (6.9) respectively. If we first extract the ζ, Z-independent terms, then there is a clear non-trivial solution for the constants $U_2,\ V_2$, given by

$$\begin{bmatrix} U_2 \\ V_2 \end{bmatrix} = \delta \begin{bmatrix} \nu_1 \\ 1 \end{bmatrix} \nu_2 \tag{7.11}$$

where

$$\nu_1 = \frac{-g_3V_0}{g_4U_0}, \quad \nu_2 = \frac{g_4}{2(g_1g_3 - g_2g_4)V_0}.$$

The remaining variables can then be analysed by considering the following ansatz to this order,

$$\begin{bmatrix} u_2 \\ v_2 \end{bmatrix} = s_0 \begin{bmatrix} \chi_0 \\ 1 \end{bmatrix} |\mathcal{A}|^2 + s_1 \begin{bmatrix} \chi_1 \\ 1 \end{bmatrix} i\mathcal{A}_Z\mathsf{e}^{ik_{\Delta_\pm}\zeta} + s_2 \begin{bmatrix} \chi_2 \\ 1 \end{bmatrix} \mathcal{A}^2\mathsf{e}^{2ik_{\Delta_\pm}\zeta} + c.c. \tag{7.12}$$

where the coefficients $s_{0,1,2}$ and $\chi_{0,1,2}$ are found by substituting the ansatz into (7.10), and solving at each order of $\mathsf{e}^{nik_{\Delta_\pm}\zeta}$, for $n = 0, 1, 2$. At $n = 0$, the ansatz

provides us with the coefficient values

$$s_0 = \frac{2g_4(g_1U_0^2 - g_2V_0^2)\aleph + (3g_1g_3 - g_2g_4)U_0V_0 - 2g_1g_4U_0V_0\aleph^2}{U_0V_0^2(g_2g_4 - g_1g_3)}, \tag{7.13}$$

$$\chi_0 = -\frac{1}{2g_1U_0^2}\left(\frac{2g_2U_0 + 4g_2V_0\aleph + 6g_1U_0\aleph^2}{s_0} + 2g_2U_0V_0\right). \tag{7.14}$$

At $n = 1$, the operator $(\mathcal{L}_0 + \mathcal{N}_0(U_0, V_0) + \mathcal{N}_1(U_0, V_0))$ acting upon $\mathcal{A}_Z$ is singular since the second derivative w.r.t ζ for this term is replaced with $-k_{\Delta_\pm}^2$. Due to this, the two components are related linearly through

$$s_1 = \frac{-2k_{\Delta_\pm}\begin{bmatrix}1 & 0\end{bmatrix}\begin{bmatrix}d_1 & 0\\ 0 & d_2\end{bmatrix}\begin{bmatrix}\aleph\\ 1\end{bmatrix}}{\begin{bmatrix}1 & 0\end{bmatrix}\mathcal{M}\begin{bmatrix}\chi_1\\ 1\end{bmatrix}}, \tag{7.15}$$

where the choice of χ_1 is arbitrary, subject to $\chi_1 \neq \aleph$, and the matrix $\mathcal{M}$ is defined by replacing $\partial_{\zeta\zeta}$ with $-k_{\Delta_\pm}^2$ in $(\mathcal{L}_0 + \mathcal{N}_0(U_0, V_0) + \mathcal{N}_1(U_0, V_0))$. Let us impose $\chi_1 = 0$ for simplicity, which yields

$$s_1 = -\frac{d_1k_{\Delta_\pm}\aleph}{g_2U_0V_0}.$$

Finally, at $n = 2$, the coefficients for the $\mathcal{A}^2$ term are given by

$$s_2 = -\frac{(4d_1k_{\Delta_\pm}^2 - 2g_1U_0^2)P_1(\aleph) + 2g_4U_0V_0P_2(\aleph)}{4(-4d_1d_2k_{\Delta_\pm}^4 + 2(d_2g_1U_0^2 + d_1g_3V_0^2)k_{\Delta_\pm}^2 + (g_2g_4 - g_1g_3)U_0^2V_0^2)}, \tag{7.16}$$

$$\chi_2 = \frac{1}{(4d_1k_{\Delta_\pm}^2 - 2g_1U_0^2)}\left(\frac{P_2(\aleph)}{s_2} + 2g_2U_0V_0\right). \tag{7.17}$$

where, the polynomials $P_{1,2}$ in $\aleph$ are given by

$$P_1(\aleph) = 3g_3V_0 + 2g_4U_0\aleph + g_4V_0\aleph^2, \quad P_2(\aleph) = g_2U_0 + 2g_2V_0\aleph + 3g_1U_0\aleph^2.$$

The final order that we will consider, $O(\epsilon^3)$ yields the equation

$$\begin{aligned}(\mathcal{L}_0 + \mathcal{N}_0(U_0, V_0) + \mathcal{N}_1(U_0, V_0)) \begin{bmatrix} u_3 + U_3 \\ v_3 + V_3 \end{bmatrix} \\ + (\mathcal{L}_1 + \mathcal{N}_2(u_1 + U_1, v_1)) \begin{bmatrix} u_2 + U_2 \\ v_2 + V_2 \end{bmatrix} \\ + (\mathcal{L}_2 + \mathcal{N}_0(u_1 + U_1, v_1) + \mathcal{N}_1(u_2 + U_2, v_2) \\ + \mathcal{N}_3(u_2 + U_2, v_2)) \begin{bmatrix} u_1 + U_1 \\ v_1 + V_1 \end{bmatrix} = \underline{0}. \end{aligned} \tag{7.18}$$

When one extracts the Z, ζ-independent terms, the only solution is that of the trivial case, i.e. $U_3,\ V_3 = 0$. The solvability condition on the remaining set of terms can be obtained by multiplying the equation by the adjoint null-eigenvector of $\mathcal{M}$. This vector is given explicitly by

$$\begin{bmatrix} \Upsilon & 1 \end{bmatrix} \mathrm{e}^{-ik_{\Delta_\pm}\zeta}, \tag{7.19}$$

where $\Upsilon = g_4\aleph/g_2$. Substituting all prior information obtained from previous orders into the equation, we find the equation which governs the envelope $\mathcal{A}$, given by

$$a_{\Delta_\pm}\mathcal{A}_{ZZ} = \delta\mathcal{A} - b_{\Delta_\pm}\mathcal{A}|\mathcal{A}|^2, \tag{7.20}$$

where we have denoted

$$a_{\Delta_\pm} = \frac{-f_{\Delta_\pm}}{h_{\Delta_\pm}}, \quad b_{\Delta_\pm} = \frac{-g_{\Delta_\pm}}{h_{\Delta_\pm}}$$

and

$$f_{\Delta_\pm} = \aleph\Upsilon d_1 + d_2(1 - 2s_1k_{\Delta_\pm}),$$

$$\begin{aligned} g_{\Delta_\pm} =& 3(g_1\Upsilon\aleph^3 + g_4\aleph^2 + g_2\Upsilon\aleph + g_3) \\ &+ 2(s_0\chi_0 + s_2\chi_2)(3g_1U_0\aleph\Upsilon + g_2V_0\Upsilon + g_4U_0 + g_4V_0\aleph) \\ &+ 2(s_0 + s_2)(g_2V_0\Upsilon\aleph + g_2U_0\Upsilon + 3g_3V_0 + g_4\aleph U_0), \end{aligned}$$

$$\begin{aligned} h_{\Delta_\pm} =& \Upsilon\aleph + 2\Upsilon\nu_2(3g_1U_0\nu_1\aleph + g_2V_0\nu_1 + g_2V_0\aleph + g_2U_0) \\ &+ 2\nu_2(3g_3V_0 + g_4U_0\aleph + g_4U_0\nu_1 + g_4V_0\nu_1\aleph). \end{aligned}$$

Similarly to the Turing analysis of FCGLE [35], Eq. (7.20) takes the form of a

time-independent Ginzburg-Landau equation with real-valued coefficients, and admits the spatially-homogeneous solution

$$\mathcal{A} = \sqrt{\frac{\delta}{b_{\Delta_\pm}}}\mathrm{e}^{i\Theta}$$

with an arbitrary phase Θ. Translating this solution back to the full ODE, the branch of solutions, near the Turing bifurcation value, form spatially-periodic oscillations given by

$$\begin{bmatrix}\phi\\ \psi\end{bmatrix} = \begin{bmatrix}U\\ V\end{bmatrix} + 2\begin{bmatrix}\aleph\\ 1\end{bmatrix}\sqrt{\frac{\omega_A-\omega_{\Delta_\pm}}{b_{\Delta_\pm}}}\cos\left(k_{\Delta_\pm}\zeta+\Theta\right), \tag{7.21}$$

periodic in the Turing wavenumber, where we have omitted higher-order terms. These periodic states rely completely on the sign of the constant $b_{\Delta_\pm}$ and bifurcate towards $\omega_A > \omega_{\Delta_\pm}$ ($\omega_A < \omega_{\Delta_\pm}$) when $b_{\Delta_\pm}$ is positive (negative). As one would expect, Eq. (7.20) also admits Z-dependent solutions. One may have subcritical bifurcations to localised states of the form

$$\begin{bmatrix}\phi\\ \psi\end{bmatrix} = \begin{bmatrix}U\\ V\end{bmatrix} + 2\begin{bmatrix}\aleph\\ 1\end{bmatrix}\sqrt{\frac{\omega_A-\omega_{\Delta_\pm}}{b_{\Delta_\pm}/2}}\operatorname{sech}\left(\sqrt{\frac{\omega_A-\omega_{\Delta_\pm}}{a_{\Delta_\pm}}}\zeta\right)\cos\left(k_{\Delta_\pm}\zeta+\Theta\right), \tag{7.22}$$

which describes the formation of a train of pulses in the Turing wavenumber. This solution is presented as a homoclinic orbit parameterised by Θ. This parameter, however, takes particular values when one considers terms beyond all algebraic orders of the expansion, as discussed in [35]. Since the background field is non-trivial, and presents no up-down symmetry, the homoclinic solutions are restricted to those of even parity ($\Theta = 0, \pi$). Henceforth, we impose a phase of $\Theta = 0$, since this is sufficient for us to consider solutions of the CNLS system. We see from Eq. (7.22) that the signs of $a_{\Delta_\pm}$ and $b_{\Delta_\pm}$ must be equivalent for a solution to exist. If the signs of these constants are positive (negative) then we expect bifurcations towards $\omega_A > \omega_{\Delta_\pm}$ ($\omega_A < \omega_{\Delta_\pm}$). Due to the SHATS analysis, we expect localised solutions to be permitted asymptotically only when the equilibrium is of type (i), i.e. a complex quartet of eigenvalues. There are also supercritical bifurcations to front-like structures, that connect two out-of-phase states in the Turing wavenumber. As one expects, these are only permitted when $a_{\Delta_\pm}$ and $b_{\Delta_\pm}$ possess different signs. We exclude these states from this analysis since we are mainly interested in the localised solutions bifurcating

from the uniform state NN. A codimension-2 transition between the subcritical and supercritical cases can be formed when one of $a_{\Delta_\pm}$ or $b_{\Delta_\pm}$ becomes zero. Near this transition point, there is also the distinct possibility of phenomena known as homoclinic snaking [194]. This will be explored further in future work and it suffices, for now, to simply note this possibility since we are interested purely in the existence of localised states. Formally, we have found approximate spatially periodic and localised solutions (ϕ, ψ) to the travelling wave ODE (5.9-5.10), in close vicinity to the Turing value, using asymptotic methods. In order to find the exact spatial solutions of Eqs. (5.9-5.10) we use the asymptotic solutions as starting points in AUTO and numerically continue these into the strongly nonlinear regime. Just as in the previous section, the numerical spatial profiles found in AUTO will then evolve in the CNLS equation as coherent, travelling localised/periodic structures and propagate as prescribed by the set of the travelling wave parameters $(C_g, \omega_{A,B}, k_{A,B})$.

Let us now showcase some examples of localised solutions found in the non-integrable CNLS equation. If we allow the system parameters to be given by $d_1 = -2$, $g_1 = -7$, $g_2 = -3$, $d_2 = -6$, $g_3 = 1$, and $g_4 = 6$, then one has both values of $\omega_{\Delta_\pm}$ in the allowed interval of $\omega_{NZ} < \omega_{\Delta_\pm} < \omega_{ZN}$. In this particular case, we choose to fix the travelling wave parameters as $(C_g, \omega_B) = (9, -4)$. Restricting to these parameters, the critical values are given as $\omega_{\Delta_+} = -9.052$ and $\omega_{\Delta_-} = -8.289$. Here, the former is a Turing bifurcation, with the latter a Belyakov-Delaney bifurcation. Therefore, we will consider the weakly nonlinear expansion around the ω_{Δ_+} value. Localised solutions, found by continuing in AUTO into the strongly nonlinear regime, are shown in Fig. 7.1(a–b) in the reference frame comoving with C_g. Figure 7.1(a) is defined closer to the critical value, $\omega_A = -9.03$, so the amplitude of the wavetrain is relatively small. At this value, the NN uniform state is linearly unstable. As one moves further away from the critical value, and into the strongly nonlinear regime, one finds solutions with smaller envelopes and larger amplitudes, like that of Fig. 7.1(b) where we have chosen $\omega_A = -8.5$. The NN state is linearly stable for these travelling wave parameters. We note that both solutions produce temporal instabilities in finite-time, which is expected when one considers the spectrum, numerically, of these solutions in the CNLS. The localised state inherits the continuous spectrum of the background field, thus, an unstable NN produces an unstable localised state, but an unstable localised state does not necessarily infer an unstable NN. It is not expected that all NN states are to be stable when the spatial eigenvalues are complex since we mentioned previously, in Sec. 5.1.4, that not all spatially hyperbolic NN states are temporally stable. We expect there to be some localised states that are stable according to the

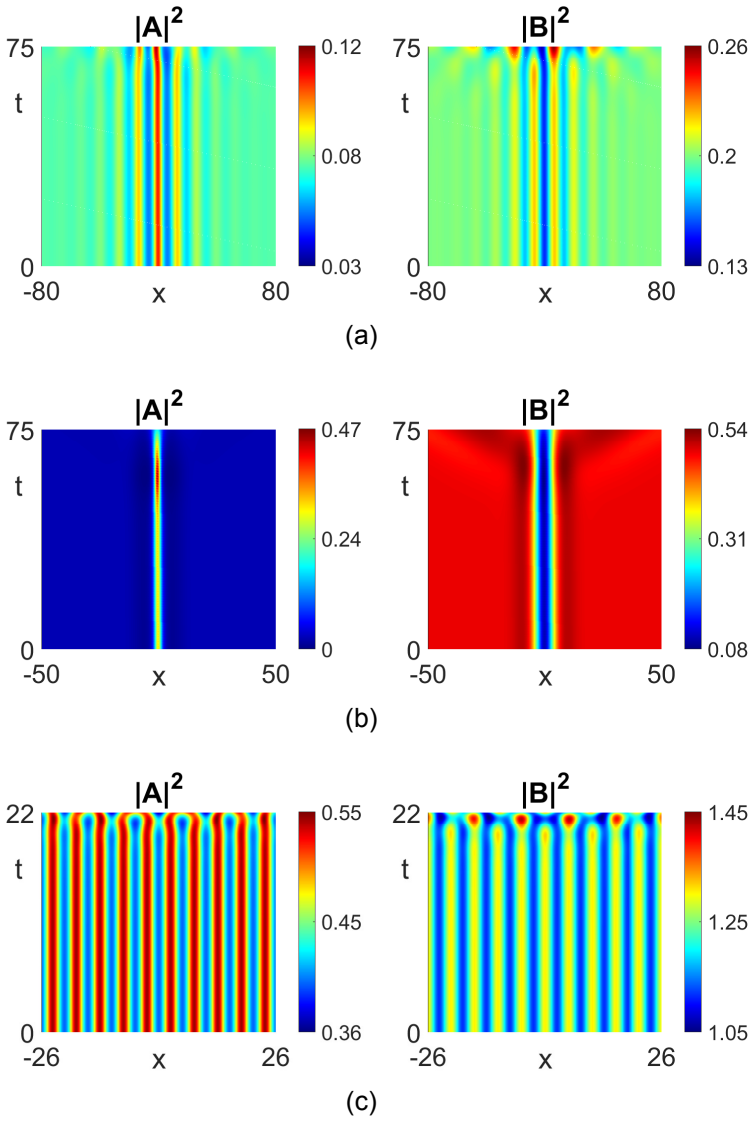

Figure 7.1: Localised and periodic states of the non-integrable CNLS system. System parameters are given by $d_1 = -2$, $g_1 = -7$, $g_2 = -3$, $d_2 = -6$, $g_3 = 1$, and $g_4 = 6$. (a,b) Localised solutions, in the comoving reference frame, with travelling wave parameters $(C_g, \omega_B) = (9, -4)$ and (a) $\omega_A = -9.03$, (b) $\omega_A = -8.5$. (c) Periodic state with travelling wave parameters $(C_g, \omega_A, \omega_B) = (0, 6.896, -4)$.

CNLS spectrum, but we are yet to find a system that exhibits this.

We can showcase an example of a periodic state by considering the same CNLS system parameters, but now fix the travelling wave parameters to $(C_g, \omega_B) = (0, -4)$. We impose a value of $C_g = 0$ for simplicity of initialising the structure on a periodic domain, but the analysis remains the same for $C_g \neq 0$. For these fixed parameter choices, one finds a Turing value at $\omega_{\Delta_+} = 6.867$ and a Belyakov-Delaney bifurcation at $\omega_{\Delta_-} = 11.752$. Continuing from the weakly nonlinear expansion of the former, we show the profile of a periodic state, found at $\omega_A = 6.896$, portrayed in Fig. 7.1(c). There is, once again, temporal instability of the solution. This modulational instability of periodic states, as well

as that of the front-like structures connecting two out-of-phase wavetrains, is commonly referred to, in pattern formation literature, as the Eckhaus instability [25, 185, 94, 92]. If one introduces a slow time scale variable $T = \epsilon^2 t$, then we find the modulation equation

$$ic_{\Delta_\pm}\mathcal{A}_T = -a_{\Delta_\pm}\mathcal{A}_{ZZ} - \delta\mathcal{A} + b_{\Delta_\pm}\mathcal{A}|\mathcal{A}|^2, \tag{7.23}$$

where $c_{\Delta_\pm} = (1+\Upsilon)/h_{\Delta_\pm}$. The classic description of the Eckhaus instability involves looking for stationary solutions of Eq. (7.23) modulated by an arbitrary finite wavenumber. The Eckhaus instability region is then formed by looking at the stability with respect to long-wavelength perturbations of the wavenumber. The modulation equation (7.23) is related to the scalar NLS equation via a constant phase multiplication, therefore, the solutions should be always stable near the Turing value when $a_{\Delta_\pm}$ and $b_{\Delta_\pm}$ take the same sign [119]. We note that Fig. 7.1(c) is embedded on a linearly unstable NN background so temporal instability is expected. It is also important to note that Eq. (7.23) is the amplitude equation for the real-valued CNLS system. Since the CNLS is generally an equation of complex field variables, to achieve the Eckhaus analysis one must generalise the ansatz (7.9) to incorporate complex envelopes. This is outside of our current framework, and thus we will consider this extended analysis in future work. As an extension to complex space, one would expect some complex form of the Ginzburg-Landau equation to govern the analysis; see for instance [18, 75]. We will see a description of the Eckhaus instability in Sec. 7.2, when we propose a comparison between the travelling localised states obtained here, and structures found in the Swift-Hohenberg equation. For the benefit of our MTI analysis, the unstable behaviour of both the localised and periodic states does not heavily impact the allowable solutions since a small time-frame in the CNLS corresponds to a much longer time-frame in the MTI.

7.1.3 Dispersion relation near Turing

In relation to temporal stability of the solutions, we will now briefly discuss the behaviour of the linear dispersion relation near the Turing value. We know from the definition of the temporal eigenvalues (5.28) that one recovers the spatial eigenvalues when $S = 0$ and $K = i\lambda$. When the spatial eigenvalues transition from type (iv) to type (i), at the Turing value, one expects some of the temporal eigenvalues to transition through zero at the point $K^2 = k_{\Delta_\pm}^2$. The transition through this point, generally, changes two of the temporal eigenvalues from purely imaginary to purely real, or vice versa. Note also that the

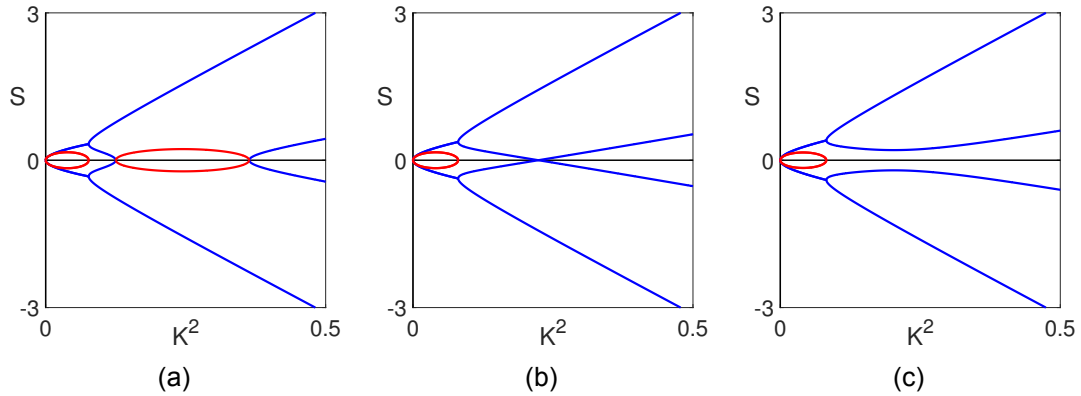

Figure 7.2: Dispersion relation $S_{1-4}(K^2)$ for the NN uniform state transitioning through the Turing value $\omega_{\Delta_+} = -9.052$ for the system from Fig. 7.1(a–b). Red (blue) curves indicate $\mathcal{R}\text{e}(S_{1-4})$ and $\text{Im}(S_{1-4})$ respectively. (a) $\omega_A = \omega_{\Delta_+} - 0.05$ (b) $\omega_A = \omega_{\Delta_+}$ (c) $\omega_A = \omega_{\Delta_+} + 0.05$.

Belyakov-Delaney bifurcation provides a similar transition of temporal eigenvalues through zero, only with restriction to the $K^2 < 0$ half plane, and is therefore unphysical. Let us consider the example Turing value shown in Fig. 7.1(a–b) of $\omega_{\Delta_+} = -9.052$. The dispersion relation, as one passes through this value, is explicitly shown in Fig. 7.2. Figure 7.2(a) provides us with the dispersion relation prior to the Turing value. In this figure, one observes two loops in the spectra, which corresponds to linear instability of NN. This is expected here as all of the spatial eigenvalues are of type (iv). As one increases the bifurcation parameter to the Turing value ω_{Δ_+}, shown in Fig. 7.2(b), the secondary loop closes in and vanishes at the value of $K^2 = k^2_{\Delta_\pm}$. Beyond the Turing value, shown in Fig. 7.2(c), the two colliding branches are now purely imaginary, which is expected since the spatial eigenvalues are now a complex quartet in this interval. Note that the additional loop originating from origin $K^2 = 0$ is permitted since not all spatially hyperbolic states are temporally stable. This secondary loop is not guaranteed to exist, and depends completely on the additional SHATS conditions for NN. Although not shown here, as one increases the parameter further, there is a critical point of $\omega_c = -8.524$ where the secondary loop vanishes and temporally stability of NN is obtained. This critical point corresponds to a value of ω_A that allows,

$$(d_1 g_1 \phi_0^2 - d_2 g_3 \psi_0^2)^2 + 4 d_1 d_2 g_2 g_4 \phi_0^2 \psi_0^2 = 0,$$

formally, when $F_2 \geq 0$ becomes satisfied for all $K^2 > 0$ in Eq. (5.28) and transitions the temporal eigenvalues from complex (unstable) to imaginary (stable). The localised state from Fig. 7.1(b) is found beyond this critical point.

From Fig. 7.2(b), when one transitions through the Turing value, it is clear that two of the temporal eigenvalues are zero and the other two are non-zero,

i.e. $S_{1,2}(k^2_{\Delta_\pm}) = 0$ and $S_{3,4}(k^2_{\Delta_\pm}) \neq 0$. One can prove that this is the expected case in general, and we would not expect all four eigenvalues to be zero, by considering a simple proof by contradiction. We know, from the structure of the temporal eigenvalues of NN in Eq. (5.28), that $S_{1-4} = 0$ can only be satisfied, for $K^2 = k^2_{\Delta_\pm}$, when $F_1 = F_2 = 0$. Let us consider $F_1 = 0$ where, by substituting the Turing wavenumber and value in, the quantity can be simplified to the form of

$$F_1 = g_3(W_1 \pm W_2\sqrt{g_2g_4(g_2g_4 - g_1g_3)}) = 0,$$

where

$$\begin{aligned}
W_1 &= (d_1^2 + d_2^2)(d_1g_4 + d_2g_1)(g_2g_4 - g_1g_3)^2 \\
&- g_1g_3(d_2g_4 - d_1g_1)(g_1g_2d_2^2 + d_1d_2g_1g_3 + d_1^2g_3g_4 - d_1d_2g_2g_4) \\
&+ g_1g_3(d_1g_2 - d_1g_1)(d_1g_4 + d_2g_1)^2 + 2d_1d_2g_2g_4^2(d_2g_2g_4 - 3d_1g_1g_2 - 2d_2g_1g_3) \\
W_2 &= (g_2g_4 - g_1g_3)(d_1^3g_4 + 3d_1d_2^2g_4 - 3d_1^2d_2g_1 - g_1d_2^3).
\end{aligned}$$

The structure of this value tells us that this can only be satisfied when $W_1 = W_2 = 0$, which is not true, generally, unless one considers specific parameters. Therefore, unless one considers specified regimes of system parameters, the values of $F_1,\ F_2 \neq 0$. Consequently, the only way in which the temporal eigenvalues can become zero, in general, is either (a) $F_1 = \sqrt{F_2}/2$ or (b) $F_1 = -\sqrt{F_2}/2$. When the former is true, the eigenvalues are given as $S_{1,2}(k^2_{\Delta_\pm}) \neq 0$ and $S_{3,4}(k^2_{\Delta_\pm}) = 0$, with the latter providing $S_{1,2}(k^2_{\Delta_\pm}) = 0$ and $S_{3,4}(k^2_{\Delta_\pm}) \neq 0$. This is shown true for the Turing value considered in Fig. 7.2(b), as one numerically finds $F_1 = -\sqrt{F_2}/2$ leading to the specific transition of temporal eigenvalues through $S_{1,2}(k^2_{\Delta_\pm}) = 0$. From this analysis, and the description of the eigenvalues in Eq. (5.28), it is clear to see that if $F_1 = \sqrt{F_2}/2$ then the remaining temporal eigenvalues will be purely real for some $K^2 > 0$ and, thus, NN is linearly unstable at the Turing value.

7.2 Comparison with the quadratic-cubic Swift-Hohenberg (SH23) equation

Motivated by the existence of travelling localised and periodic states in the CNLS equation, we will now explore and compare these structures to similarly formed spatially-periodic travelling solutions of pattern forming systems. Arguably, the Swift-Hohenberg equation with a quadratic-cubic nonlinearity (SH23 model) is the most commonly studied pattern forming system where there has

been significant progress made in characterising the localised and periodic states found [34, 25, 75]. We write the equation explicitly as

$$u_t + u_{xxxx} + 2\alpha u_{xx} + (r + \alpha^2)u = 3bu^2 - 2cu^3 \tag{7.24}$$

where u is a real, scalar function of the generic space and time variables x and t respectively, α, b, c are arbitrary coefficients, with $\alpha > 0$, and r is commonly referred to as the bifurcation parameter. This dissipative equation, which we henceforth denote as dSH23, is important in the context of pattern formation, as we will see that the equation describes the formation of states periodic with wavenumbers near $\sqrt{\alpha}$. The equation with this chosen nonlinearity possesses bistability of the uniform and patterned states. Our main aim of this section is to formulate a conservative analogue of the dSH23 model, which exhibits travelling localised states similar to the CNLS system. This analysis may then infer certain information back onto the travelling states of the CNLS system and is formed in the same manner as the CNLS. We first reduce the dSH23 equation (7.24) to a system of spatial ODEs, where the periodic and localised stationary states are found near the critical Turing value using a multiple scale expansion. One can then numerically continue these approximate spatial solutions in the spatial ODEs, using AUTO, which allows us to find branches of solutions in the strongly-nonlinear regime. These spatial solutions, found by numerical continuation, are then shown to evolve as stationary states in the SH23 equation (7.24) providing that they are temporally stable. Just as the CNLS and the corresponding dissipative equation in Eqs. (5.38–5.39) produced the same reduced spatial ODE dynamical system, we produce a conservative analogue of the SH23 model that exhibits the same spatial ODE system as the dSH23 model. The stationary, patterned states of the dSH23 model will then correspond to travelling localised and periodic states in the conservative analogue, similarly to those we found previously in the CNLS.

7.2.1 Dissipative SH23 equation

Treating the quantity r as the bifurcation parameter, we may consider bifurcation of the uniform states in this system. The first observation to note for the dSH23 system is the existence of three spatially uniform steady states, given by

$$u_0 = 0, \quad u_\pm = \frac{3b}{4c} \pm \frac{\sqrt{9b - 8c(r + \alpha^2)}}{4c}, \tag{7.25}$$

where the $u_\pm$ branches form as a saddle-node bifurcation from the value of $r_s = 9b^2/8c - \alpha^2$. It can be shown that the spatial eigenvalues of the time-

independent form of the system (7.24) are given by

$$\lambda_{1,2}^2 = -\alpha \pm \sqrt{-r}, \tag{7.26}$$

for the uniform state u_0. As analysed in [34], the u_- branch forms as a trans-critical bifurcation of the u_0 branch at $r_{TB} = -\alpha^2$. The key bifurcation value that we consider here is that of $r_H = 0$ on the trivial branch u_0. To the right of the value ($r > 0$), the eigenvalues are a complex quartet and, therefore, spatially hyperbolic, whilst the eigenvalues to the left ($r < 0$) are purely imaginary, up to the point r_{TB}. Since the eigenvalues collide pair-wise, with double multiplicity, on the imaginary axis at $\lambda = \pm i\sqrt{\alpha}$, this critical value of r_H is a reversible Hopf bifurcation with 1:1 resonance, like $\omega_{\Delta_\pm}$ in the CNLS system. It is also important to note that temporal stability of the u_0 state relies on the criterion $S = -r - (\alpha - k^2)^2 \leq 0$ for all perturbation wavenumbers k. For uniform perturbations ($k = 0$), the state is linearly stable providing that $r \geq r_{TB}$, which is always true in the defined region of $r > r_H$. When $k \neq 0$, a maximum is formed, in the variable space (k^2, S), for the function S at $k_m^2 = \alpha$. For linear stability, we required quadrant 1 to be empty in this variable space. This is achieved purely when $r > r_H$, which is always true for the complex quartet region. Therefore, by our definition, the u_0 uniform state is SHATS where localised states may form, $r > 0$.

We may consider a weakly nonlinear analysis near this Turing value of $r = r_H$, following the work of [34], and propose the existence of branches containing localised states near this value. Let us consider stationary solutions of Eq. (7.24) by writing the reduced spatial ODE,

$$u_{xxxx} + 2\alpha u_{xx} + (r + \alpha^2)u - 3bu^2 + 2cu^3 = 0. \tag{7.27}$$

Similarly to the CNLS in Sec 7.1, let us implement a multiple scale ansatz of,

$$u(x) = \epsilon u_1(x, X) + \epsilon^2 u_2(x, X) + h.o.t's, \tag{7.28}$$

where we have defined the slow spatial variable $X = \epsilon x$ and a small perturbation variable $|\epsilon| << 1$; $h.o.t's$ refers to higher-order terms. We also introduce an expansion of the bifurcation parameter as $r = r_H + \epsilon^2\delta$ which, since $r_H = 0$, may be simplified to $r = \epsilon^2\delta$. Note that, since we are dealing with a trivial background field, all of the uniform state expansion variables $U_0,\ U_1, \cdots = 0$ unlike the previous CNLS Turing analysis. We can now consider the solvability conditions at each order of ϵ when Eq. (7.28) is substituted into Eq. (7.27). Since the background field is zero, the $O(1)$ equation is trivial. At $O(\epsilon)$, we find that

the solvability condition gives us an ansatz of

$$u_1 = \mathcal{B}(X)\mathrm{e}^{i\sqrt{\alpha}x} + c.c., \tag{7.29}$$

where we see that the Turing wavenumber is precisely given by the pair-wise collision of eigenvalues, located at $\lambda = \pm\sqrt{\alpha}i$. At the next order of $O(\epsilon^2)$, we find that the following definition of u_2

$$u_2 = \frac{6b}{\alpha^2}|\mathcal{B}|^2 + \frac{b}{3\alpha^2}\mathcal{B}^2\mathrm{e}^{2i\sqrt{\alpha}x} + c.c., \tag{7.30}$$

solves the governing equation at this order. Finally, at $O(\epsilon^3)$, we find that the solvability condition at this order is governed by

$$-4\alpha\mathcal{B}_{XX} + \delta\mathcal{B} - \Gamma\mathcal{B}|\mathcal{B}|^2 = 0, \tag{7.31}$$

where

$$\Gamma = \frac{38b^2}{\alpha^2} - 6c.$$

Other residual terms at this order can be removed by considering higher-order terms in the ansatz. Spatially homogeneous solutions of Eq. (7.31) translate to spatially periodic solutions of Eq. (7.27), given by

$$u(x) = 2\sqrt{\frac{r}{\Gamma}}\cos(\sqrt{\alpha}x + \Theta) + h.o.t's, \tag{7.32}$$

where Θ is, once again, an arbitrary phase. When the nonlinear coefficient $\Gamma > 0$ ($\Gamma < 0$) the bifurcation parameter must take the sign of $r > 0$ ($r < 0$) for the periodic state to exist and the bifurcation at the origin is subcritical (supercritical). We also expect a branch of localised states, from the subcritical bifurcation, that corresponds to the solutions

$$u(x) = 2\sqrt{\frac{2r}{\Gamma}}\mathrm{sech}\left(\frac{1}{2}\sqrt{\frac{r}{\alpha}}x\right)\cos(\sqrt{\alpha}x + \Theta) + h.o.t's, \tag{7.33}$$

that asymptotically tend to $u \to 0$ as $x \to \pm\infty$. As mentioned in [34], the choice of the phase Θ is restricted, by higher-order analysis, to 0 and π. These two choices of the phase are the only ones which preserve the reversibility of the system ($x \to -x, u \to u$), therefore we have two branches that produce localised solutions from the Turing value.

Let us consider a specific case of Eq. (7.24) with the system parameters that are presented in [34, 141], i.e. $\alpha = 0.25$, $b = 0.41/3$, and $c = 0.5$. These parameters give a nonlinear coefficient of $\Gamma \approx 8.412$, so we expect localised

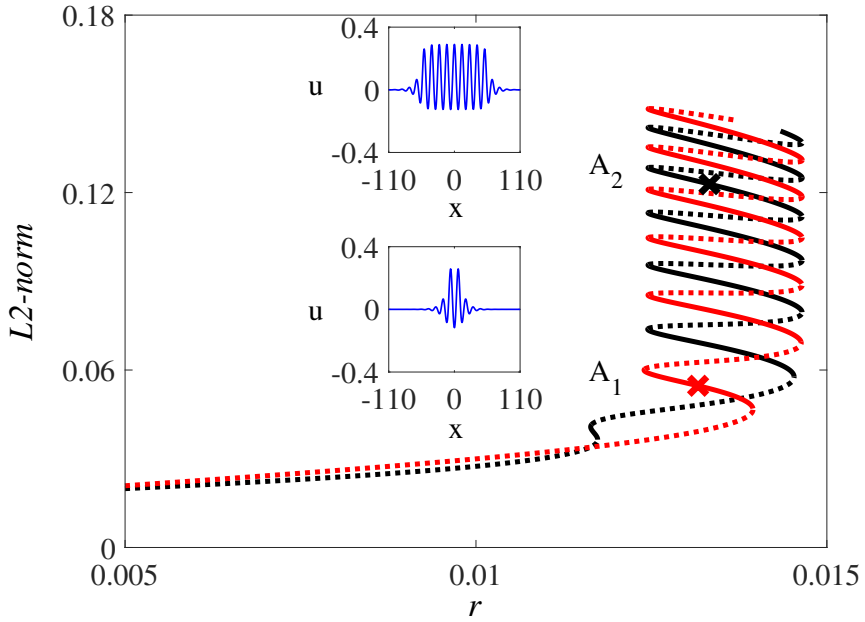

Figure 7.3: AUTO continuation in the parameter r for localised solutions starting from Eq. (7.33). The $\Theta = 0$ ($\Theta = \pi$) branch is shown in black (red) and the branch is plotted by thick lines (dotted lines) when the solution is stable (unstable). Example profiles on the $\Theta = \pi$ and $\Theta = 0$ branches are considered at the points A_1 and A_2 respectively.

states to exist in the region of $r > 0$. To find these branches, we may consider the solution (7.33) as starting points for numerical continuation in AUTO and impose Neumann boundary conditions on both the left and right boundaries. The AUTO output is shown in Fig. 7.3, where we have terminated the two branches at some arbitrary point up the helical region. The two branches of $\Theta = 0$ and $\Theta = \pi$ are shown in black and red respectively and solid (dotted) lines represent stable (unstable) solutions. Stability of the profiles is found numerically for dSH23 by considering a centred finite-difference scheme, obtaining the spectrum. The stability of the profiles depends primarily on an even and an odd eigenmode. The figure presented here is similar to that of Fig. 8 in [34], only with a reflection of the bifurcation parameter ($r \to -r$). The solutions on the two branches are similar, which is expected, with a profile maximum (minimum) found at $x = 0$ for $\Theta = 0$ ($\Theta = \pi$) and reversible, oscillating wavetrains either side that decay to u_0. As one increases the parameter r from $r_H = 0$, the envelope becomes narrower and the maximum (minimum) amplitude grows in absolute value. This behaviour continues up until the point in which the amplitude is comparable to that of the underlying patterned, periodic state, and subsequently when the envelope is comparable to that of the wavelength $2\pi/\sqrt{\alpha}$, as discussed thoroughly in [34]. Beyond this point there is a winding, helical nature of the two branches. This helical nature is referred to as homoclinic snaking, where the branches undergo saddle-node bifurcations,

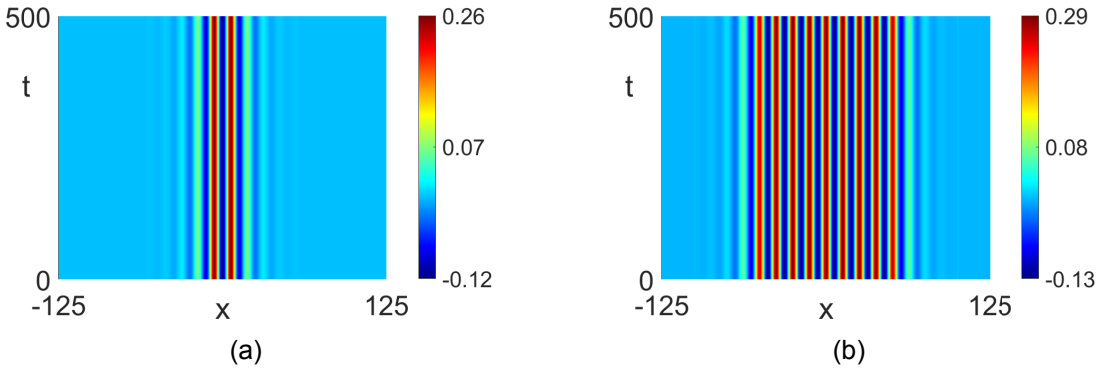

Figure 7.4: Localised states of the dSH23 model with system parameters $\alpha = 0.25$, $b = 0.41/3$, and $c = 0.5$. Profiles correspond to the examples of (a) A_1 and (b) A_2 shown respectively in Fig. 7.3, i.e. (a) $\Theta = \pi$ branch with $r = 0.0132$; (b) $\Theta = 0$ branch with $r = 0.0133$.

adding oscillations to each tail of the envelope as one moves up the snaking region. The saddle-node bifurcations are accompanied by the eigenvalue of the even eigenmode passing through zero. The eigenvalue of the odd eigenmode passing through zero corresponds to branches of asymmetric solutions connecting the $\Theta = 0$ and $\Theta = \pi$ branches across the snaking region. These branches are commonly referred to as ladders (or rungs) and are not explicitly shown here as they are not important for our analysis; they are shown in Fig. 8 of [34]. The snaking provides an infinite number of solutions, but the number of solutions is finite on a finite domain length L, and the 'top' of the region terminates when the solutions are comparable to the periodic state on the finite domain. The width of the region depends on the amplitude of the periodic states.

Example profiles in the snaking region, on the $\Theta = \pi$ and $\Theta = 0$ branches, are shown in Fig. 7.3 at A_1 and A_2 respectively. These profiles are stable and, therefore, propagate as stationary solutions in Eq. (7.24). The evolution of these two localised solutions are shown in Fig. 7.4(a) and Fig. 7.4(b) respectively. Note that, since A_2 is found much later up the snaking region, there are many more oscillations in the profile of A_2 in comparison to the profile of A_1. Both profiles are evolved on a periodic domain of fixed domain size $L \approx 251.327$.

Let us now consider the spatially-periodic states near the Turing bifurcation. Periodic, patterned solutions of this type are stationary in Eq. (7.24), providing that they are Eckhaus stable. The concept of Eckhaus instability has been studied in great detail for the Swift-Hohenberg equation [25, 185, 133]. To present the classical description of the Eckhaus instability, in relation to our equation, we first write the full amplitude/modulation equation near the Turing value. By introducing a slow time variable to the weakly nonlinear analysis, denoted by $T = \epsilon^2 t$, we may write the full amplitude equation in the form of a

time-dependent Ginzburg-landau equation,

$$\mathcal{B}_T = 4\alpha\mathcal{B}_{XX} - \delta\mathcal{B} + \Gamma\mathcal{B}|\mathcal{B}|^2. \tag{7.34}$$

We then look for solutions of Eq. (7.34) by considering the ansatz of $\mathcal{B} = R\exp(iqX)$. Since we are free to choose the periodic domain size, we do not limit ourselves to discrete values of Q, and consider a domain size L which incorporates any change in the choice of wavenumber. The uniform solution (with $q = 0$) corresponds to the uniform state of Eq. (7.34) obtained for the periodic solution in Eq. (7.32), i.e. $R_0^2 = \delta/\Gamma$. Steady solutions of Eq. (7.34) are found to satisfy $R^2 = R_0^2 + 4\alpha q^2/\Gamma$. These solutions correspond to a variation of the critical Turing wavenumber in (7.32) by a fixed amount to $\sqrt{\alpha} + \epsilon q$. To analyse the stability of these patterned states, we closely follow the work of [92, 185] by perturbing the pattern amplitude and phase by a small amount. We do so by substituting the ansatz

$$\mathcal{B} = R(1 + w(X,T))\mathrm{e}^{i(qX+Q(X,T))}$$

into the amplitude equation (7.34), where $|w|,\ |Q| << 1$. One then linearises in w and Q, and segregates the real and imaginary parts of the equation to get the system of equations,

$$w_T = 4\alpha w_{XX} - 8\alpha q Q_X + 2\Gamma R^2 w, \tag{7.35}$$

$$Q_T = 8\alpha q w_X + 4\alpha Q_{XX}. \tag{7.36}$$

We then look for long wave effects by considering the modes $w = \tilde{w}\exp(\sigma T + ikX)$ and $Q = \tilde{Q}\exp(\sigma T + ikX)$, where $\tilde{w},\ \tilde{Q}$ are arbitrary real constants. Solving the system as an eigenvalue problem, one finds a quadratic equation in σ given by,

$$(\sigma + 4\alpha k^2 - 2\Gamma R^2)(\sigma + 4\alpha k^2) = (8\alpha q k)^2, \tag{7.37}$$

where the solutions of Eq. (7.37) correspond to the growth rate of the modes. These eigenvalues are given by the following,

$$\sigma_\pm = \Gamma R^2 - 4\alpha k^2 \pm \sqrt{\Gamma^2 R^4 + (8\alpha q k)^2} \tag{7.38}$$

with accompanying eigenvectors. By substituting the definition of R into these values, we see that $\sigma_-(k = 0) = 0$ and $\sigma_+(k = 0) < 0$ is subsequently stable when the condition $-\Gamma R_0^2 > 4\alpha q^2$ is satisfied. Since $\alpha > 0$, this may only be satisfied when $\Gamma < 0$, which also forces the bifurcation at the origin to be supercritical ($\delta < 0$). This condition is precisely the existence condition, as seen

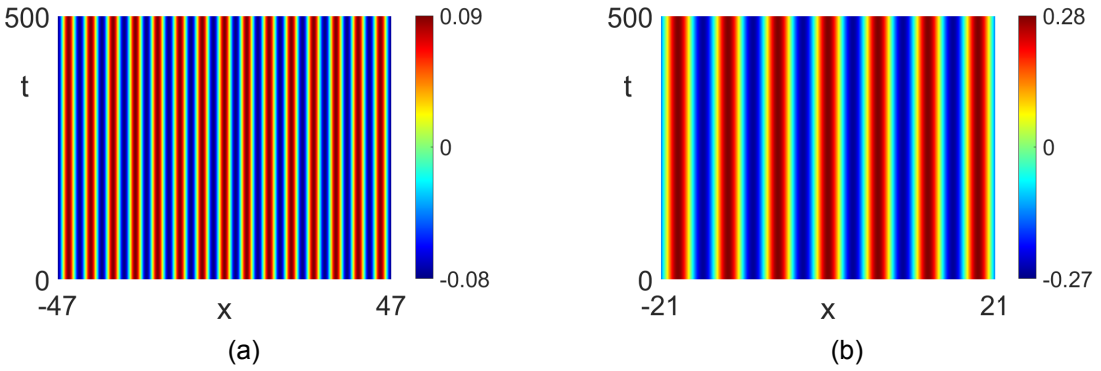

Figure 7.5: Periodic states of the dSH23 model with system parameters $\alpha = 1$, $b = 0.1$, and $c = 1$. Eckhaus stable solutions with the bifurcation parameter (a) $r = -0.01$ and (b) $r = -0.1$.

from the interval of wavenumbers q that satisfy the definition of R. The Eckhaus solutions exist providing that $4\alpha q^2 < -\delta$. Within this region of existence the σ_- eigenvalue is always negative for any $k > 0$, so stability relies purely on the remaining eigenvalue σ_+. By setting the eigenvalue to zero, one finds $k-$parabolas that satisfy the relation, given explicitly by

$$\delta_E(q,k) = 4\alpha\left(\frac{k^2}{2} - 3q^2\right), \tag{7.39}$$

where stability ($\sigma_+ < 0$) requires $\delta < \delta_E(q,k)$. The critical parabola $\delta_E(q,0) = -12\alpha q^2$ is the threshold for instability and is proportional (by a factor of -4α) to the commonly-derived Eckhaus parabola [185, 133]. By considering $\delta < \delta_E(q,0)$ it is subsequently shown that the threshold for stability is $12\alpha q^2 < -\delta$, and R states are marginally unstable w.r.t long-wave perturbations along this line $\delta = -12q^2\alpha$. Therefore, the amplitude of the wavetrain that becomes Eckhaus unstable is $R^2 = \frac{2}{3}R_0^2$, with associated wavenumber $q^2 = -\frac{\delta}{12\alpha}$. The region of Eckhaus instability is given by $-\delta < 12\alpha q^2 < -3\delta$, where we restrict $\delta < 0$. To find Eckhaus stable patterned solutions, one must implement values (δ, q) that fall outside of the instability region, but still exist according to the definition of R^2.

Since we have shown that the sign of the nonlinear coefficient Γ must be negative in our analysis, the previous choice of the system parameters implemented in Fig. 7.4 does not suffice for the stable patterned states here. We instead impose the choice of system parameters as $\alpha = 1$, $b = 0.1$, and $c = 1$, which leads to a nonlinear term of $\Gamma = -5.62$. By allowing the bifurcation parameter to vary, such that a supercritical Turing bifurcation is imposed, we find solutions governed by Eq. (7.32) periodic in the wavenumber $\sqrt{\alpha} = 1$. For this set of parameters, the Eckhaus instability region is then given by $-\delta < 12q^2 < -3\delta$. By imposing a fixed value of δ, we find the set of perturbed Turing wavenum-

bers that exist and are found outside this region of instability. A simple solution to this, and one we wish to impose for the sake of periodicity of the domain, is to set $q = 0$ and allow the patterned state to be completely governed by the Turing wavenumber $\sqrt{\alpha} = 1$. As we can see, providing that $\delta < 0$, the choice of δ does not impact the stability of the states in our case since 0 is found in the Eckhaus existence region $0 < -3\delta$ and inside the region of stability $0 < -\delta$. We can see specific examples of periodic states in dSH23, with imposed $q = 0$, in Fig. 7.5. The two panels show choices of the initial bifurcation parameter (a) $r = -0.01$ and (b) $r = -0.1$ respectively, and we observe both patterned solutions propagating stably in dSH23. As the magnitude of r becomes larger, so does the amplitude of the rolls. The domain size has been altered between the two solutions, purely to show that the domain has no effect on the solution, providing that it is periodic w.r.t to the wavenumber $\sqrt{\alpha}$. On an arbitrary large domain ($L \to \infty$) the periodic solution extends to an infinite number of rolls.

7.2.2 Conservative SH23 equation

Let us now focus on a conservative analogue of the dSH23, which we will henceforth denote as cSH23. This model is very similar to that of Eq. (7.24), only replacing the time derivative with a secondary derivative in time. This model is proposed in [161], where it is used as an appropriate system to qualitatively model 2D surface solitons on a magnetic fluid. The equation can be explicitly written as,

$$u_{tt} + u_{xxxx} + 2k_0^2 u_{xx} + (a + k_0^4)u = 3bu^2 - 2cu^3 \tag{7.40}$$

where the nonlinear terms are restricted to $b,\ c > 0$ in [161]. Since our previous analysis on the dSH23 model incorporates this restriction we will remain within this imposed parameter range. The reason we study this model is that Eq. (7.40) can be reduced to the same spatial ODE as the dSH23 model. This is achieved by considering solutions to Eq. (7.40) of the form $u = u(x - Ct) = u(\zeta)$, where C is a travelling wave speed, which reduces the cSH23 to the ODE,

$$u_{\zeta\zeta\zeta\zeta} + (2k_0^2 + C^2)u_{\zeta\zeta} + (a + k_0^4)u - 3bu^2 + 2cu^3 = 0. \tag{7.41}$$

Note the similarities between Eq. (7.41) and the spatial ODE obtained for dSH23 in Eq. (7.27). If one considers the transformation of the spatial ODE $\zeta \to x$ and rewrite the coefficients as $\alpha = k_0^2 + C^2/2$ and $a = r + C^2(k_0^2 + C^2/4)$, then the two ODEs are equivalent. Therefore, the prior analysis of the ODE for the dissipative case carries over to the conservative case with substitutions made. We

expect that localised and periodic states of dSH23 can be translated to travelling localised and periodic states of cSH23. Throughout the analysis the values of k_0 and C are fixed and therefore correspond to a fixed value of α in dSH23; a choice of α corresponds to a solution space of (k_0, C) where we restrict the parameter $k_0 \neq 0$. The variation of the bifurcation parameter of r translates to a variation of a by the same amount. The Turing value corresponds to the point $a_H = C^2(k_0^2 + C^2/4)$ in the cSH23 system parameters, and the Turing wavenumber is given as $\sqrt{k_0^2 + C^2/2}$. The weakly nonlinear analysis then follows as in the dSH23 model. One can substitute the coefficient terms and rewrite the dependent variable back ($x \to \zeta$) into Eq. (7.32) to obtain the travelling periodic states of cSH23 given by,

$$u(\zeta) = 2\sqrt{\frac{a - a_H}{\Gamma}}\cos\left(\sqrt{k_0^2 + \frac{C^2}{2}}\zeta + \Theta\right), \tag{7.42}$$

where higher-order terms have been omitted and Γ is now redefined as

$$\Gamma = \frac{38b^2}{\left(k_0^2 + \frac{C^2}{2}\right)^2} - 6c.$$

The travelling localised solutions of cSH23 are also given by

$$u(\zeta) = 2\sqrt{\frac{2(a - a_H)}{\Gamma}}\text{sech}\left(\frac{1}{2}\sqrt{\frac{(a - a_H)}{\left(k_0^2 + \frac{C^2}{2}\right)}}\zeta\right)\cos\left(\sqrt{k_0^2 + \frac{C^2}{2}}\zeta + \Theta\right). \tag{7.43}$$

We will first consider the localised solutions where we should find travelling forms of the previously found states. In general, the temporal stability of these localised solutions depends on the spectrum of cSH23, which is slightly different from the dSH23 model. We found that, in the systems that we have considered, increasing the value of C decreases all eigenvalues of the spectrum and 'pushes' the previously unstable odd and even eigenvalues into the stable regime. For the purpose of our analysis, we will consider the stable localised states of dSH23 as these are also stable in cSH23. Previously, we enforced the system parameters of $b = 0.41/3$, $c = 0.5$, and $\alpha = 0.25$ for the localised states portrayed in Fig. 7.4. Let us fix a value of the group velocity C to calculate the cSH23 system parameter $k_0^2 = \alpha - C^2/2$, so that the dissipative and conservative models are comparable. Firstly, we will consider the localised state from the $\Theta = \pi$ branch that is shown in Fig. 7.4(a). This localised state is translated to travelling localised solutions with group velocities $C = 0.1$ and $C = 0.5$, shown in Fig. 7.6(a) and Fig. 7.6(b) respectively. A similar process is imposed on the localised state from the $\Theta = 0$ branch shown in Fig. 7.4(b). This

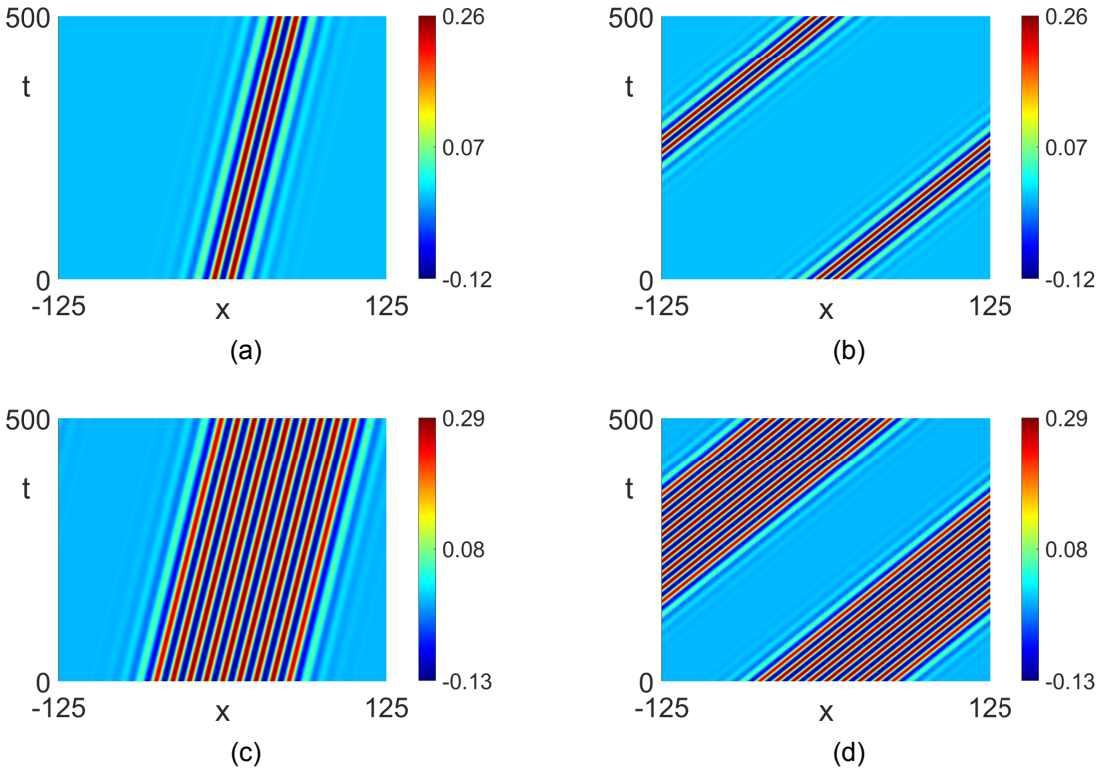

Figure 7.6: Travelling localised states of the cSH23 model with system parameters $\alpha = 0.25$, $b = 0.41/3$, and $c = 0.5$. (a,b) Travelling analogues of the $\Theta = \pi$ localised state shown in Fig. 7.4(a), with cSH23 parameters (a) $(k_0^2, C) = (0.245, 0.1)$ and (b) $(k_0^2, C) = (0.125, 0.5)$. (c,d) Travelling analogues of the $\Theta = 0$ localised state shown in Fig. 7.4(b), with cSH23 parameters (c) $(k_0^2, C) = (0.245, 0.1)$ and (d) $(k_0^2, C) = (0.125, 0.5)$.

state is translated to travelling localised solutions with group velocities $C = 0.1$ and $C = 0.5$, shown in Fig. 7.6(c) and Fig. 7.6(d) respectively. As we can see from all of these cSH23 figures, the localised states travel with the differing group velocities stably. The width of the solution has no adverse effect on the evolution of the structure.

Let us now focus on the periodic travelling states that may be forged from those found previously in the dSH23 model. In order to efficiently translate these states to cSH23, we must again ensure Eckhaus stability of the states in the conservative system. We must write the full amplitude equation for this system near the Turing value. We introduce a rescaled slow time variable into the weakly nonlinear analysis, now denoted by $T = \epsilon t$, and write the amplitude equation as,

$$\mathcal{B}_{TT} = 4\alpha\mathcal{B}_{XX} - \delta\mathcal{B} + \Gamma\mathcal{B}|\mathcal{B}|^2. \tag{7.44}$$

Note that we have kept the equation in terms of the dSH23 variables here for ease of notation, but recall that these parameters are governed by the substitution of the cSH23 system parameters. We can analyse the Eckhaus instability of the conservative problem, just as before, by perturbing the pattern amplitude

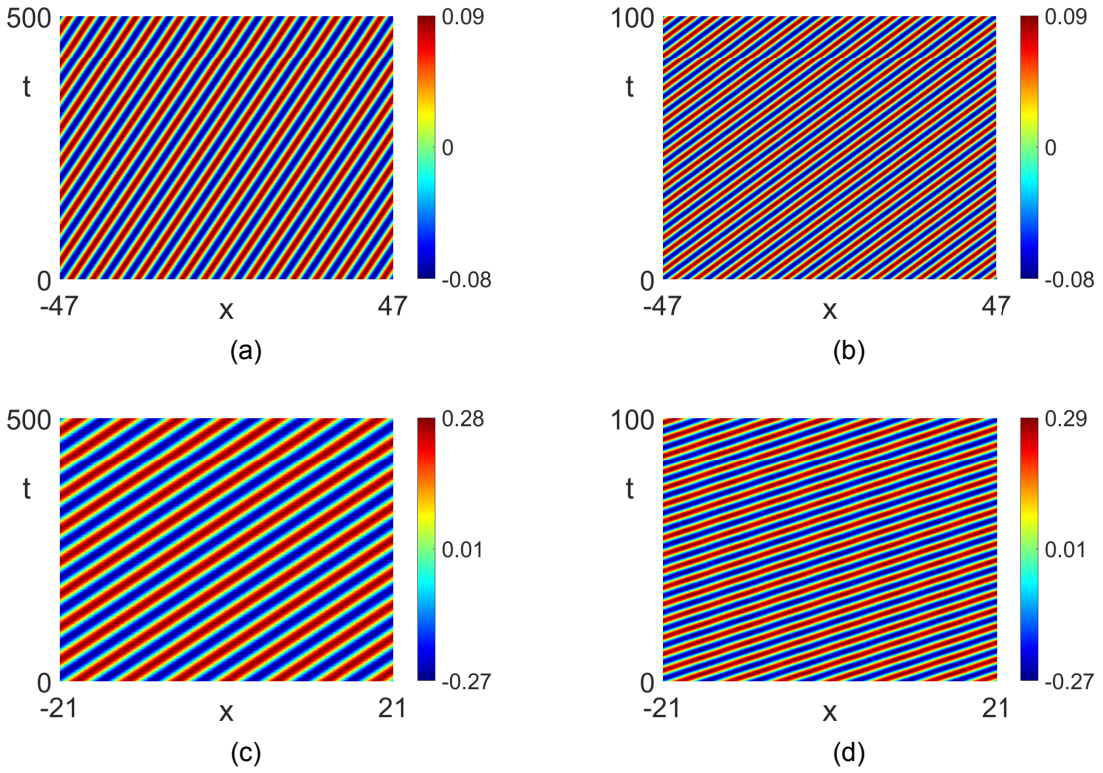

Figure 7.7: Travelling periodic states of the cSH23 model with system parameters $\alpha = 1$, $b = 0.1$, and $c = 1$. (a,b) Travelling analogues of the patterned state shown in Fig. 7.5(a), with cSH23 parameters (a) $(k_0^2, C) = (0.995, 0.1)$ and (b) $(k_0^2, C) = (0.5, 1)$. (c,d) Travelling analogues of the patterned state shown in Fig. 7.5(b), with cSH23 parameters (c) $(k_0^2, C) = (0.995, 0.1)$ and (d) $(k_0^2, C) = (0.5, 1)$.

and phase. When one applies the process that was performed for dSH23, we get a system of equations similar to that of Eqs. (7.35–7.36), only now with a secondary time-derivative, i.e.

$$w_{TT} = 4\alpha w_{XX} - 8\alpha q Q_X + 2\Gamma R^2 w, \tag{7.45}$$

$$Q_{TT} = 8\alpha q w_X + 4\alpha Q_{XX}. \tag{7.46}$$

Looking for long-wave effects, we find that the growth rate is now governed by Eq. (7.37) with σ^2 replacing σ, i.e.

$$(\sigma^2 + 4\alpha k^2 - 2\Gamma R^2)(\sigma^2 + 4\alpha k^2) = (8\alpha q k)^2, \tag{7.47}$$

which is a quadratic function in σ^2. Since instability corresponds to $\mathcal{R}\mathrm{e}(\sigma) > 0$, we see that this is only a possibility if $\sigma > 0$, which is equivalent to before. Therefore, the previous Eckhaus analysis carries over to the conservative description and stable Eckhaus states in dSH23 are also Eckhaus stable in cSH23.

Let us consider the patterned states that we previously obtained in dSH23,

which propagated stably, shown in Fig. 7.5. Recall that the nonlinear parameters were chosen here as $b = 0.1$ and $c = 1$, with the coefficient $\alpha = 1$. By fixing the travelling wave speed C, one fixes the cSH23 parameter $k_0^2 = 1 - C^2/2$. Similarly to the localised states, we may consider the small-amplitude patterned state seen in Fig. 7.5(a) and impose this solution as travelling periodic solutions in the cSH23. Figures 7.7(a–b) show examples of these travelling solutions with group velocities (a) $C = 0.1$ and (b) $C = 1$. We can impose the same process on the patterned state with larger amplitude rolls, shown in 7.5(b) for $r = -0.1$. Figures 7.7(c–d) show examples of this periodic state as travelling solutions in cSH23 with group velocities (c) $C = 0.1$ and (d) $C = 1$. We see from all of these figures that, similarly to the localised states, these solutions propagate stably in the cSH23 system, which is what one would expect given the comparative nature of the dissipative and conservative systems. We expect a plethora of these travelling patterned states to be available in the cSH23 system.

7.3 Discussion

In this chapter we have described and analysed the existence of more 'unique' solutions to the CNLS system in the form of periodic and localised states. These states occur close to the Turing bifurcation, which is only possible through the eigenvalues of the NN uniform state. We have developed criteria for the existence of these critical Turing values and conclude with the limitation of the analysis being in an anti-bubble format, that may only transition through imaginary $\rightarrow$ complex quartet $\rightarrow$ imaginary eigenvalue composition, as opposed to the bubble format of eigenvalue transition studied in [77]. If one of the Turing critical values does not collide the eigenvalues pair-wise on the imaginary axis, but rather on the real axis, then the configuration is no longer an anti-bubble and the value is now a Belyakov-Delaney bifurcation point. The number of conditions on the system and travelling wave parameters is substantial for the Turing value to exist, paired with the NN SHATS conditions, so these solutions are not expected to appear in a wide number of CNLS systems.

We studied certain CNLS systems that do allow a Turing value and considered situations in which periodic and localised states are formed. The stability of these solutions were briefly considered but we note that we are yet to find stable propagation of either type of state. The stability of the localised state relies primarily on the spectrum of the CNLS for these solutions and we expect, with a more in-depth exploration, stable localised states to present themselves. In regards to the stability of periodic states, our weakly nonlinear analysis is limited

to purely real envelope solutions so Eckhaus stability is not valid in this context for full CNLS systems. As previously mentioned, one must form a complex framework to allow a study into the general Eckhaus stability of these states. As stated at the end of Sec. 7.1.2, we are not entirely concerned, for now, with the stability of these solutions since many of them persist for reasonable time-frames in the CNLS, which can be translated to longer time-frames in the MTI. The stability analysis in the complex framework is vital in general, and this is something that we aim to consider in the near future; we expect the formation of a complex-coefficient Ginzburg-Landau equation in the weakly nonlinear analysis.

As a comparison of the expected travelling 'exotic' states in CNLS, we considered well-known formations of localised and periodic states in the dissipative Swift-Hohenberg equation. By imposing a conservative analogue of this system, we briefly analysed the translation of the dissipative solutions to travelling periodic and localised solutions in the conservative system. Analysis of stability is formed between the dissipative and travelling solutions, which may be important in the future when considering the stability of the CNLS states. For instance, we concluded that analysing the solutions and stability of the dissipative system was enough to form stable solutions of the conservative system. When a complex framework is implemented into the Turing analysis of the CNLS, it may suffice to first consider the stability of the stationary solutions in the comparative dissipative system (5.38-5.39).

Chapter 8

Coupled NLS solutions in Nonlinear MTIs

In this chapter we collect our analysis on solutions to the non-integrable CNLS system and apply them to the nonlinear mechanical topological insulator. We first consider the MTI that we adapted in Chapter 4 to produce points of equal group velocity, which subsequently allows the CNLS system to govern the nonlinearly interacting envelopes of edge modes. A brief analysis of this system shows us that, in general, the type of CNLS system parameters in the adapted MTI does not allow for SHATS states or for stably propagating soliton/front solutions. The solutions still propagate for moderate time-frames in the MTI and we compare the edge evolution to the CNLS evolution and show that the underlying, interacting envelopes are truly governed by the CNLS system. We name this nonlinear MTI, MTI1.

To ensure more favourable CNLS system parameters we combine the adaptation of edge springs, presented in Chapter 4, with a new MTI design similar to that of [96]. The design of this MTI involves gluing together two MTIs with current flowing in the same direction through opposite flux of each sub-lattice and, thus, allows edge states at the interface of the two. This nonlinear MTI is named MTI2 for descriptive purposes. By adapting the simple spring connections between the two lattices, we can impose CNLS system parameter regimes of our liking and, in particular, allow either a focusing or defocusing non-integrable regime. In both regimes we impose a CNLS system far enough away from the symmetrically-coupled case, where the two edge modes are similar, so that the interacting dynamics are not mistaken for NLS dynamics. In the focusing regime, we consider solutions available to us as previously analysed in Chapters 5-7. Since we know that BB solitons allow an energy transfer between the two nonlinear structures, we explicitly show this type of energy transfer along the MTI edge interface. We also show the available solutions

in the defocusing CNLS regime, including the travelling front solution that we found in an abundance of defocusing CNLS systems.

Finally, as we did with the scalar bright solitons, we analyse and explore the topological protection of the BB soliton solutions. In particular, we look at the effect of non-trivial domains by carving symmetric and asymmetric shapes into the edge interface and performing a numerical scattering analysis on the envelopes of the vector solitons.

8.1 MTI1 solutions

We showed previously, in Chapter 4, that one may adapt the connections of the edge springs in MTI1 to alter the dispersion relation accordingly and find subsequent points of EGV. Since we now have a catalogue of solutions that can occur in the non-integrable CNLS equation, we can look for these solutions as governing envelopes of edge modes in the nonlinear MTI. Consistent with the types of CNLS systems we have considered in the previous analysis, we will look for CNLS equations where the system parameters $d_{1,2}$ and g_{1-4} are quantities of a similar order. Evolution is considered with an appropriate domain size and we will fix the small MTI parameter as $\epsilon = 0.1$, unless otherwise stated.

The first MTI system we propose is the lattice with adaptation parameter $\Omega = 2.168$ where an EGV point is found with carrier wavenumber $k_0 = 10\pi/11$. This particular case yields two nonlinearly interacting edge modes from each of the two band gaps. The coupled system governing the envelopes provides a specific choice of CNLS parameters, given by

$$\begin{aligned} d_1 = -0.088,\ g_1 = 0.038,\ g_2 = 0.035, \\ d_2 = 0.117,\ g_3 = 0.041,\ g_4 = 0.027, \end{aligned}$$

where the governing envelopes move with group velocity $\alpha_0' = \beta_0' = -0.56$. This EGV point is precisely the one found via a numerical search, where we previously showed bright and dark soliton propagation of the decoupled modes in Fig. 4.3. Unfortunately, this type of non-integrable CNLS system with $d_1 < 0$, $d_2 > 0$, $g_{1-4} > 0$, and $g_2 g_4 - g_1 g_3 < 0$ limits our available solutions quite significantly. From our analysis of the CNLS we find that these particular system parameters only permit the ZZ and NZ uniform states to be SHATS. Further to this, the physicality of BB amplitudes can never be satisfied for our analytical solutions. The only viable option presented for this system is, therefore, that of the DB soliton solution. We may obtain the profile numerically by continuing from the weakly nonlinear approximations presented in Sec. 6.1.3, with trav-

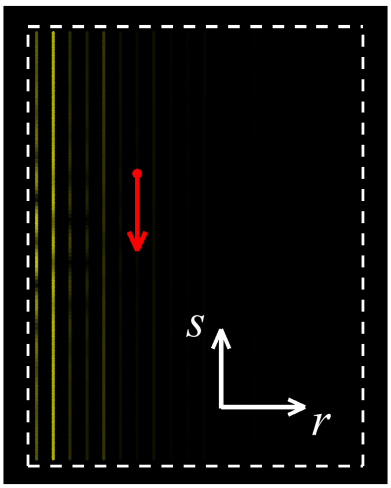

(a)

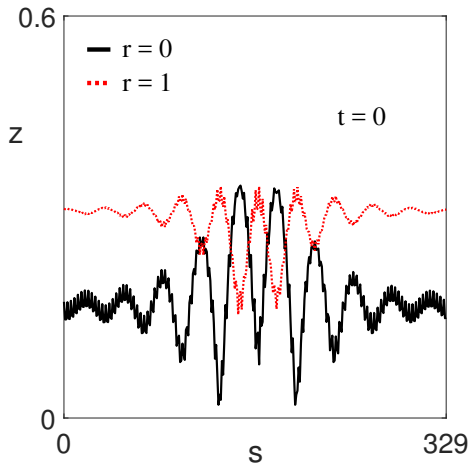

(b)

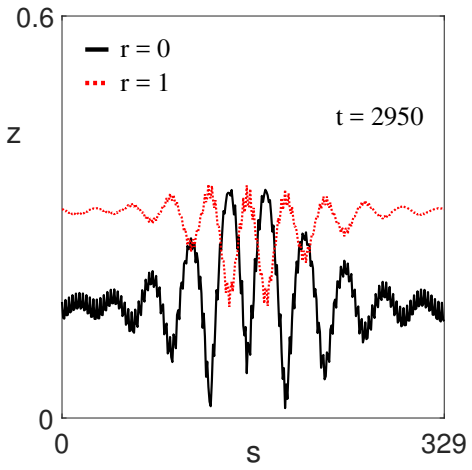

(c)

Figure 8.1: DB solutions of the nonlinear MTI1 lattice, with $N_r \times N_s = 20 \times 330$ sites. (a) 2D snapshot of the domain initially, where the red arrow indicates direction of propagation and the white-dashed lines indicate domain boundaries. (b,c) Profiles on the $r = 0$ (black-solid) and $r = 1$ (red-dashed) sites (b) initially, and (c) at $t = 2950$.

elling wave parameter choices that allow for the solution to be accommodated on the lattice edge.

To consider propagating CNLS solutions as vector edge solitons, we implement the envelope into the bimodal ansatz (4.1). One solves the MTI system with the new initial condition explicitly written as

$$\boldsymbol{X}_{r,S}(t=0) = \epsilon \left\{ \left(A(S)\boldsymbol{X}_r^{(1)} + B(S)\boldsymbol{X}_r^{(2)} \right) e^{isk_0} + c.c \right\}, \tag{8.1}$$

where the envelopes A, B are governed by the corresponding CNLS system, and $\boldsymbol{X}_r^{(1)}, \boldsymbol{X}_r^{(2)}$ are the EGV edge modes. An example DB initial condition is shown in Fig. 8.1, where we have considered the DB soliton solution governed by travelling wave parameters $(C_g, \omega_A, \omega_B) = (0, -0.801, -0.652)$. Note that, to

preserve periodicity on the domain and the MTI group velocity of the solution, we have imposed a soliton with zero velocity in the CNLS, but solutions are not limited to this decision and one can impose different CNLS travelling solutions on appropriate domain sizes. We see from the top-down view of the 2D lattice, shown in Fig. 8.1(a), that the structure of the DB profile is not clearly seen within the initial condition, taking the form of a decay from the left $r = 0$ edge into the bulk. The red arrow indicates the direction of propagation of the envelope. The unclear DB profile occurs due to differences of the eigenmodes where, in this particular instance, the α eigenmode dominates the $r = 1$ sites, with the β eigenmode dominating the $r = 0$ sites. This property is the main reason why a bright-soliton envelope can be approximately seen, in Fig. 8.1(b–c), in the initialisation of the $r = 0$ sites, and a dark-soliton on the $r = 1$ sites. The two figures respectively show the profiles initially and after many cycles of the envelope propagating periodically up the left edge $(t = 2950)$. We see that there is not much change to the profile in this evolution on a s-periodic domain. There is an obvious nonlinear interaction between the two eigenmodes since the envelopes of the two modes seemingly do not change in time, as expected from the CNLS governance. Other CNLS systems, like those obtained from the crossing point of the edge modes in Sec. 4.3.1, do not exhibit any SHATS states that reproduce any of our known solutions. In general, the CNLS system takes a parameter regime of $d_1 < 0$, $d_2 > 0$, $g_{1-4} > 0$, and $g_2 g_4 - g_1 g_3 > 0$. From our analysis we know that ZZ, ZN and NN states can be SHATS and, further to this, the nonlinear parameters tell us that the analytical BB and DD solutions can not be formed. The weakly nonlinear analysis also does not permit DB solitons for these particular parameter sets and BD solitons are not structurally stable since NZ can not be SHATS. The rare occasion when $g_2 g_4 - g_1 g_3 < 0$ is satisfied, from the crossing mode analysis, requires a significantly larger domain size to accommodate the nonlinear edge modes in the MTI; our numerical software, MATLAB R2020b, can not store arrays of this size so one must use different software to consider these solutions. Since we want to show these solutions on an arbitrary domain size, rather than specifically large lattices, we will look to form a nonlinear MTI system that exhibits a greater freedom with the choice of CNLS system parameters, so that we may showcase the different kinds of CNLS solutions.

8.2 Designing MTI2

One unique property of TIs is the ability to formulate more complicated lattices that exhibit bulk-edge correspondence at different edge interfaces. For instance, just as in the photonic case [96], one may build a MTI by combining two MTIs with opposite topological sectors (interchanging the flux/spin) such that there is a current flowing in the same direction along the interface. The MTI with reversed flux was also described in [177] to validate topological protection, in the context of beam splitters, and can be achieved by reversing the diagonal blocks of the matrix H, which we formed for the original description of the lattice as Eq. (1.25). This new matrix takes the form of

$$H_2 = \begin{pmatrix} H_- & 0 \\ 0 & H_+ \end{pmatrix}, \tag{8.2}$$

where we recall that $H_\pm$ are 3×3 matrices that represent the opposing spins. Following the same process as in [177], one can deduce that the dynamical matrix will be given by the explicit formulation

$$D = U^\dagger H_2 U = \begin{bmatrix} \mathcal{R}\mathrm{e}H_+ & \mathrm{Im}H_- \\ \mathrm{Im}H_+ & \mathcal{R}\mathrm{e}H_+ \end{bmatrix}, \tag{8.3}$$

where the matrix U is given previously by Eq. (1.28). We can see from the formulation of Eq. (8.3) that coupling strength between $x - x$ and $y - y$ sites are unchanged since the diagonal blocks are unchanged from previous. The off-diagonal blocks are reversed in this matrix, however, which equates to reversing the signs of all transverse connections between the x and y pendula in the lattice. For notation purposes, we will refer to the two dynamical matrices as D_1 and D_2 for the originally imposed MTI lattice and the new MTI lattice, with opposing flux, respectively.

If the two lattices are completely decoupled then the two separate systems are solved as before, with no further dynamics present to us. The dispersion relation of the full system then yields two copies of the previous dispersion relation, shown in Fig. 1.4, on top of each other. When one adds simple springs, connecting one edge of a lattice to the edge of the other lattice, we build an interface between the two MTIs that will produce new dynamics. Adding these springs yields two non-equivalent edge modes decaying from the interface sites into the bulk of each lattice. The two edge-interface modes will be even and odd with subtle differences between the intensity of the sites. For a complete analysis of how the eigenvalues/eigenmodes are altered when one adds springs

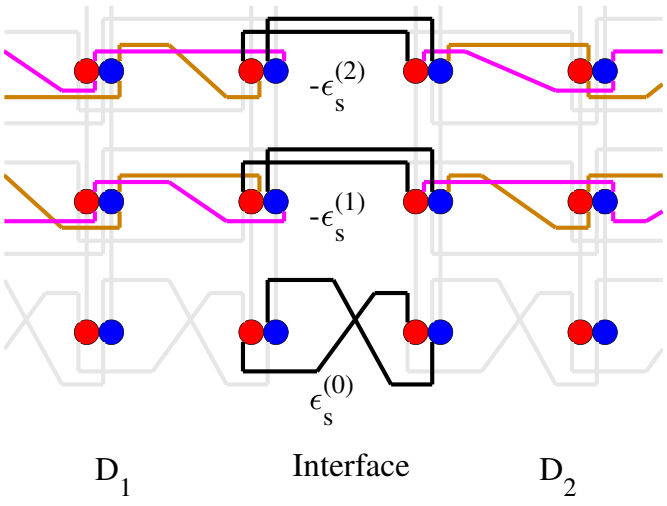

Figure 8.2: Schematic view of the edge-interface of MTI2. Bottom row represents $x^{(0)}_{r,s}, y^{(0)}_{r,s}$ sites, the second row $x^{(1)}_{r,s}, y^{(1)}_{r,s}$, and the third row $x^{(2)}_{r,s}, y^{(2)}_{r,s}$. Brown and magenta cross couplings are reversed in D_1 and D_2, and unchanged connections within the lattice are greyed out for visual purposes. Black connections represent simple spring connections created on the interface between the two separate MTI lattices. The number of horizontal sites N_r is taken to be even and the interface is presented at the half-way point between $N_r/2$ and $N_r/2+1$.

to the interface, matrix perturbation theory is required [20]. For the purpose of our work, it suffices to find specific connections that fit our requirements, which have been obtained by numerical exploration of the dispersion relation.

The interface of the two lattices, governed by D_1 and D_2, is depicted in Fig. 8.2. Note that connections of the lattices that are unaltered from MTI1 are greyed out as they are not of interest in this discussion. The connections between x and y sites of D_1 and D_2 are notably different if one follows a brown or magenta path transversely in each lattice. Recall, from Fig. 1.2, that the original MTI connections are implemented such that there are 3 levels of connections, corresponding to $x-x$ and $y-y$ connections in s, $x-x$ and $y-y$ connections in r, and $x-y$ and $y-x$ cross-connections in r. In general, we use simple springs to impose connections between the $x-x$ and $y-y$ sites at the interface with no cross-couplings imposed. These new interface springs are added to a new 4$^{\text{th}}$ level of connections on the pendula and are comparable to that of the strength of connections in the lattice bulk. One can imagine a level of black site connections added to the experimental diagram of Fig. 1.2(A). This quantitatively means that the values $\epsilon_s^{(j)}$ for $j=0,1,2$, which correspond to connections between the $x^{(j)}-x^{(j)}$ and $y^{(j)}-y^{(j)}$ sites on the interface, are proportional to f, i.e. $\epsilon_s^{(j)} \propto f$. Generally, as seen from Fig. 8.2, the values of $\epsilon_s^{(j)}$ are considered positive in the depicted case, but one can also impose negative values by swapping between one and two lever arms. Recall that one lever arm governs a negative coupling strength and two lever arms a pos-

itive coupling strength. There is greater freedom of setting up the mechanical lattice, such as altering x and y connections separately, but the current setup suffices for our analysis. As mentioned in the caption of Fig. 1.3, solid walls replace the outside sites of the decoupled lattices in order to implement edge sites with equivalent self-interaction term $A_s = 3 + \sqrt{3}$. To avoid altering the self-interaction term A_s of an interface pendulum, due to the new springs being added, we propose that as one increases the connection strength of the new simple springs we also decrease the strength of the connections from these interface sites to the solid walls. This process of adapting the edge-wall strength was seen explicitly in Fig. 4.1. The number of springs, and the subsequent coupling strength, connecting interface sites to solid walls tells us that one has the freedom of initialising $\epsilon_s^{(0)} \in [0, \sqrt{3}f]$ and $\epsilon_s^{(1)}, \epsilon_s^{(2)} \in [0, (1+\sqrt{3})f/2]$, without the need of altering the number of lever arms. Beyond these values, one must also adapt A_s accordingly or keep A_s equivalent by adapting other site connections. To keep the building blocks of the mechanical lattice as simple as possible we will consider values of $\epsilon_s^{(j)}$ within the appropriate ranges. This new nonlinear MTI is henceforth denoted as MTI2 to classify the lattice differently from the original MTI1 system. Consistent with our NLS analysis and [177], we keep the implementation of all other sites the same, with restoring forces as $\omega_0 = 3\pi/2$ and $f = 4.16\pi^2$.

8.3 Focusing coupled NLS parameters

Recall that we proposed a definition of focusing/defocusing non-integrable CNLS systems in Sec. 5.1.4. To ensure focusing parameters, one needs to ensure that we search for CNLS system parameters which allow the ZZ uniform state to be SHATS, whilst ZN/NZ are not SHATS. We, therefore, propose a MTI system that gives $d_1 g_1 > 0$ and $d_2 g_3 > 0$, which stems directly from the second derivative of the edge mode dispersion curves α_0'' and β_0''. Since the nonlinear terms g_{1-4} are strictly positive for the positive frequency choices $\alpha, \beta > 0$, one must ensure an EGV point where the secondary derivatives are positive, $\alpha_0'', \beta_0'' > 0$. We also seek connection strengths, at the interface, which exhibit edge modes that are different enough so that the dynamics of evolution are far away from NLS-described dynamics. Providing that $\alpha_0 \neq \beta_0$, to an appropriate order, one can clearly propose a BB solution that has no equivalent evolution of the single mode bright soliton, as described by the NLS. We find that this is generally the case providing that the connection variables $\epsilon_s^{(j)}$ are sufficiently large. Numerically, it is found that imposing the interface connections with strength

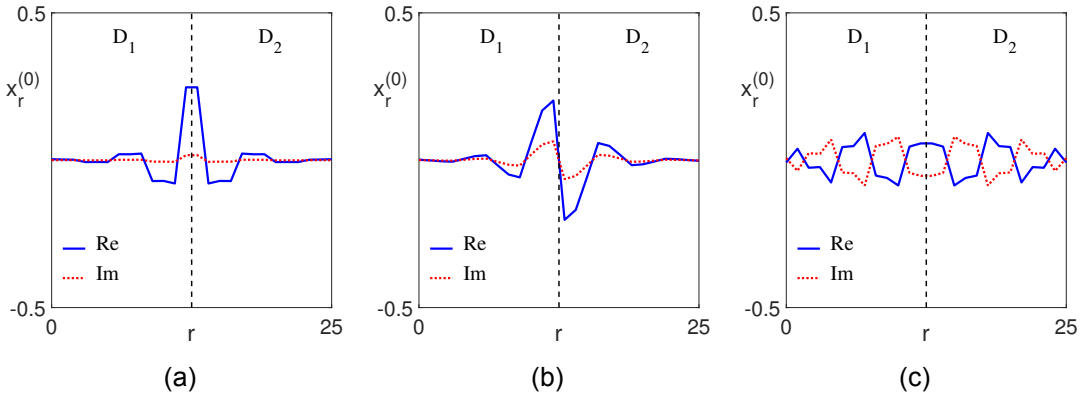

Figure 8.3: Example $x_r^{(0)}$ component of MTI2 eigenmodes with $N_r = 26$. Edge modes are shown decaying from the interface; (a) even mode and (b) odd mode. (c) A bulk mode is shown for comparison. Real and imaginary parts are depicted as blue-solid (red-dotted) lines and the interface of the two dynamical matrices $D_{1,2}$ is shown as a black-dashed line.

$\epsilon_s^{(0)} = \Omega_0 f$, $\epsilon_s^{(1)} = \epsilon_s^{(2)} = \Omega_0 f/2$, and $\Omega_0 = 0.994$ gives an EGV point between the odd and even edge-interface modes at the carrier wavenumber $k_0 = 2.011$. This particular choice of Ω_0 closely resembles the connection strength of the other sites, i.e. $\Omega_0 = 1$, but, since the two separate lattices have opposing $x-y$ connections, the full MTI2 lattice is very different from that of MTI1. These MTI2 parameters give rise to a focusing CNLS system with the system parameters,

$$d_1 = 0.105,\ g_1 = 0.022,\ g_2 = 0.036,$$
$$d_2 = 0.105,\ g_3 = 0.019,\ g_4 = 0.036,$$

where the governing envelopes move with group velocity $\alpha_0' = \beta_0' = 0.697$. Note that the governing CNLS equation is comparable to that of a symmetrically coupled CNLS and, in particular, similar to the FM2 equation with non-unity dispersion coefficients. This is primarily caused by the similarity of $\alpha_0 = 11.797$ and $\beta_0 = 11.805$.

An example component, chosen here as $x_r^{(0)}$, of the EGV edge modes found in the lower band gap is shown in Fig. 8.3(a–b) with even and odd parity respectively. The interface between the two sub-lattices is depicted by the black-dashed line, where we see the parity of the two edge modes explicitly, and the number of horizontal sites is chosen as $N_r = 26$. For comparison, Fig. 8.3(c) depicts a bulk mode of MTI2, at the EGV wavenumber, found in the bulk band between the lower and upper gaps of the dispersion relation.

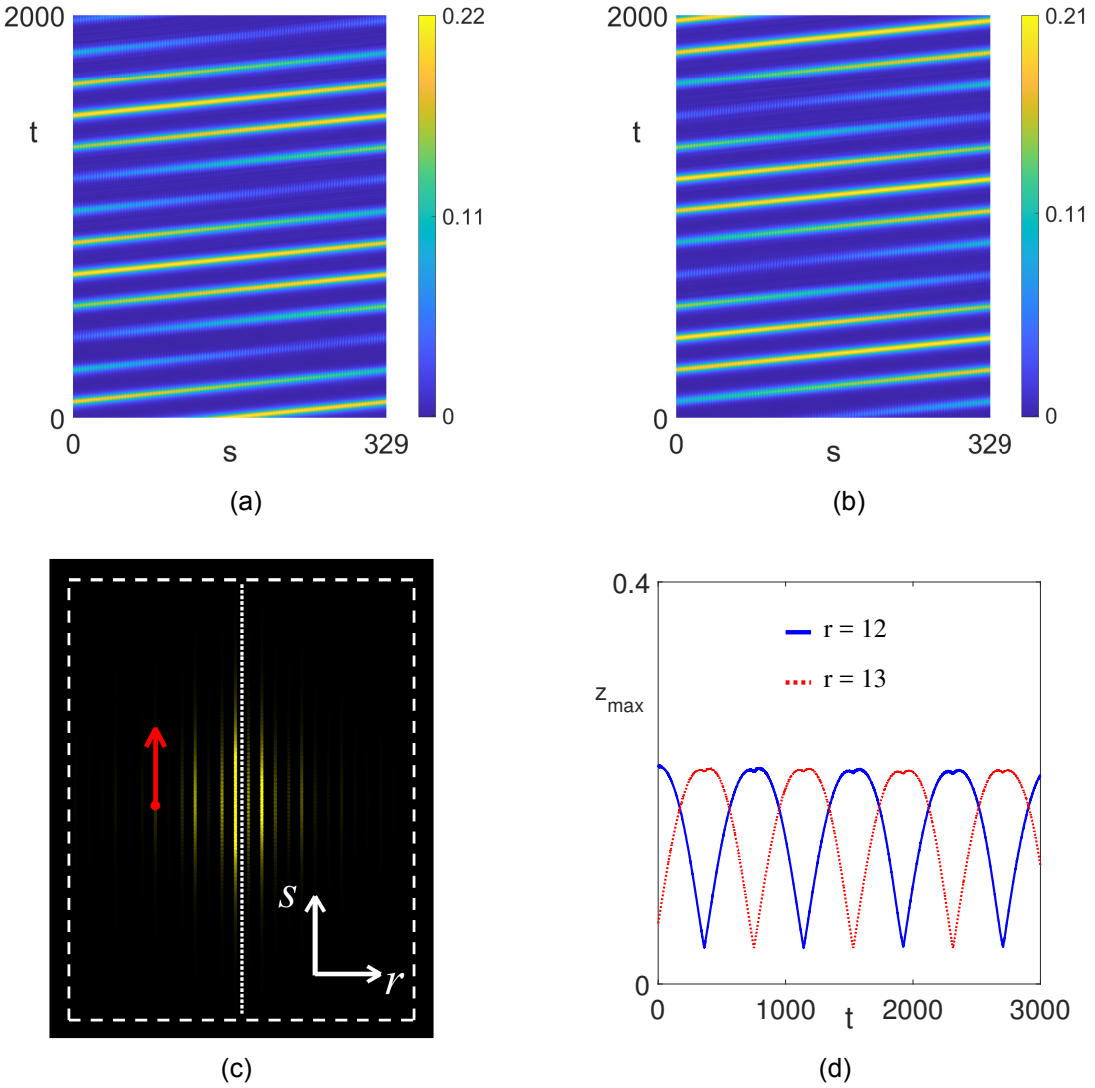

Figure 8.4: BB soliton propagation on a rectangular MTI2 lattice, with $N_r \times N_s = 26 \times 330$ sites. (a,b) Space-time evolution of the edge-interface sites located at $r = 12$ and $r = 13$ respectively. (c) 2D snapshot showing the initialisation of BB on the lattice. White-dashed lines are the site boundaries, white-dotted line is the interface, and the red arrow indicates envelope propagation direction. (d) Maximum amplitude vs time for the $r = 12$ (blue-solid) and $r = 13$ (red-dashed) sites.

8.3.1 Vector edge solitons

We will now consider the type of solutions that one can expect, from our previous non-integrable CNLS analysis, in the focusing regime found in the implemented MTI2 lattice. Since the parameters are focusing, by our definition, we note that ZN and NZ are not a viable option for SHATS states, so one can not expect stably propagating DB or BD vector solitons. By the same argument, one can not obtain travelling front solutions. BB soliton solutions, described by Eqs. (6.32-6.36), are viable since ZZ can be SHATS and the amplitudes can be physically implemented, providing that the width condition (6.35) is satis-

fied. Note that the quantity relating the nonlinear coefficients takes the sign of $g_2 g_4 - g_1 g_3 > 0$, which is important for allowing physical amplitudes. Though the NN state can be SHATS, we note that the amplitudes $|A_{1,2}|^2$ of the DD soliton solution take the opposite signs to that of the BB solution, so if BB solitons exist then DD solitons can not. This particular set of system parameters also does not permit the localised/periodic solutions that we obtained from the weakly nonlinear analysis of the Turing bifurcation. One can not obtain a critical value $\omega_{\Delta_\pm}$ that falls within the appropriate table of existence, Table 7.1.

To consider propagating BB solutions as vector edge solitons, we implement the BB envelope into the bimodal initial condition (8.1), such that the physical width of the envelope is accommodated by the number of vertical sites N_s. We consider the BB soliton that is governed by the travelling wave parameters $(C_g, \omega_A) = (0, -0.15)$, which leads to the frequency $\omega_B = -0.151$, and where we have imposed no initial phase multiplication $(\Theta_A, \Theta_B) = (0, 0)$. The choice of these parameters leads us to a soliton width of $W = 1.196$ and soliton amplitudes $A_1 = 2.399$ and $A_2 = 2.197$. Note that we considered a solution that is stationary in the CNLS system, but the MTI solution will travel with the envelope group velocity α_0'. If one instead considers a non-zero C_g, then the overall solution velocity, with respect to the cell variable S, is approximated from the ansatz as $\alpha_0' + \epsilon C_g$. The evolution of the BB soliton is shown in Fig. 8.4 on a rectangular domain of $N_r \times N_s = 26 \times 330$ sites, periodic in s. Figures 8.4(a–b) show the space-time evolution of the column of sites $r = 12$ and $r = 13$ respectively. These two columns of sites are precisely those edge sites at the interface, as shown in Fig. 8.4(c) where we have taken a snapshot of the 2D lattice initially. The white-dotted line shows the location of the interface and the red arrow indicates the direction of envelope propagation. The space-time plots show little energy loss from the BB envelope solution, with only a small amount of radiation lost to the tails of the profile. One key property of the evolution is that of the 'beating' propagation of the profile on either side of the interface. Figure 8.4(d) depicts this beating in time, as we see the maximum of the profiles, on each side of the interface, complementing each other. This beating is inherent to our design of the MTI due to the EGV edge modes being of odd and even parity. From the ansatz (4.1), it is obvious that a superposition of the two modes, when the two modes are similar with an odd/even structure, will cause a superposition of different harmonics in time respectively involving the carrier frequencies α_0 and β_0. The period of the beating can then be approximated by $2\pi/(\alpha_0 - \beta_0) \approx 778.9$, which matches up well with the beating portrayed in Fig. 8.4(d). The section of the profile that exhibits this periodic nature is observed when the product of the two envelopes are non-zero, i.e. $(A \cdot B)(S) \neq 0$.

8.3.2 Energy transfer of BB edge solitons

One key aspect of the CNLS equation is that the collision of VS may exhibit an energy and polarisation transfer amongst the two colliding solitons and components, as discussed in Sec. 6.3.1. Since the NLS does not exhibit an energy transfer, the observation of this transfer in BB solutions of the MTI lattice will further validate the CNLS equation governing the bimodal envelope dynamics. The problem with formulating this transfer is that the profile evolving on the sites is a superposition of both components, which makes it difficult to see directly the amplitude of each component soliton. We can, however, develop a process to extract this information from the component profiles by introducing two new excitation variables z_A and z_B. This process is apparent to us from the beating of the evolution, caused by the EGV edge modes being the odd and even modes of the lattice. Let us consider a generic site location, s, on the interface edge of each sub-lattice by the pendula x_R and y_R, with $R = N_r/2, N_r/2+1$. Let us also assume that the α mode is the even eigenmode, with the β mode odd. We know, for any moment in time, that the the solution is well-described by the ansatz (4.1), which we may write for the generic edge pendula as,

$$x_{\frac{N_r}{2}} = 2\mathcal{R}\mathsf{e}(A_1 X^{(1)}_{\frac{N_r}{2}}) + 2\mathcal{R}\mathsf{e}(B_1 X^{(2)}_{\frac{N_r}{2}}), \tag{8.4}$$

$$y_{\frac{N_r}{2}} = 2\mathcal{R}\mathsf{e}(A_1 Y^{(1)}_{\frac{N_r}{2}-1}) + 2\mathcal{R}\mathsf{e}(B_1 Y^{(2)}_{\frac{N_r}{2}}), \tag{8.5}$$

$$x_{\frac{N_r}{2}+1} = 2\mathcal{R}\mathsf{e}(A_1 X^{(1)}_{\frac{N_r}{2}+1}) + 2\mathcal{R}\mathsf{e}(B_1 X^{(2)}_{\frac{N_r}{2}+1}), \tag{8.6}$$

$$y_{\frac{N_r}{2}+1} = 2\mathcal{R}\mathsf{e}(A_1 Y^{(1)}_{\frac{N_r}{2}+1}) + 2\mathcal{R}\mathsf{e}(B_1 Y^{(2)}_{\frac{N_r}{2}+1}), \tag{8.7}$$

where $X^{(j)}, Y^{(j)}$ for $j = 1, 2$, are the values of the intra-cell variation, for the x and y pendula, of the α and β edge mode respectively. The values of A_1 and B_1, of a particular cell S_1 ($\tilde{S}_1$) and at time t_1 (τ_1), correspond to the intensity contribution from the remaining inter-cell terms of the ansatz (4.1) for each eigenmode, namely $A_1 = A(\tilde{S}_1, \tau_1)\,\mathsf{exp}(ik_0 S_1 - i\alpha_0 t_1)$ and $B_1 = B(\tilde{S}_1, \tau_1)\,\mathsf{exp}(ik_0 S_1 - i\beta_0 t_1)$. By definition of the even and odd eigenmodes, we may assume that

$$X^{(1)}_{\frac{N_r}{2}} = X^{(1)}_{\frac{N_r}{2}+1}, \quad Y^{(1)}_{\frac{N_r}{2}} = Y^{(1)}_{\frac{N_r}{2}+1}, \quad X^{(2)}_{\frac{N_r}{2}} = -X^{(2)}_{\frac{N_r}{2}+1}, \quad Y^{(2)}_{\frac{N_r}{2}} = -Y^{(2)}_{\frac{N_r}{2}+1}.$$

If we introduce the following notation,

$$x_A = \mathcal{R}\mathsf{e}(A_1 X^{(1)}_{\frac{N_r}{2}}), \quad y_A = \mathcal{R}\mathsf{e}(A_1 Y^{(1)}_{\frac{N_r}{2}}),$$
$$x_B = \mathcal{R}\mathsf{e}(B_1 X^{(2)}_{\frac{N_r}{2}}), \quad y_B = \mathcal{R}\mathsf{e}(B_1 Y^{(2)}_{\frac{N_r}{2}}),$$

then one can solve the system of equations (8.4-8.7) to yield the explicit definition of the new pendula variables as

$$x_A = \frac{x_{\frac{N_r}{2}} + x_{\frac{N_r}{2}+1}}{4}, \quad y_A = \frac{y_{\frac{N_r}{2}} + y_{\frac{N_r}{2}+1}}{4} \tag{8.8}$$

$$x_B = \frac{x_{\frac{N_r}{2}} - x_{\frac{N_r}{2}+1}}{4}, \quad y_B = \frac{y_{\frac{N_r}{2}} - y_{\frac{N_r}{2}+1}}{4}. \tag{8.9}$$

We may produce the excitation variables $z_A = \sqrt{x_A^2 + y_A^2}$ and $z_B = \sqrt{x_B^2 + y_B^2}$, which will, approximately, show how each CNLS component will evolve over time on the edge of the lattice.

Let us now consider the collision of two BB solitons initialised on the same edge interface. To accommodate the two VS we must increase the edge size. The only way to efficiently increase the edge size, in MATLAB R2020b, is to decrease the value of N_r simultaneously. This process provides a much smaller area for the decay of the edge-interface modes into the bulk, but the carrier frequencies are not yet degenerate and there is still a well-defined decay. The domain size is chosen as $N_r \times N_s = 16 \times 675$ sites, where an EGV point is found with connection parameter $\Omega_0 = 1$, at the carrier wavenumber $k_0 = 2.123$. Recall that the collision of analytically-described BB solitons are governed by the parameter space $(C_g, \omega_A, \Theta_A, \Theta_B)$ of each VS. We impose two BB solitons with equivalent amplitudes and opposing CNLS velocities, governed by $(C_g, \omega_A, \Theta_A, \Theta_B) = (0.4, -0.6, 0, 0)$ and $(C_g, \omega_A, \Theta_A, \Theta_B) = (-0.4, -0.6, 0, 0)$ respectively. The parameter choices subsequently give $\omega_B = -0.608$ and define the width as $W = 1.397$. Amplitudes are given as $A_1 = 2.736$ and $A_2 = 2.487$. Note that we have initialised two identical VS to showcase the possibility of negligible energy transfer, but one is free to implement and collide any CNLS-governed BB solutions with different widths/ampltiudes. The choice of $\Theta_{A,B} = 0$ previously showed no energy transfer, in Sec. 6.3.1, so we expect the same dynamics to be carried into the MTI evolution. Indeed, this is apparent from Fig. 8.11(a–b), shown at the end of this Chapter for clarity. The two figures show the evolution of the VS in the MTI and the CNLS respectively, where we have shown the MTI evolution w.r.t the excitation variables $z_{A,B}$. Both solutions are depicted on comparable domain sizes and over a comparable time frame. Recall that the MTI envelope propagates spatially for domain size $\epsilon N_s/3 = 22.5$ and on the slow time scale, governed by $\epsilon^2 t = 0.01t$. The MTI evolution is plotted in the reference frame comoving with $3\alpha_0'$. Note that there is no energy transfer between the two colliding structures and the collision point occurs exactly where is predicted by the CNLS evolution. There is excess radiation propagating in the MTI, which is expected since we omitted higher-order terms

of the solution and one only expects the profiles to propagate well on the time scale $O(\epsilon^{-2})$. The significant difference in the amplitudes of the profiles is expected due to how $z_{A,B}$ is calculated and the product with other terms in the bimodal ansatz.

We showed previously that one expects, in general, the most prominent energy transfer between the two BB when we initialise one of the VS with a $\Theta = \pi/2$ phase multiplication. To showcase this, we implement the left BB with the free phase parameters $(\Theta_A, \Theta_B) = (\pi/2, 0)$, and make no change to the phase of the right BB. Figure 8.11(c–d) showcase the energy transfer of the two VS qualitatively. It is clear from the comparison of the MTI and CNLS evolution, (c) and (d) respectively, that the underlying collision dynamics are governed by the CNLS system. As expected, the approximate loss/gain of energy after collision is well-described by the CNLS evolution, only with excess radiation and a difference in amplitude. Due to the reconstructive nature of $z_{A,B}$ and excess radiation of the MTI evolution it is difficult to quantify the loss/gain of energy of each component but, for the purpose of our analysis, the qualitative description suffices. The existence of such an energy transfer further validates our claim of the CNLS system governing the nonlinearly interacting edge modes of the MTI lattice.

8.3.3 The CNLS amplitude

Just as was done for the unimodal case, one can further validate the CNLS solutions by forcing different amplitudes for the solitons. A particular choice of travelling wave parameters forces a specific set of the component amplitudes $A_{1,2}$. By imposing a different amplitude, one can initialise a BB solution that no longer satisfies the underlying CNLS system. One would expect a significantly worse propagation of the imposed structure on the lattice interface.

As a case study, let us propose the BB soliton solution that we showed previously in Fig. 8.4. The most efficient way to visualise the effect of altering the amplitudes is to use the, previously described, excitation variables z_A and z_B. The description of the evolution in these variables will show the effect on the bright soliton of each component separately. Figure 8.5(a) shows these excitation variables initially (blue-solid profile) and after a long time frame (red-dashed profile), where we see little difference in the two component profiles. Since we expect similar effects by altering either A_1 or A_2, it suffices for us to choose one of these to differ from the analytically predicted value, say A_1. The effect on the BB propagation of halving and doubling this amplitude can be seen in Fig 8.5(b) and Fig. 8.5(c) respectively. When one considers an amplitude

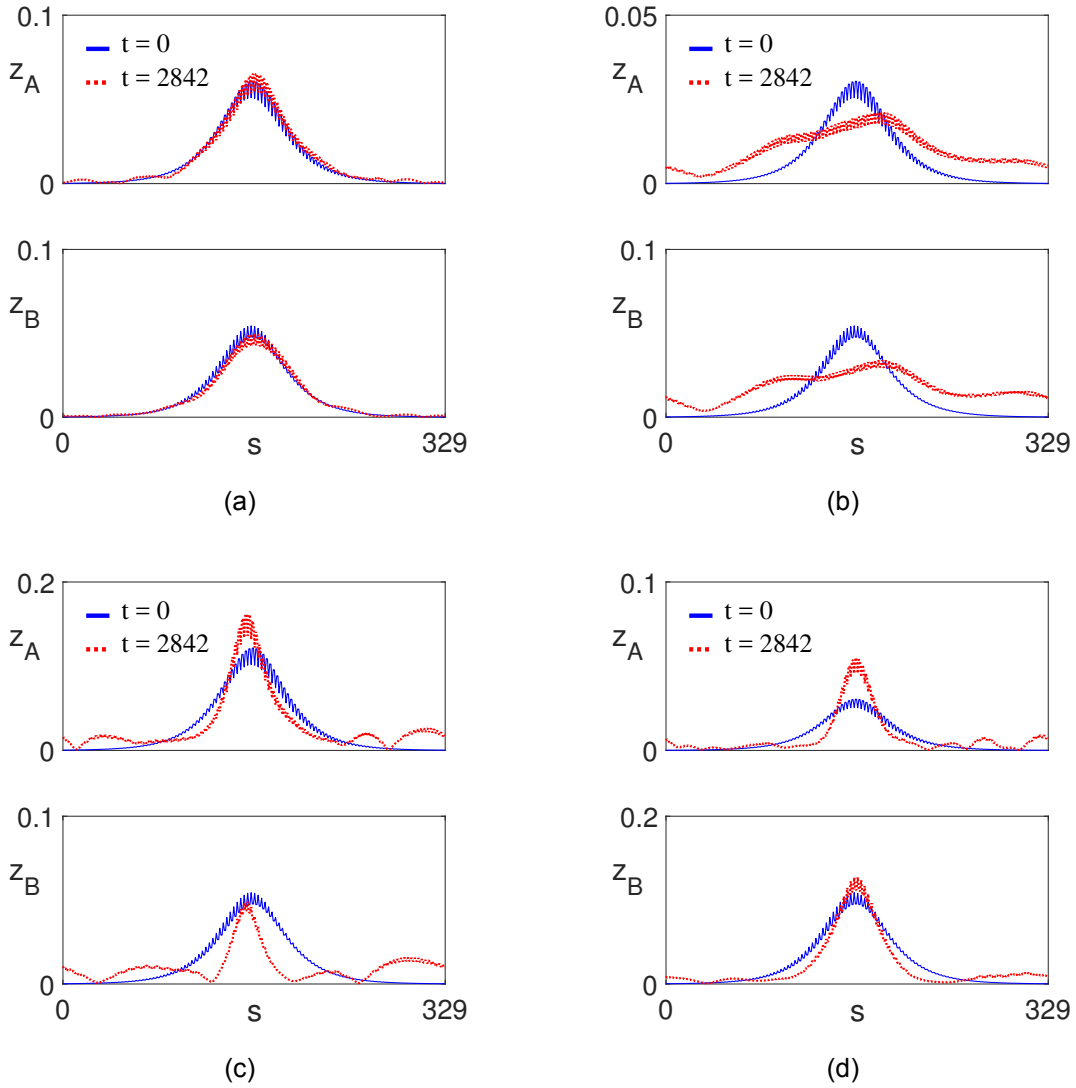

Figure 8.5: Propagation of BB solitons with adapted amplitudes on the MTI2 lattice with $N_r \times N_s = 26 \times 330$ sites. (a) $z_{A,B}$ excitation variables of the evolution in Fig. 8.4. (b,c,d) The amplitudes are adapted from Fig. 8.4 by numerically forcing the amplitudes to take the values (b) $(A_1/2, A_2)$, (c) $(2A_1, A_2)$, and (d) $(A_1/2, 2A_2)$.

smaller than that of the analytically predicted, there is a distinct increase in dispersion of the profile, whereas a greater amplitude causes an overfocusing effect on the profile. These two phenomenon are caused by the imbalance of dispersion and nonlinear terms, hence leading to an added effect from the respective terms.

One may additionally question the consequence of altering both A_1 and A_2 simultaneously. Figure 8.5(d) shows the BB soliton after numerically halving A_1 and doubling A_2 amplitudes. This process attempts to re-balance terms again but, since there is only one value in the amplitude space (A_1, A_2) that satisfies the analytical width, there is still an overfocusing effect caused by a simulated larger nonlinearity. The Euclidean distance of the adapted amplitudes, from the

original amplitudes, is large in comparison to the original amplitudes, so we expect the evolution to be significantly worse. When one adapts both amplitudes, there is likely to be a threshold within the (A_1, A_2) space that distinguishes between the overfocusing and dispersive effects. This is not important here as the above analysis is presented only to show that the soliton amplitudes must be governed by the CNLS system for the best BB propagation. We also note that reversing the process, i.e. doubling A_1 and halving A_2, causes a similar overfocusing effect which is expected.

8.4 Defocusing coupled NLS parameters

To ensure defocusing CNLS parameters, by our definition, we require $d_1 g_1 < 0$ or $d_2 g_3 < 0$ such that NZ or ZN states can be SHATS respectively. For the purpose of the MTI analysis, we will search for a regime in which both criteria are satisfied, so that one may also consider front solutions. Numerically it is found that imposing the interface connections with strength $\epsilon_s^{(0)} = \epsilon_s^{(1)} = \epsilon_s^{(2)} = \Omega_0 f/2$, where we define $\Omega_0 = 0.698$, yields an EGV point between the odd and even edge modes at the carrier wavenumber $k_0 = \pi/10$ in the upper band gap. This EGV point gives rise to a defocusing CNLS system with system parameters,

$$d_1 = -0.067,\ g_1 = 0.019,\ g_2 = 0.036,$$
$$d_2 = -0.071,\ g_3 = 0.018,\ g_4 = 0.035,$$

where the governing envelopes move with group velocity $\alpha_0' = \beta_0' = 0.617$. The carrier frequencies of the two modes are $\alpha_0 = 16.537$ and $\beta_0 = 16.766$.

8.4.1 Front solutions

The particular structure of the CNLS system parameters allows one to search for front solutions of the system. Both ZN and NZ are permitted to be SHATS, depending on the travelling wave parameters, and the front solutions obtained via the analysis carried out in Sec. 5.2 are viable envelope solutions. The solution is found numerically using the dissipative equation (5.38–5.39), as before, on an appropriate domain size that is then inserted into the bimodal initial condition (8.1). We find a stably propagating front in the CNLS with travelling wave parameters $(C_g, \omega_A, \omega_B) = (0, -0.297, -0.293)$, which leads to a heteroclinic connection of the two uniform states $(\phi_0, \psi_0) = (0, 4)$ and $(\phi_0, \psi_0) = (4, 0)$. Note that we have implemented a stationary front in the CNLS system, to en-

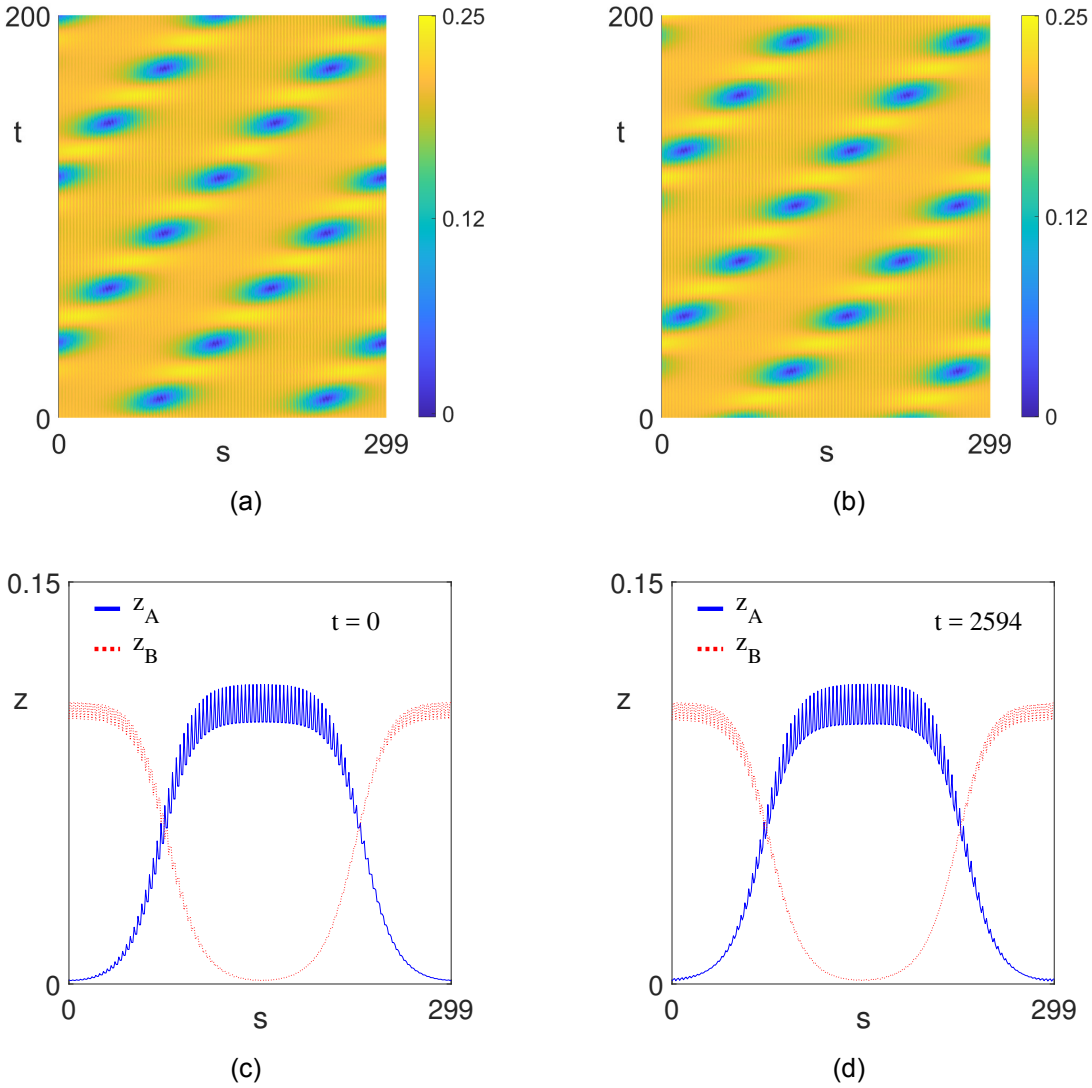

Figure 8.6: Front propagation on a rectangular MTI2 lattice, with $N_r \times N_s = 26 \times 300$ sites. (a,b) Space-time evolution of the edge-interface sites located at $r = 12$ and $r = 13$ respectively. (c,d) Profiles of the extracted z_A and z_B variables (c) initially and (d) after a long time frame $(t = 2594)$.

force $k_A = k_B = 0$, which keeps the solution viable on the domain periodic in the carrier wavenumber k_0. Since the system parameters are close to the symmetrically coupled regime, one expects the two uniform states to take similar magnitudes for any choice of physically-viable travelling wave parameters.

The front solution is evolved as an initial condition on the MTI2 lattice, with the results shown in Fig. 8.6. The space-time evolution on the columns of sites $r = 12$ and $r = 13$ are depicted in Fig. 8.6(a) and Fig. 8.4(b) respectively. Note that the original front profile is difficult to see, due to the superposition of edge modes, and the complementary beating is apparent where the envelope product $(A \cdot B)(S) \neq 0$. This beating now coincides with the time period of $2\pi/(\alpha_0 - \beta_0) \approx 27.4$, which is significantly smaller than the focusing regime

due to α_0 and β_0 being a greater distance apart. The evolution can be translated back to the original front profile if we recall the definition of the excitation variables z_A and z_B from Sec. 8.3.2. By plotting these variables, one recovers the front structure initially, depicted in Fig. 8.6(c), and after a long time frame, depicted in Fig. 8.6(d). The profile remains almost identical after a long propagation time with little energy loss to either z_A or z_B.

8.4.2 Vector edge solitons

Similarly to the focusing regime, we may consider vector soliton solutions of the defocusing CNLS system, that propagate stably, as vector edge solitons of the MTI. Since the front solution has already been uncovered in this system, we have the opportunity for numerical continuation as provided in Sec. 6.2. The fact that the front solutions already exhibit ZN and NZ SHATS states tells us that there is a strong possibility that nearby states with ω_A shifted may be SHATS also. One can then use this information to find numerical profiles of stable BD and DB solutions, depending on the direction of numerical continuation.

Let us consider a particular example of a BD profile propagating on the MTI2 interface. By considering the previous stationary front solution from Fig. 8.6, we numerically continue along the solution branch to the profile governed by the travelling wave parameters $(C_g, \omega_A, \omega_B) = (0, -0.332, -0.293)$. The CNLS profile velocity, and therefore plane-wave frequencies $k_{A,B}$, are considered zero as before. This particular parameter choice exhibits an overlap of the component profiles, with the peak of the bright component extending beyond the trough of the dark component. Figures 8.7(a–b) depict the evolution of the BD solution on the sites to the left $(r = 12)$ and right $(r = 13)$ of the interface respectively. Since the two modes are respectively odd and even, one can think of the initial profile on the two sets of sites as the combination of the CNLS profiles $|A(S) + B(S)|$ and $|A(S) - B(S)|$, which is the explicit reason behind the small rise in energy between the two dips of energy. If the peak of the bright soliton does not surpass the trough of the dark soliton then this rise of energy does not exist. As the solution evolves on the lattice, the profile swaps between the two different combinations in a periodic beating, just as with the previous solutions. The original structure of the bright and dark components has been lost due to the superposition of states so, just as we did with the front solution, we will translate to the variables z_A and z_B to visualise the soliton components. Figures 8.7(c–d) show the profiles of z_A and z_B initially and after a long time frame $(t = 2919)$, where we see negligible differences in the overall profile of

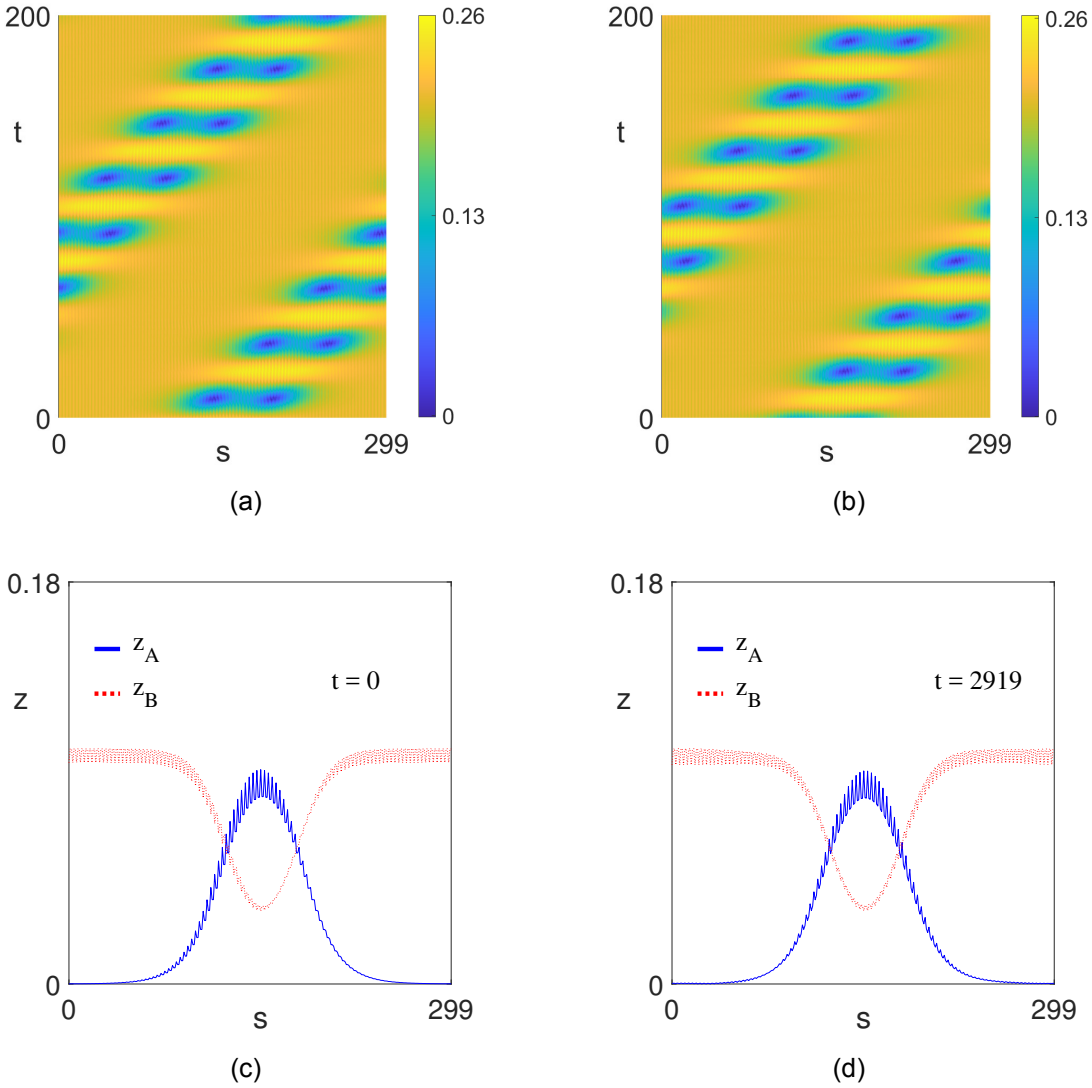

Figure 8.7: BD soliton propagation on a rectangular MTI2 lattice, with $N_r \times N_s = 26 \times 300$ sites. (a,b) Space-time evolution of the edge-interface sites located at $r = 12$ and $r = 13$ respectively. (c,d) Profiles of the extracted z_A and z_B variables (c) initially and (d) after a long time frame $(t = 2919)$.

each component. There is minimal energy lost to the bulk sites of the lattice and there is little energy redistribution across the edge sites.

We briefly note that the existence of DB solitons is also permitted via the same process. These solutions are not shown explicitly since they produce no difference in dynamics to the BD solutions, only with a reversal of the component solitons. Complex BD and DB profiles, obtained by numerically breaking the original assumption $C_g = k_A = k_B$, are also viable solutions providing that the profile can be made periodic on the column of sites. We do not explicitly show these solutions here since the number of vertical sites N_s would need to be increased to accommodate both the profile and its conjugate profile, an array size outside the capability of the software MATLAB R2020b.

The specific structure of the nonlinear parameters $g_2 g_4 - g_1 g_3 > 0$, with $d_1, d_2 < 0$, tells us that SHATS NN states are not possible since $d_1 d_2 (g_2 g_4 - g_1 g_3) > 0$ is an explicit criterion for spatial hyperbolicity of the state. If either (both) of the $d_{1,2}$ signs are flipped then the physical viability of one (both) of $|A_{1,2}|^2$ is no longer satisfied, so one can not have DD soliton solutions in these cases. DD solitons as RHOs from NN are only available if one has $d_1, d_2 < 0$ and $g_2 g_4 - g_1 g_3 < 0$, as discussed in Sec. 5.1.2. The problem with this is that the MTI2 system is unlikely to produce a CNLS system in which the XPM terms are smaller than the SPM terms. This is due to the structure of the eigenvectors. In particular, for comparable connection strengths $\epsilon_s^{(j)}$, the eigenvectors are similar, i.e. $\|\mathbf{X^{(1)}}\|_4^4 \approx \|\mathbf{X^{(1)}X^{(2)}}\|_2^2$, so the XPM terms are approximately twice the magnitude of the SPM terms, written as $g_2 \approx 2g_1$ and $g_4 \approx 2g_3$.

It is possible that we may formulate DD solutions with non-SHATS NN, though we do not expect a stable CNLS evolution in general. It suffices for us to say that a DD solution that propagates stably for a reasonable time frame $(t > 100)$ in the CNLS, will propagate well in the MTI for a long time frame. Instability presented by the CNLS system will, therefore, be observed well beyond the expected time frame of the MTI evolution, where the edge solitons are derived on the $O(\epsilon^{-2})$ time scale. An example DD solution, propagating on the MTI2 interface, is shown in Fig 8.8. This profile is governed by the travelling wave parameter choice of $(C_g, \omega_A, k_A, k_B) = (0, -0.23, 0, 0)$, which leads to the plane-wave frequency $\omega_B = -0.246$. The DD solution then exhibits a soliton width of $W = 1.313$ embedded on the background fields $A_1 = 2.231$ and $A_2 = 1.962$. The evolution of the profile is seen on the sites to the left $(r = 12)$ and right $(r = 13)$ of the interface in Fig. 8.8(a) and Fig. 8.8(b) respectively. Two DD solitons have been initialised for spatial periodicity reasons. Note that complementary beating of the profile is observed for the sections of the profile away from the dark soliton minimum. The zero-valued diagonal lines are precisely the dark soliton solutions, with the zero-valued lines parallel to s-axis being the minimum value of the beating periodicity located every 27.4 seconds. The profile of the DD solution is apparent from the evolution of the initial condition in MTI2, so we don't require the translation to the variables z_A and z_B here. The profiles of the sites to the left $(r = 12)$ and right $(r = 13)$ of the interface are shown initially and after a long time frame $(t = 2919)$ in Fig. 8.8(c) and Fig. 8.8(d) respectively. Note that there is very little change to either profile over the time evolution, other than the periodic beating, and the width of the profiles remain almost constant throughout.

All of the solutions presented in the defocusing CNLS regime propagate well in the nonlinear MTI. The beating of solutions observed in both the focusing

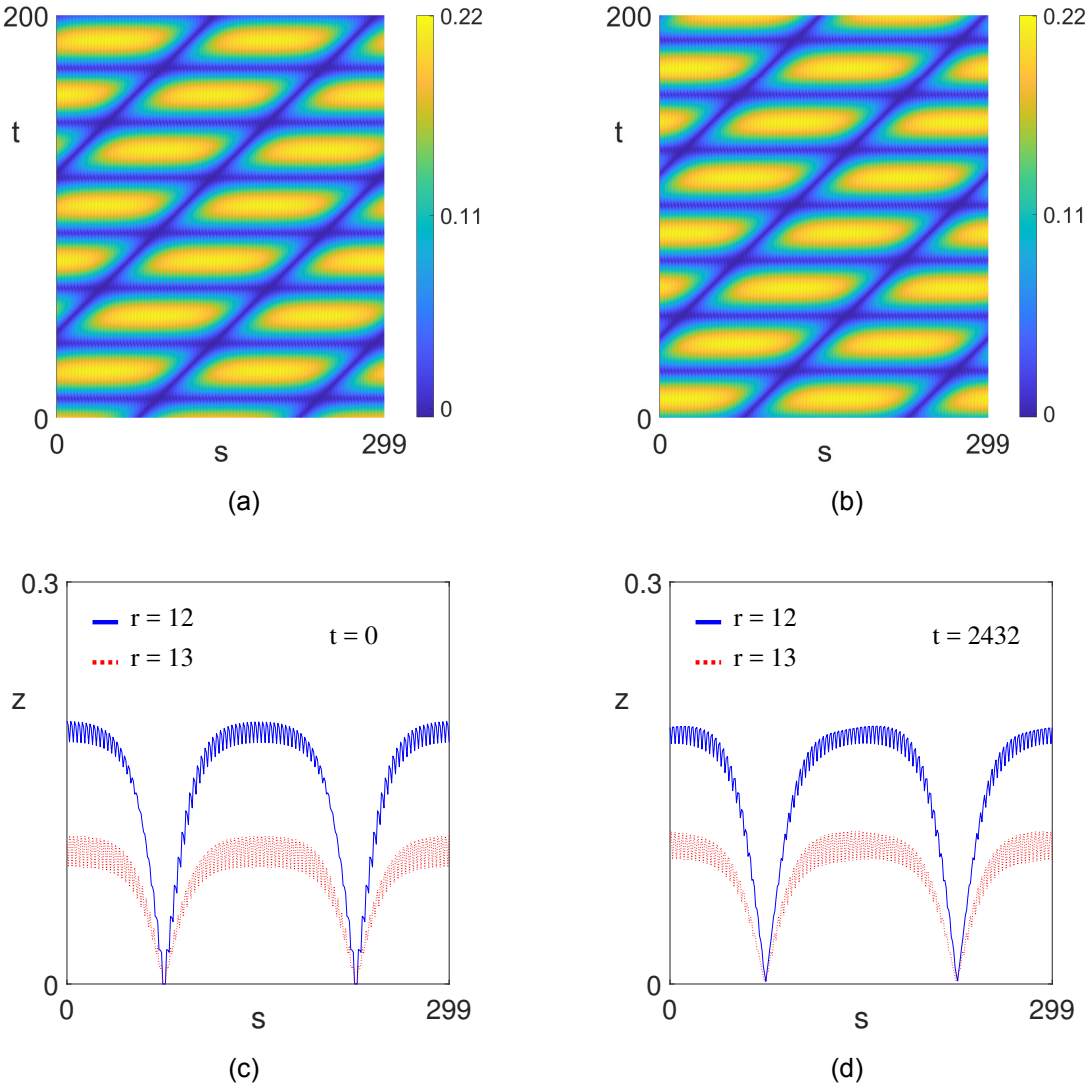

Figure 8.8: DD soliton propagation on a rectangular MTI2 lattice, with $N_r \times N_s = 26 \times 300$ sites. (a,b) Space-time evolution of the edge-interface sites located at $r = 12$ and $r = 13$ respectively. (c,d) Profiles of the $r = 12$ and $r = 13$ sites (c) initially and (d) after a long time frame $(t = 2432)$.

and defocusing regimes is a property of the CNLS envelopes only, as opposed to NLS unimodal behaviour, so these topologically protected edge solutions are truly governed by the bimodal analysis. Note that localised/periodic solutions were also not permitted in this defocusing regime. Particular choices of travelling wave parameters made either the NN state non-physical or the Turing critical value became a Belyakov-Delaney value instead. The significant number of criteria and the particular nature of system parameters mean that a physically-viable Turing value is unlikely to be found in the focusing/defocusing-type parameters we have proposed. Numerically, all CNLS systems that we have found to exhibit the Turing bifurcation require different signs of nonlinear parameters g_{1-4}, which is not possible given the current definition of the MTI parameters.

8.5 Topological Protection

Though we have shown explicitly the formation of nonlinear edge solutions, and the subsequent energy transfer that can be obtained through collisions, we are yet to fully explore the resistance to backscattering that one expects from topologically protected vector edge solitons (TPVES). The most efficient way to show the topological protection of the TPVES is to analyse how these nonlinear structures propagate through boundary defects. We may carve defects into the interface between the two sub-lattices, which will now act as differently-shaped holes in the s-periodic domain. As a case study, the propagation of the BB soliton solution considered in Fig. 8.4 is proposed to travel through a rectangular defect. This rectangular defect is taken by removing a straight, free tetronimo [2] of sites out of the edge of each sub-lattice, with dimensions 1×20. The new lattice boundary can be seen explicitly in Fig. 8.9(c), where the rectangular defect represents a hole in the s-periodic domain. By considering the excitation variables $z_{A,B}$ we may analyse how each soliton component is affected by the defect in the domain. Profiles of z_A and z_B initially, and after a long time frame, are shown in Fig. 8.9(a) and Fig. 8.9(b) respectively. There is some distortion of the profile, in comparison to the domain with no defect, but the profile of each component still remains as expected. One may propose definitions for the relative energy (L^2-norm of the excitation relative to the initial value) and the maximum amplitude (L^∞-norm of the excitation) to numerically quantify how energy is lost/redistributed due to the removal of these sites.

Let us measure the energy on the interface sites after one complete cycle of the domain. We can quantify this energy on the left and right edge sites, as well as produce an average of the two, which may be plotted against the propagation cycle. A line of best fit may be plotted through the average energy to show a general trend for the loss over time. The maximum amplitude of z_A and z_B may also be taken after one complete cycle of the domain, and an average of the two gives a trend for how the amplitude of the components are redistributed over time. These trends are shown in Fig. 8.9(d), where we have plotted the average energy relative to the initial value, E_{Rel}, with the line of best fit included, and the maximum amplitudes, $z_{A,B}$, as well as the average of the two z_{Av}, over a very long time frame $(t > 6000)$. The first observation is that each of the maximum amplitudes of $z_{A,B,Av}$ trend downwards after many cycles of the domain indicating an overall loss of amplitude over time. As one expects, the average of the energy over the two variables is lost over time so there is some decay of the BB profiles whilst repeatedly travelling through the defect. Small fluctuations of the energy and amplitude are seen here as this energy

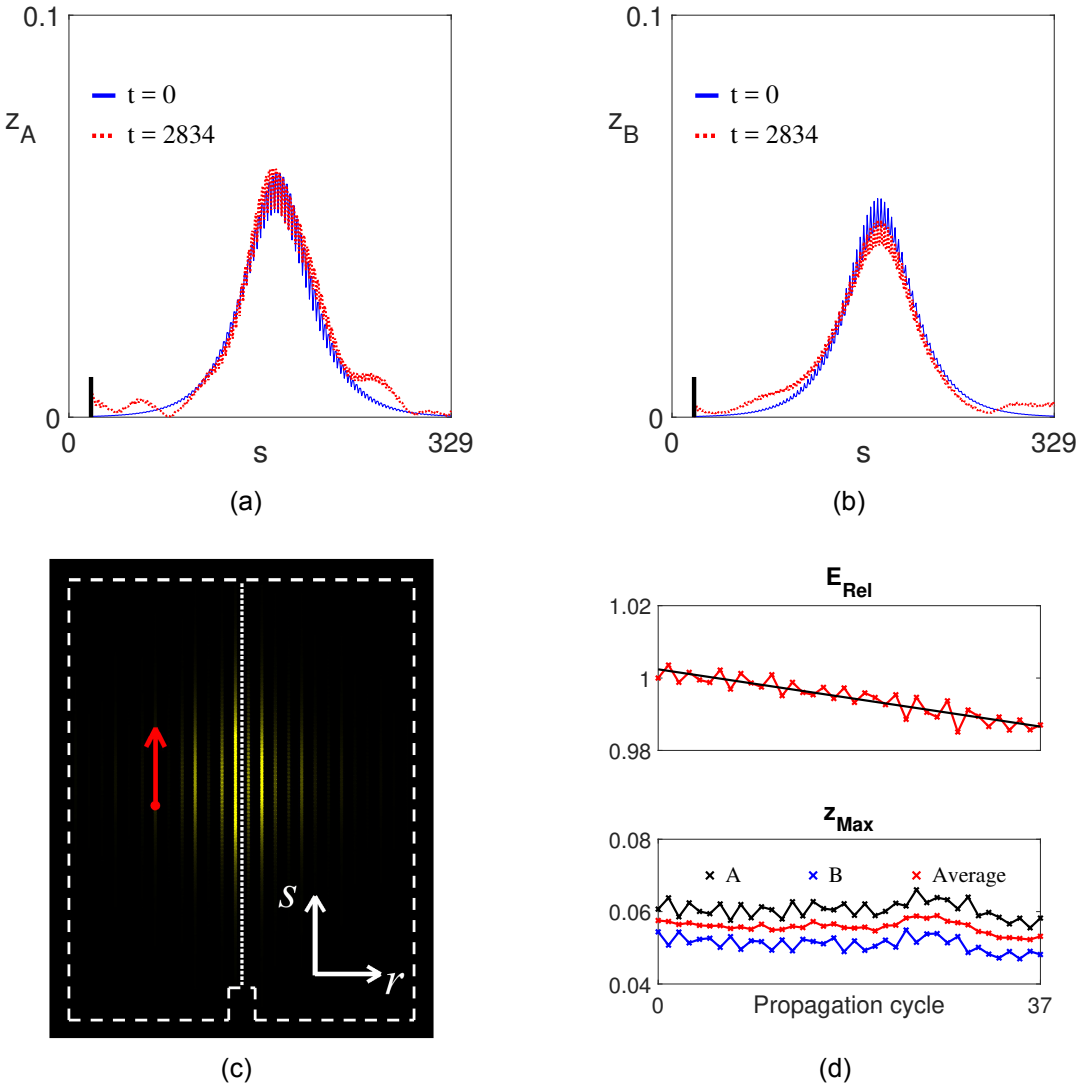

Figure 8.9: Propagation of a BB soliton through a rectangular defect. (a,b) Excitation variables (a) z_A and (b) z_B shown initially (blue-solid profile) and after a long time frame (red-dashed profile). The solid-black line indicates where the defect is located. (c) 2D snapshot of the lattice initially. (d) The trend of energy (relative to the initial value) and maximum amplitude of the $z_{A,B}$ profiles, along with the trend of the average of the two, z_{Av}, after many cycles of the domain.

is gained and lost from neighbouring sites in small quantities. The general trends of this figure tells us that a small amount of energy is lost from the BB soliton structure over time, which translates to phononic scattering into the bulk at the defect. Quantitatively, this scattering is very small compared to the total energy of the sites as the average energy of both components after 37 cycles of the domain only falls to $\approx 98.7\%$ of the initial value. The average maximum amplitude falls to $\approx 92.4\%$ of the initial value. This tells us that the peaks of the BB components are somewhat redistributed amongst the profiles, rather than lost to scattering at the defect, which matches up well with the profiles shown in Fig. 8.9(a–b).

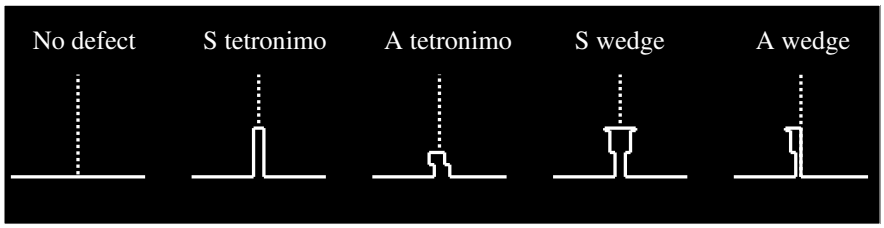

(a)

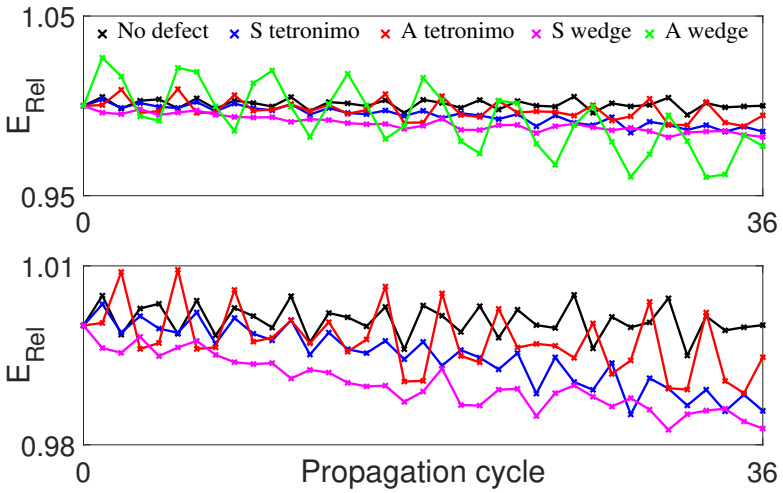

(b)

Figure 8.10: Numerical scattering analysis for BB solitons. (a) Different defects carved into the bottom edge of the MTI2 lattice; S (A) denotes symmetric (asymmetric). (b) Relative energy for each domain type over many domain cycles. The upper panel includes all 5 domains, whilst the lower panel doesn't include the asymmetric wedge domain and focuses on the similar trends.

8.5.1 Numerical scattering analysis

To further validate the topological protection of these vector edge solitons, we may consider the propagation of BB solitons through different defects of the lattice and perform a numerical scattering analysis of the excitation. For the greatest variation of defects, we consider the 5 domain types shown in Fig. 8.10(a), where the label S (A) denotes symmetric or asymmetric structures. The symmetric tetronimo is precisely the defect shown previously, in Fig. 8.9, and the asymmetric tetronimo (pseudonym skew tetronimo) is created via the same 4 building blocks of the straight defect, only with a restructuring. The wedge defect is formed roughly by imposing a staircase towards the bottom edge of the lattice, with the asymmetric version inscribed by calving the staircase into the left sub-lattice only.

To compare the propagation of the BB profile through these defects we consider the relative energy, as depicted previously in Fig. 8.9(d). We note that the maximum amplitude is difficult to compare between symmetric and asymmetric defects since the trend of $z_{A,B}$ for asymmetric defects produces large

Table 8.1: Percentage loss of the average energy after $t > 6000$, in comparison to initially, using a fitted trend line through the points.

Defect type	Energy (% of initially)
No defect	99.8
S tetronimo	98.4
A tetronimo	99.1
S wedge	98.6
A wedge	95.7

oscillations of these variables in time. This is likely caused by the formulation of the $z_{A,B}$ variables from Eqs. (8.8–8.9), and where the envelope must propagate through extra sites on one side of the interface only. The energy trends for all 5 domain types are plotted in Fig. 8.10(b), where we have plotted the average energy over many cycles. Note that the upper panel includes all 5 domain types, where as the lower panel does not consider the energy of the asymmetric wedge, in order to better compare the other 4 similar trends. Quantitatively, the percentage loss of the average energy after $t > 6000$ in comparison to initially, using lines of best fit, are shown in Table 8.1. The best propagation is that of the BB soliton travelling on the domain with no defect imposed, which is an expected result. We also see that, early in the evolution, the BB soliton traversing the tetronimos behaves similarly to that of no defect. After this, the general trend of energy loss tells us that the defect that produces the least amount of scattering into the bulk is that of the asymmetric tetronimo. This is likely due to the fewer number of missing edge sites, in comparison to the symmetric counterpart. Small asymmetric changes to the defect also makes little difference to the BB propagation, but we do see larger fluctuations of the energy for the asymmetric structures. When the defect is heavily asymmetric, such as missing sites on one sub-lattice only, the propagation becomes significantly worse and we see a greater scattering effect, with large scale fluctuations of the energy being lost/gained to neighbouring sites. This is enforced by the energy of the asymmetric wedge in the upper panel of Fig. 8.10(b). We also note that larger defects, such as the wedge, generally have a greater effect on how much energy is lost to the neighbouring sites initially, but after a long time frame this effect becomes less apparent. It is vital to note that, even in the case of large asymmetric defects, the energy loss over a long time frame is still small relative to the initial energy.

To summarise this chapter, we have explicitly designed a new MTI that exhibits interacting edge modes at the interface of two sub-lattices with opposing spin Chern numbers. The freedom of altering site connections at this interface leads to greater control over the types of CNLS systems that one may expect

to govern the bimodal behaviour of the MTI. Using the previous analysis on solutions that one may expect in these non-integrable systems, we have presented a plethora of TPVES, in the form of bright and dark components, as well as the construction of front solutions. We explored the validity of these solutions by considering a brief analysis on the amplitude of BB solitons, as well as exploring the possibility of energy transfer between the two edge modes of the TPVES. Finally, we considered the topological protection of these structures by imposing non-uniform interfaces in which BB solitons traverse arbitrary defects with little scattering into the neighbouring sites.

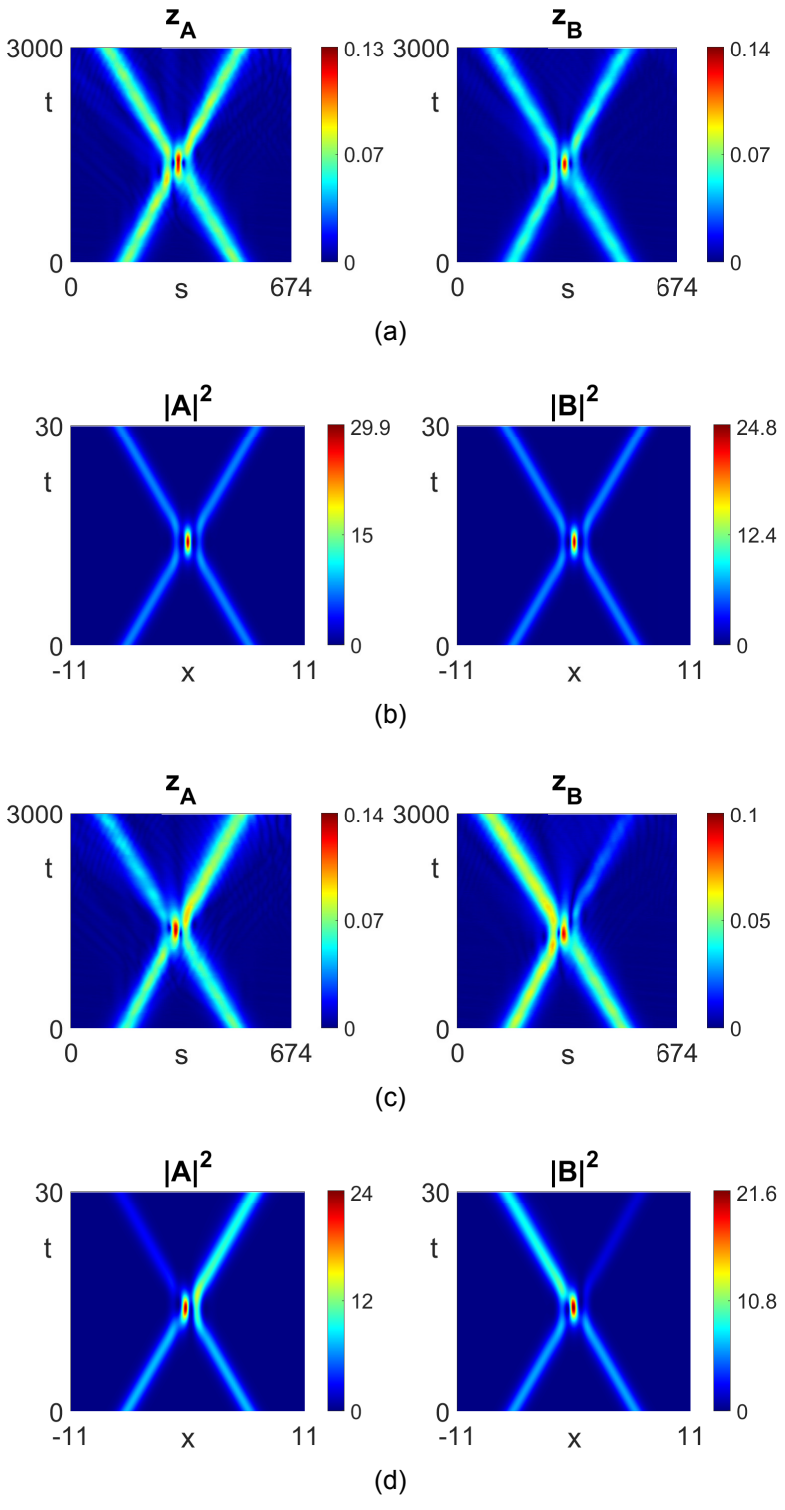

Figure 8.11: Energy transfer of BB solitons on the MTI2 edge-interface. Right BB has free phase parameters $(\Theta_A, \Theta_B) = (0, 0)$. (a,b) No energy transfer with left BB parameters $(\Theta_A, \Theta_B) = (0, 0)$. (a) MTI evolution and (b) corresponding CNLS evolution. (c,d) Prominent energy transfer with left BB parameters $(\Theta_A, \Theta_B) = (\pi/2, 0)$. (c) MTI evolution and (d) corresponding CNLS evolution.

Chapter 9

Discussion and Conclusions

Formally, the bulk of the work in this thesis has been dedicated to the discovery of TPES and TPVES in nonlinear MTIs. Though there is appropriate literature on the discovery of these special solutions in PTIs [7, 10, 125, 96], our work represents a first step into the nonlinear mechanical (phononic) world. To conclude the work, we will discuss the relevance of each Chapter, and present further considerations and future improvements that one may take into consideration. We also present the repercussions of the work to physical applications of acoustical devices.

In Chapter 3 we presented the mathematical framework for incorporating the inherent nonlinear effects of the MTI first studied by Susstrunk and Huber [177]. Through the method of multiple scales, and dimension reduction, we showed that the NLS equation governs the underlying envelope dynamics of the edge modes of the system. The TPES are also shown numerically by direct simulations of the spring-oscillator system for a wide variety of NLS solitons including bright, dark, and rogue edge solitons. The TPES are special as they inherit the topological protection of the linear system. By contrast, non-topologically protected edge solitons around the corners are found to exhibit a combination of transmission, reflection and scattering into the bulk. We note that the solutions portrayed here are the standard solutions of the NLS equation, but one can expect more exotic solutions such as multi-breathers/multi-rogue waves [73], as well as the distinct possibility of soliton tunnelling [173]. The presented system is only one of a plethora of ways to incorporate nonlinearity into MTIs. For instance, it is entirely possible that the inclusion of nonlinear springs may yield different envelope equations, just as the FPUT lattice yields the KdV envelope equation [68, 5].

In Chapter 4 we showed that nonlinearly interacting envelopes of the edge modes of the system are well-governed by the non-integrable CNLS equation with EGV. We also presented a simple approach to deforming the Hamiltonian

of the system and subsequently deforming the dispersion relation of the conductive edge states of the MTI, so that the EGV condition may be satisfied. The straightforward nature of the MTI allows us to alter spring constants with relative ease and should be appropriate for experimental implementations of the mechanical lattice like in the original paper [177]. We note that the way we have adapted the MTI Hamiltonian is only one of many possibilities and a full analysis, through matrix perturbation methods [20], with a larger variety of spring constants/lattice setup/self wall-springs included will likely produce a wide-variety of CNLS system parameters. These parameters could be more favourable, and thus TPVES obtained in a simpler manner, than those presented here.

Due to the non-integrable nature of the underlying equation, in Chapters 5-7 we looked for appropriate solutions of the system which could then be translated back to the original MTI lattice. Chapter 5 was dedicated to travelling front solutions of the CNLS. We considered necessary conditions for the existence of the travelling front solutions. The decreased number of constraints on the system parameters here, in comparison to existing literature [82, 101, 16], allows front propagation in a wider array of CNLS systems. This is particularly useful in situations, like ours, where CNLS models physical phenomena where the system parameters are rarely ideal [9, 96]. Systems that permit front solutions through the derived conditions include, but are not limited to, the system of symmetrically coupled CNLS [82, 101] or non-symmetric CNLS with equal masses [16]. The mathematical framework is also adaptable to those systems with additional linear terms, often seen in the BEC literature [63, 83, 58, 172], CNLS with $N-$components [112], or CNLS with higher-order nonlinearities [157, 81]. Due to our development of SHATS conditions for the NZ/ZN equillibria, we found that these front solutions propagate stably in the CNLS; this is confirmed by direct numerical simulations of the CNLS. The behaviour of grey soliton-front collisions can also be partially explained by conservation equations, particular in those CNLS closer to the defocusing Manakov system.

We also briefly discuss the possible extension of the front analysis to discrete forms of the CNLS equation. For instance, one may apply a discretisation procedure to the reduced travelling wave ODE system (5.9-5.10) and produce a $2N$-dimensional set of ODEs given by,

$$i\phi_n' + d_1(\phi_{n+1} + \phi_{n-1}) + (\omega_A - 2d_1)\phi_n + g_1|\phi_n|^2\phi_n + g_2|\psi_n|^2\phi_n = 0, \tag{9.1}$$

$$i\psi_n' + d_2(\psi_{n+1} + \psi_{n-1}) + (\omega_B - 2d_2)\psi_n + g_3|\psi_n|^2\psi_n + g_4|\phi_n|^2\psi_n = 0, \tag{9.2}$$

for $n = 1, \ldots, N$, where $'$ denotes the time-derivative. Note that we have con-

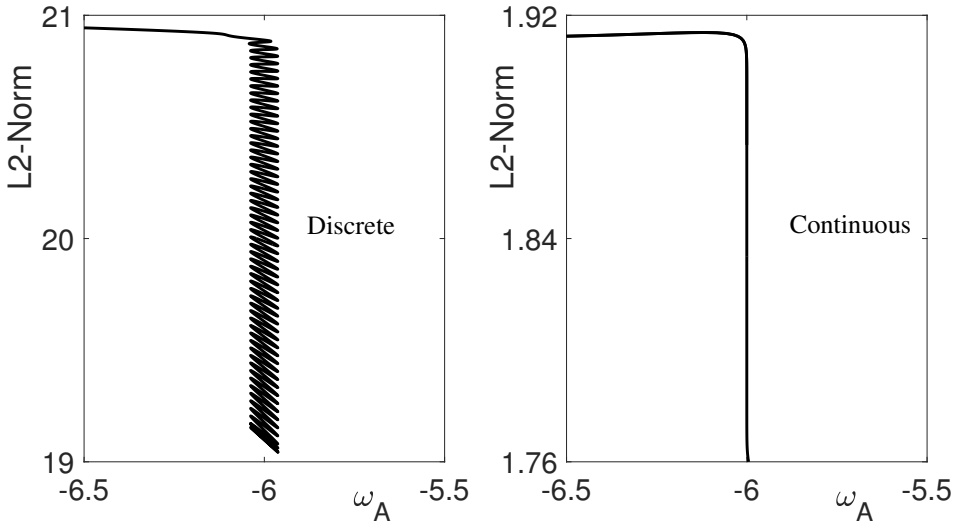

Figure 9.1: AUTO continuation, in the parameter ω_A, for a stationary front in the discrete CNLS (left panel) and continuous CNLS (right panel) equations.

sidered a discretisation of the spatial derivative only, whereas some discretisation processes also involve nearest site nonlinear interactions [4]. We also consider stationary solutions $(C_g = k_{A,B} = 0)$ to avoid having to overcome the Peierls-Nabarro barrier [118]. Using AUTO, we can look for stationary solutions of the discrete $2N$-dimensional system with implicitly imposed Neumann boundary conditions. The analysis of Chapter 5 lets us find a stationary front, for the CNLS with system parameters $d_{1,2} = -1$, $g_{1-3} = 2$, and $g_4 = 3$, at the chosen point $(C_g, \omega_A, \omega_B) = (0, -6, -7.349)$ in the travelling wave parameter space. One would expect a discrete analogue of this front in (9.1-9.2), which is precisely what is shown in Fig. 9.1. Here, we see the AUTO continuation of both the discrete and continuous CNLS fronts. The key difference is the expansion of the front branch into a pinning region for the discrete system, like the snakes seen in the analysis of the SH23 equation in Sec. 7.2; the pinning region is found to be $[-6.038, -5.962]$. Note that the different scales in the y-axis for each panel is directly caused by the different definitions of the $L2$-norm between the two problems in AUTO. The continuous front is precisely the continuum limit of the pinning region, as one would expect. Just outside of this pinning region, we also observe a depinning transition when solutions are evolved in the discrete CNLS. A more in-depth study into the phenomenon of the discrete CNLS should yield the possibility of weakly nonlinear localised states and homoclinic defected snakes in the discrete regime. The analysis may be similar to that of the Brusselator model [186] or, more generally, in reversible systems [41].

In Chapter 6 we considered the formation of VS solutions. Nonlinear front

solutions made ideal starting points for numerically continuing into VS solutions, since branching shows direct structural relationships between the two types of nonlinear solutions. The VS, front, and equillibria were all found to be related via numerical continuation in the chosen bifurcation parameter ω_A. The continuation process allowed us to find the numeral profiles of BD/DB soliton solutions, which were shown to propagate stably, via direct numerical simulations, for the chosen system and travelling wave parameters. We were then able to formulate a qualitative analysis for the collision dynamics in some CNLS systems. Exact BB and DD soliton solutions were then formed, with appropriate criteria developed for their existence in the non-integrable regime. The governing family of parameters were shown for each type of structure and we subsequently considered the qualitative analysis of BB collisions. The collisions of both BB and BD/DB were found to be inelastic (shape-changing), with excess radiation propagating from the collision point, which is expected for non-integrable regimes. The VS solutions in non-integrable regimes also permit the exchange of energy amongst components and across solitons, though predicting the energy transfer quantitatively is not considered here. In future, it would be favourable to consider the interaction of VS and front solutions through the conservation equations presented in Sec. 5.3. Providing that the governing VS parameters are in a sufficiently small parameter space, e.g. BD solitons governed by (C_g, ω_B), then it is possible to use the conserved quantities to describe interactions involving these structures, where radiation is negligible. This could then extend the current literature on non-integrable collisions in the CNLS, to incorporate a wider-variety of situations and help categorise, qualitatively and quantitatively, the dynamics of these collisions. Another problem that one faces whilst defining the structures is temporal stability of the solution. In a lot of cases, a solution may propagate unstably despite being embedded on a SHATS (linearly stable) background field. Here, we expect more in-depth analysis of the linear stability of the localised structure to yield greater insight into the solution. Most soliton solutions that we have shown here translate into physically-viable structures, though the impact of non-integrable soliton stability as a whole, including orbital stability and spectral analysis [33, 165], is a fruitful topic that provides one with many questions.

In Chapter 7 we briefly discussed the concept of more exotic solutions to the non-integrable CNLS equation. These solutions were classified as localised and periodic states occurring near the Turing critical value of the travelling wave ODE system. We developed minimum criteria for the existence of the Turing value, where these branches of solutions may be found bifurcating from the NN equilibrium. The solutions were also presented in particular CNLS sys-

tems that were found, numerically, to satisfy the SHATS and Turing criteria. Both the travelling, localised states and periodic states were shown to propagate stably for relatively short time-frames before temporal instability caused visible differences in the structures. The temporal stability of the localised solution can be inferred from the numerical spectrum of the CNLS, just as with the aforementioned soliton solutions. We did not find a stably-propagating localised solution in the CNLS systems that we considered, via direct numerical simulations, but there is no immediate evidence gathered here to discount the existence of such stable structures. In regards to the periodic states, we discussed the concept of the Eckhaus instability through the derived modulation equation (7.23). As mentioned previously, one must derive a modulation equation that encompasses the complex-valued nature of the CNLS field variables. This could be a significant result in the grand scheme of the CNLS, with the existence of stably-propagating periodic, travelling states indicating a world of CNLS solutions not yet considered. We have formulated a key comparison of these states to states of the more-commonly studied SH23 equation. It was found that localised and periodic states of the dissipative SH23 equation may exhibit a travelling-wave counterpart in the conservative SH23 equation. The travelling wave counterparts are precisely what one may expect in the CNLS equation, therefore, it is plausible that a Turing-Eckhaus analysis of the stationary states of the dissipative equation may be sufficient to provide unique, travelling states of the CNLS like those seen in Fig. 7.6 and Fig. 7.7.

In Chapter 8 we brought together the work of non-integrable CNLS solutions, from the previous chapters, and applied this to the nonlinear MTI. We first considered EGV CNLS solutions of the MTI1 lattice, obtained through the method of adapting the lattice in Chapter 4, and it was shown that the particular structure of the CNLS system parameters permitted only DB solitons. These TPVES acted as expected in the MTI, however, the structure was difficult to see visually, other than an apparent envelope of modulations, due to the difference in magnitudes in the sites of the edge eigenmodes. We then formulated a way to depict these TPVES more clearly, as well as consider other CNLS solutions, by connecting two sub-lattices of the MTI with opposing topological sectors. Due to bulk-edge correspondence, the system exhibited edge-interface conduction that allows the formation of TPVES on a periodic strip of sites. It was subsequently shown that altering the strength of connection sites between the two sub-lattices produced CNLS systems that permitted the propagation of BB, DD, front, and BD/DB TPVES solutions. We then discussed, and formulated analysis on, the topic of topological protection by imposing different-shaped holes in the periodic domain, concluding that there is a clear insensitivity to

small disorders of the lattice shape. We also discussed the concept of energy transfer amongst the two edge envelopes, which is a concept that has not been introduced in previous literature to our knowledge. The ability to impose energy transfer amongst TPVES is unique, in comparison to the TPES counterparts, and indicates a robust manipulation of the phononic conduction on the edge. For instance, providing one can predict the outcome of two colliding CNLS solitons, one can impose soliton suppression/amplification of a TPVES by colliding it with another TPVES along the edge.

In regards to further work on the subject, it is immediately apparent that we have not imposed the exotic solutions of Chapter 7 in MTI2. This is due to the very particular nature of the conditions allowing the Turing value to exist and NN to be SHATS. A major problem with the current hardware/software specifications, as mentioned previously, is the limitation on the MTI domain size. Even when one finds physically-viable Turing solutions, the MTI domain size must be increased to permit the more intricate localised solutions. Though we have not explicitly shown the Turing states, we expect, with larger domain sizes and with the many varieties of ways to adapt the lattice, these states to be found and for Turing state edge modes to exist. Note that, even though the states may not propagate stably for a long-time frame $(t < 100)$, they translate to a sufficiently stable propagation in the MTI $(t < 10000)$ when $\epsilon = 0.1$. We note also that a full analysis of the topological protection may be considered by utilising a bi-layer geometry of the mechanical lattice, where each site of one sub-lattice is connected to the equivalent site of the other sub-lattice. By taking this approach, one may consider how the TPVES will propagate on a much more physically-viable full 2D domain, rather than on the periodic domain we have considered.

The tunable and lossless nature of TPES and TPVES may have significant impacts on existing applications of TIs such as optical and acoustic delay lines [84, 212] and robust manipulation of light and sound [49, 205]. In photonic TIs, TPES have been applied to nonlinear filtering and switching [125] and optical isolation [214]; analogues in mechanical TIs may soon emerge which may have significant implications on the design of acoustic delay lines. Thus, the existence of TPES/TPVES could serve as an important benchmark in incorporating nonlinearity into the design of perturbative topological metamaterials [137], especially since they enable robust transport of mechanical states along the edge and robust manipulation of sound along arbitrary pathways. Compared to photonic TIs, mechanical TIs contain much simpler components, which may allow TPES/TPVES to be observed in tabletop experiments. Moreover, the time reversal symmetry of mechanical systems implies bidirectional wave propagation

and thus potentially richer dynamics than their photonic counterparts. For example, recall the unique property of mechanical TIs, discussed in Sec. 3.2.2, that widening the spectral parameter ϵ may cause interference between the envelopes of the two Kramer's pairs at carrier wavenumbers k_0 and $2\pi - k_0$.

On the fundamental level, we expect to motivate further studies on nonlinear coherent structures in mechanical TIs, and thus help establish a new research area of nonlinear topological mechanics at the intersection of condensed matter physics, nonlinear dynamics, and classical mechanics. The underlying mathematical framework can be readily generalised to other mechanical TIs with discrete elements [147, 164], possibly with dissipation [198] and forcing [148] included. Further extensions may also include TIs in nonlinear continuous media, such as recent proposals based on magnetic solitons [115] and water waves [195].

Bibliography

[1] Kramer's pairs: Topology in condensed matter, tudelft opencourseware. https://ocw.tudelft.nl/course-readings/helical-edge-states-kramers-pairs. Accessed: 04-01-2021.

[2] Tetronimo. https://en.wikipedia.org/wiki/Tetromino. Accessed: 08-12-2020.

[3] M. Ablowitz and J. Ladik. Nonlinear differential–difference equations and fourier analysis. *Journal of Mathematical Physics*, 17(6):1011–1018, 1976.

[4] M. Ablowitz and B. Prinari. Nonlinear schrodinger systems: continuous and discrete. *Scholarpedia*, 3(8):5561, 2008.

[5] M. J. Ablowitz. *Nonlinear dispersive waves: asymptotic analysis and solitons*, volume 47. Cambridge University Press, 2011.

[6] M. J. Ablowitz, M. Ablowitz, P. Clarkson, and P. A. Clarkson. *Solitons, nonlinear evolution equations and inverse scattering*, volume 149. Cambridge university press, 1991.

[7] M. J. Ablowitz, C. W. Curtis, and Y.-P. Ma. Linear and nonlinear traveling edge waves in optical honeycomb lattices. *Physical Review A*, 90(2):023813, 2014.

[8] M. J. Ablowitz, C. W. Curtis, and Y.-P. Ma. Adiabatic dynamics of edge waves in photonic graphene. *2D Materials*, 2(2):024003, 2015.

[9] M. J. Ablowitz and T. P. Horikis. Interacting nonlinear wave envelopes and rogue wave formation in deep water. *Physics of Fluids*, 27(1):012107, 2015.

[10] M. J. Ablowitz and Y.-P. Ma. Strong transmission and reflection of edge modes in bounded photonic graphene. *Optics letters*, 40(20):4635–4638, 2015.

[11] M. J. Ablowitz and Y. Zhu. Evolution of bloch-mode envelopes in two-dimensional generalized honeycomb lattices. *Physical Review A*, 82(1):013840, 2010.

[12] A. Adamatzky and J. Durand-Lose. Collision-based computing. In *Handbook of Natural Computing*, pages 1949–1978. Springer, 2012.

[13] V. Afanasyev, Y. S. Kivshar, V. Konotop, and V. Serkin. Dynamics of coupled dark and bright optical solitons. *Optics letters*, 14(15):805–807, 1989.

[14] G. P. Agrawal. Nonlinear fiber optics. In *Nonlinear Science at the Dawn of the 21st Century*, pages 195–211. Springer, 2000.

[15] N. Akhmediev, V. Eleonskii, and N. Kulagin. Exact first-order solutions of the nonlinear schrödinger equation. *Theoretical and mathematical physics*, 72(2):809–818, 1987.

[16] S. Alama, L. Bronsard, A. Contreras, and D. E. Pelinovsky. Domain walls in the coupled gross–pitaevskii equations. *Archive for Rational Mechanics and Analysis*, 215(2):579–610, 2015.

[17] Y. Ando. Topological insulator materials. *Journal of the Physical Society of Japan*, 82(10):102001, 2013.

[18] I. S. Aranson and L. Kramer. The world of the complex ginzburg-landau equation. *Reviews of modern physics*, 74(1):99, 2002.

[19] J. E. Avron, D. Osadchy, and R. Seiler. A topological look at the quantum hall effect. *Physics today*, 56(8):38–42, 2003.

[20] B. Bamieh. A tutorial on matrix perturbation theory (using compact matrix notation). *arXiv preprint arXiv:2002.05001*, 2020.

[21] W. Bao, D. Jaksch, and P. A. Markowich. Numerical solution of the gross–pitaevskii equation for bose–einstein condensation. *Journal of Computational Physics*, 187(1):318–342, 2003.

[22] F. Baronio, M. Conforti, A. Degasperis, S. Lombardo, M. Onorato, and S. Wabnitz. Vector rogue waves and baseband modulation instability in the defocusing regime. *Physical review letters*, 113(3):034101, 2014.

[23] C. M. Bender and S. A. Orszag. *Advanced mathematical methods for scientists and engineers I: Asymptotic methods and perturbation theory*. Springer Science & Business Media, 2013.

[24] T. B. Benjamin and J. Feir. The disintegration of wave trains on deep water. *J. Fluid mech*, 27(3):417–430, 1967.

[25] A. Bergeon, J. Burke, E. Knobloch, and I. Mercader. Eckhaus instability and homoclinic snaking. *Physical Review E*, 78(4):046201, 2008.

[26] N. G. Berloff and C. Yin. Turbulence and coherent structures in two-component bose condensates. *Journal of Low Temperature Physics*, 145(1-4):187–207, 2006.

[27] B. A. Bernevig and T. L. Hughes. *Topological insulators and topological superconductors*. Princeton university press, 2013.

[28] B. A. Bernevig, T. L. Hughes, and S.-C. Zhang. Quantum spin hall effect and topological phase transition in hgte quantum wells. *science*, 314(5806):1757–1761, 2006.

[29] B. A. Bernevig and S.-C. Zhang. Quantum spin hall effect. *Physical review letters*, 96(10):106802, 2006.

[30] Y. V. Bludov, V. Konotop, and N. Akhmediev. Matter rogue waves. *Physical Review A*, 80(3):033610, 2009.

[31] R. W. Bomantara, W. Zhao, L. Zhou, and J. Gong. Nonlinear dirac cones. *Physical Review B*, 96(12):121406, 2017.

[32] M. Born and E. Wolf. *Principles of optics: electromagnetic theory of propagation, interference and diffraction of light*. Elsevier, 2013.

[33] J. P. Boyd. *Chebyshev and Fourier spectral methods*. Courier Corporation, 2001.

[34] J. Burke and E. Knobloch. Localized states in the generalized swift-hohenberg equation. *Physical Review E*, 73(5):056211, 2006.

[35] J. Burke, A. Yochelis, and E. Knobloch. Classification of spatially localized oscillations in periodically forced dissipative systems. *SIAM Journal on Applied Dynamical Systems*, 7(3):651–711, 2008.

[36] I. A. Butt and J. A. Wattis. Discrete breathers in a two-dimensional hexagonal fermi–pasta–ulam lattice. *Journal of Physics A: Mathematical and Theoretical*, 40(6):1239, 2007.

[37] H. M. Byrne. A weakly nonlinear analysis of a model of avascular solid tumour growth. *Journal of mathematical biology*, 39(1):59–89, 1999.

[38] A. Chabchoub, N. Hoffmann, and N. Akhmediev. Rogue wave observation in a water wave tank. *Physical Review Letters*, 106(20):204502, 2011.

[39] A. Champneys and J. Toland. Bifurcation of a plethora of multi-modal homoclinic orbits for autonomous hamiltonian systems. *Nonlinearity*, 6(5):665, 1993.

[40] A. R. Champneys. Homoclinic orbits in reversible systems and their applications in mechanics, fluids and optics. *Physica D: Nonlinear Phenomena*, 112(1-2):158–186, 1998.

[41] A. R. Champneys, E. Knobloch, Y.-P. Ma, and T. Wagenknecht. Homoclinic snakes bounded by a saddle-center periodic orbit. *SIAM Journal on Applied Dynamical Systems*, 11(4):1583–1613, 2012.

[42] E. Charalampidis, P. Kevrekidis, D. Frantzeskakis, and B. Malomed. Dark-bright solitons in coupled nonlinear schrödinger equations with unequal dispersion coefficients. *Physical Review E*, 91(1):012924, 2015.

[43] E. Charalampidis, J. Lee, P. Kevrekidis, and C. Chong. Phononic rogue waves. *Physical Review E*, 98(3):032903, 2018.

[44] R. Chaunsali, E. Kim, A. Thakkar, P. G. Kevrekidis, and J. Yang. Demonstrating an in situ topological band transition in cylindrical granular chains. *Physical review letters*, 119(2):024301, 2017.

[45] B. G.-g. Chen, N. Upadhyaya, and V. Vitelli. Nonlinear conduction via solitons in a topological mechanical insulator. *Proceedings of the National Academy of Sciences*, 111(36):13004–13009, 2014.

[46] F. Chen and M. Herrmann. Kdv-like solitary waves in two-dimensional fpu-lattices. *Discrete and Continuous Dynamical Systems-A*, 38(5):2305–2332, 2018.

[47] W.-J. Chen, S.-J. Jiang, X.-D. Chen, B. Zhu, L. Zhou, J.-W. Dong, and C. T. Chan. Experimental realization of photonic topological insulator in a uniaxial metacrystal waveguide. *Nature communications*, 5(1):1–7, 2014.

[48] Z.-G. Chen and Y. Wu. Tunable topological phononic crystals. *Physical Review Applied*, 5(5):054021, 2016.

[49] X. Cheng, C. Jouvaud, X. Ni, S. H. Mousavi, A. Z. Genack, and A. B. Khanikaev. Robust reconfigurable electromagnetic pathways within a photonic topological insulator. *Nature materials*, 15(5):542, 2016.

[50] R. Y. Chiao, E. Garmire, and C. H. Townes. Self-trapping of optical beams. *Physical Review Letters*, 13(15):479, 1964.

[51] C. Chong, M. A. Porter, P. Kevrekidis, and C. Daraio. Nonlinear coherent structures in granular crystals. *Journal of Physics: Condensed Matter*, 29(41):413003, 2017.

[52] C. Christov, S. Dost, and G. Maugin. Inelasticity of soliton collisions in systems of coupled nls equations. *Physica Scripta*, 50(5):449, 1994.

[53] T. Congy, G. El, M. Hoefer, and M. Shearer. Nonlinear schrödinger equations and the universal description of dispersive shock wave structure. *Studies in Applied Mathematics*, 142(3):241–268, 2019.

[54] S. M. Cox and P. C. Matthews. Exponential time differencing for stiff systems. *Journal of Computational Physics*, 176(2):430–455, 2002.

[55] J. D. Crawford. Introduction to bifurcation theory. *Reviews of Modern Physics*, 63(4):991, 1991.

[56] J. Cuevas, L. Q. English, P. G. Kevrekidis, and M. Anderson. Discrete breathers in a forced-damped array of coupled pendula: modeling, computation, and experiment. *Physical review letters*, 102(22):224101, 2009.

[57] J. Cuevas, G. James, P. G. Kevrekidis, B. A. Malomed, and B. Sanchez-Rey. Approximation of solitons in the discrete nls equation. *Journal of Nonlinear Mathematical Physics*, 15(sup3):124–136, 2008.

[58] B. Deconinck, P. Kevrekidis, H. Nistazakis, and D. Frantzeskakis. Linearly coupled bose-einstein condensates: From rabi oscillations and quasiperiodic solutions to oscillating domain walls and spiral waves. *Physical Review A*, 70(6):063605, 2004.

[59] A. Degasperis and S. Lombardo. Integrability in action: solitons, instability and rogue waves. In *Rogue and Shock Waves in Nonlinear Dispersive Media*, pages 23–53. Springer, 2016.

[60] A. Degasperis, S. Lombardo, and M. Sommacal. Rogue wave type solutions and spectra of coupled nonlinear schrödinger equations. *Fluids*, 4(1):57, 2019.

[61] E. J. Doedel, A. R. Champneys, F. Dercole, T. F. Fairgrieve, Y. A. Kuznetsov, B. Oldeman, R. Paffenroth, B. Sandstede, X. Wang, and C. Zhang. Auto-07p: Continuation and bifurcation software for ordinary differential equations. 2007.

[62] J. R. Dormand and P. J. Prince. A family of embedded runge-kutta formulae. *Journal of computational and applied mathematics*, 6(1):19–26, 1980.

[63] N. Dror, B. A. Malomed, and J. Zeng. Domain walls and vortices in linearly coupled systems. *Physical Review E*, 84(4):046602, 2011.

[64] Y. Duguet, O. Le Maitre, and P. Schlatter. Stochastic and deterministic motion of a laminar-turbulent front in a spanwisely extended couette flow. *Physical Review E*, 84(6):066315, 2011.

[65] K. B. Dysthe and K. Trulsen. Note on breather type solutions of the nls as models for freak-waves. *Physica Scripta*, 1999(T82):48, 1999.

[66] R. Eftimie, G. de Vries, and M. Lewis. Weakly nonlinear analysis of a hyperbolic model for animal group formation. *Journal of mathematical biology*, 59(1):37–74, 2009.

[67] G. El and M. Hoefer. Dispersive shock waves and modulation theory. *Physica D: Nonlinear Phenomena*, 333:11–65, 2016.

[68] E. Fermi, P. Pasta, S. Ulam, and M. Tsingou. Studies of the nonlinear problems. Technical report, Los Alamos Scientific Lab., N. Mex., 1955.

[69] C. Fernandez-Oto, O. Tzuk, and E. Meron. Front instabilities can reverse desertification. *Physical review letters*, 122(4):048101, 2019.

[70] M. G. Forest, D. W. McLaughlin, D. J. Muraki, and O. Wright. Nonfocusing instabilities in coupled, integrable nonlinear schrödinger pdes. *Journal of Nonlinear Science*, 10(3):291–331, 2000.

[71] M. G. Forest and O. C. Wright. An integrable model for stable: unstable wave coupling phenomena. *Physica D: Nonlinear Phenomena*, 178(3-4):173–189, 2003.

[72] M. Först, C. Manzoni, S. Kaiser, Y. Tomioka, Y. Tokura, R. Merlin, and A. Cavalleri. Nonlinear phononics as an ultrafast route to lattice control. *Nature Physics*, 7(11):854, 2011.

[73] P. Gaillard. Families of quasi-rational solutions of the nls equation and multi-rogue waves. *Journal of Physics A: Mathematical and Theoretical*, 44(43):435204, 2011.

[74] R. Gardner and C. Jones. Traveling waves of a perturbed diffusion equation arising in a phase field model. *Indiana University Mathematics Journal*, pages 1197–1222, 1990.

[75] L. Gelens and E. Knobloch. Traveling waves and defects in the complex swift-hohenberg equation. *Physical Review E*, 84(5):056203, 2011.

[76] J. Ginibre and G. Velo. The global cauchy problem for the non linear klein-gordon equation. *Mathematische Zeitschrift*, 189(4):487–505, 1985.

[77] K. Gowda, H. Riecke, and M. Silber. Transitions between patterned states in vegetation models for semiarid ecosystems. *Physical Review E*, 89(2):022701, 2014.

[78] C. Grossmann, H.-G. Roos, and M. Stynes. *Numerical treatment of partial differential equations*, volume 154. Springer, 2007.

[79] D. R. Gulevich, D. Yudin, D. V. Skryabin, I. V. Iorsh, and I. A. Shelykh. Exploring nonlinear topological states of matter with exciton-polaritons: Edge solitons in kagome lattice. *Scientific Reports*, 7(1):1780, 2017.

[80] B. Guo, L. Ling, and Q. Liu. Nonlinear schrödinger equation: generalized darboux transformation and rogue wave solutions. *Physical Review E*, 85(2):026607, 2012.

[81] I. Hacinliyan and S. Erbay. Coupled quintic nonlinear schrödinger equations in a generalized elastic solid. *Journal of Physics A: Mathematical and General*, 37(40):9387, 2004.

[82] M. Haelterman and A. Sheppard. Bifurcations of the dark soliton and polarization domain walls in nonlinear dispersive media. *Physical Review E*, 49(5):4512, 1994.

[83] M. Haelterman and A. Sheppard. Polarization domain walls in diffractive or dispersive kerr media. *Optics Letters*, 19(2):96–98, 1994.

[84] M. Hafezi, E. A. Demler, M. D. Lukin, and J. M. Taylor. Robust optical delay lines with topological protection. *Nature Physics*, 7(11):907, 2011.

[85] F. Haldane and S. Raghu. Possible realization of directional optical waveguides in photonic crystals with broken time-reversal symmetry. *Physical review letters*, 100(1):013904, 2008.

[86] F. D. M. Haldane. Model for a quantum hall effect without landau levels: Condensed-matter realization of the" parity anomaly". *Physical review letters*, 61(18):2015, 1988.

[87] B. I. Halperin. Quantized hall conductance, current-carrying edge states, and the existence of extended states in a two-dimensional disordered potential. *Physical Review B*, 25(4):2185, 1982.

[88] M. Z. Hasan and C. L. Kane. Colloquium: topological insulators. *Reviews of Modern Physics*, 82(4):3045, 2010.

[89] E. Hecht and A. Zajac. Optics addison-wesley. *Reading, Mass*, 19872:350–351, 1974.

[90] D. R. Hofstadter. Energy levels and wave functions of bloch electrons in rational and irrational magnetic fields. *Physical review B*, 14(6):2239, 1976.

[91] J. Holmer and M. Zworski. Geometric structure of nls evolution. *arXiv preprint arXiv:0809.1844*, 2008.

[92] R. Hoyle and R. B. Hoyle. *Pattern formation: an introduction to methods*. Cambridge University Press, 2006.

[93] S. D. Huber. Topological mechanics. *Nature Physics*, 12(7):621, 2016.

[94] G. Iooss and M.-C. Pérouème. Perturbed homoclinic solutions in reversible 1: 1 resonance vector fields. *Journal of differential equations*, 102(1):62–88, 1993.

[95] V. G. Ivancevic, T. T. Ivancevic, et al. Sine–gordon solitons, kinks and breathers as physical models of nonlinear excitations in living cellular structures. *Journal of Geometry and Symmetry in Physics*, 31:1–56, 2013.

[96] S. K. Ivanov, Y. V. Kartashov, A. Szameit, L. Torner, and V. V. Konotop. Vector topological edge solitons in floquet insulators. *ACS Photonics*, 7(3):735–745, 2020.

[97] M. H. Jakubowski, K. Steiglitz, and R. Squier. State transformations of colliding optical solitons and possible application to computation in bulk media. *Physical Review E*, 58(5):6752, 1998.

[98] M. H. Jakubowski, K. Steiglitz, and R. Squier. Computing with solitons: a review and prospectus. *Collision-based computing*, pages 277–297, 2002.

[99] Y. Jiang, B. Tian, W.-J. Liu, K. Sun, M. Li, and P. Wang. Soliton interactions and complexes for coupled nonlinear schrödinger equations. *Physical Review E*, 85(3):036605, 2012.

[100] J. D. Joannopoulos, P. R. Villeneuve, and S. Fan. Photonic crystals. *Solid State Communications*, 102(2-3):165–173, 1997.

[101] Z. Jovanoski, N. Ansari, I. Towers, and R. Sammut. Exact domain-wall solitons. *Physics Letters A*, 372(5):610–612, 2008.

[102] C. Kane and T. Lubensky. Topological boundary modes in isostatic lattices. *Nature Physics*, 10(1):39, 2014.

[103] C. L. Kane and E. J. Mele. Quantum spin hall effect in graphene. *Physical review letters*, 95(22):226801, 2005.

[104] C. L. Kane and E. J. Mele. Z2 topological order and the quantum spin hall effect. *Physical review letters*, 95(14):146802, 2005.

[105] T. Kanna and M. Lakshmanan. Exact soliton solutions, shape changing collisions, and partially coherent solitons in coupled nonlinear schrödinger equations. *Physical review letters*, 86(22):5043, 2001.

[106] T. Kanna, M. Lakshmanan, P. T. Dinda, and N. Akhmediev. Soliton collisions with shape change by intensity redistribution in mixed coupled nonlinear schrödinger equations. *Physical Review E*, 73(2):026604, 2006.

[107] Y. V. Kartashov, B. A. Malomed, and L. Torner. Solitons in nonlinear lattices. *Reviews of Modern Physics*, 83(1):247, 2011.

[108] Y. V. Kartashov and D. V. Skryabin. Modulational instability and solitary waves in polariton topological insulators. *Optica*, 3(11):1228–1236, 2016.

[109] S. Katz and S. Givli. Solitary waves in a bistable lattice. *Extreme Mechanics Letters*, 22:106 – 111, 2018.

[110] D. Kaup and B. Malomed. Soliton trapping and daughter waves in the manakov model. *Physical Review A*, 48(1):599, 1993.

[111] P. Kelley. Self-focusing of optical beams. *Physical Review Letters*, 15(26):1005, 1965.

[112] P. Kevrekidis and D. Frantzeskakis. Solitons in coupled nonlinear schrödinger models: a survey of recent developments. *Reviews in Physics*, 1:140–153, 2016.

[113] A. B. Khanikaev, S. H. Mousavi, W.-K. Tse, M. Kargarian, A. H. MacDonald, and G. Shvets. Photonic topological insulators. *Nature materials*, 12(3):233, 2013.

[114] C. Kharif and E. Pelinovsky. Physical mechanisms of the rogue wave phenomenon. *European Journal of Mechanics-B/Fluids*, 22(6):603–634, 2003.

[115] S. K. Kim and Y. Tserkovnyak. Chiral edge mode in the coupled dynamics of magnetic solitons in a honeycomb lattice. *Physical review letters*, 119(7):077204, 2017.

[116] P. Kirrmann, G. Schneider, and A. Mielke. The validity of modulation equations for extended systems with cubic nonlinearities. 1992.

[117] C. Kittel, P. McEuen, and P. McEuen. *Introduction to solid state physics*, volume 8. Wiley New York, 1996.

[118] Y. S. Kivshar and D. K. Campbell. Peierls-nabarro potential barrier for highly localized nonlinear modes. *Physical Review E*, 48(4):3077, 1993.

[119] Y. S. Kivshar and B. Luther-Davies. Dark optical solitons: physics and applications. *Physics reports*, 298(2-3):81–197, 1998.

[120] Y. S. Kivshar and B. A. Malomed. Raman-induced optical shocks in nonlinear fibers. *Optics letters*, 18(7):485–487, 1993.

[121] K. v. Klitzing, G. Dorda, and M. Pepper. New method for high-accuracy determination of the fine-structure constant based on quantized hall resistance. *Physical Review Letters*, 45(6):494, 1980.

[122] M. König, S. Wiedmann, C. Brüne, A. Roth, H. Buhmann, L. W. Molenkamp, X.-L. Qi, and S.-C. Zhang. Quantum spin hall insulator state in hgte quantum wells. *Science*, 318(5851):766–770, 2007.

[123] D. Kordeweg and G. de Vries. On the change of form of long waves advancing in a rectangular channel, and a new type of long stationary wave. *Phil. Mag*, 39:422–443, 1895.

[124] M. Levin and A. Stern. Fractional topological insulators. *Physical review letters*, 103(19):196803, 2009.

[125] D. Leykam and Y. D. Chong. Edge solitons in nonlinear-photonic topological insulators. *Physical review letters*, 117(14):143901, 2016.

[126] C. Li, F. Ye, X. Chen, Y. V. Kartashov, A. Ferrando, L. Torner, and D. V. Skryabin. Lieb polariton topological insulators. *Physical Review B*, 97(8):081103, 2018.

[127] J.-M. Liu. *Photonic devices*. Cambridge University Press, 2009.

[128] W.-J. Liu, B. Tian, and M. Lei. Elastic and inelastic interactions between optical spatial solitons in nonlinear optics. *Laser Physics*, 23(9):095401, 2013.

[129] L. Lu, J. D. Joannopoulos, and M. Soljačić. Topological photonics. *Nature Photonics*, 8(11):821, 2014.

[130] G. Ma and P. Sheng. Acoustic metamaterials: From local resonances to broad horizons. *Science advances*, 2(2):e1501595, 2016.

[131] Y. Ma. *Localized structures in forced oscillatory systems*. PhD thesis, UC Berkeley, 2011.

[132] Y.-C. Ma. The perturbed plane-wave solutions of the cubic schrödinger equation. *Studies in Applied Mathematics*, 60(1):43–58, 1979.

[133] Y.-P. Ma, J. Burke, and E. Knobloch. Defect-mediated snaking: A new growth mechanism for localized structures. *Physica D: Nonlinear Phenomena*, 239(19):1867–1883, 2010.

[134] Y.-P. Ma and E. Knobloch. Depinning, front motion, and phase slips. *Chaos: An Interdisciplinary Journal of Nonlinear Science*, 22(3):033101, 2012.

[135] V. G. Makhankov. Quasi-classical solitons in the lindner-fedyanin model-"hole"-like excitations. *Physics Letters A*, 81(2-3):156–160, 1981.

[136] S. V. Manakov. On the theory of two-dimensional stationary self-focusing of electromagnetic waves. *Soviet Physics-JETP*, 38(2):248–253, 1974.

[137] K. H. Matlack, M. Serra-Garcia, A. Palermo, S. D. Huber, and C. Daraio. Designing perturbative metamaterials from discrete models. *Nature materials*, 17(4):323, 2018.

[138] C. Menyuk. Nonlinear pulse propagation in birefringent optical fibers. *IEEE Journal of Quantum electronics*, 23(2):174–176, 1987.

[139] J. E. Moore. The birth of topological insulators. *Nature*, 464(7286):194, 2010.

[140] S. H. Mousavi, A. B. Khanikaev, and Z. Wang. Topologically protected elastic waves in phononic metamaterials. *Nature communications*, 6(1):1–7, 2015.

[141] H. M'F, S. Métens, P. Borckmans, and G. Dewel. Pattern selection in the generalized swift-hohenberg model. *Physical Review E*, 51(3):2046, 1995.

[142] L. M. Nash, D. Kleckner, A. Read, V. Vitelli, A. M. Turner, and W. T. Irvine. Topological mechanics of gyroscopic metamaterials. *Proceedings of the National Academy of Sciences*, 112(47):14495–14500, 2015.

[143] F. I. Ndzana, A. Mohamadou, and T. C. Kofané. Modulational instability in the cubic–quintic nonlinear schrödinger equation through the variational approach. *Optics communications*, 275(2):421–428, 2007.

[144] C. Nore, M. Brachet, and S. Fauve. Numerical study of hydrodynamics using the nonlinear schrödinger equation. *Physica D: Nonlinear Phenomena*, 65(1-2):154–162, 1993.

[145] Y. Ohta, D.-S. Wang, and J. Yang. General n-dark–dark solitons in the coupled nonlinear schrödinger equations. *Studies in Applied Mathematics*, 127(4):345–371, 2011.

[146] T. Ozawa, H. M. Price, A. Amo, N. Goldman, M. Hafezi, L. Lu, M. C. Rechtsman, D. Schuster, J. Simon, O. Zilberberg, et al. Topological photonics. *Reviews of Modern Physics*, 91(1):015006, 2019.

[147] R. K. Pal, M. Schaeffer, and M. Ruzzene. Helical edge states and topological phase transitions in phononic systems using bi-layered lattices. *Journal of Applied Physics*, 119(8):084305, 2016.

[148] R. K. Pal, J. Vila, M. Leamy, and M. Ruzzene. Amplitude-dependent topological edge states in nonlinear phononic lattices. *Physical Review E*, 97(3):032209, 2018.

[149] F. Palmero, J. Han, L. Q. English, T. Alexander, and P. Kevrekidis. Multifrequency and edge breathers in the discrete sine-gordon system via subharmonic driving: Theory, computation and experiment. *Physics Letters A*, 380(3):402–407, 2016.

[150] D. E. Pelinovsky and Y. Shimabukuro. Existence of global solutions to the derivative nls equation with the inverse scattering transform method. *International Mathematics Research Notices*, 2018(18):5663–5728, 2018.

[151] D. Peregrine. Water waves, nonlinear schrödinger equations and their solutions. *The ANZIAM Journal*, 25(1):16–43, 1983.

[152] V. M. Perez-Garcia, H. Michinel, J. Cirac, M. Lewenstein, and P. Zoller. Dynamics of bose-einstein condensates: Variational solutions of the gross-pitaevskii equations. *Physical Review A*, 56(2):1424, 1997.

[153] A. Pikovsky, M. Rosenblum, J. Kurths, and J. Kurths. *Synchronization: a universal concept in nonlinear sciences*, volume 12. Cambridge university press, 2003.

[154] L. P. Pitaevskii. Vortex lines in an imperfect bose gas. *Sov. Phys. JETP*, 13(2):451–454, 1961.

[155] B. Prinari, M. J. Ablowitz, and G. Biondini. Inverse scattering transform for the vector nonlinear schrödinger equation with nonvanishing boundary conditions. *Journal of mathematical physics*, 47(6):063508, 2006.

[156] X.-L. Qi and S.-C. Zhang. Topological insulators and superconductors. *Reviews of Modern Physics*, 83(4):1057, 2011.

[157] R. Radhakrishnan, A. Kundu, and M. Lakshmanan. Coupled nonlinear schrödinger equations with cubic-quintic nonlinearity: integrability and soliton interaction in non-kerr media. *Physical Review E*, 60(3):3314, 1999.

[158] R. Radhakrishnan, M. Lakshmanan, and J. Hietarinta. Inelastic collision and switching of coupled bright solitons in optical fibers. *Physical Review E*, 56(2):2213, 1997.

[159] D. Rand and K. Steiglitz. Computing with solitons. *Computational Complexity: Theory, Techniques, and Applications*, pages 646–665, 2012.

[160] M. C. Rechtsman, J. M. Zeuner, Y. Plotnik, Y. Lumer, D. Podolsky, F. Dreisow, S. Nolte, M. Segev, and A. Szameit. Photonic floquet topological insulators. *Nature*, 496(7444):196, 2013.

[161] R. Richter and I. V. Barashenkov. Two-dimensional solitons on the surface of magnetic fluids. *Physical review letters*, 94(18):184503, 2005.

[162] G. Roskes. Some nonlinear multiphase interactions. *Studies in Applied Mathematics*, 55(3):231–238, 1976.

[163] R. Saeed, A. Shah, and M. Noaman-ul Haq. Nonlinear korteweg–de vries equation for soliton propagation in relativistic electron-positron-ion plasma with thermal ions. *Physics of Plasmas*, 17(10):102301, 2010.

[164] G. Salerno, A. Berardo, T. Ozawa, H. M. Price, L. Taxis, N. M. Pugno, and I. Carusotto. Spin–orbit coupling in a hexagonal ring of pendula. *New Journal of Physics*, 19(5):055001, 2017.

[165] B. Sandstede. Stability of travelling waves. In *Handbook of dynamical systems*, volume 2, pages 983–1055. Elsevier, 2002.

[166] A. Shabat and V. Zakharov. Exact theory of two-dimensional self-focusing and one-dimensional self-modulation of waves in nonlinear media. *Soviet physics JETP*, 34(1):62, 1972.

[167] D. Sheng, Z. Weng, L. Sheng, and F. Haldane. Quantum spin-hall effect and topologically invariant chern numbers. *Physical review letters*, 97(3):036808, 2006.

[168] T. Shi, H. Kimble, and J. I. Cirac. Topological phenomena in classical optical networks. *Proceedings of the National Academy of Sciences*, page 201708944, 2017.

[169] S. R. Sklan and B. Li. A unified approach to nonlinear transformation materials. *Scientific reports*, 8(1):4436, 2018.

[170] N. F. Smyth and W. L. Kath. Radiative losses due to pulse interactions in birefringent nonlinear optical fibers. *Physical Review E*, 63(3):036614, 2001.

[171] D. D. J. M. Snee and Y.-P. Ma. Edge solitons in a nonlinear mechanical topological insulator. *Extreme Mechanics Letters*, page 100487, 2019.

[172] D. Son and M. Stephanov. Domain walls of relative phase in two-component bose-einstein condensates. *Physical Review A*, 65(6):063621, 2002.

[173] P. Sprenger, M. Hoefer, and G. El. Hydrodynamic optical soliton tunneling. *Physical Review E*, 97(3):032218, 2018.

[174] K. Steiglitz. Time-gated manakov spatial solitons are computationally universal. *Physical Review E*, 63(1):016608, 2000.

[175] S. H. Strogatz. *Nonlinear dynamics and chaos with student solutions manual: With applications to physics, biology, chemistry, and engineering*. CRC press, 2018.

[176] C. Sulem and P.-L. Sulem. *The nonlinear Schrödinger equation: self-focusing and wave collapse*, volume 139. Springer Science & Business Media, 2007.

[177] R. Süsstrunk and S. D. Huber. Observation of phononic helical edge states in a mechanical topological insulator. *Science*, 349(6243):47–50, 2015.

[178] R. Süsstrunk and S. D. Huber. Classification of topological phonons in linear mechanical metamaterials. *Proceedings of the National Academy of Sciences*, 113(33):E4767–E4775, 2016.

[179] E. Tadmor. A review of numerical methods for nonlinear partial differential equations. *Bulletin of the American Mathematical Society*, 49(4):507–554, 2012.

[180] N. W. Taylor, L. E. Kidder, and S. A. Teukolsky. Spectral methods for the wave equation in second-order form. *Physical Review D*, 82(2):024037, 2010.

[181] D. J. Thouless, M. Kohmoto, M. P. Nightingale, and M. den Nijs. Quantized hall conductance in a two-dimensional periodic potential. *Physical review letters*, 49(6):405, 1982.

[182] L. N. Trefethen. *Spectral methods in MATLAB*. SIAM, 2000.

[183] M. Trippenbach, K. Góral, K. Rzazewski, B. Malomed, and Y. Band. Structure of binary bose-einstein condensates. *Journal of Physics B: Atomic, Molecular and Optical Physics*, 33(19):4017, 2000.

[184] F. Tsitoura, U. Gietz, A. Chabchoub, and N. Hoffmann. Phase domain walls in weakly nonlinear deep water surface gravity waves. *Physical review letters*, 120(22):224102, 2018.

[185] L. S. Tuckerman and D. Barkley. Bifurcation analysis of the eckhaus instability. *Physica D: Nonlinear Phenomena*, 46(1):57–86, 1990.

[186] J. Tzou, Y.-P. Ma, A. Bayliss, B. J. Matkowsky, and V. Volpert. Homoclinic snaking near a codimension-two turing-hopf bifurcation point in the brusselator model. *Physical Review E*, 87(2):022908, 2013.

[187] G. Vahala, L. Vahala, and J. Yepez. Inelastic vector soliton collisions: a lattice–based quantum representation. *Philosophical Transactions of the Royal Society of London. Series A: Mathematical, Physical and Engineering Sciences*, 362(1821):1677–1690, 2004.

[188] M. Vijayajayanthi, T. Kanna, and M. Lakshmanan. Bright-dark solitons and their collisions in mixed n-coupled nonlinear schrödinger equations. *Physical Review A*, 77(1):013820, 2008.

[189] M. Vijayajayanthi, T. Kanna, and M. Lakshmanan. Multisoliton solutions and energy sharing collisions in coupled nonlinear schrödinger equations with focusing, defocusing and mixed type nonlinearities. *The European Physical Journal Special Topics*, 173(1):57–80, 2009.

[190] P. Wang, L. Lu, and K. Bertoldi. Topological phononic crystals with one-way elastic edge waves. *Physical review letters*, 115(10):104302, 2015.

[191] P. Wang, J. Shim, and K. Bertoldi. Effects of geometric and material nonlinearities on tunable band gaps and low-frequency directionality of phononic crystals. *Physical Review B*, 88(1):014304, 2013.

[192] Z. Wang, Y. Chong, J. D. Joannopoulos, and M. Soljačić. Observation of unidirectional backscattering-immune topological electromagnetic states. *Nature*, 461(7265):772, 2009.

[193] S. Watabe, Y. Kato, and Y. Ohashi. Excitation transport through a domain wall in a bose-einstein condensate. *Physical Review A*, 86(2):023622, 2012.

[194] P. Woods and A. Champneys. Heteroclinic tangles and homoclinic snaking in the unfolding of a degenerate reversible hamiltonian–hopf bifurcation. *Physica D: Nonlinear Phenomena*, 129(3-4):147–170, 1999.

[195] S. Wu, Y. Wu, and J. Mei. Topological helical edge states in water waves over a topographical bottom. *New Journal of Physics*, 20(2):023051, 2018.

[196] L. Xie, L.-j. Yang, and H.-y. Ye. Instability of gas-surrounded rayleigh viscous jets: Weakly nonlinear analysis and numerical simulation. *Physics of Fluids*, 29(7):074101, 2017.

[197] J. Xin. Front propagation in heterogeneous media. *SIAM review*, 42(2):161–230, 2000.

[198] Y. Xiong, T. Wang, and P. Tong. The effects of dissipation on topological mechanical systems. *Scientific reports*, 6:32572, 2016.

[199] C. Xu and J. E. Moore. Stability of the quantum spin hall effect: Effects of interactions, disorder, and z 2 topology. *Physical Review B*, 73(4):045322, 2006.

[200] Y. Xu, T. Alexander, H. Sidhu, and P. G. Kevrekidis. Instability dynamics and breather formation in a horizontally shaken pendulum chain. *Physical Review E*, 90(4):042921, 2014.

[201] H. Xue, Y. Yang, G. Liu, F. Gao, Y. Chong, and B. Zhang. Realization of an acoustic third-order topological insulator. *Physical review letters*, 122(24):244301, 2019.

[202] J. Yang and Y. Tan. Fractal structure in the collision of vector solitons. *Physical review letters*, 85(17):3624, 2000.

[203] L. Yang, C. Wang, Q. Fu, M. Du, and M. Tong. Weakly nonlinear instability of planar viscous sheets. *Journal of fluid mechanics*, 735:249, 2013.

[204] A. Yochelis and A. Garfinkel. Front motion and localized states in an asymmetric bistable activator-inhibitor system with saturation. *Physical Review E*, 77(3):035204, 2008.

[205] S. Yves, R. Fleury, F. Lemoult, M. Fink, and G. Lerosey. Topological acoustic polaritons: robust sound manipulation at the subwavelength scale. *New Journal of Physics*, 19(7):075003, 2017.

[206] N. J. Zabusky and M. D. Kruskal. Interaction of" solitons" in a collisionless plasma and the recurrence of initial states. *Physical review letters*, 15(6):240, 1965.

[207] N. J. Zabusky and M. A. Porter. Soliton. *Scholarpedia*, 5(8):2068, 2010.

[208] V. Zakharov and S. Manakov. Resonant interaction of wave packets in nonlinear media. *Zh. Eksp. Teor. Fiz. Pisma Red*, 18:413, 1973.

[209] V. Zakharov and A. Shabat. Interaction between solitons in a stable medium. *Sov. Phys. JETP*, 37(5):823–828, 1973.

[210] V. E. Zakharov and E. Schulman. To the integrability of the system of two coupled nonlinear schrödinger equations. *Physica D: Nonlinear Phenomena*, 4(2):270–274, 1982.

[211] F. Zhang. *The Schur complement and its applications*, volume 4. Springer Science & Business Media, 2006.

[212] Z. Zhang, Y. Tian, Y. Cheng, Q. Wei, X. Liu, and J. Christensen. Topological acoustic delay line. *Physical Review Applied*, 9(3):034032, 2018.

[213] T. Zhao, T. Bo, J. Yan, W. Pan, and L. Min. Dynamics of the manakov solitons in biased guest-host photorefractive polymer. *Communications in Theoretical Physics*, 60(2):150, 2013.

[214] X. Zhou, Y. Wang, D. Leykam, and Y. D. Chong. Optical isolation with nonlinear topological photonics. *New Journal of Physics*, 19(9):095002, 2017.

[215] A. Zvezdin and A. Popkov. Contribution to the nonlinear theory of magnetostatic spin waves. *Sov. Phys. JETP*, 2(350):150, 1983.

Appendix A

Connections between ZZ and NN

We will briefly consider the heteroclinic connections between the uniform states of ZZ and NN. The existence of a heteroclinic connection between these states depends on if there is a set of values in the travelling wave parameter space $(C_g, \omega_A, \omega_B)$ that provides a solution to $\mathcal{E}^{ZZ} = \mathcal{E}^{NN}$. If one substitutes the equilibria in to Eq. (5.31) and equates the two then, just as with ZN and NZ, we can write the equality as a quartic equation in C_g, given by

$$M_1 C_g^4 + 8d_1 d_2 (M_2\omega_A + M_3\omega_B) C_g^2 + 16 d_1^2 d_2^2 (g_3 g_4 \omega_A^2 + g_1 g_2 \omega_B^2 - 2 g_2 g_4 \omega_A \omega_B) = 0. \tag{A.1}$$

where,

$$\begin{aligned} M_1 &= (g_1 g_2 d_1^2 + g_3 g_4 d_2^2 - 2 d_1 d_2 g_2 g_4), \\ M_2 &= g_4 (d_1 g_2 - d_2 g_3), \\ M_3 &= g_2 (d_2 g_4 - d_1 g_1). \end{aligned}$$

We see that this equation can be reduced, once again, to a quadratic equation in C_g^2. A physical solution is deemed possible when there exists a root to the equation such that the group velocity is defined in real space $C_g^2 \in \mathcal{R}$ and $C_g^2 \geq 0$. The roots of the equation (A.1) are given explicitly by

$$C_{g\pm}^{\ 2} = -\frac{4 d_1 d_2}{M_1} \Big[\omega_B (M_3 \pm d_2 \sqrt{g_2 g_4 (g_2 g_4 - g_1 g_3)}). + \omega_A (M_2 \mp d_1 \sqrt{g_2 g_4 (g_2 g_4 - g_1 g_3)}) \Big] \tag{A.2}$$

There is a simple relationship between the travelling wave parameter space of the form $C_{g\pm}^2 = \omega_B N_{1\mp} + \omega_A N_{2\pm}$. Firstly, we observe that the denominator of Eq. (A.2) is zero for the Manakov systems ($|d_1| = |d_2|$, $|g_1| = |g_2| = |g_3| =$

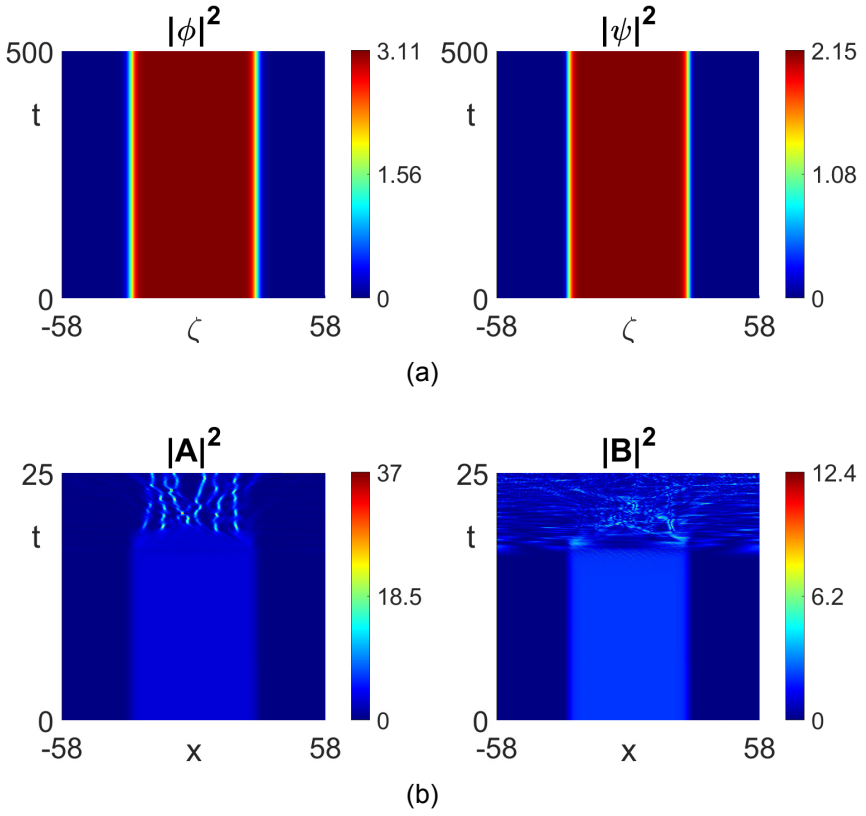

Figure A.1: Solution obtained through the connection between ZZ and NN. (a) The structure of $\phi(\zeta)$ and $\psi(\zeta)$ is shown to propagate in the dissipative PDE (5.38-5.39). (b) The steady state of Fig. A.1(a) is taken and shown to evolve in the CNLS. The structure is stationary for all time in (a), and is plotted in the comoving reference frame in (b).

$|g_4|$), which is due to the vanishing C_g^4 term of Eq. (A.1). One can not produce a solution in the Manakov systems as the denominator of the NN equilibria becomes zero, and is therefore undefined. Providing that $g_1 \neq g_2$, there is the possibility of a physical group velocity in the symmetrically-coupled CNLS, as long as $|g_2| > |g_1|$ is satisfied. This condition, however, directly contradicts the SHATS conditions for NN. Therefore, we can conclude that no connections between ZZ and NN can be formed in either the Manakov systems or the symmetrical equation scenarios.

There are some CNLS systems which allow a connection to form between these two uniform states, but due to the number of SHATS conditions, they are not analytically obvious. If one searches for the CNLS system parameters that permit SHATS numerically, then we can refine further and consider those travelling wave parameters that satisfy Eq. (A.2). As stated previously, the large number of constraints required to produce these fronts is non-favourable, especially in comparison to the connection between ZN and NZ. One example of a system that permits these connections is the CNLS with system parameters $d_1 = d_2 = -5$, $g_1 = -1$, $g_2 = 1$, $g_3 = 4$, and $g_4 = -5$. This system

allows for a plethora travelling wave parameters that provide SHATS ZZ and NN, and satisfies the condition (A.2). An example connection is shown in Fig. A.1 for the travelling wave parameters $(C_g, \omega_A, \omega_B) = (5.408, -0.5, 5.5)$. This set of parameters leads to the equilibria $(\phi_0, \psi_0) = (1.765, 1.467)$. Firstly, the structure evolves stably in the dissipative PDE (5.38-5.39) and a steady state solution is found; see Fig. A.1(a). The problem of stability comes when one attempts to evolve this steady state in the CNLS, as shown in Fig. A.1(b). Since the uniform states are SHATS, the instability of the structure is caused by the connection itself. This is also reflected if one considers the spectrum of the CNLS equation. Previously, for the front connecting ZN to NZ, the CNLS spectrum showed stability of the structure. This stability is enforced because the travelling front inherits the SHATS stability of the uniform states. For the connection from ZZ to NN, this is not the case and therefore, for stable profiles, one can not rely on the SHATS conditions alone. The analysis of stable ZZ and NN connections falls outside of our current framework and analysis of these structures will be considered in future work. We may note, however, that some of these connections remain stable for a small period of time. This may be considered useful when proposing solutions to the MTI, but the very particular constraints on the system parameters leaves very little freedom for such structures to be found. As mentioned in Sec. 5.2, we focus primarily on the connections between ZN and NZ, since these connections are typically what is referred to in the literature, when one mentions a travelling front.